UNIVERSITAT DE
BARCELONA

Statistical detection of tidal streams generated by globular clusters and their application to measure the axis ratio of the Milky Way dark matter halo

Carles Garcia Palau

PhD THESIS

STATISTICAL DETECTION OF TIDAL STREAMS GENERATED BY GLOBULAR CLUSTERS AND THEIR APPLICATION TO MEASURE THE AXIS RATIO OF THE MILKY WAY DARK MATTER HALO

CARLES GARCIA PALAU

UNIVERSITAT DE
BARCELONA

STATISTICAL DETECTION OF TIDAL STREAMS GENERATED BY GLOBULAR CLUSTERS AND THEIR APPLICATION TO MEASURE THE AXIS RATIO OF THE MILKY WAY DARK MATTER HALO

Memòria presentada per optar al grau de doctor per la

Universitat de Barcelona

Programa de doctorat en Enginyeria i Ciències Aplicades

Autor:

Carles Garcia Palau

Director:

Jordi Miralda Escudé

Tutor:

Atilà Herms Berenguer

UNIVERSITAT DE BARCELONA

Acknowledgements

I would like to thank my supervisor Jordi Miralda Escudé for giving me the opportunity to work on this project on the dynamics of the Milky Way and on stellar streams. His motivation, knowledge and advice have been indispensable for the elaboration of this thesis. I would like to thank Hamish Silverwood, Mark Gieles, and Daisuke Kawata for their comments that have helped me to improve the content of this thesis. I also thank Francesca Figueras, Roger Mor, Mercè Romero, and all my colleagues of the *Gaia* team at the University of Barcelona for helpful discussions and useful insights. I am also very grateful to my parents. Without their support, this thesis would not have been possible.

Abstract

In this thesis we have presented a new method to search for tidal streams generated by globular clusters in the *Gaia* catalogue. This method is based on the maximum likelihood technique to distinguish stream stars from foreground field stars. It uses the phase-space location of each star and a realistic phase-space model of the stellar stream and of the Milky Way to evaluate a statistical test to determine whether the stream exists or not. If the statistical test is positive, the method is designed to select the stars with the highest probability of being members of the stream using their phase-space coordinates. Finally, in our final selection, we include only those that are colour and magnitude compatible with the progenitor cluster.

We apply the statistical method to *Gaia* Data Release 2 catalogue. We detect a clear tidal stream generated by the globular cluster M68 (NGC 4590) that spans the entire North Galactic hemisphere. A section of this stream coincides with a previously discovered stream named Fjörm. We select 115 stream stars that are colour and magnitude compatible with the progenitor cluster. We also detect the tidal stream generated by the globular cluster NGC 3201 extending about 140 deg in the sky. A section of the trailing arm of this stream coincides with the previously catalogued stream Gjöll. We select 170 highly likely member stars of this stream. We have also applied the statistical method to identify 126 stars belonging to the already known Palomar 5 stellar stream.

We use these three streams to constrain the shape of the dark halo of the Milky Way within 20 kpc from the Galactic centre. We assume an axisymmetric mass model of the Galaxy constructed from the sum of two exponential profiles for the thin and thick disc, a flattened bulge, and a two power-law density profile for the dark halo. We compute the best-fitting values of the parameters characterising the model using a Bayesian statistical method, which includes constraints on the mass distribution, the circular velocity curve of the Milky Way, and several kinematical and dynamical properties of the Galaxy in the vicinity of the Sun.

We focus our analysis on the shape of the dark matter halo out of the plane of the disc. In particular, we study the halo density axis ratio q_ρ^{dh}. The stream of NGC 3201 does not provide a strong constraint on this parameter giving $q_\rho^{\mathrm{dh}} = 2.06 \pm 0.93$. The stream of M68 favours a moderately prolate dark halo but compatible with a spherical shape of $q_\rho^{\mathrm{dh}} = 1.14^{+0.21}_{-0.14}$. Palomar 5 requires a prolate or oblate halo of $q_\rho^{\mathrm{dh}} = 1.01 \pm 0.09$ which fits well with the spherical shape. All three streams together favour a prolate dark halo of $q_\rho^{\mathrm{dh}} = 1.06 \pm 0.06$ compatible with the spherical shape. These results are

compatible with previous studies using stellar streams and recent studies using different fitting methodologies based on different observational data, such as globular clusters or halo stars in equilibrium with the dark halo. These results are in tension with cosmological simulations in which the influence of baryons on the distribution of dark matter have been included. In general, the simulations predict oblate halos for Milky Way-like galaxies, with axis ratios typically in the range $q_\rho^{\mathrm{dh}} \in [0.6\,\text{-}\,0.8]$.

Resum

En aquesta tesi s'ha presentat un nou mètode per cercar rieres de marea generades per cúmuls globulars al catàleg *Gaia*. Aquest mètode es basa en la tècnica de màxima probabilitat per distingir les estrelles de la riera de les estrelles del fons. El mètode utilitza la ubicació a l'espai de fase de cada estrella i un model realista de l'espai de fase de la riera estel·lar i de la Via Làctia per avaluar una prova estadística que determina si la riera existeix o no. Si la prova estadística és positiva, el mètode està dissenyat per seleccionar les estrelles amb la probabilitat més gran de ser membres de la riera utilitzant les seves coordenades a l'espai de fase. Finalment, només es seleccionen aquelles estrelles que són compatibles en color i magnitud amb el cúmul progenitor.

El mètode estadístic s'ha aplicat a la segona versió del catàleg de *Gaia* (*Gaia* Data Release 2). S'ha detectat clarament una riera de marea generada pel cúmul globular M68 (NGC 4590) que s'estén al llarg de tot l'Hemisferi Nord Galàctic. Una secció d'aquesta riera coincideix amb una riera prèviament descoberta i anomenada Fjörm. S'han seleccionat 115 estrelles de la riera que són compatibles en color i magnitud amb el cúmul progenitor. També s'ha detectat la riera de marea generada pel cúmul globular NGC 3201 que s'estén al llarg de 140 graus en el cel. Una secció del braç posterior d'aquesta riera coincideix amb la riera prèviament catalogada Gjöll. S'han seleccionat 170 estrelles que són molt probablement membres de la riera. També s'ha aplicat el mètode estadístic per identificar 126 estrelles que pertanyen a la ja coneguda riera estel·lar de Palomar 5.

Aquestes tres rieres s'han emprat per constrènyer la forma de l'halo de matèria fosca de la Via Làctia fins a 20 kpc del centre Galàctic. S'ha assumit un model de massa axisimètric de la Galàxia construït a partir de la suma de dos perfils exponencials pel disc prim i el gruixut, un bulb aplanat i un perfil de densitat format per dues lleis potencials per a l'halo de matèria fosca. S'han calculat els valors de millor encaix dels paràmetres que caracteritzen el model utilitzant un mètode estadístic Bayesià, que inclou constrenyiments a la distribució de massa, la corba de velocitat circular de la Via Làctia, i diverses propietats cinemàtiques i dinàmiques de la galàxia a les proximitats del Sol.

L'anàlisi s'ha concentrat en la forma de l'halo de matèria fosca fora del pla del disc. En particular, s'ha estudiat la relació d'eixos que caracteritzen la densitat de l'halo o paràmetre d'aplanament q_ρ^{dh}. La riera de NGC 3201 no proporciona un constrenyiment significatiu en aquest paràmetre essent $q_\rho^{\text{dh}} = 2.06 \pm 0.93$. La riera de M68 afavoreix un halo de matèria fosca moderadament prolat però compatible amb una forma esfèrica de $q_\rho^{\text{dh}} = 1.14^{+0.21}_{-0.14}$. Palomar 5 requereix un halo prolat o oblat de $q_\rho^{\text{dh}} = 1.01 \pm 0.09$ que encaixa bé amb

la forma esfèrica. Les tres rieres juntes afavoreixen un halo de matèria fosca prolat de $q_\rho^{\mathrm{dh}} = 1.06 \pm 0.06$ compatible amb la forma esfèrica. Aquests resultats són compatibles amb estudis anteriors que utilitzen rieres estel·lars i estudis recents que utilitzen diferents metodologies d'encaix basades en diverses dades observacionals, com ara cúmuls globulars o estrelles de l'halo en equilibri amb l'halo de matèria fosca. Aquests resultats estan en tensió amb els resultats obtinguts amb simulacions cosmològiques en les quals s'ha inclòs la influència dels barions en la distribució de la matèria fosca. En general, les simulacions prediuen halos oblats per galàxies semblants a la Via Làctia, amb relació d'eixos típicament en el rang $q_\rho^{\mathrm{dh}} \in [0.6\text{-}0.8]$.

PUBLICATIONS

List of articles published and under review at the time of the thesis deposit:

Peer-reviewed articles

- Palau C. G. and Miralda-Escudé J. "Statistical detection of a tidal stream associated with the globular cluster M68 using Gaia data". MNRAS, 488(2):1535–1557, September 2019. doi: 10.1093/mnras/stz1790

- Palau C. G. and Miralda-Escudé J. "The tidal stream generated by the globular cluster NGC 3201". MNRAS, 504(2):2727–2741, June 2021. doi: 10.1093/mnras/stab1024

Articles under review

- Palau C. G. and Miralda-Escudé J. "The oblateness of the Milky Way dark matter halo from the stellar streams of NGC 3201, M68, and Palomar 5"

Contents

Chapter 1

Introduction

The Milky Way is a barred spiral galaxy, it is the second largest member of the Local Group of galaxies (see e.g. van den Bergh, 2000; McConnachie, 2012). The largest member, the Andromeda galaxy (or M31), is also a spiral galaxy. The Milky Way and Andromeda are surrounded by a large number of smaller galaxies orbiting as satellites, and galaxies that have remained too far from both of them to have completed any orbit. The highest density peak of the Milky Way is defined as the position of the supermassive black hole Sagittarius A* (Reid and Brunthaler, 2004). There is a dense nucleus of stars around the black hole surrounded by a bulge connected to an elongated rotating bar of about 5 kpc in length. These components contain about 10 per cent of the stars in the Galaxy (see e.g. Bland-Hawthorn and Gerhard, 2016b). Most of the stars, almost 90 per cent, are found in the disc. The Galactic disc is a very flattened structure extending up to 25 kpc from the Galactic centre. The disc can be divided into a dominant thin disc and a less massive thick disc according to its chemistry and age. The two components can also be distinguished by their spatial distribution. They have a similar scale length, but the thick disc has a larger scale height than the thin disc. The Galactic disc also presents other features such as spiral arms, but we cannot provide a fully consistent picture of their characteristics because they are barely visible from the position of the Sun (Eilers et al., 2020). The Sun lies in the plane of the disc, at about 8.2 kpc from the centre (Gravity Collaboration et al., 2019). The bulge and the disc of the Galaxy are surrounded by a faint halo of stars and several satellites such as dwarf galaxies, open clusters or globular clusters. We show an artist's impression of the Milky Way in Figure 1.1. The Galactic bar and the disc with its spiral arms are shown in the left panel, and each component is labeled in the right panel.

The Milky Way bar and disc rotate. The disc presents a rotational curve that reaches a maximum of about 230 km s^{-1} at a Galactocentric radius r between 5 and 10 kpc from the Galactic centre (Eilers et al., 2019). Newton's law predicts rotation velocity falling as $r^{-1/2}$ outside the region containing most mass. That is not observed in the rotational curve of the Milky Way. Outside the solar circle, the rotational curve decreases with a small slope, being nearly flat at 20 kpc from the centre. On the outskirts of the disc, the terminal rotational velocity is about 200 km s^{-1}, a velocity too large to be sustained by the gravitational acceleration produced by the visible matter such as stars,
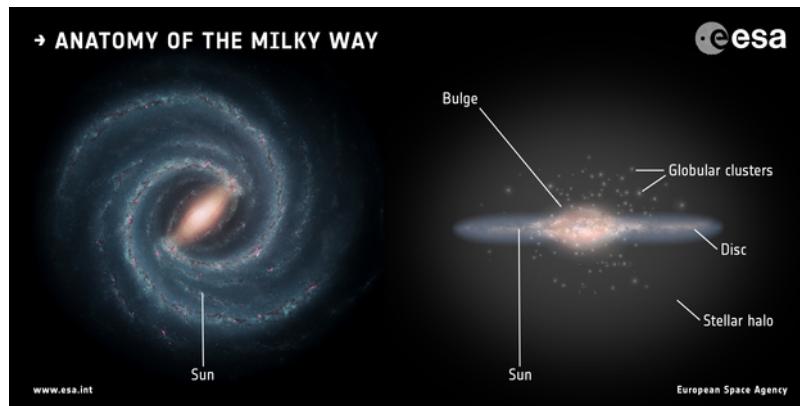
Figure 1.1: Artist's impression of the Milky Way galaxy.
(Copyright: Left: NASA/JPL-Caltech; Right: ESA; layout: ESA/ATG medialab)

dust, or gas according to Newton's laws. The visible matter is often called baryonic matter since most of the mass is made up of baryons, the particles that compose the nuclei of the atoms. This baryonic matter, only accounts for about 60 per cent of the total terminal velocity of the Galaxy.

The same flattened rotational curve has been observed systematically in other spiral galaxies (see e.g. Lelli et al., 2016). Similar discrepancies between the gravitational acceleration inferred from the distributions of baryons and the observed gravitational acceleration appear in general from small dwarf galaxies to galaxy clusters (see e.g. Binney and Tremaine, 1987). Usually, baryonic mass is not sufficient to explain the formation and evolution of galaxies, their motion in clusters, the merger processes, or gravitational lensing observations. To solve this problem, it has been proposed that galaxy clusters and galaxies are embedded in halos of non-baryonic matter (Zwicky, 1937; Rubin et al., 1978). It is called dark matter because it neither absorb nor emits light. This matter is usually assumed to consist of exotic particles such as Axions or WIMPs (see e.g. Feng, 2010; Arcadi et al., 2018) moving very slowly compared to initial infall velocities, or as it is usually stated, they are dynamically cold. Dark matter is also an important ingredient of cosmology, as it is necessary to explain the cosmic microwave background (CMB) or the current structure of the universe (see e.g. Mukhanov, 2005). Even so, these discrepancies have been attempted to be explained without adding any kind of new matter, only by modifications of the laws of general relativity, of which Newton's laws are an approximation (e.g. Famaey and McGaugh, 2012). In general, these modifications can accommodate flat rotation curves, but do not provide a consistent cosmological picture.

According to the Cold Dark Matter paradigm (e.g. Rees, 2000), dark halos are formed by mergers of small clusters of dark matter particles. In general, after a time to reach partial equilibrium, the halos have a triaxial spheroidal shape with a density profile that follows a well-defined power-law. Once the halo is formed, gas clouds fall to the centre by the loss of energy due to the emission of radiation, and form the galaxies we observe (e.g. Blumenthal et al.,

1984; Springel et al., 2005, 2006). The shape of the halos and their density profile are then modified by the effect of the growth of baryonic structures at their centres. This picture can be tested by measuring the density profile and the ellipticity of dark matter halos around external galaxies or galaxy clusters by X-ray observations of hot gas (e.g. Buote et al., 2002) or by weak lensing (Umetsu, 2020). In addition, the study of dark halos can provide constraints on the properties of dark matter particles that are crucial for their experimental detection. We can also test this paradigm by studying the dark halo of the Milky Way. In this case, we can constrain the distribution of dark matter by multiple observations and compare it with simulations of Milky Way-like galaxies.

1.1 The dark matter halo of the Milky Way

The dark halo of the Milky Way is the most unknown component of our galaxy. The shape of the halo cannot be studied by direct observation like the luminous baryonic matter, but their properties can be inferred from its dynamical effects on bodies under its gravitational influence. Similarly, it is difficult to study by simple analytical models that account for the spatial distribution of dark matter particles and their velocities due to the multi-component structure of the Galaxy. Alternatively, cosmological simulations offer predictions for the formation and evolution of Milky Way-like galaxies that can be used to estimate the general characteristics of the halo of the Galaxy. Cosmological simulations in which only dark matter has been taken into account suggest that the dark halos of Milky Way-like galaxies are triaxial spheroids (see e.g. Bullock et al., 2001). Their radial distribution ρ_{dh} is usually well described by a two-power law density profile with scale density $\rho_{0\mathrm{dh}}$, inner slope α, and outer slope β:

$$\rho_{\mathrm{dh}}(s) = \rho_0^{\mathrm{dh}} \left(\frac{s}{a_1}\right)^{-\alpha} \left(1 + \frac{s}{a_1}\right)^{\alpha-\beta} \ , \tag{1.1}$$

constant over ellipsoids of equation

$$s^2 \equiv a_1^2 \left(\frac{x^2}{a_1^2} + \frac{y^2}{a_2^2} + \frac{z^2}{a_3^2}\right) \ , \tag{1.2}$$

where a_i for $i = 1, 2, 3$ are the scale lengths of each axis. In general, galaxies in these simulations have a dark halo characterised by $\alpha = 1$ and $\beta = 3$. This model is called NFW density profile (Navarro et al., 1996). These halos have a steep rise of the density near the centre of slope $\alpha \sim 1$ (see e.g. Moore et al., 1999) which appears to be in contradiction with observations of the rotational curves of disc galaxies. In general, most of them fit better with cored distributions of dark matter with $\alpha \sim 0$ (see e.g. Li et al., 2020). This discrepancy is known as the core-cusp problem (de Blok, 2010).

The growth of a bulge and a disc at the centre of the halo modifies the triaxial NFW distribution of dark matter making the halo more spherical. In general, due to the effect of the flattened gravitational potential of the disc, the halos become axisymmetric with $a_1 \approx a_2$ and with the perpendicular axis (a_3) nearly parallel to the disc symmetry axis (Prada et al., 2019). We define the
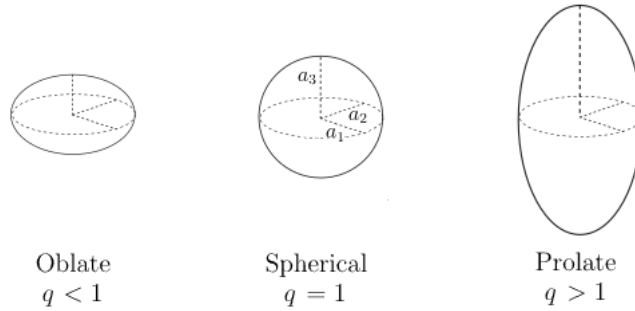
Figure 1.2: Oblate, spherical and prolate spheroids and their axis ratio $q \equiv a_3/a_1$.
(Copyright: Kot et al. (2017))

density axis ratio or flattening parameter as

$$q_\rho^{\mathrm{dh}} \equiv \frac{a_3}{a_1} \ .$$ (1.3)

When $q_\rho^{\mathrm{dh}} = 1$ the halo has spherical symmetry and equation 1.2 is equal to r^2. When $q_\rho^{\mathrm{dh}} < 1$ the halo is oblate (flattened), and when $q_\rho^{\mathrm{dh}} > 1$ it is prolate. We show in Figure 1.2 the shape of an oblate, spherical, and prolate spheroid and the axis ratio for each case. Cosmological simulations that include baryonic effects predict oblate dark halos with q_ρ^{dh} in the range [0.6 - 0.8] (e.g. Chua et al., 2019; Prada et al., 2019). Baryons also concentrate dark matter in the centre making the halo denser in the inner region of the galaxies, this phenomenon is known as halo contraction (see e.g. Cautun et al., 2020).

The radial profile of the dark matter halo of the Milky Way has been studied using different observational data, mainly by fitting the Galactic rotational curve. This method only constrains the halo in the plane of the disc. Therefore, it is necessary to include additional data beyond the disc to describe the overall shape of the halo. Several methods have been proposed to study the global distribution of dark matter around the Galaxy, producing a variety of inconsistent results. One approach is to assume that the halo stars are in dynamical equilibrium and fit a parametric model of the halo to their distribution using Jeans equations. For example, Loebman et al. (2012, 2014) using SDSS Segue halo star kinematic measurements obtained an oblate halo of $q_\rho^{\mathrm{dh}} = 0.4 \pm 0.1$ within 20 kpc. However, Bowden et al. (2016) found a prolate halo of $q_\rho^{\mathrm{dh}} \in [1.5 - 2.0]$. A recent study by (Wegg et al., 2019) using *Gaia* measurements of phase-space coordinates of RR Lyrae in the stellar halo obtained a halo compatible with the spherical shape of $q_\rho^{\mathrm{dh}} = 1 \pm 0.09$ within 30 kpc. A similar conclusion is obtained by Hattori et al. (2020). In this case, limitations of the fitting method restrict the study of the halo flattening to $q_\rho^{\mathrm{dh}} < 1$, finding a 99 per cent of the posterior distribution located at $q_\rho^{\mathrm{dh}} > 0.963$. On the other hand, Posti and Helmi (2019) use globular clusters as a dynamical tracers in equilibrium finding a prolate halo of $q_\rho^{\mathrm{dh}} = 1.3 \pm 0.25$. A different approach is taken by Nitschai et al. (2020). Using a method based on Jeans equations, they construct a dynamical model of the Galactic disc from a sample of disc stars with

six phase-space coordinates measured by *Gaia*. They obtain a prolate halo of $q_\rho^{\mathrm{dh}} = 1.14 \pm 0.21$.

Cosmological simulations also predict ratios between baryonic matter and total dark matter that can be tested by estimating the fraction of each type of matter in the Milky Way. The total mass of the Galaxy can be defined as the mass enclosed in a sphere of radius equal to the virial radius. Usually, the virial radius is defined as the radius such that the mean density of the galaxy is 200 times larger than the critical density of the universe, and is denoted r_{200}. From this definition, the total mass of the Milky Way has been inferred using different methods (Wang et al., 2020). For example, using the kinematics of various dynamical tracers of the Galactic halo such as stars or globular clusters, estimating the escape velocity using high-velocity objects, or using the rotational curve. In general, these studies use observational data contained in the inner region of the Galaxy. To compute the virial mass, they require extrapolations to the virial radius, which is expected to be $r_{200} \sim 200$ kpc. Alternatively, the mass can be estimated by modelling the motion of the Local Group or by modelling the phase-space distribution of the classical satellites of the Milky Way. These satellites are spread over a wider range of about 50 to 250 kpc from the Galactic centre. These estimates find a total mass that lies in the interval $[0.5\text{-}2] \times 10^{12}$ M$_\odot$, with the halo being the dominant component of the Galaxy with between 85 and 95 per cent of the total mass.

1.2 Stellar streams

An alternative method to study the shape of the dark halo of the Milky Way is by fitting stellar streams. These structures form when a progenitor satellite galaxy or cluster is tidally perturbed by the gravitational force of its host galaxy (Küpper et al., 2008, 2010, 2012). For a disc galaxy such as the Milky Way, the tidal forces are maximum when the satellite crosses the disc or passes near the bulge. Each tidal shock produces a loss of mass in the satellite in form of stripped stars. These stars approximately follow the orbit of the progenitor with small deviations in phase space and energy. The orbit of the progenitor can be reconstructed by fitting its stellar streams, and this orbit can be used to constrain the gravitational potential of the host galaxy (see e.g. Varghese et al., 2011; Price-Whelan et al., 2014; Bonaca et al., 2014).

Several streams have been discovered near the Milky Way (see e.g. Grillmair and Carlin, 2016; Shipp et al., 2018; Ibata et al., 2019b; Piatti and Carballo-Bello, 2020). The most massive are the streams associated with the Large Magellanic Cloud (LMC) and the Sagittarius dwarf galaxy. We plot the sky location of the streams in the Milky Way Streams Library (Galstreams, Mateu et al., 2018) in Figure 1.3. We indicate their heliocentric distance and their name. Some of them have been used to constrain the dark halo of the Milky Way. Early studies using Sagittarius stream provided contradictory results obtaining triaxial (Law et al., 2009; Law and Majewski, 2010; Deg and Widrow, 2013), oblate (Johnston et al., 2005; Fellhauer et al., 2006), and prolate halos (Helmi, 2004). Even so, the most recent study favours a prolate halo of $q_\rho^{\mathrm{dh}} = 1.17 \pm 0.1$ (Fardal et al., 2019). In general, most of the studies using Sagittarius stellar stream that conclude that the halo is oblate or prolate assume that the

Figure 1.3: Sky map in equatorial coordinates of the streams from the Milky Way Streams Library (Galstreams, Mateu et al., 2018). The heliocentric distance is shown with colours and labelled in the plot. The grey cross marks the Galactic centre, and the grey dashed lines indicate Galactic latitude $b = \pm 15$ deg.

halo is axisymmetric. In principle, the main cause of deviations from a general axisymmetric Galactic potential is the presence of the LMC. Despite its large mass of about $[1.4\text{-}25] \times 10^{10}$ $M_\odot$ (Erkal et al., 2019), it is often neglected. Even so, the influence of its potential and the non-inertial effects due to the Milky Way fall towards the LMC have recently been included in some models, questioning those claiming a triaxial shape of the dark halo. (see e.g. Gardner et al., 2020).

There are many stellar streams that are not associated with a known progenitor. For example, the GD-1 stream (Grillmair and Dionatos, 2006; Price-Whelan and Bonaca, 2018) is one of the most populated. It is believed to have originated from a disrupted globular cluster (Webb and Bovy, 2019). We show the sky coordinates of stars belonging to GD-1 and to the foreground field in Figure 1.4. This stream spans about 60 deg in the sky, and lies at a mean distance of about 9 kpc from the Sun. As a consequence that the orbit of the progenitor cannot be directly reconstructed, in general, the orbit is fitted by following the average phase-space position of the stars along the stream. Using GD-1, Bovy et al. (2016) found a preference for a prolate halo of $q_\rho^{\mathrm{dh}} = 1.27^{+0.22}_{-0.27}$, and Malhan and Ibata (2019) for an oblate halo of $q_\rho^{\mathrm{dh}} = 0.82^{+0.13}_{-0.25}$. Even so, both estimates are compatible near the spherical shape. The lack of a known progenitor makes it difficult to use this stream to constrain the galactic potential. The same is true for other streams with no known progenitor, such as the Orphan stream (Grillmair, 2006; Belokurov et al., 2006b), among others.

Better results can be obtained using stellar streams generated by a known progenitor, especially if it is a globular cluster. A globular cluster is a spherical group of stars of approximately 10^5 $M_\odot$ orbiting a galaxy as a satellite. There are more than 150 globular clusters in the Milky Way and more are expected to be discovered (Harris, 1996). We show in the right panel of Figure 1.1 a

Figure 1.4: Sky map in equatorial coordinates of the GD-1 stellar stream. Each point is a source from the Early *Gaia* Data Release 3 (EDR3) catalogue (Gaia Collaboration et al., 2020). The grey dashed line indicates Galactic latitude $b = 15$ deg.

representation of these clusters around the Milky Way. In this case, we can more easily reconstruct the orbit of the progenitor because we know that it passes through the centre of the cluster, and we can accurately model the stream from the current properties of the progenitor. Most globular clusters should have an associated stellar stream. There are many identified star over-densities surrounding globular clusters (see e.g. Myeong et al., 2017; Carballo-Bello et al., 2018; Shipp et al., 2018), but in general, they are faint, shapeless or too short to be useful for constraining the Galactic potential. One of the clearest examples is the star debris following the globular cluster Omega Centauri (Ibata et al., 2019a). In general, when a globular cluster orbits near the galactic centre or follows a highly eccentric orbit, strong tidal forces tend to destroy its tidal streams. On the other hand, globular clusters located far from the Galactic centre generate long, narrow, and dynamically cold streams which can be accurately modelled. Some globular clusters have been associated with a well-defined stream with identified star candidates. The main examples are Palomar 5 (Odenkirchen et al., 2001), NGC 5466 (Belokurov et al., 2006a; Grillmair and Johnson, 2006), and M5 (NGC 5904) (Grillmair, 2019).

The streams of NGC 5466 and M5 are difficult to distinguish from foreground stars due to their distance and location on the sky. In contrast, Palomar 5 presents a prominent stream of about 10 kpc in length, located about 20 kpc from the Sun. It spans a range of about [13 - 17] kpc from the Galactic centre and [12 - 15] kpc from the Galactic disc. It was discovered by Odenkirchen et al. (2001) by observing an excess of stars around the globular cluster using photometric data. Subsequent studies improved the definition, extended its longitude to 23 deg in the sky, and provided star candidates belonging to the stream (e.g. Starkman et al., 2020; Price-Whelan et al., 2019). This stream has been used to constrain the potential of the Milky Way, requiring a slightly flattened halo but compatible with a spherical shape of $q_\rho^{\mathrm{dh}} = 0.9 \pm 0.2$ (Bovy et al., 2016).

Some cosmological models predict the existence of many small dark matter halos surrounding the galaxies called sub-halos (Springel et al., 2008). The interaction of these satellite sub-halos with stellar streams can cause density variations and gaps along the streams (Carlberg, 2009). By determining the abundance and shape of these gaps, it is possible to constrain the cosmological model and the properties of the dark matter particles. These gaps have been observed in some stellar streams, for example in GD-1 (see Figure 1.4), finding evidence for interactions with dark matter substructure (Bonaca et al., 2019; Banik et al., 2021). However, some authors have explained these gaps by interactions with baryonic components (e.g. Ibata et al., 2020). These studies can be improved and complemented by detecting new stellar streams and better modelling their characteristics. As streams are powerful tools for determining the properties of the dark matter and for modelling galaxies, it has become necessary to develop new methods to discover more.

1.3   Detection of stellar streams

So far, tidal streams have often been found serendipitously by noticing an excess of stars along bands in the sky after applying certain cuts based on proper motions or photometry. The publication of the *Gaia* Data Release 2 (GDR2) star catalogue has motivated the creation of different methods to systematically search for new streams. This catalogue was published on April 25, 2018 and is based on data collected during the first 2 years of the Gaia Mission (Gaia Collaboration et al., 2016). It provides five-parameter astrometric solutions (parallaxes, sky coordinates, and proper motions) and multiband photometry (G, G_{BP}, and G_{RP} magnitudes) for more than 1 billion stars covering the entire sky. In addition, it includes radial velocities for about 7.2 million sources. A complete description of its contents can be found in Gaia Collaboration et al. (2018b).

Some algorithms have been developed to systematize the detection of streams using phase-space coordinates, magnitudes, and colours of stars from GDR2. Usually, they are also designed to select accurately the stars belonging to the stream:

- Brown et al. (2005) compute the energy and the angular momentum of the stream stars assuming a steady axisymmetric potential for the Milky Way. This method requires high-quality data, as the large background population and the observational uncertainties make it difficult to detect a stream as a single structure projected on the two-dimensional space of the two integrals of motion.

- Sanderson et al. (2015) compute the action-angle coordinates of the stream stars and identifies them as an over-densities using a clustering algorithm. This method has similar problems to the previous one, as it requires high-quality data. Moreover, the oversimplified potential model needed to compute the action-angle coordinates may scatter the real stream members over a large region of the action-angle space.

- Mateu et al. (2017) developed the Great Circle Method, which exploits the fact that streams are confined in a plane if the Galactic potential has spherical symmetry. This algorithm selects the stars with positions and proper motions that approximately lie in a plane characteristic of each stream. Consequently, this method is not suitable for long streams close to the disc, since the potential is not expected to be spherical.

- Malhan and Ibata (2018) present an algorithm, called Streamfinder. It assumes a fixed potential and computes a six-dimensional tube in phase space that follows the orbit of a star and has a width similar to the size of the expected stream. When a large number of observed stars are compatible with this tube, taking into account the uncertainties in the measurements, it is then an indication of the existence of a stream.

1.4   Goals and structure of the thesis

Most of the constraints on the shape of the dark matter halo of the Milky Way come from kinematic data in the Solar neighbourhood or in the plane of the disc. For example, the position and velocity of the Sun, the vertical gravitational acceleration in the Solar vicinity, the velocity dispersion of the stars in the disc, or the rotational curve. With these data, we can describe the contribution of the halo to the magnitude of the gravitational acceleration in the disc plane, as well as its radial distribution, but not the overall shape of the halo.

Several methods using observational data out of the galactic plane have been applied to describe the shape of the halo, especially its density axis ratio q_ρ^{dh}. In general, methods using tracers such as halo stars or globular clusters require the assumption that the tracers are in equilibrium and also require strong assumptions on the dark matter density profile. In general, these studies offer conflicting results, even so, the most recent ones tend to prefer spherical-prolate halos. Similar results are obtained when the Sagittarius stream or stellar streams with no known progenitor, such as GD-1 or Orphan stream, are used to constrain the dark halo of the Milky Way. Usually, these streams are difficult to model and are found in the outer halo, where the influence of the LMC is significant. These studies offer a wide range of results, from oblate to prolate shapes with large uncertainties.

The most promising results come from the stellar stream of Palomar 5. In this case, the orbit of the progenitor is easier to reconstruct because we know one point of the orbit, the current position of the globular cluster. Furthermore, we can use the current properties of the cluster to accurately model its associated stream. The large number of stars available in the GDR2 catalogue and the high quality of the measurements of their phase-space coordinates, magnitudes, and colours, allow us to better characterise this stream and improve its capabilities to constrain the dark halo of the Milky Way. Moreover, the *Gaia* catalogue also gives us the opportunity to identify new stellar streams generated by globular clusters that pass through the solar neighbourhood. In principle, fitting several streams in different areas separately will allows us to describe the dark matter halo in different locations. In addition, by including

all possible streams together, the number of assumptions made for the distribution of the dark matter halo can be reduced and we can obtain better estimates of its properties.

In this thesis, for the above reasons, we focus on the streams generated by globular cluster to estimate the shape of the dark matter halo of the Milky Way. We define the following goals for the present work:

(1) Develop a statistical method to discover new stellar streams generated by globular clusters in the *Gaia* catalogue. The algorithm has to statistically distinguish stream stars from the foreground field stars using the phase-space coordinates of each star convolved with its observational errors. Defining a statistical test, it has to establish whether the stellar stream exists or not. If it gives a positive result, it has to choose the stars that most likely belong to the stream and are compatible with colours and magnitudes with the progenitor.

(2) Apply the algorithm to the most suitable globular clusters for detecting new stellar streams. These clusters are those that theoretically generate elongated, narrow, and dynamically cold streams. To observe the streams in the *Gaia* catalogue, it is also useful that they are located near the Sun to minimise the stars lost by magnitude extinction and minimise the observational uncertainties. In general, these streams have significantly larger proper motions than the foreground stars due to the effect of apparent acceleration with decreasing distance with respect to the Sun. In addition, they are easier to observe if projected away from areas of the sky with larger foreground contamination, such as the disc or the Galactic centre.

(3) Use the developed statistical method to select *Gaia* stars belonging to the known stellar stream generated by the globular cluster Palomar 5. The large number of stars and the high quality of the measurements will allow us to make a more complete and accurate selection of stream stars than the existing ones.

(4) Use newly discovered stellar streams together with Palomar 5 stream to constrain the Milky Way potential. Using more streams with higher quality data, will allow us to minimise the number of assumptions on the dark matter distribution by using a more general profile than the usual NFW. In principle, the use of several streams in the same fit will allow us to obtain stronger constraints on the halo density parameters, specially on the inner slope and the axis ratio, two of the most unknown characteristics of the Milky Way dark halo.

This thesis is organised as follows:

- In Chapter 2, we describe our statistical method and test it with a simulation of the stellar stream of M68 (NGC 4590) and a mock *Gaia* catalogue. We then apply this method to the same cluster finding a new stellar stream. We identify the stars most likely to belong to the stream and provide the list.

- In Chapter 3, we apply the statistical method to the globular cluster NGC 3201. We observe a clear stellar stream generated by tidal forces in this cluster. We also identify the stars most likely to belong to the stream and provide the list.

- In Chapter 4, we use the stellar streams generated by NGC 3201, M68, and Palomar 5 to constrain the mass distribution of the Milky Way. We present four models, each one computed with each stream separately and with all the streams together. We discuss the constraint that these streams impose on the flattening of the dark matter halo and compare our results with previous estimates and predictions from cosmological simulations.

- Finally, in Chapter 5, we present our conclusions and propose future investigations that our research has opened up.

CHAPTER 2

DESCRIPTION OF THE STATISTICAL METHOD AND DETECTION OF THE STELLAR STREAM GENERATED BY M68

2.1 Introduction

In this chapter, we present a new method based on maximum likelihood analysis that searches for streams in a large data set, computing orbits in a gravitational potential that can be varied together with the kinematic initial conditions of a stream progenitor. The method takes into account the probability of stars to belong to a model of the stellar foreground and to belong to a stellar stream, and can be applied for known candidate progenitors or for blind searches with unknown progenitor orbits. The search for a stream is carried out after a preselection that eliminates most of the stars in the data set that are very unlikely to belong to any tidal stream in the phase-space region being searched, which is used to reduce computational time. Our statistical method improves on some of the previous methods by generalizing the likelihood function, using a model of the phase-space density of the Milky Way for the stellar foreground, and a variable gravitational potential and a realistic dynamical treatment of a tidal stream taking into account the intrinsic and observational uncertainties at the pre-selection and best-fitting stages.

This type of method has so far not been exhaustively applied to the list of known globular clusters. In this chapter, we develop this method to search for tidal tails around a known progenitor, with the goal of identifying them even though they will generally not be intuitively visible to the eye as an excess under any projections and cuts and can only be detected as a statistical excess above the foreground or background stars with known observational errors. We apply the method specifically to the globular cluster M68 (NGC 4590) in this chapter, because of several characteristics that make it the best candidate for observing any associated tidal stream. We find clear evidence of a long stream with more than 100 member stars that promises many applications for studies of the Galactic potential and the dynamics of tidal stream formation.

As this work was being completed, we became aware that the stream we detect was already discovered in Ibata et al. (2019b), who baptized it with the name Fjörm; however, they did not associate it with the globular cluster M68. We find incontrovertible evidence for this association, which makes this stream

even more interesting for studies of the dynamics of globular clusters and the Milky Way potential.

Our method is described in detail in Section 2.2, and Section 2.3 presents tests on simulations of the *Gaia* catalogue, applying them specifically to stream models of M68. In Section 2.4, we search for a real stellar stream associated with M68 using *Gaia* data and we present our conclusions in Section 2.5.

2.2 Statistical method to detect tidal streams

In this section we describe the method we have developed to search for tidal streams. Our goal is to be able to detect a tidal stream even when seen against a large number of foreground stars with similar kinematic characteristics, and when large observational errors on the distance and proper motions and the absence of radial velocities make it difficult to visualize the tidal stream directly from any projection of the data. In many cases, there may be no individual stars that can be assigned to a tidal stream with high confidence, even though the existence of the tidal stream itself may be highly significant from a large set of candidate members. The method is based on the maximum likelihood technique, although the likelihood function has to be defined in an approximate way because of the difficulty of numerically computing precise distributions of a tidal tail for many models, and of correctly characterizing the foreground. The approximations used are tested and calibrated using mocks of the *Gaia* data.

Stars in a tidal stream are stripped out from a bound object (a globular cluster or a dwarf galaxy) by the external tidal force of the Milky Way galaxy. Tidal stripping occurs when the mean density of the Galaxy within the cluster orbit is comparable to the mean cluster density, which also implies that the orbital times of the stripped stars in the cluster are comparable to the orbital time of the cluster around the Galaxy. Tidal stripping is therefore strongest at the closest pericentre passages. In addition, tidal shocks occur when the cluster crosses the disc. The escaped stars approximately follow the progenitor orbit, with small variations of the conserved integrals of the motion. Stars moving to lower orbital energy form a leading tail ahead of the cluster trajectory, while stars left at a higher orbital energy form a trailing tail behind. The shape of these tails is a first approximation to the cluster orbit, although in detail, they are different (Küpper et al., 2010; Bovy, 2014; Fardal et al., 2015).

2.2.1 Likelihood function and parameter estimation methodology

The maximum likelihood method is used to determine parameters of a model that maximize a posterior function, given a set of observational data. The likelihood function is the probability density of obtaining the observed data as a function of the model parameters. The data generally consist of N independent observations of a set of n_{p} variables w^μ (labelled by an index $\mu = 1, ..., n_{\mathrm{p}}$), with a covariance matrix for observational errors $\sigma^{\mu\nu}$. We want to compute a probability density $P(w^\mu|\theta_\kappa; \sigma^{\mu\nu})$ in the space of the w^μ variables, depending on K model parameters θ_κ (with $\kappa = 1, ..., K$) that are to be estimated. The dependence on the covariance matrix is assumed to be a convolution with Gaussian errors, in the appropriately chosen w^μ variables. In our case, N is the number of stars in a selected catalogue where we search for evidence of

a tidal tail, w^μ are the $n_\mathrm{p} = 6$ observed coordinates of each star of parallax, angular position, radial velocity and proper motion, and the covariance $\sigma^{\mu\nu}$ can be different for every star. The likelihood function $L(\theta_\kappa)$ is the product of the probability densities of all the data points:

$$L(\theta_\kappa) = \prod_{n=1}^{N} P(w_n^\mu | \theta_\kappa; \sigma_n^{\mu\nu}) \ . \tag{2.1}$$

A prior probability function $p(\theta_\kappa)$ is assumed for the parameters θ_κ.

In addition to fitting parameter values, the likelihood function can be used to calculate a statistical confidence level to establish if a certain hypothesis is true or false. Usually a null-hypothesis H_0 states that the K model parameters obey a set of T restricting equations, meaning that the K parameters lie in a sub-space of dimensionality $K - T$, while the one-hypothesis H_1 asserts that the parameters do not obey the T restrictions and are outside of this sub-space. Let the parameters $\hat\theta_\kappa^0$ and $\hat\theta_\kappa^1$ be the values that maximize the posterior function, defined as the product $L(\theta_\kappa)\,p(\theta_\kappa)$, with the T restrictions and without them, respectively. The truth of H_0 can be tested using the likelihood ratio statistic Λ, defined as:

$$\Lambda \equiv -2\ln\left[\frac{L(\hat\theta_\kappa^0)\,p(\hat\theta_\kappa^0)}{L(\hat\theta_\kappa^1)\,p(\hat\theta_\kappa^1)}\right] \ . \tag{2.2}$$

We use Wilks' theorem (see e.g., Casella and Berger, 2002) to choose the criterion $\Lambda < k$ for favouring the null-hypothesis H_0, where k is computed from a conventionally chosen value of the probability ϵ of inappropriately rejecting the null-hypothesis when H_0 is actually true, using the equation

$$\epsilon = \int_k^\infty \chi_T^2(z)\ \mathrm{d}z = \frac{\Gamma(T/2, k/2)}{\Gamma(T/2)} \ , \tag{2.3}$$

where χ_T^2 is the standard χ^2 distribution with T degrees of freedom. We shall use a confidence level $\epsilon = 0.01$ throughout this chapter, which for one degree of freedom implies $k = 6.635$.

In general, the N stars of any set in which we search for a tidal stream contain a fraction τ of stars that belong to the tidal stream, and a fraction $1 - \tau$ that belong to the foreground containing the general stellar population of the Galaxy (note that what we refer to as "foreground" stars may actually be foreground or background compared to the stream, and we simply mean that they are superposed in the sky with the hypothesized stream and belong to the set in which the stream is being searched for). The null-hypothesis is simply the restriction $\tau = 0$. The probability density of the data variables for each star n is

$$P(w_n^\mu | \theta_\kappa; \sigma_n^{\mu\nu}) = \tau\,P_S(w_n^\mu | \theta_s, \theta_c, \theta_\phi; \sigma_n^{\mu\nu}) + (1 - \tau)\,P_F(w_n^\mu | \theta_s; \sigma_n^{\mu\nu}) \ . \tag{2.4}$$

Here, P_S is the probability density that a star belonging to the stream has variables w_n^μ, convolved with errors $\sigma_n^{\mu\nu}$, while P_F is the probability density for a star that belongs to the foreground. We have split the K model parameters into three groups: θ_s refers to parameters of the distribution of stars in various

components of the Galaxy (disc, bulge, and halo), θ_c are the present coordinates of the orbiting object generating the tidal stream, and θ_ϕ are parameters of the Milky Way potential. In general, the parameters θ_s also affect the potential if the stellar components are assumed to imply a mass component with the same distribution (i.e., if a fixed mass-to-light ratio of the stellar population is assumed), so we include these parameters in P_S as well. The likelihood function is then given by equations (2.1) and (2.4). The values of the parameters for which the likelihood function is maximum $\hat{\theta}_\kappa$ are computed using a Nelder-Mead Simplex algorithm, which does not require neither a smooth function nor the evaluation of its derivatives (see Conn et al., 2009, for details). The covariance matrix for the errors of the parameter solutions σ^{ij} are computed by calculating second derivatives of the posterior function logarithm

$$\sigma^{ij} = \left(-\frac{\partial^2 \ln\big(L(\theta_\kappa)\, p(\theta_\kappa)\big)}{\partial \theta_i\, \partial \theta_j}\bigg|_{\hat{\theta}_\kappa} \right)^{-1} . \tag{2.5}$$

The stellar phase-space density model depending on parameters θ_s is described in detail in Section 2.2.2, and the calculation of P_F taking into account an observational selection approximation is explained in Section 2.2.4. The computation of the probability density P_S from a density model of the stream, using the stream progenitor orbit and a model of the Milky Way potential, is described in Section 2.2.5.

We have not included information about colours and magnitudes of the stars in the likelihood function since it would be necessary to model the colour-magnitude distribution of the foreground stars as seen by *Gaia*. Although the inclusion of photometric data might improve the detection capability, we leave this modification for future further improvement of the statistical method. In Section 2.3, we use the phase-space data to establish the existence of a simulated tidal stream and to compute the best adjustment of the model parameters using a foreground simulated star catalogue. We use colours and magnitudes in Section 2.3.5 to improve the final identification of the star candidates to belong to the stellar stream choosing those that are compatible with the H-R diagram of the progenitor cluster.

2.2.2   Phase-space stellar model of the Milky Way

We define a simple model of the phase-space distribution of stars in the Milky Way, f, to enable an estimate of the probability density that a star belongs to the Galactic foreground, P_F. The distribution in our model is the sum of four components: thin disc, thick disc, bulge and stellar halo. We write each of the four components, labelled by the index γ, as the product of a stellar mass density function of space, ρ_γ, and a velocity distribution function g_γ:

$$f(x_i, v_j) = \frac{1}{M} \sum_{\gamma=1}^{4} \rho_\gamma(x_i)\, g_\gamma(x_i, v_j) , \tag{2.6}$$

where x_i and v_j are three-dimensional components of position and velocity vectors, and M is the total mass of stars in the four components. The velocity

Table 2.1: Properties of the disc density model.

Properties		Thin disc	Thick disc
$\Sigma_{1,2}$	$(\mathrm{M}_\odot\ \mathrm{kpc}^{-2})$	8.17×10^8	2.1×10^8
$h_{1,2}$	(kpc)	2.9	3.31
$z_{1,2}$	(kpc)	0.3	0.9
$M_{1,2}$	$(\mathrm{M}_\odot)$	4.31×10^{10}	1.44×10^{10}

Note. Ref.: McMillan (2011).

distribution g_γ is normalized to unity at each position x_i, when integrating over all the velocity space. We make the simplified assumption that the number of stars per unit stellar mass at a given luminosity in the *Gaia* band is the same for all components.

The disc density

The disc is constructed as the sum of two exponential profiles, for the thin and thick disc. In Cylindrical coordinates (R, φ, z), the mass density for each component is

$$\rho_\gamma(R,z) = \frac{\Sigma_\gamma}{2z_\gamma} \exp\left(-\frac{R}{h_\gamma} - \frac{|z|}{z_\gamma}\right) \ . \tag{2.7}$$

We use the parameter values in McMillan (2011), which are listed in Table 2.1.

The bulge density

For simplicity, we assume an axisymmetric bulge, even though the bulge is a rotating bar, since our conclusions in this chapter do not depend on accurately modelling orbits in the inner part of the Galaxy. The bulge density is a power law with slope α and a Gaussian truncation at a scale length a_1:

$$\rho_3(s) = \rho_0 \left(1 + as\right)^{-\alpha} \exp\left(-s^2\right) \ , \tag{2.8}$$

where

$$s^2 \equiv \frac{R^2}{a_1^2} + \frac{z^2}{a_3^2} \ . \tag{2.9}$$

The bulge parameters are listed in Table 2.2, taken from McMillan (2011).

The stellar halo density

The Galaxy is surrounded by a faint stellar halo made by old and metal-poor stars. We model it as an oblate ellipsoidal object with a density profile as a function of the radial variable in equation (2.9) following a two power-law model:

$$\rho_4(s) = \rho_0 \, s^{-\alpha} \left(1 + s\right)^{\alpha - \beta} \ . \tag{2.10}$$

We use the parameters of Robin et al. (2014), listed in Table 2.2.

Table 2.2: Properties of the bulge, dark halo and stellar halo density models.

Properties		Bulge	Stellar halo	Dark halo
ρ_0	$(\mathrm{M}_\odot \ \mathrm{kpc}^{-3})$	9.93×10^{10}	2.66×10^3	$\rho_{0\mathrm{dh}}$
a_1	(kpc)	2.1	2.1	$a_{1\mathrm{dh}}$
a_3	(kpc)	1.05	1.68	$a_{3\mathrm{dh}}$
a		28	–	–
α		1.8	1	1
β		–	3.8	β_{dh}
M	$(\mathrm{M}_\odot)$	8.96×10^9	1.72×10^5	–

Note. Bulge Ref.: McMillan (2011).
Stellar Halo Ref.: Robin et al. (2014).

Table 2.3: Velocity dispersions of the bulge, dark halo and stellar halo density models and asymmetric drift.

	σ_r (km s^{-1})	σ_θ (km s^{-1})	σ_ϕ (km s^{-1})	v_{ad} (km s^{-1})
Thin disc	31	12.6	20	-229.4
Thick disc	67	42	51	-185
Bulge	113	100	115	-159
Stellar halo	131	85	106	-12

Note. Ref.: Robin et al. (2012).

The velocity distribution model

For all the stellar components, we assume that the velocity distribution function is a Gaussian with principal axes oriented along spherical coordinates,

$$
g_\gamma(v_r, v_\theta, v_\phi) = \frac{1}{(2\pi)^{3/2} \, \sigma_{\gamma r} \sigma_{\gamma \theta} \sigma_{\gamma \phi}} \, \exp\left(-\frac{v_r^2}{2\sigma_{\gamma r}^2} - \frac{v_\theta^2}{2\sigma_{\gamma \theta}^2} - \frac{(v_\phi - v_{\mathrm{ad}})^2}{2\sigma_{\gamma \phi}^2} \right),
$$
(2.11)

where the index γ labels the four stellar components. The three-velocity dispersion eigenvalues are determined observationally. We use the values for each component from Robin et al. (2012), assuming the average of all stellar populations for the thin disc. The values are listed in Table 2.3.

2.2.3 Potential model of the Milky Way

We assume the dark matter halo density profile also follows equation (2.10). For the case $\alpha = 1$ and $\beta = 3$, this density profile reduces to the NFW profile (Navarro et al., 1996), which fits the dark matter halo profiles obtained in cosmological simulations. For simplicity we also assume an axisymmetric shape

for the dark halo, even though in general it can be triaxial. In the models in this chapter, we fix $\alpha = 1$ and we leave the other parameters listed in Table 2.2 to be free when fitting the model. In practice this gives enough freedom to our halo profile to model the dynamics of tidal tails we examine here.

Two baryonic components are added to this dark halo: the disc and the bulge. Their potentials are computed following the previous stellar density profiles in equations (2.7) and (2.8). The stellar halo and gas components are neglected because of their expected small mass compared to the dark halo.

2.2.4   The probability function P_{F}

In general, stellar surveys provide measurements of phase-space coordinates of stars in the form of parallaxes π, angular positions δ and α, radial velocity v_r, and proper motions μ_δ and μ_α. These are our six-dimensional variables for each star, $w^\mu = (\pi, \delta, \alpha, v_r, \mu_\delta, \mu_\alpha)$, where the proper motions are $\mu_\delta = \mathrm{d}\delta/\mathrm{d}t$ and $\mu_\alpha = \mathrm{d}\alpha/\mathrm{d}t$. Note that the physical proper motion component in right ascension is $\mu_{\alpha*} = \mu_\alpha \cos\delta$. The *Gaia* mission is at present providing the largest star survey. We designate as w_o^μ the observed value of each variable, and their observational errors are characterized by a covariance matrix $\sigma^{\mu\nu}$. The values of the true variables w^μ are assumed to follow Gaussian distributions that we write as $G(w^\mu - w_o^\mu | \sigma^{\mu\nu})$.

To calculate the probability density of the observed coordinates for foreground stars, we need to take into account the flux-limited survey selection. Let $\psi_{\text{s}}(L)$ be the cumulative luminosity function of stars with a luminosity in the observed photometric band greater than L. Neglecting the effect of dust absorption (which generally has small variations for the halo stars we are interested in), the density of stars included in the survey as a function of the heliocentric distance r_{h} is proportional to $\psi_{\text{s}}(L_1 r_{\text{h}}^2/r_1^2)$, where L_1 is the luminosity corresponding to the survey flux threshold at a distance r_1. We can take the normalizing distance r_1 to be 1 parsec, and then the parallax expressed in arc seconds is $\pi = r_1/r_{\text{h}}$. We will assume here as a simple model that $\psi_{\text{s}}(L) \propto L^{-1}$ in the range of interest, meaning that there is a roughly constant luminosity coming from stars in any range of $\mathrm{d}\log L$. This is roughly correct for stellar populations lying between the main-sequence turn-off and the tip of the red giant branch. A detailed modelling of the foreground to obtain an accurate estimate of the likelihood function would clearly require a more careful evaluation of the stellar luminosity function, but given all the uncertainties in our modelling (i.e., the velocity distribution, dust absorption, etc.) we decide to use this very approximate and simple approach in this work.

The foreground probability density can then be written as

$$P_{\text{F}}(w^\mu | \theta_s, \sigma^{\mu\nu}) = \frac{1}{C} \int \mathrm{d}^6 w \, f(w^\mu | \theta_s) \frac{r_1^5 \cos^2\delta}{\pi^6} \, \psi_{\text{s}}(L_1/\pi^2) \, G(w^\mu - w_o^\mu | \sigma^{\mu\nu}), \quad (2.12)$$

where the Jacobian of the transformation from the cartesian (x_i, v_j) variables of phase space to the w^μ coordinates has a space part $(r_1^3 \cos\delta)/\pi^4$, and a velocity part $(r_1^2 \cos\delta)/\pi^2$. The constant C renormalizes the probability density in the

observed variables after the flux-threshold selection is included, and is

$$C = \int \mathrm{d}^6 w \; \frac{r_1^5 \cos^2\delta}{\pi^6} \; \psi_{\mathrm{s}}(L_1/\pi^2) \; f(w^\mu|\theta_s) \; . \tag{2.13}$$

For our choice $\psi_{\mathrm{s}}(L) \propto L^{-1}$, the function ψ_{s} is simply replaced by π^2 in equations (2.12) and (2.13).

We now assume that the observational errors are dominated by the parallax error ε_π and the radial velocity ε_{v_r}, neglecting errors in proper motion compared to the intrinsic velocity dispersion of stars. Errors in the angular positions are always negligibly small. The integral yielding our foreground probability density is then

$$P_{\mathrm{F}}(w^\mu|\theta_s) = \frac{r_1^5 \cos^2\delta}{C} \int_0^\infty \frac{\mathrm{d}\pi}{\pi^4} \int_{-\infty}^\infty \mathrm{d}v_r \; G(\pi - \pi_o|\varepsilon_\pi^2) \; G(v_r - v_{ro}|\varepsilon_{v_r}^2) \; f(x_i, v_j|\theta_s) \; .$$
$$\tag{2.14}$$

In the absence of any radial velocity measurement, we can simply use a very large value of ε_{v_r}, or redefine the probability P_{F} by integrating over all radial velocities. Our assumption of small proper motion errors is not always valid, and in this case, an improved estimate needs to integrate over the full three-dimensional velocity distribution.

The integral in equation (2.14) is computed numerically, converting the observable coordinates w^μ to heliocentric cartesian coordinates and Galactocentric ones as described in Appendix A.1 to evaluate $f(w^\mu|\theta_s)$.

2.2.5 The probability function P_{s}

The most accurate way to model tidal streams is through direct N-body simulations. However, these require the introduction of a softening radius when particles are a random representation of collisionless matter instead of real stars. Including a sufficient number of particles to model the evolving gravitational potential of the globular cluster and its tidal tail would increase the computational time by more than a factor ~ 10 even with the use of a tree-code or other techniques. In addition, we should include the perturbation on the Milky Way potential by the globular cluster because it would be of similar importance, thus increasing the computational requirements of the model. In practice, we need to compute the trajectories of thousands of stars in a tidal tail, and to repeat the calculation for hundreds of models to minimize the likelihood function and to obtain a fit. To make this computationally feasible, we neglect the self-gravity of the stream and compute test particle trajectories in the fixed Milky Way potential plus the fixed potential of the satellite system orbiting around the Milky Way, neglecting any dynamical perturbation on the satellite and on the Milky Way.

Based on these simplifications, a wide range of studies are based on releasing test particles near the Lagrange points, with a random offset in position and velocities following Gaussian distributions (see e.g., Lane et al., 2012). This method reasonably reproduces N-body simulations with a large reduction in computational time, and has been studied in detail in Küpper et al. (2008) and in Küpper et al. (2012). The potential of the progenitor is sometimes not taken

into account in these simulations, even though its effects can be significant, as was shown for example in Gibbons et al. (2014).

In this work, we use neither N-body simulations because of their impractical computational demand, nor the above-mentioned algorithms because we want to simulate the kinematic structure of streams in a general orbit and general potential for the Milky Way. We simulate trajectories of test particles including an unperturbed potential for the progenitor system, following these steps:

1. Compute backwards in time the orbit of the progenitor globular cluster (or other bound satellite) from a reasonably well-known present position and velocity.

2. Spread out stars around the globular cluster using a model derived from its internal stellar phase-space distribution function.

3. Compute forwards in time the orbits of the stars within the potential of the Galaxy, including the moving potential of the globular cluster with its mass fixed.

4. Use the stars that have escaped from the progenitor to create a model of the phase-space density of the stellar stream.

Simulation of the tidal stream

We generally refer to the stellar system being tidally stripped as a globular cluster, although tidal streams can of course be formed by any stellar systems orbiting around our Galaxy. We assume the globular cluster is initially in dynamic equilibrium, spherical, and with an isotropic velocity dispersion, and adopt the Plummer Model for its internal structure, with two parameters: the total cluster mass M_{gc} and a core radius a_{gc}. The density profile as a function of the distance to the cluster centre, r_{gc}, is

$$\rho(r_{\mathrm{gc}}) = \frac{3M_{\mathrm{gc}}}{4\pi a_{\mathrm{gc}}^3} \left(1 + \frac{r_{\mathrm{gc}}^2}{a_{\mathrm{gc}}^2} \right)^{-5/2} . \tag{2.15}$$

The velocity distribution at any radius can be expressed in terms of the modulus of the escape velocity,

$$v_{\mathrm{esc}} = \sqrt{2\,\Phi(r_{\mathrm{gc}})} , \tag{2.16}$$

where the gravitational potential is

$$\Phi_{\mathrm{gc}}(r_{\mathrm{gc}}) = \frac{GM_{\mathrm{gc}}}{\sqrt{r_{\mathrm{gc}}^2 + a_{\mathrm{gc}}^2}} . \tag{2.17}$$

The probability distribution of the modulus of the velocity v is

$$g_{\mathrm{gc}}(v) = \frac{512}{7\pi} \frac{v^2}{v_{\mathrm{esc}}^2} \left(1 - \frac{v^2}{v_{\mathrm{esc}}^2} \right)^{7/2} . \tag{2.18}$$

We first compute orbits for a large number of test particles with random initial conditions, obtained by generating an initial radius r_{gc} according to the density profile of equation (2.15), a velocity modulus according to equation (2.18), and two random angles for the position from the cluster centre and for the velocity vector. The orbits of the test particles are computed in the combined potential obtained by adding that of the Milky Way (as described above) and that of the cluster Plummer model in equation (2.17). The orbit of the globular cluster in the Milky Way potential is computed first, also as a test particle and stored. The test particles are computed next by considering the cluster potential to be fixed in shape (neglecting the changes in the mass distribution caused by the tidal perturbation) and moving along the computed orbit.

A technical problem appears because most of the particles generated in this way have orbits close to the cluster core, which is typically much smaller than the tidal radius of the cluster, leaving only a very small fraction of stars that can escape. Moreover, integrating the trajectory of test particles near the cluster core is computationally expensive because orbital periods in the cluster core are usually much shorter than the orbital period around the Milky Way, so many short time-steps are required. To avoid this problem, we restrict the generated test particles to a subset representing cluster stars that are more likely to escape than the majority, while making sure that particles that are not selected would very rarely escape and not significantly contribute to stars in the simulated tidal tail.

Although it is not possible to determine analytically if a star in a model cluster with any orbit is able to escape, we can obtain an approximate restricted region of phase space where most escaping stars should be located. For this purpose, we consider the restricted circular 3-body problem of a cluster in a circular orbit, where the combined potential is time independent in the rotating frame following the cluster motion. Considering a characteristic cluster orbital radius R_{c}, the distance between the centre of the cluster and the first Lagrange point (see Renaud et al., 2011) is approximately given by the tidal radius:

$$r_{\mathrm{t}} \equiv R_{\mathrm{c}} \left(\frac{M_{\mathrm{gc}}}{3 M_t} \right)^{\frac{1}{3}} . \tag{2.19}$$

With respect to the rotating reference frame where the two bodies are at rest, the movement of a test particle can be described adding an extra term to the potential needed to account for the centrifugal force giving the following effective potential in spherical Galactocentric coordinates:

$$\Phi_{\mathrm{eff}}(r) = \Phi_{\mathrm{MW}}(r) + \Phi_{\mathrm{gc}}(r) + \frac{1}{2} \frac{G M_t}{R_{\mathrm{c}}^3} r^2 , \tag{2.20}$$

where G is the gravitational constant and Φ_{MW} is the potential of the Milky Way. Using the theorem of conservation of energy, we define a limiting velocity taking a fixed radius R_{c}:

$$v_{\mathrm{lim}} \equiv \sqrt{2 \Phi_{\mathrm{eff}}(r) - 2 \Phi_{\mathrm{eff}}(R_{\mathrm{c}} - r_{\mathrm{t}})} \tag{2.21}$$

For the simulation of the density of a tidal stream we use a sample generated via a Monte Carlo method taking only the stars with initial velocity such that $v > v_{\text{lim}}$ and $r > r_{\text{t}}$. The stars of the globular cluster are considered test particles and their orbits are integrated using a Runge-Kutta scheme from the past to the current position within the potential of the Milky Way and within the potential of the globular cluster keeping its mass constant.

Density model of the tidal stream

Once the orbits of the stars are computed, we construct a probability density function of the tidal stream in the space of the directly observed variables $(\pi, \alpha, \delta, v_r, \mu_\alpha, \mu_\delta)$, designated as $p_{\text{s}}(w^\mu | \theta_s, \theta_c, \theta_\phi)$. We use a Kernel Density Estimation method, with a Gaussian as a kernel. If N_{e} is the total number of escaped stars at the present time, the stream probability density is

$$p_{\text{s}}(w^\mu | \theta_s, \theta_c, \theta_\phi) = \frac{1}{N_{\text{e}}} \sum_{i=1}^{N_{\text{e}}} G(w^\mu - w_{ci}^\mu, \Xi_i^{\mu\nu}) \ . \tag{2.22}$$

The centre of each Gaussian distribution, w_{ci}^μ, is the current position of the simulated stream star, and the covariance matrix $\Xi_i^{\mu\nu}$ is computed from the distribution of positions of neighbouring stream stars, using weighting factors c_{ij} that average over neighbours out to some characteristic kernel size:

$$\Xi_i^{\mu\nu} = \left(\sum_{j=1}^{N_{\text{e}}} c_{ij} \right)^{-1} \sum_{j=1}^{N_{\text{e}}} c_{ij} \ (w_{cj}^\mu - w_{ci}^\mu) \ (w_{cj}^\nu - w_{ci}^\nu) \ . \tag{2.23}$$

The weights are defined depending on the distance between every pair of stream stars,

$$c_{ij} = (d_0 + d_{ij})^{-9/2} \ ; \qquad d_{ij}^2 = \sum_{l=1}^{3} (x_{cj}^l - x_{ci}^l)^2 \ , \tag{2.24}$$

where x_{ci}^l are the Cartesian space coordinates of each stream star at the present time in the simulation. We have tested that a value $d_0 = 250\,\text{pc}$ and the exponent $9/2$ in the previous equation gives a reasonable reproduction of the shape and density profile of the stellar stream, and we use these values in this work. These quantities can, however, be varied to optimize any specific application of the method.

Note that although we use the physical distances d_{ij} to compute the kernel weights, the stream structure is modelled in the space of directly observed coordinates w^μ. The probability density p_{s} that we model as the sum of Gaussians in equation (2.22) is therefore the product of a phase-space density times the Jacobian to transform from phase-space Cartesian coordinates to the w^μ variables of the observations.

The probability function P_{s}

We can now write the probability density that a star belonging to the stream and following the distribution as modelled in Section 2.2.5 is observed to have

the variables w_o^μ:

$$P_{\mathrm{s}}(w^\mu|\theta_s,\theta_c,\theta_\phi;\sigma^{\mu\nu}) = \frac{1}{C} \int G(w^\mu - w_o^\mu|\sigma^{\mu\nu})\,\psi_{\mathrm{s}}(L_1/\pi^2)\,p_{\mathrm{s}}(w^\mu|\theta_s,\theta_c,\theta_\phi)\,\mathrm{d}^6 w \ . \quad (2.25)$$

We assume that the dispersion of the stream is much smaller than the parallax observational error of a star, i.e., $\Xi_i^{\pi\pi} \ll \sigma^{\pi\pi}$, to approximate $\psi_{\mathrm{s}}(\pi) \simeq \psi_{\mathrm{s}}(\pi_{ci})$. In this case the integral in equation (2.26) is easily performed because the convolution of two Gaussians is a Gaussian with the sum of the dispersions. Using this result, the probability of a star to have the observed position w^μ with observational errors $\sigma^{\mu\nu}$, assuming it is a member of the stream, is

$$P_{\mathrm{s}}(w^\mu|\theta_s,\theta_c,\theta_\phi;\sigma^{\mu\mu}) = \frac{1}{C} \sum_{i=1}^{N_{\mathrm{e}}} \psi_{\mathrm{s}}(L_1/\pi_{ci}^2)\,G(w^\mu - w_{ci}^\mu|\sigma^{\mu\nu} + \Xi_i^{\mu\nu}) \qquad (2.26)$$

where the normalization constant is:

$$C = \sum_{i=1}^{N_{\mathrm{e}}} \psi_{\mathrm{s}}(L_1/\pi_{ci}^2) \ . \qquad (2.27)$$

2.2.6   Definition of the prior function

We use the prior function given by the direct observational measurements of the distance, proper motions and radial velocity of M68, with their quoted errors, as given in Table 2.4 below. These four globular cluster orbit parameters, labelled as θ_c with $c = 1,\ldots,4$, follow Gaussian distributions:

$$p(\theta_c) = \prod_{c=1}^{4} G\big(\theta_c - \theta_{c\mathrm{o}}|\sigma_c^2\big) \ , \qquad (2.28)$$

with observed values $\theta_{c\mathrm{o}}$ and uncertainties σ_c^2 listed in Table 2.4. We assume a uniform prior for the four gravitational potential parameters of the dark halo in the same table.

Given the values $\hat{\theta}_c$ that maximize the posterior function in equation (2.2), the deviation with respect to the observed measurements can be quantified by

$$Q \equiv 2\ln\left(\frac{p(\hat{\theta}_c^0)}{p(\hat{\theta}_c^1)}\right) = \sum_{c=1}^{4} \frac{(\hat{\theta}_c^1 - \theta_{c\mathrm{o}})^2}{\sigma_c^2} \ . \qquad (2.29)$$

A value of Q substantially larger than the number of parameters 4 would mean that the fit to a detected stream is not consistent with the measured distance and velocities of the globular cluster progenitor, indicating perhaps an inadequate potential parameterization or an underestimation of the errors.

2.3   Validation of the statistical method

In this section, we simulate the tidal stream of a globular cluster and the way it can be observed in the *Gaia* survey to test if our algorithm is able to detect the stream against a simulated foreground and recover some of the parameters of the progenitor orbit and the gravitational potential in which the stream moves.

2.3.1　Description of the simulated *Gaia* catalogue

We start describing a simulation of the entire *Gaia* catalogue that we then use to generate a realistic set of foreground stars that a tidal tail would be observed against.

The *Gaia* Universe Model Snapshot (GUMS) is a simulated catalogue of the full sky *Gaia* survey for stellar sources, which is useful for testing many types of statistical studies. Based on Besançon Galaxy model (Robin et al., 2003), the simulation includes parallaxes, kinematics, apparent magnitudes, and spectral characteristics for ~ 1 billion objects with G-band magnitude $G \leqslant 20$ mag. A complete statistical analysis of the 10th version of this catalogue is found in Robin et al. (2012).

The *Gaia* Object Generator (GOG) is a simulation of the contents of the final *Gaia* catalogue based on the sources in the GUMS, and provides the *Gaia* expected measurements of astrometric, photometric, and spectroscopic parameters with observational errors based on the *Gaia* performance models[1]. These estimated observational errors depend on instrument capabilities, stellar properties, and the number of observations. A statistical analysis of this catalogue was presented in Luri et al. (2014a). We use the 18th version of this simulation[2] (GOG18) in this work.

The GOG18 simulates the end-of-mission *Gaia* catalogue, so the predicted errors are smaller than in the current available version (GDR2). We correct the GOG18 uncertainties by scaling them to make them applicable to the GDR2 catalogue. Given the simulated observational error ε_μ of the phase-space coordinates, we obtain the scaled uncertainties $\lambda_\mu \varepsilon_\mu$, where the scale factor is computed to match the resulting distribution of simulated errors to the real distribution of GDR2 errors. For the variables $(\pi, \alpha, \delta, v_r, \mu_\alpha, \mu_\delta)$, we find the required six scale factors to be

$$\lambda_\mu = (1.4, 1.4, 1.4, 0.4, 4.5, 4.5) \ . \tag{2.30}$$

Radial velocities are most frequently not available, and in this work we simply set the error to a large enough value to make our results insensitive to it. We choose $\varepsilon_{v_r} = 10^3$ km s^{-1} and then, we set the observed value of the heliocentric radial velocity to zero for all stars (this value is irrelevant when the radial velocity error is large enough); we have tested that this value of ε_{v_r} is large enough that our results are not affected.

2.3.2　The M68 globular cluster and its tidal stream

Among several globular clusters we have considered as targets for a search for associated tidal tails, M68 (NGC 4590) stands out because of its proper motions and distance are measured with good precision, it is projected on to the halo, its relative proximity to us, and a predicted orbit that brings it close to us and keeps it far from the inner region of the Galaxy. All these properties make any putative tidal tail easier to find: a long orbital period far from the Galactic centre means that the tidal tail has not been strongly broadened and

---

[1] https://www.cosmos.esa.int/web/gaia/science-performance
[2] https://wwwhip.obspm.fr/gaiasimu/

dispersed by phase mixing, and a small distance to at least part of the tidal tail allows us to discover member stars of relatively low luminosity, especially if the foreground is far from the plane of the Galactic disc. After going through the list of known globular clusters, we selected M68 to be the most promising candidate for finding an associated tidal tail for these reasons.

The parameters for the computed orbit of the globular cluster M68 in our model of the Galactic potential are listed in Table 2.4, including its pericentre, apocentre, and angular momentum component perpendicular to the Galactic plane. As with other globular clusters, the proper motion measured by *Gaia* has significantly improved the precision of the predicted orbit, which has been computed for several potential models (Gaia Collaboration et al., 2018c). In all the models, the obtained orbit has an apocentre ~ 30 kpc, pericentre ~ 7 kpc, and a radial period of ~ 400 Myr, producing an elongated stream with little phase mixing and breadth. The globular cluster is approaching us and will come within ~ 5 kpc of the present position of the Sun in about 30 Myr, at the time when it is near its pericentre, flying almost vertically above our present position. This implies that any tidal tail should have a leading arm along this future part of the orbit, extending over the northern Galactic hemisphere, with the trailing arm being more difficult to see because of its position closer to the Galactic plane and further from us.

Simulation of the M68 tidal stream

To simulate the tidal tail produced by M68, we use the Milky Way dark halo model described by equation (2.10) with parameters listed in Table 2.4, corresponding to a total mass $M_{200} \sim 8 \times 10^{11} \, \mathrm{M_\odot}$ and an axial ratio $q \equiv a_{3\mathrm{dh}}/a_{1\mathrm{dh}} = 0.8$, and an implied potential flattening $q_\Phi = 0.91$ at the position of M68. The baryonic components of the mass distribution are added as described in Section 2.2.3.

The tidal stream is simulated following the steps described in Section 2.2.5, without applying the cuts in the simulated test particles described at the end of Section 2.2.5. These cuts are only applied later when the tidal tail needs to be computed for many models and the required computational time needs to be reduced. The orbit of M68, with properties listed in Table 2.4, is shown as a grey curve in Figure 2.1 in two projections in space and two projections in velocity space. The blue star indicates the present position of the Sun and the red circle is the present position of M68. We calculate the orbits of a total of 10^6 test stars, out of which $N_\mathrm{e} = 68\,839$ escape the potential of the globular cluster and form the tidal tail, shown in Figure 2.1 as black dots. The simulation is run over 10 Gyr, first retracing the orbit of the globular cluster backwards in time and then calculating the orbits of the test stars starting with the initial conditions of the Plummer model 10 Gyr ago. At the beginning of the simulation, many stars are released because no radial cut-off is imposed on the assumed Plummer model in the initial conditions. The first pericentre passage and disc crossings also release many stars, but the rate of escape is reduced later once the globular cluster has already been stripped. For this reason, more stars are produced at

---

[3]http://physwww.mcmaster.ca/~harris/mwgc.dat

Table 2.4: Mass, core radius, present position, and velocity of the M68 (NGC 4590) globular cluster; parameters of the dark halo mass density used in our simulation of the tidal stream, and computed properties of the orbit integrated for 10 Gyr.

Properties M68			Ref.
M_{gc}	$(\mathrm{M}_\odot)$	$(5.7 \pm 2.7) \times 10^4$	[1]
a_{gc}	(pc)	6.4 ± 2	[1]
r_{h}	(kpc)	10.3 ± 0.24	[2]
δ	(deg)	-26.7454	[3]
α	(deg)	189.8651	[3]
v_r	(km s^{-1})	-94.7 ± 0.2	[2]
μ_δ	(mas yr^{-1})	1.7916 ± 0.0039	[3]
μ_α	(mas yr^{-1})	-3.0951 ± 0.0056	[3]
Properties dark halo			
$\rho_{0\mathrm{dh}}$	$(\mathrm{M}_\odot \ \mathrm{kpc}^{-3})$	8×10^6	
$a_{1\mathrm{dh}}$	(kpc)	20.2	
$a_{3\mathrm{dh}}$	(kpc)	16.16	
β_{dh}		3.1	
M_{200}	$(\mathrm{M}_\odot)$	8.32×10^{11}	
q		0.8	
q_Φ		0.91	
Properties orbit			
r_{peri}	(kpc)	6.87	
r_{apo}	(kpc)	35.14	
L_z	(km s^{-1} kpc)	-2397.48	

Note. [1]: Lane et al. (2010).
[2]: Harris (1996) (2010 Edition[3]).
     Relative heliocentric distance error: ~ 2.3 per cent.
[3]: Gaia Collaboration et al. (2018c).
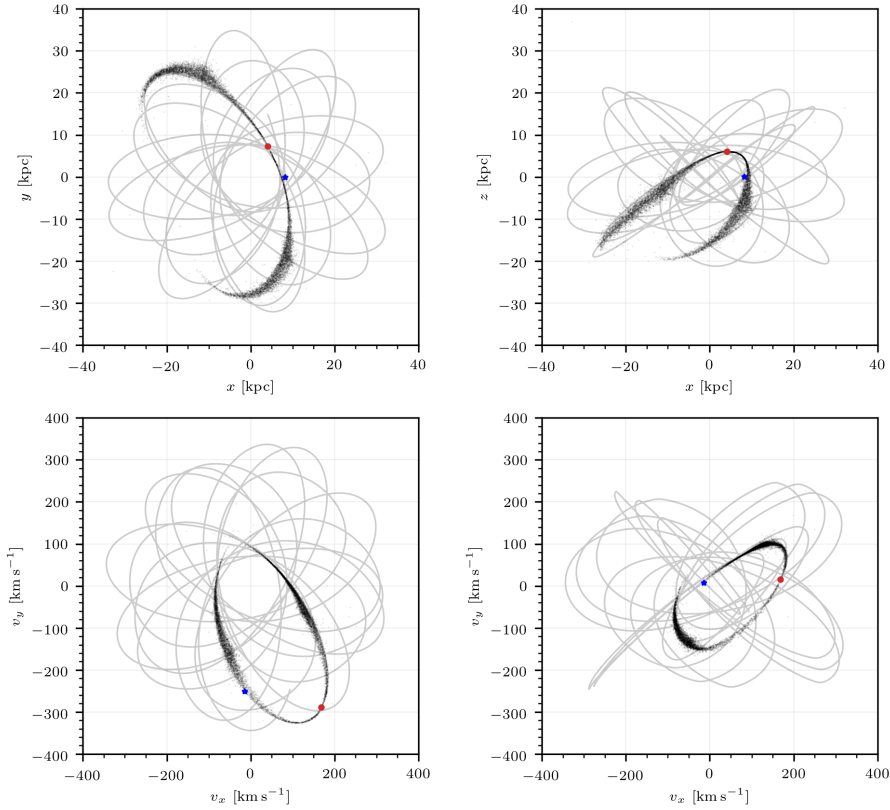
Figure 2.1: Simulated orbit of M68 from 10 Gyr ago to the present time in the Galactic disc plane (x, y) and in the perpendicular plane (x, z), and the simulated tidal stream (sample of 10^4 stars). The blue star is the present solar position and the red dot is the position of M68.

the edges of the tidal tails, which also broaden with increasing distance from the cluster. This large number of stars released in the first orbits is a feature that obviously depends on the history of the cluster and the Milky Way, which our model does realistically predict. The part of the tidal tail closer to the cluster, released at later times, should be more realistic because it is produced after the cluster has already reached a steady rate of escaping stars.

Among the cluster stars generated according to the initial conditions of equations (2.15) and (2.18), the fraction of escaped stars at the end of the 10 Gyr simulation is shown in Figure 2.2. This figure shows that our criterion to select only stars that are likely to escape ($v > v_{\text{lim}}$, shown as the red line), used in later simulations, is adequate to include most of the stars in the cluster that will actually be released in the tidal tail.

Simulation of the *Gaia* observational uncertainties for stream stars

We now include realistic observational uncertainties in the simulated stream stars according to the expected measurement errors in the *Gaia* mission. We apply this to the total number $N_{\text{e}} = 68\,839$ of escaped stars in our simulation
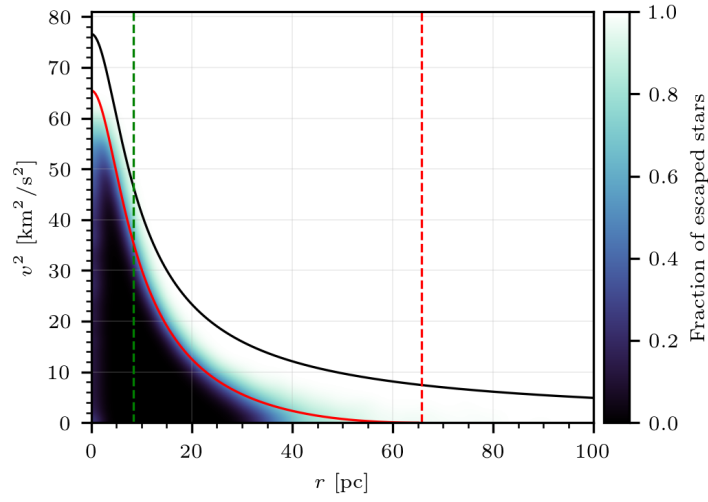
Figure 2.2: Fraction of escaped stars after 10 Gyr. The green dashed line is the half mass radius r_{h} and the dashed red line the tidal radius for $R_{\mathrm{c}} = 21$ kpc. The black line is the escape velocity v_{esc} and the red line is the limiting velocity v_{lim}.

to simulate the observed tidal tail. Naturally, the total number of stars in the tidal tail is highly uncertain, but our estimate of the number of available stars can be a reasonable one to the extent that the total number of globular cluster stars we have simulated is comparable to the expected number of stars in M68, and that the rate of escaping stars is also reasonable.

The *Gaia* observational uncertainties σ_μ for the stream stars have been simulated using the Python toolkit PyGaia[4], which implements the *Gaia* performance models. Observational errors depend on the *Gaia* G-band magnitude, the Johnson-Cousins V-band magnitude, the colour index V-$I_{\rm c}$, and the spectral type of each star. These magnitudes have been simulated as follows:

1. Assign randomly to each star a G-band absolute magnitude and a $G_{\rm BP}-G_{\rm RP}$ colour index following the H-R diagram of M68 that we show in Figure 2.3, which we have generated using 2929 GDR2 stars (see Appendix A.2).

2. Compute the colour index V-$I_{\rm c}$ and the V-band magnitude from the following approximations (Jordi et al., 2010a), valid in the range $-0.4 < V$-$I_{\rm c} < 6$:

$$G_{\rm BP}-G_{\rm RP} = -0.0660 + 1.2061\,(V\text{-}I_{\rm c})$$
$$- 0.0614\,(V\text{-}I_{\rm c})^2 + 0.0041\,(V\text{-}I_{\rm c})^3 \,, \quad (2.31)$$

$$G - V = -0.0257 - 0.0924\,(V\text{-}I_{\rm c})$$
$$- 0.1623\,(V\text{-}I_{\rm c})^2 + 0.0090\,(V\text{-}I_{\rm c})^3 \,. \quad (2.32)$$

3. Determine the spectral type using the effective temperature approximation (Carrasco et al., 2019):

$$T_{\rm eff} = 5040\left[0.43547 + 0.55278\,(G_{\rm BP}-G_{\rm RP})\right.$$
$$\left.- 0.046397\,(G_{\rm BP}-G_{\rm RP})^2\right]^{-1} \quad (\text{K}) \,. \quad (2.33)$$

4. Compute the apparent G-band and V-band magnitudes of the stream stars, neglecting the dust extinction, and correcting the generated G-band magnitude and the previously computed V-band magnitude from the heliocentric distance of the globular cluster $r_{\rm gc}$, to the heliocentric distance of the stream star.

The PyGaia functions give the end-of-mission *Gaia* errors, so we correct them by multiplying by the scale factors λ_μ (equation 2.30). The simulated observed coordinates of stream stars, w_o^μ, are generated by adding a random Gaussian variable with dispersion $\lambda_\mu \varepsilon_\mu$ to the true coordinates. The GDR2 measurements generally cannot be performed on stars fainter than $G = 21$, so only stars $G \leqslant 21$ mag are included in our simulated catalogue of stream stars. In addition, the small number of simulated bright stars satisfying $4 \leqslant G \leqslant 13$ mag and $3550 \leqslant T_{\rm eff} \leqslant 6900$ K are given a radial velocity with the *Gaia* observational error.

The resulting quantity of simulated stream stars after these cuts is 33 228, and is shown in the top row of Table 2.5 as the total number of stream stars in our simulated catalogue before we apply a number of pre-selection cuts that we describe next.

---

[4] https://pypi.org/project/PyGaia/
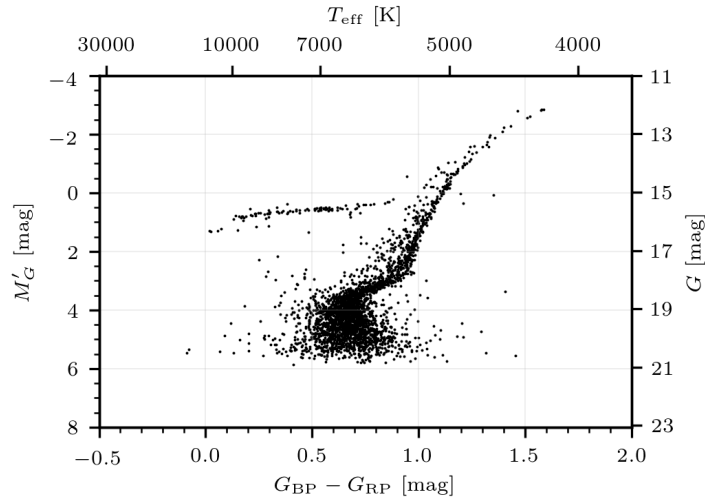
Figure 2.3: Observed $G_{\mathrm{BP}} - G_{\mathrm{RP}}$ colour index and G-band absolute magnitude M'_G for all stars measured in M68 in GDR2.

2.3.3 Data pre-selection

We now imagine that we have a catalogue with all the stars in the GOG18 simulation (a total of ~ 1.5 billion), and that includes in addition some fraction of our 33 228 simulated stream stars. Our method needs to detect the presence of the stellar stream in an optimal way and to identify the most likely candidate members.

To speed up the computation of the likelihood function and reduce the number of foreground stars of the final selection, most of which are in sky regions of high stellar density and far from the possible stream associated with M68, we apply a set of pre-selection cuts to the star catalogue. The stars that fulfil the following conditions are pre-selected:

(1) $G \leqslant 21\,\mathrm{mag}$, to eliminate faint stars with large astrometric errors.

(2) $\pi < 1/0.3\,\mathrm{mas}$, e.g. large distance, to eliminate foreground disc stars.

(3) $|b| > 15\,\mathrm{deg}$, to avoid the regions of high stellar density close to the disc

For our fourth condition (4), we use a more complex pre-selection method to further restrict the number of stars that are used to evaluate the likelihood function for different stream models. The goal is to eliminate most of the foreground stars that can be ruled out as members of any possible stream associated with M68, within the uncertainties of the M68 orbit arising from observational errors and the Galactic potential. Our pre-selection method is described in detail in Appendix A.3.1; here we explain its basic idea, which uses the fact that the tidal stream is close to the orbit of the progenitor. We use a range of parameters for the orbit of M68 and the potential of the Milky Way to compute a bundle of possible orbits of M68 during the time interval from $t_0 - t_l$

to $t_0 + t_l$, where t_0 is the present time and t_l is chosen to obtain the relevant part of the orbit for the stream. Our simulations show that $t_l = 50\,\mathrm{Myr}$ results in an adequate coverage of the reliable part of the stream in the case of M68, and we adopt this value in this chapter. Many of the stars that are released by the cluster in the first few orbits, when the rate of escaping stars has not yet settled to a steady state, are located further from the globular cluster than this section of the orbit, and they are eliminated from the final catalogue in this fourth pre-selection condition.

The bundle of orbits computed in this way is used to define a region in phase space where stars have to be located to be pre-selected, also taking into account the observational errors. This is done by characterizing the bundle of orbits by a series of Gaussians, which are convolved with the Gaussians of observational errors. Stars have to be located within this region (involving conditions of the sky positions, proper motions, and parallaxes) to be pre-selected.

As the final fifth step (5), we remove stars that are within an angular distance of the globular cluster that gives rise to the tidal tail, and also stars in any other globular clusters that are within the pre-selected region, since they have highly correlated kinematics. The list of globular clusters that have been removed in this way are shown in Appendix A.3.2.

The number of stars in GOG18 and in the simulated stream of M68 after each one of these cuts is specified in Table 2.5. The first three steps reduce the general GOG18 catalogue by a factor close to six, and a smaller factor for the stream stars which are all sufficiently far from us and mostly at high Galactic latitude. The fourth step achieves the largest reduction in the number of foreground stars, a factor ~ 400, by restricting the stars we look for to be consistent with our range of models in sky position, proper motion, and parallax. The stream stars are reduced by a factor of nearly 3, mostly due to the stars ejected in the first few orbits in the simulation that are near the edge of the stream, with a distribution that we consider as insufficiently reliable. The fifth step eliminates a very small fraction of stars, and is important mostly to remove stars that are bound or very close to M68.

The distribution of pre-selected stars in the GOG18 catalogue is shown as blue dots in the left-hand panels of Figure 2.4, and the pre-selected stream stars are shown as black dots in the right-hand panels. Top panels show angular positions and bottom panels show proper motions. The tidal stream of M68 is particularly favourable to be observed because of the long stretch of the orbit that is close to us in a region of low foreground stellar density in the position and proper motion space.

2.3.4   Recovery of the dark halo parameters

We now test the detection of a tidal stream in the GOG18 simulated data set by adding a number of stars N_{str} selected randomly among the 6564 stars of our simulated tidal stream. We find the maximum of the Λ function described in Section 2.2.1 (equation 2.2), with the prior in equation (2.28) that incorporates the measurements of the M68 kinematics, when the parameters τ (fraction of tidal stream stars in the data set), θ_c (orbital parameters of M68), and θ_ϕ (gravitational potential parameters) are allowed to vary. Each time we evaluate
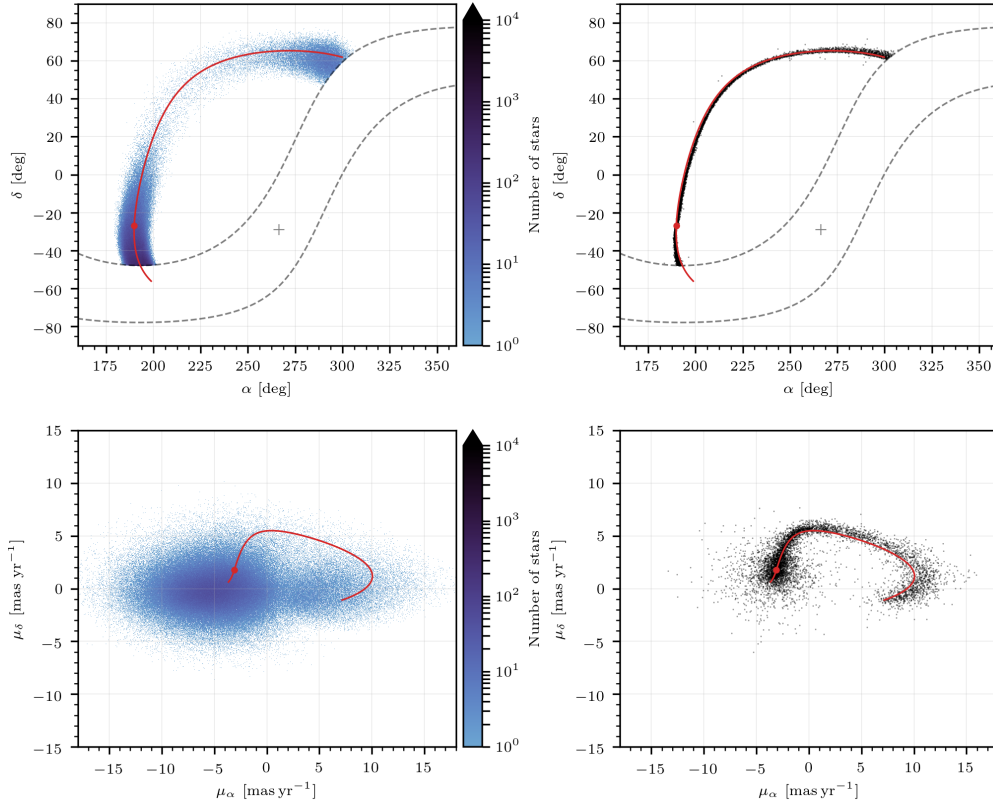
Figure 2.4: *Left*: Distribution of the pre-selected stars from the GOG18 catalogue. *Right*: Pre-selected stars from the M68 simulated tidal stream. The red dot marks the current position of the cluster and the red line is its simulated orbit over $t_l = 50$ Myr backwards and forwards from its current position. Grey dashed lines mark the Milky Way disc cut at $b = \pm 15$ deg and the grey cross indicates the Galactic centre.

Table 2.5: Number of stars in the simulated catalogue and simulated stream that pass our successive pre-selection cuts.

Pre-selection cut	GOG18	Stream stars
All catalogue	1510 398 719	33 228
(1) - (2) - (3)	269 125 739	17 183
(4)	613 098	6627
(5)	612 909	6564

the likelihood for a new set of parameters, we need to resimulate the tidal stream and calculate the probability density of the stars with equation (2.22). To make this computationally easier, we calculate this stream probability density only for the fixed set of pre-selected stars described earlier, and we recompute orbits for the tidal stream only for a fixed set of 1200 test particles in the M68 globular cluster. These particles are selected among the ones with initial velocities $v > v_{\lim}$ and $r > r_{\rm t}$ (see equations 2.21 and 2.19) using a mean cluster orbital radius $R_{\rm c} = 21$ kpc in equation (2.19), which increases the fraction of escaped stars and the efficiency of the calculation. Typically, the number of stars among these 1200 that escape M68 and form the tidal stream is about 1000, and is always greater than 750. We use these stream stars to recompute the smoothed phase-space density model of the tidal stream with equations (2.22) and (2.26), for each pre-selected star. We find these number of stream stars is sufficient to obtain a reasonable accuracy for the best-fitting tidal stream. We note that choosing fixed initial conditions within the M68 Plummer model for the simulated stream stars as we vary the model parameters is important to ensure differentiability of the final stream star positions and velocities and a smooth likelihood function when we vary model parameters.

We compute the maximum likelihood and find the best-fitting stream model for a total of 30 cases: for six values of the number of stream stars added to the catalogue, $N_{\rm str} = \{10, 50, 100, 300, 500, 1000\}$, we do five independent cases with different random selections of $N_{\rm str}$ stars among all the 6564 selected escaped stars in our base simulation of the M68 tidal stream (bottom row of Table 2.5). Results are shown in Figure 2.5. In each panel, the solid line connects the average results for the five cases of each value of $N_{\rm str}$, while the grey band is their range. The top panel shows the value of Λ. When $\Lambda > k = 6.635$ (shown as the horizontal dashed line), the detection of the stream is significant at the $\epsilon = 0.01$ probability of rejecting the null-hypothesis. This happens always when $N_{\rm str} > 100$, and in most cases for $N_{\rm str} > 50$.

The second panel is the fraction τ of stream stars in the catalogue. The recovered fraction is generally lower than the true value (equal to the ratio of added stream stars to the total number of pre-selected stars), indicated by the dashed line. In general, τ can be different than the true value for two reasons: our foreground model is highly approximate and does not accurately reflect the distribution of stars in GOG18, and the stream phase-space density model we construct by adding Gaussians is also imprecise. The latter may explain the increasing ratio of the measured to the true τ with $N_{\rm str}$, if the algorithm tends to match the positions of a fraction of the stream stars while ignoring the rest at low $N_{\rm str}$.

The third panel is the value of Q from equation (2.29). This value is small when the detected stream does not impose significantly improved constraints on the globular cluster orbit compared to the prior (the measured proper motions, radial velocity, and distance), but grows as the stream stars provide more stringent constraints on the orbit. If $Q > 4$, the detected stream is pushing the best-fitting orbit away from the measured values. Significant deviations start to occur in our simulations for our largest value of $N_{\rm str}$, probably due to the

approximate evaluation of the tidal tail phase-space distribution in our method. These deviations are not so large as to substantially affect our best fits.

Finally, the last two panels show the recovered values of the dark halo mass and its axial ratio. These recovered values are consistent with the true ones, and the errors are as small as ~ 10 per cent for the mass and ~ 3 per cent for the axial ratio when $N_{\mathrm{str}} \sim 1000$. Of course, realistic errors on these potential parameters are expected to increase when allowing for variations in other parameters such as the disc mass and scale length or the halo density profile.

2.3.5 Identification of stream stars

Our final goal is to identify the stars that are most likely to be members of the stream among our simulated stars, and check if the true stream stars that were inserted in the catalogue are recovered. We first identify stars that are consistent with a phase-space model of the tidal stream and then we select those that are compatible with the colour and magnitude of the globular cluster progenitor.

Phase-space identification

We start by considering only the phase-space variables. We construct again the phase-space density model of the stream with the same procedure as in Section 2.2.5, using the estimated best-fitting parameters $\hat{\theta}_\kappa$ and increasing now the number of simulated escaped stars to $N_{\mathrm{e}} = 10^4$, which yields a more accurate and smoother model than the smaller number used when the model parameters are varied. We compute the probability density of a star to belong to the tidal stream with equation (2.26), although without considering this time the selection function ψ_{s},

$$P_{\mathrm{SEL}}(w^\mu | \hat{\theta}_s, \hat{\theta}_c, \hat{\theta}_\phi; \sigma^{\mu\nu}) = \frac{1}{N_{\mathrm{e}}} \sum_{i=1}^{N_{\mathrm{e}}} G(w^\mu - w_{ci}^\mu | \sigma^{\mu\nu} + \Xi_i^{\mu\nu}) \ . \qquad (2.34)$$

We identify as candidate stream members the set of stars that pass a sixth cut (6), requiring a probability density above a fixed threshold:

$$P_{\mathrm{SEL}} \geqslant \chi_{\mathrm{sel}} \ . \qquad (2.35)$$

The threshold χ_{sel}, with units of the inverse product of the six w^μ coordinates that we shall express in $\mathrm{yr}^3 \, \mathrm{deg}^{-2} \, \mathrm{pc}^{-1} \, \mathrm{mas}^{-3}$, can be conveniently chosen to retain as many candidates as possible without excessively contaminating the sample that is obtained with foreground stars.

Colour-magnitude selection

As the final condition to consider a star as a candidate member of a stellar stream, we consider the colour information that is obtained in the *Gaia* photometric measurements. A stellar stream member should have colours and absolute magnitude (which can be computed assuming the model distance of the stellar stream) consistent with the H-R diagram of the progenitor cluster.

The GOG18 catalogue includes a simulation of the *Gaia* photometric measurements of the G-band magnitude, roughly corresponding to unfiltered light
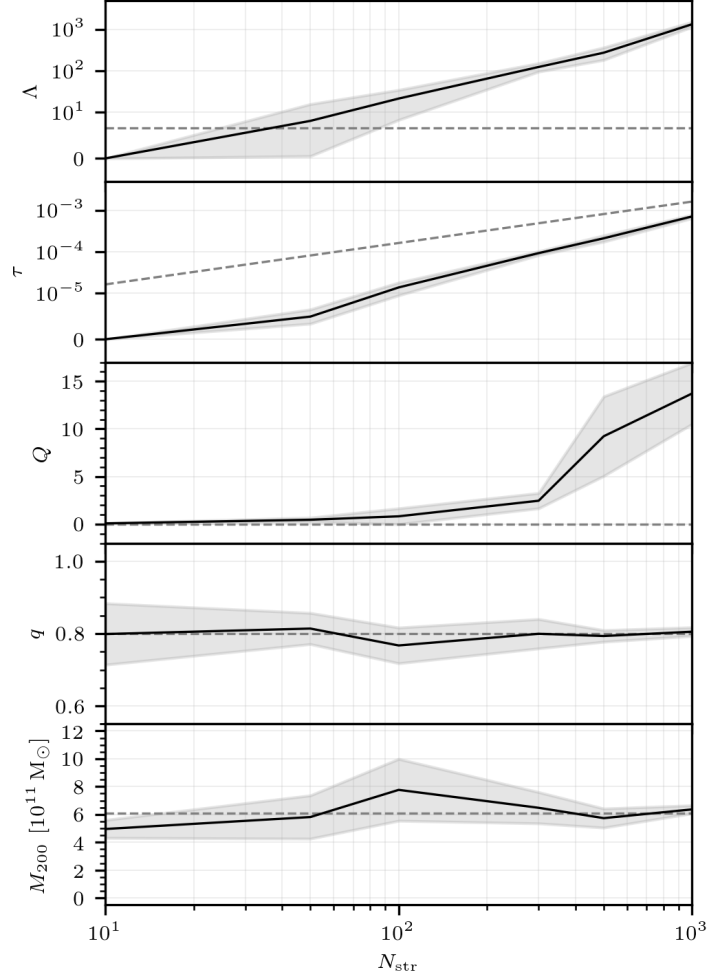
Figure 2.5: Computed statistical parameters and best estimates of the halo mass and axial ratio using the GOG18 pre-selected data and five different random samples of sets of N_{str} simulated stream stars, with $N_{str} = \{10, 50, 100, 300, 500, 1000\}$. The first grey dashed line marks the threshold $k = 6.635$, and the next lines the true parameter values that were used in the tidal stream simulation (see Table 2.4). Solid lines show the average best fit obtained for each N_{str}, with the range shown by the grey band.

over the wavelength range from ~ 330 to 1050 nm. Two additional magnitudes are also measured in a blue (BP) and red (RP) broad passbands from 330 to 680 nm, and from 630 to 1050 nm, respectively, yielding the two magnitudes G_{BP} and G_{RP}. To compute the absolute magnitude M'_G, we do not use *Gaia* parallaxes because the observational errors are too large. Instead, we assign to each star the heliocentric distance of the closest point to the star of the computed orbit of the progenitor cluster, in our model of the Galactic potential that has given the best-fitting stellar stream. We then select the stars with colours and absolute magnitude that are consistent with the H-R diagram of the progenitor cluster, following the procedure that is described in detail in Appendix A.4.

In the case of M68, the tidal stream is expected to pass at ~ 5 kpc from the Sun, so the detectable stream stars close to us should often have lower luminosity than the least luminous detectable stars at the M68 distance of ~ 10 kpc. These stars cannot be directly compared to the M68 H-R diagram as measured by *Gaia*. We solve this problem by including also as candidate stars those with absolute magnitude $M'_G \geqslant 5.68$, and colour $0.5 \leqslant G_{BP} - G_{RP} \leqslant 1$ mag, which adequately brackets the main-sequence for stars in the relatively narrow range of distances the M68 stream extends over. We neglect any impact of dust extinction, which is small and fairly constant along the tidal stream according to the STILISM[5] extinction model (Capitanio et al., 2017; Lallement et al., 2018). In summary, our seventh selection cut (7) is that the star colours and absolute magnitude are either compatible with the M68 H-R diagram observed by *Gaia*, or obey the above conditions for main-sequence stars in M68 of lower luminosity than the *Gaia* detection threshold.

The results of our simulations where we add a randomly selected set of N_{str} stars of the simulated stream to the GOG18 catalogue is presented in Figure 2.6. The number of selected stars N_{sel} from GOG18 alone after our first six cuts are applied is the black line, shown as a function of the selection threshold, χ_{sel}. The red line is the number of stars that are in addition colour-magnitude compatible with M68 (cut 7). The other coloured lines show the number of selected stars when we add N_{str} simulated stream stars to GOG18, taking several random samples of these added stars to compute a mean of N_{sel} and its dispersion (shown as the shaded area around each curve). For each case, we have constructed the phase-space model of the tidal stream using the computed values of the parameters shown in Figure 2.5. The added stream stars pass all of our seven cuts, although the seventh cut in this case is automatically satisfied because the model stream stars are assumed to have compatible colours with M68. The figure shows that for the M68 simulated stream, and by choosing a threshold $\chi_{sel} \sim 3 \ \mathrm{yr^3 \, deg^{-2} \, pc^{-1} \, mas^{-3}}$, we select ~ 10 per cent of the stream stars measured in the catalogue while including only 1 foreground star among the selected ones. This performance improves if we restrict our selection to phase-space regions of low background contamination, and is also sensitive to the way the selection function ψ_s is treated (which has been ignored here).

Figure 2.6 also shows that the use of the colour information is not essential

---

[5] https://stilism.obspm.fr/
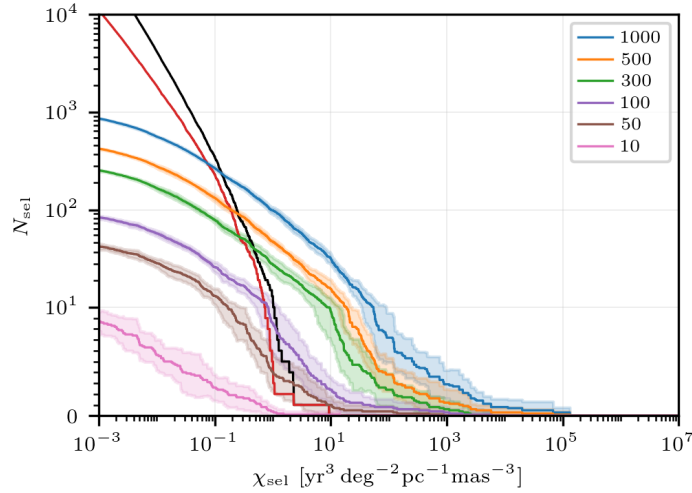
Figure 2.6: Number of selected stars N_{sel} as a function of the selection threshold χ_{sel} in our sixth cut. The black line indicates the number of GOG18 stars compatible with the phase-space model of the stellar stream (cuts from 1 to 6 applied), and the red line shows stars that are additionally colour-magnitude compatible with M68 (passing the seventh cut as well). Colour lines are the number of stream passing all seven cuts from six different cases with N_{str} stars in our model stream added, with their range in several random samples indicated by the shaded areas.

to the ability to find the stellar stream, although it certainly helps to constrain further the member stars as quantified by the separation between the black and red lines. As long as the number of stars in the stream is $N_{\mathrm{str}} \gtrsim 100$, the stream is detected as an excess of stars above the probability threshold χ_{sel}, and when colours are used this minimum number of required stream stars is reduced to $N_{\mathrm{str}} \simeq 50$, assuming that the orbit of the progenitor cluster is known. This, of course, varies for each candidate cluster progenitor, depending on the level of foreground contamination of the zones covered by the predicted stellar streams and the complexity and breadth of the predicted stellar stream.

2.4   Application to *Gaia* DR2 data

2.4.1   Data pre-selection

The full sky GDR2 star catalogue, published on 2018 April 25 based on data collected during the first 2 yr of the *Gaia* Mission (Gaia Collaboration, 2016), includes five-parameter astrometric solutions (parallaxes, sky coordinates, and proper motions) and multiband photometry (G, G_{BP}, and G_{RP} magnitudes) of ~ 1.7 billion sources. In addition, it includes radial velocities for ~ 7.2 million sources. A complete description of its contents is found in Gaia Collaboration et al. (2018a).

   We apply the pre-selection method described in Section 2.3.3 to GDR2, as well as to the GOG18 simulated catalogue to compare results. The numbers of stars that pass each of our cuts are given in Table 2.6. The first three cuts produce a number of selected stars similar in GOG18 and GDR2. The fourth

cut, requiring stars to be close to the predicted M68 orbit for a variety of models, results in the largest reduction. The number of stars in GDR2 after this cut is smaller than in GOG18, which we think is attributable to imperfections in the model of the stellar distribution of the GOG18 simulation and our approximate treatment of the effect of measurement errors in GDR2. The fifth step results in a larger reduction of GDR2 compared to GOG18, because of the presence of stars belonging to the globular cluster M68 (which are not actually simulated in GOG18), although the reduction is still small.

As a first exploration of the GDR2 pre-selection, we plot the sky coordinates of the pre-selected stars. This is shown in Figure 2.7 for all the 440 499 stars after our cut 5, plotted as very small black dots. The large red dot indicates the position of M68 and the light red curve is its computed orbit in our standard model (central parameters in Table 2.4). The cross shows the Galactic centre and the two dashed lines indicate a Galactic latitude $b = \pm 15\,\mathrm{deg}$. Without our more strict selection from cut 6, the presence of any tidal stream is not clearly discerned owing to the large foreground. Figure 2.7 shows, however, the presence of variations of stellar density in the form of parallel streaks due to the *Gaia* exposure variations, most clearly visible in the range $-30\,\mathrm{deg} < \delta < 0\,\mathrm{deg}$. There are also regions of low density that run parallel and close to the predicted M68 orbit, which is a reason to be concerned with our method of identifying a tidal stream.

To see if the stream can be more easily identified using only our broad pre-selection in cut 4 when we include the colour information, we apply now the extra cut 7 defined in Section 2.3.5 and described in detail in Appendix A.4, to select stars with *Gaia* colours compatible with the M68 H-R diagram. This reduces the number of pre-selected stars to 127 615. The positions of these stars are plotted as black dots in the top panel of Figure 2.8. The expected elongated overdensity of stars along the predicted orbit of the globular cluster is now more clearly discerned extending over a large part of the North Galactic hemisphere.

2.4.2 Dark halo parameters

The values of the model parameters maximizing the likelihood ratio Λ (which includes the likelihood function of the stream and the kinematic measurements of M68, equations 2.2 and 2.28) have been calculated applying the Nelder-Mead Simplex algorithm to the GDR2 pre-selected data after our first five cuts. A total of nine parameters are varied: the fraction of pre-selected stars τ in the stellar stream, the four parameters $\rho_{0\mathrm{dh}}, a_{1\mathrm{dh}}, a_{3\mathrm{dh}}$, and β_{dh} of the halo gravitational potential and the distance and three velocity components of M68. In this case, we have computed only the diagonal elements of the covariance matrix in equation (2.5) and used them to compute errors of the parameters assuming that all the other ones remain fixed. The results are listed in Table 2.7.

The main conclusions we infer from these results are the following:

- The maximum value found for the likelihood ratio statistic is $\Lambda = 84.6$, implying that the null-hypothesis ($\tau = 0$) is rejected at high confidence because $\Lambda > k = 6.635$ represents the 99 per cent confidence level.
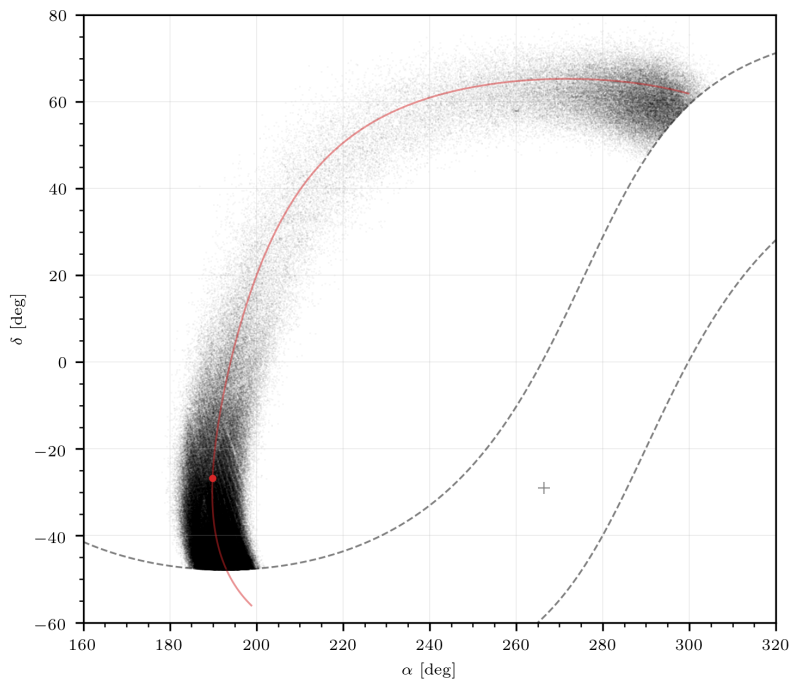
Figure 2.7: Sky map in equatorial coordinates of pre-selected stars passing our first five cuts. Grey dashed lines indicate a Galactic latitude $b = \pm 15$ deg and the grey cross is the Galactic centre. Red dot marks the present position of the cluster M68 and the red curve is its predicted orbit over 50 Myr forwards and backwards respect its current position.

Table 2.6: Total number of stars in GOG18 and GDR2 and number of stars that pass each cut. For the last two cuts 6 and 7, this is shown for three separate sky regions defined in Section 2.4.3, in which the tidal tail is detected in different foreground conditions. Numbers in parentheses for GOG18 indicate the expected number of stars in the absence of any tidal tail if GOG18 had the same number of pre-selected stars as GDR2 in each of the three regions.

Pre-selection cut	GOG18	GDR2
All catalogue	1510 398 719	1692 919 135
(1) - (2) - (3)	269 125 739	276 019 797
(4)	613 098	446 982
(5)	612 909	440 499
Region (i) Circle		
(6) $\chi_{\mathrm{sel}} = 0.554$	1 (1)	13
(7)	1 (1)	13
Region (ii) Disc 1		
(6) $\chi_{\mathrm{sel}} = 1.392$	6 (4)	12
(7)	2 (1)	4
Region (iii) Halo		
(6) $\chi_{\mathrm{sel}} = 5.65 \times 10^{-3}$	17 (33)	126
(7)	1 (2)	98
Final selection		
(6)	24 (38)	151
(7)	4 (4)	115
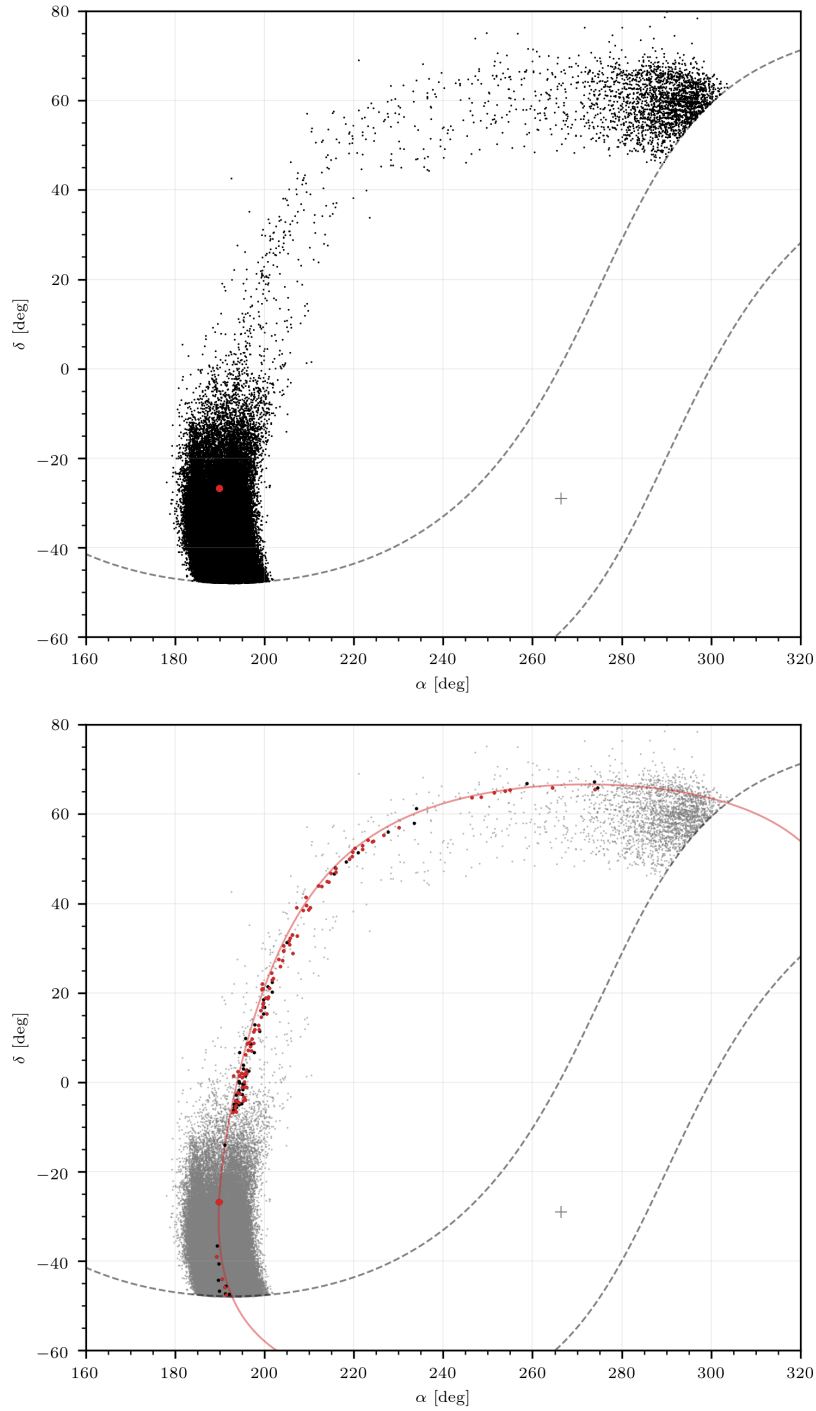
Figure 2.8: *Top*: Same as Figure 2.7, but restricted now to stars that pass our seventh cut in addition to the first 5 (i.e., with photometry compatible with the M68 H-R diagram), which leaves ~ 30 per cent of the stars in Figure 2.7. *Bottom*: Final selection of stars. Grey small dots are the same as in top panel, black dots are stars compatible with the density model of the stellar stream (cut 6) and red dots are stars that are also compatible with the M68 H-R diagram (cut 7). The small number of selected stars in the range -50 deg $\leqslant \delta \leqslant -7$ deg and the abrupt change for $\delta > -7$ deg is caused by our selection method.

- Comparing with the simulation results in Figure 2.5, we find that the value $\Lambda \sim 80$ suggests that there are $N_{\mathrm{str}} \sim 250$ stars that belong to the detected tidal tail and that the tidal stream would have been detected as long as the number of stars is $N_{\mathrm{str}} \gtrsim 100$ using only the kinematic data (without using any colour information).

- The estimated distance and velocity of the globular cluster M68 change little compared to the directly measured values of the proper motion, distance, and radial velocity (Table 2.4). The reason is that the detected stream does not constrain the orbit of the cluster with greater precision than the kinematic measurements of M68 themselves. This shows that the detected stream is fully consistent with originating in M68.

- The best-fitting model of the Milky Way dark matter halo has the parameters shown in Table 2.7. The implied total circular velocity at the solar radius is $v_{\mathrm{c}} = 225.38$ km s^{-1}, compatible with the circular velocity of the Local Standard of Rest (LSR) (Bland-Hawthorn and Gerhard, 2016a, see Appendix A.1). The errors of the halo free parameters have been computed using the second derivatives of the posterior function (eq. 2.5). This approximation tends to underestimate their values, as it only uses local information of the posterior function, but not the entire distribution over the whole parameter space. Furthermore, the error has been computed only for our parameterized model and is not marginalized over the other parameters determining the radial profile. Constraints on the halo oblateness need to be obtained by considering possible variations in the mass and radial profile of the disc and the bulge mass, which is beyond the scope of this chapter. We examine constraints on the shape of the dark matter halo in the Chaper 4, using also data for other streams.

2.4.3 Selection of stream stars

We now seek to identify the stars among our pre-selected set of 440 499 which have a high probability of belonging to the identified M68 tidal stream. We do this by applying our sixth cut in a similar way as with our simulated stream in Section 2.3.5, choosing the threshold χ_{sel} that maximizes the ratio between the GDR2 and the GOG18 selections. This maximum occurs for a low number of GOG18 selected stars and its value is affected by Poisson fluctuations of the sample. This selection criterion minimizes the foreground contamination in the final selected sample, taking only a few expected foreground stars.

The foreground stellar density has large variations over the sky area of the pre-selected sample (after applying our first five cuts), implying that a single value of χ_{sel} would not be an efficient way of obtaining the largest possible sample of reliable stream candidates while minimizing the foreground contamination. We therefore divide the pre-selected sample into four sky zones:

(i) *Circle*: A circle of angular radius 0.5 deg centred on M68.

(ii) *Disc 1*: $-50 \leqslant \delta \leqslant -7$ $180 \leqslant \alpha \leqslant 200$ (deg)

Table 2.7: Best-fitting results for the orbit of M68 and the dark halo parameters, using the GDR2 pre-selected data.

Statistical parameters		
Λ		84.6
τ		$(2.17 \pm 0.42) \times 10^{-4}$
Q		0.6723
Best-fitting kinematics of M68		
r_{h}	(kpc)	10.24 ± 0.05
v_r	(km s^{-1})	-94.544 ± 0.052
μ_δ	(mas yr^{-1})	1.7917 ± 0.0020
μ_α	(mas yr^{-1})	-3.0953 ± 0.0035
Best-fitting parameters of dark halo		
$\rho_{0\mathrm{dh}}$	(M$_\odot$ kpc^{-3})	$(7.268 \pm 0.076) \times 10^6$
$a_{1\mathrm{dh}}$	(kpc)	18.59 ± 0.73
$a_{3\mathrm{dh}}$	(kpc)	16.17 ± 0.96
β_{dh}		3.102 ± 0.039
M_{200}	(M$_\odot$)	$(6.37 \pm 0.35) \times 10^{11}$
q		0.87 ± 0.06
q_Φ		0.94 ± 0.03
Derived orbital parameters of M68		
r_{peri}	(kpc)	6.95 ± 0.03
r_{apo}	(kpc)	42.3 ± 3.4
L_z	(km s^{-1} kpc)	-2414.7 ± 4.4

(iii) *Halo*: $-7 < \delta \leqslant 80$ $180 \leqslant \alpha \leqslant 275$ (deg)

(iv) *Disc 2*: $45 \leqslant \delta \leqslant 80$ $275 < \alpha \leqslant 310$ (deg)

The second region called Disc 1 excludes the circle region around M68. Notice also that the circle region includes stars that are within 0.5 deg, but further than 0.3 deg from the centre of M68 because of our cut 5 in the pre-selected sample.

The number of selected stars N_{sel} in the GOG18 and the GDR2 catalogues as a function of the selection threshold χ_{sel} is shown in Figure 2.9, as the black dashed and solid lines, respectively. We show this only for the first three regions (results for the fourth region, called Disc 2, are similar to the Disc 1 region). When we apply, in addition, the colour selection cut 7 to require that the star colours are consistent with the M68 H-R diagram, we obtain the solid and dashed red lines for GDR2 and GOG18.

In general, at low χ_{sel}, the number of stars in GOG18 and GDR2 is not exactly the same: there are more stars in GDR2 compared to GOG18 in the halo and a similar number (slightly higher in GOG18) in the other three regions. As discussed previously, we believe this is due to imperfections of the model used to construct the GOG18 catalogue in modelling the real Milky Way galaxy and also to approximations we have used to take into account the effect of astrometric errors in GDR2. At high χ_{sel}, the number of stars in GDR2 increases compared to GOG18, mainly in the Circle and Halo regions, as expected if the tidal stream is real, and from the presence of stars bound to M68. In the Disc regions, the tidal stream is barely noticed due to the high foreground contamination.

To correct for the different number of foreground stars in the GOG18 simulation and the real GDR2 data, we multiply the number of stars found in GOG18 to pass the cut 6 in each region by the ratio of the total number of pre-selected stars in GDR2 to that in GOG18 (passing the first five cuts). This corrected number is given in parenthesis in Table 2.6 in the GOG18 column. We also give the value of χ_{sel} used in each region. In the halo region, we can afford using a low number because of the very low foreground contamination, but in the other regions, the threshold needs to be set to a much higher value to avoid picking up too many foreground stars as candidates. The number of stars left after applying also the colour cut 7 are also given in Table 2.6 for GOG18 and GDR2.

We find the following results for the stars that are finally selected as likely members in each zone:

(i) *Circle*: The selected stars are at a projected distance of 50 - 90 pc from the centre of the progenitor because of our cut 5 in the pre-selection and the definition of this region, so they lie in the transition between the cluster and the stream. The 26 stars with the highest intersection with the stream density model are colour-magnitude compatible with the cluster and 13 of them are selected above our chosen χ_{sel}. Only one of these stars should belong to the foreground on average. Many of these

stars, even if unbound from M68, may be orbiting practically at the same orbital energy and may therefore be moving in loops around M68.

(ii) *Disc 1*: This is the most contaminated zone because it is near the Galactic disc and the proper motions of the disc stars overlap that of the globular cluster. This forces us to choose the high value $\chi_{\mathrm{sel}} = 1.392$, for which we expect 4 foreground stars to be included after cut 6, and we find a total of 12. After applying also the colour cut 7, the number of stream candidate stars is reduced to 4, with 1 expected to be foreground. It is not possible to find more reliable stream candidates in this zone because of the high value of χ_{sel} we need to impose, but this situation will improve in the future as the *Gaia* proper motion errors and stream model accuracy are improved.

(iii) *Halo*: Here we can choose a much lower value of the threshold, $\chi_{\mathrm{sel}} = 5.65 \times 10^{-3}$, with a corrected GOG18 expectation of 33 foreground stars after cut 6, and we find a total of 126. In this case, the foreground stars are much more effectively eliminated by our cut 7, so only two foreground stars are expected after cut 7 for the corrected GOG18 simulation. In contrast, in the GDR2 data, we find that 98 out of the 126 stars also pass cut 7, providing strong evidence that these stars are indeed members of the M68 stream that are near the distance inferred from our stream model. We also remark that the 17 stars with the highest intersection with the stream model (highest value of χ_{sel}) are all colour-magnitude compatible with M68 and that 90 per cent are compatible among the 50 stars with the highest χ_{sel}. We therefore expect most of the 98 stars in our final selection from this region to be true stream members.

(iv) *Disc 2*: In this region we actually obtain a larger number of stars selected from GOG18 than from GDR2 when choosing a high value of χ_{sel}, probably due to a Poisson fluctuation. This indicates that the number of stream members in this region is likely to be already very low. We have not selected any stars from this region, although future improved *Gaia* data may allow interesting stream candidates to be identified.

With the first 3 zones together, we finally have 151 stars that are compatible with the phase-space model of the stellar stream (cut 6), out of which 115 are also compatible with the H-R diagram of M68 (cut 7). If our estimate of foreground contamination from GOG18 is correct, we expect an average of only 4 of the final 115 stellar stream candidates to be chance foreground projections. These stars are plotted in the bottom panel of Figure 2.8 as large dots, with the red ones being the stars that pass the cut 7 as well.

These finally selected stars are also shown in three panels in Figure 2.10, where we see their distribution in parallax, proper motions and in the M68 H-R diagram. The red curve in the first two panels is the expected trajectory from our stream model. Parallaxes are mostly of insufficient accuracy to test the predicted distance to these stars, and were mostly used in the pre-selection

stage to rule out nearby foreground disc stars. The middle panel, showing proper motions, reflects also the consistency with the stream model. The H-R diagram in the bottom panel shows that most of the final stream candidates are inferred to be near the main-sequence turn-off.

A list of the 115 stars passing our final selection is included in Appendix A.5. GDR2 does not provide a radial velocity for any of these stars. We have also checked the RAVE DR5 (Kunder et al., 2017) and the LAMOST DR4 (Luo et al., 2015) catalogues, and have not found any of these stars.

2.5 Conclusions

A new method is presented in this chapter to search for tidal streams, based on maximization of a likelihood function that is calculated from a model of the stream and of the foreground stellar population. The method identifies the stream when there is sufficient statistical evidence that a subset of the stars in the given catalogue are compatible with a stream generated from a progenitor orbit that is fitted in the maximization procedure, together with parameters of the gravitational potential. The stream can be modelled as a superposition of Gaussians, which facilitates the inclusion of the intrinsic stream dispersion and observational errors for computing a realistic likelihood function. We present tests of the method, and its first application to the tidal stream of the globular cluster M68.

The stream we find coincides with the one previously discovered by Ibata et al. (2019b), who named it Fjörm. They found the stream in a blind search using the Streamfinder method (Malhan and Ibata, 2018), based on using six-dimensional tubes in phase-space with the expected stream dispersion and counting the number of stars compatible with a single stream. We have instead identified this stream by searching specifically for one associated with M68. The stream is detected in our method as an overdensity with respect to a phase-space model of the Milky Way that is fitted to a physical simulation of the stream caused by tidal shocking of the globular cluster, by adjusting the Galactic gravitational potential and the orbit of M68.

The resulting orbit of our fit is fully consistent with the measured kinematics of M68 and a simple Milky Way potential with only four free parameters. Although we find preliminary constraints on the potential in this chapter, this needs to be further explored, combining with data from other known streams and allowing for realistic variations of the potential contributed by the halo, disc and bulge that are compatible with other observations. So far, we have discovered one of the most visually obvious and easily detectable streams. As our method is improved with an increasingly accurate foreground model and *Gaia* selection function and a more flexible and realistic parameterization of the Milky Way gravitational potential, many more streams containing fewer stars that are not obvious to the eye should likely be discovered.

The M68 stream we have found is particularly promising to constrain the Milky Way potential and to study the dynamical process of mass segregation and tidal perturbations on a globular cluster as it crosses the disc. The stream passes within only 5 kpc from us, implying that accurate velocities from proper motions of relatively low-luminosity stars are easier to measure than for other
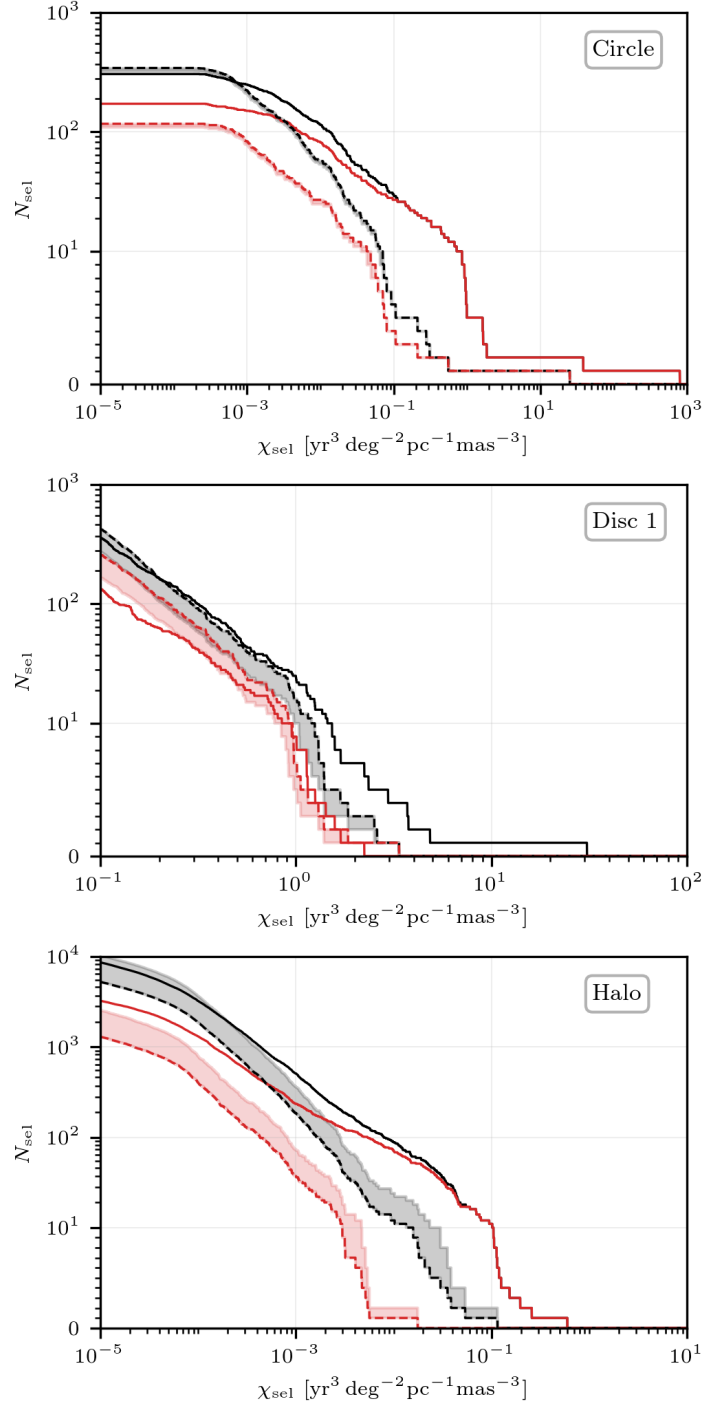
Figure 2.9: Number of selected stars N_{sel} as a function of the selection threshold χ_{sel}. Black line is the number of GDR2 stars compatible with the stellar stream phase-space model, red line are stars additionally compatible with the M68 colour-magnitude diagram. Dashed lines are the same quantities for GOG18 stars. The shaded space marks the difference between GOG18 and its correction. *Top*: Zone (i) Circle. *Middle*: Zone (ii) Disc 1. *Bottom*: Zone (iii) Halo.
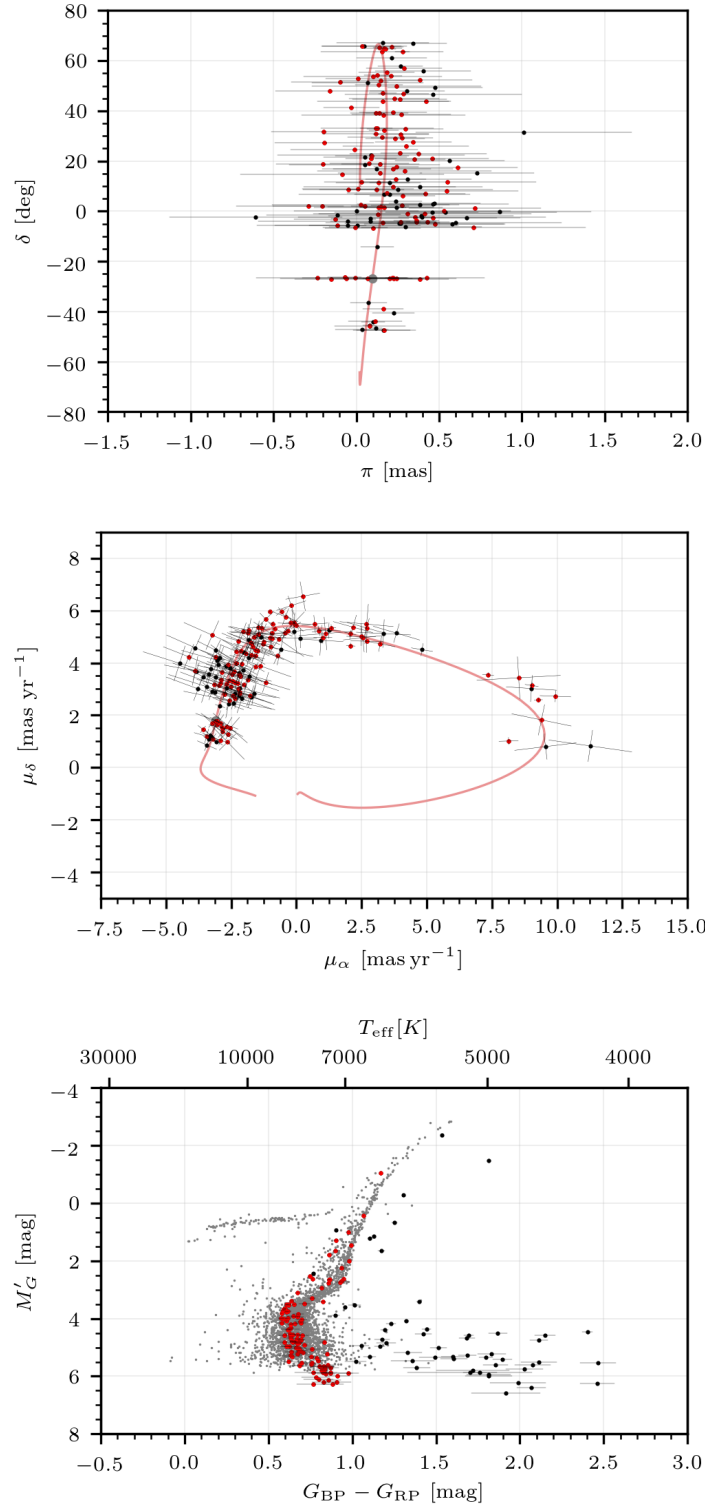
Figure 2.10: Distributions of the finally selected 151 stars after our cut 6 using the kinematic data. Red dots show the 115 stars that pass also our cut 7 of compatibility with the M68 H-R diagram and black dots are the other 36 stars. *Top*: Declination versus parallax. *Middle*: Proper motions. Grey dot marks the current position of M68 and red line the orbit of the cluster during 100 Myr backwards and forwards from its current position. *Bottom*: Grey dots are stars that have been used to make the magnitude-space density model of M68. Red dots have been selected to be compatible, whereas black dots are not, using the inferred distance from the stream model.

streams. Accurate radial velocities of the stars we identify as likely stream members will also add new constraints, and surveys reaching down to fainter magnitudes over the sky region of the stream should measure the abundance of low-mass main-sequence stars that are below the *Gaia* flux limit of detection. There is also a promising potential to study the variable rate at which stars in M68 are inserted into the tidal stream from the distribution of velocities in the stream stars, which should reflect the peaks of insertion associated with disc crossings.

In summary, the discovery of the M68 tidal stream opens the way to increasing the sample of tidal streams and using them to determine the potential of the Milky Way and to study the physical process of tidal perturbation of clusters orbiting the Milky Way and creation of the streams. In the future, we foresee the detection of new tidal streams by systematically applying our statistical method to other globular clusters with similar characteristics than M68.

Chapter 3

Detection of the stellar stream generated by NGC 3201

3.1 Introduction

In Chapter 2, we developed a new statistical method based on maximum-likelihood analysis designed to detect stellar streams associated with a known stellar system such as a globular cluster, when a small number of stream members appear superposed on a large catalogue of foreground stars. The method searches for a statistically significant overdensity of stars compared to a phase-space density model of the Milky Way. A stream model is constructed with free parameters that include the potential model of the Galaxy determining the orbits, plus the distance and velocity of the globular cluster within the constraints of the available observations. Numerical simulations of the stream are used to construct its phase-space density model. Then, the likelihood of each star in a catalogue is computed for the simulated model of the stream, given the observed phase-space coordinates and their observational errors. The model-free parameters that maximize the likelihood function are obtained, and a statistical test for this best-fitting model is performed to infer whether the stream exists or not. If the statistical evidence for the stream existence is sufficient, we use the stream density model to select stars that are most likely to be stream members based on the kinematic evidence. Finally, our final selection is obtained by requiring the stars to be also compatible with the H-R diagram of the cluster, assuming the distance to each star to be that predicted by the stream model.

Applying this method to the globular cluster M68, we found a long tidal stream stretching over the North Galactic hemisphere, and passing about 5 kpc from the Sun. This stream was found to match the stellar stream named Fjörm, independently discovered by Ibata et al. (2019b). For that study, absorption and reddening by Galactic dust was neglected when using the photometric observations to require stream members to be compatible with the H-R diagram of M68. We have further checked if other streams generated by globular clusters can be found in the GDR2 catalogue. Here, we study the case of NGC 3201, for which we also find a new stellar stream in which the effect of dust absorption and reddening is large and crucial for recognizing the stream members.

In Section 3.2 we describe NGC 3201 and our simulation of its tidal stream, and discuss the expected background using a simulation of the *Gaia* catalogue.

In Section 3.3, our statistical method is applied to select the GDR2 star candidate members of the NGC 3201 tidal stream and to estimate its statistical significance, and we conclude in Section 3.4.

3.2 Simulations of the NGC 3201 tidal stream and detection method

Our stream detection method, fully described in Chapter 2, starts by computing an initial simulation of the tidal stream of NGC 3201 using a fiducial model for the Galactic potential and the central observed values of the velocity and distance to the globular cluster. Then, a bundle of possible stream models is computed by considering a range of parameter values for both the Galactic potential and the globular cluster kinematics, which is used to pre-select a sample of stars in GDR2 as possible candidates of the stream, greatly reducing the number of stars to be used in the final model fit of the stream. One important difference we will find in this chapter compared to the previous one on the globular cluster M68 is that NGC 3201 is close to the Galactic plane, at $b = 8.64$ deg, with a high density of foreground stars and dust obscuration. We will start ignoring the presence of dust obscuration in this section (like we did in Chapter 2 for the M68 tidal stream), but in the next section we shall include a model for obscuration and reddening, showing how it has substantial impact in our final selection of candidate members of the NGC 3201 tidal stream.

The NGC 3201 cluster is ~ 5 kpc away from the Sun, near the Galactic plane and at longitude $l = 277.23$ deg, and has an extreme radial velocity of $494\,\mathrm{km\,s^{-1}}$, the highest of all globular clusters in the Milky Way, which indicates a retrograde orbit coming from a large apocentre. The implied long orbital period motivates searches for a tidal stream associated to this cluster, which may have formed from its outer envelope and not have been exposed to a large degree of phase mixing during its orbital history. Some evidence for this tidal stream has been pointed out in Chen and Chen (2010), who noted aligned star clumps of 2MASS sources in the cluster envelope. Kunder et al. (2014) obtained similar conclusions using stars with radial velocity from the RAVE survey, identifying unbound stars extending a few arc minutes away from the cluster. This was extended by Anguiano et al. (2016), who found tidal stream candidates out to ~ 80 deg from the cluster. Recent work using *Gaia* data has confirmed these observations, reporting an excess of RR Lyrae (Kundu et al., 2019) and a high velocity dispersion profile beyond the Jacobi radius together with aligned stellar overdensities near the cluster (Bianchini et al., 2019).

3.2.1 Initial stream simulation

We carry out a simulation of the formation and evolution of the tidal stream of NGC 3201, following the method that is described in detail in Section 2.2.5. Briefly, the method consists of integrating the orbits of tests particles initially distributed in a fixed Plummer potential that models the globular cluster, which is at the same time orbiting in a fixed potential of the Milky Way. Initial conditions for the cluster orbit are taken from Harris (1996, 2010) for the heliocentric distance r_h, right ascension α, and declination δ, and radial velocity v_r, and we use the proper motion $\mu_{\alpha*} = \mu_\alpha \cos(\delta)$ and μ_δ from the *Gaia* catalogue (Gaia
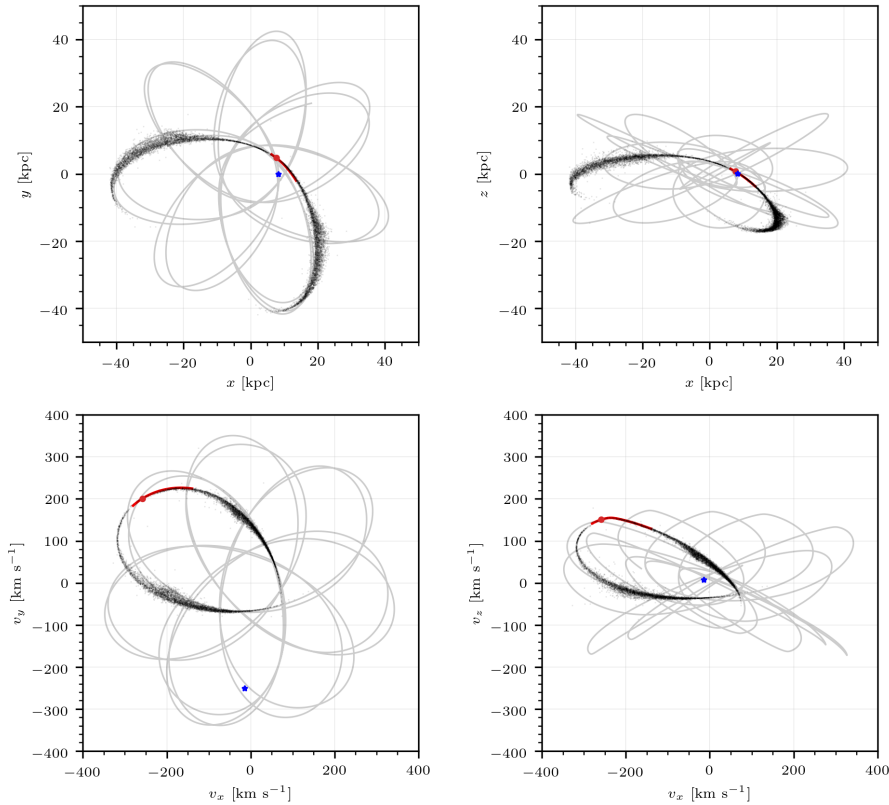
Figure 3.1: Computed orbit of NGC 3201 over the last 10 Gyr (grey line). The section from $-60\,\mathrm{Myr}$ (trailing arm) to $+10\,\mathrm{Myr}$ (leading arm) from the present position of the cluster (red dot) is highlighted in red. The black dots indicate the position of 10^4 tidal stream stars that have escaped the cluster potential, and the blue star is the current position of the Sun. *Top:* Projection on the Galactic disc plane (x, y) and the (x, z) plane. *Bottom:* Same projections in velocity space.

Collaboration et al., 2018c). Central observed values and errors are listed in Table 3.1. Note that the heliocentric distance was obtained from modelling the H-R diagram, with an estimated error of 2.3 per cent, because the parallax error from *Gaia* is much larger.

The cluster orbit is integrated first as that of a test particle in the Milky Way potential model described in Chapter 2. This model has fixed bulge and disc components, and an axisymmetric oblate dark halo with the parameters listed in Table 3.1, obtained as the best fit of the M68 tidal stream and other observational constraints in Chapter 2. The parameters are a constant of proportionality $\rho_{0\mathrm{dh}}$, a Galactic plane scale length $a_{1\mathrm{dh}}$, a vertical scale height $a_{3\mathrm{dh}}$, and inner slope α_{dh} and an outer slope β_{dh}. This profile is very close to an oblate NFW profile (which has $\beta_{\mathrm{dh}} = 3$; Navarro et al. (1996)), with a concentration parameter $c = 10.4$, virial radius $r_{200} = 175.9\,\mathrm{kpc}$, a total mass $M_{200} = 6.37 \times 10^{11}\,\mathrm{M_\odot}$, and an axis ratio $q = a_{3\mathrm{dh}}/a_{1\mathrm{dh}} = 0.87$. The corresponding potential flattening is $q_\Phi = 0.94$ at the cluster position.

Table 3.1: Mass, core radius, present position, radial velocity, and proper motion of the NGC 3201 globular cluster. Dark halo mass density profile parameters used for tidal stream simulation, and computed cluster orbit properties.

Properties NGC 3201			Ref.
M_{gc}	$(\mathrm{M}_\odot)$	$(6.47 \pm 0.45) \times 10^4$	[1]
a_{gc}	(pc)	4.9	[1]
r_{h}	(kpc)	4.9 ± 0.11	[2]
δ	(deg)	-46.4125	[3]
α	(deg)	154.3987	[3]
v_r	$(\mathrm{km\ s^{-1}})$	494 ± 0.2	[2]
μ_δ	$(\mathrm{mas\ yr^{-1}})$	-1.9895 ± 0.002	[3]
μ_α	$(\mathrm{mas\ yr^{-1}})$	12.0883 ± 0.0031	[3]
Dark halo properties			
$\rho_{0\mathrm{dh}}$	$(\mathrm{M}_\odot\ \mathrm{kpc^{-3}})$	7.27×10^6	[4]
$a_{1\mathrm{dh}}$	(kpc)	18.59	[4]
$a_{3\mathrm{dh}}$	(kpc)	16.17	[4]
α_{dh}	-	1	[4]
β_{dh}	-	3.102	[4]
q	-	0.87	
q_Φ	-	0.94	
c_{200}	-	10.4	
r_{200}	(kpc)	175.9	
M_{200}	$(\mathrm{M}_\odot)$	6.37×10^{11}	
Orbit properties			
r_{peri}	(kpc)	7.71	
r_{apo}	(kpc)	43.25	
L_z	$(\mathrm{km\ s^{-1}\ kpc})$	2765.45	

[1]: Sollima and Baumgardt (2017)
[2]: Harris (1996, 2010)
[3]: Gaia Collaboration et al. (2018c)
[4]: Chapter 2, Table 2.7

We plot the cluster orbit as a grey line in Galactocentric Cartesian coordinates in the top panels of Figure 3.1, on the x-y and x-z projections. The current cluster position and the Sun are marked as a red and blue dot, respectively. We highlight in red the section of the orbit from a time $-60\,\mathrm{Myr}$ (trailing arm) to $+10\,\mathrm{Myr}$ (leading arm) from the present time cluster position. The orbit in the v_x-v_y and v_x-v_z velocity space projections is shown in the bottom panels. Our computed orbital pericentre and apocentre of NGC 3201 and its vertical angular momentum component, listed in Table 3.1, are similar to the orbit of the tidal stream designated as Gjöll, discovered by Ibata et al. (2019b), which has $r_{\mathrm{peri}} = 7.96 \pm 0.22\,\mathrm{kpc}$, $r_{\mathrm{apo}} = 31.9 \pm 4.4\,\mathrm{kpc}$, and $L_z = 2721 \pm 159\,\mathrm{km\,s^{-1}\,kpc}$. We shall show in this chapter that the Gjöll tidal stream does in fact originate from the NGC 3201 globular cluster. The differences in the orbital parameters are consistent with observational and modelling uncertainties and the expected difference between the cluster orbit and the tidal stream.

We compute the orbits of 10^6 tidal stream stars as mentioned earlier and described in detail in Chapter 2, using a fixed Plummer sphere model for the globular cluster potential with a scale parameter $a_{\mathrm{gc}} = 4.9\,\mathrm{pc}$ and a total stellar mass $M_{\mathrm{gc}} = (6.47 \pm 0.45) \times 10^4\,\mathrm{M_\odot}$ from Sollima and Baumgardt (2017). In the same reference, the inferred dynamical mass for a King-Michie model is included being a factor 2 higher. An accurate estimate of the cluster mass is not relevant for our analysis since we are assuming a fixed mass throughout the evolution and the details of the phase-space distribution of the stream are not relevant to our detection method. The tidal stream orbits are started at the cluster position 10 Gyr ago, and integrated forwards in time up to the present, assuming the Plummer sphere potential follows the cluster orbit previously computed as a test particle in the Milky Way potential, and simply adding the Plummer and Milky Way potentials. Of all the simulated stream stars that have escaped further than 0.1 deg from the cluster centre, a randomly selected subset of 10^4 of them are shown in Figure 3.1 as small black dots (we do not plot all of them only to better visualize their distribution). As seen in these plots, the cluster is on a relatively low inclination orbit and has recently crossed the Galactic disc moving upwards. The tidal shock it experienced may be the explanation for the overdensities observed in the cluster neighbourhood. The part of the tidal stream closest to us is the trailing arm, at ~ 4 kpc from us and 1 to 2 kpc below the disc. The large population of stars at the ends of the tidal stream is due to our initial conditions, which do not have any radial cut-off in the initial distribution of stars in the Plummer sphere, so many stars escape during the first orbits. In reality, the existence of any initial overdensities from the time the globular cluster started tidally interacting with the Milky Way depends on the history of the cluster and the Milky Way potential, which are likely to cause phase mixing and violent relaxation to a much greater extent than in our simple, fixed potential simulation.
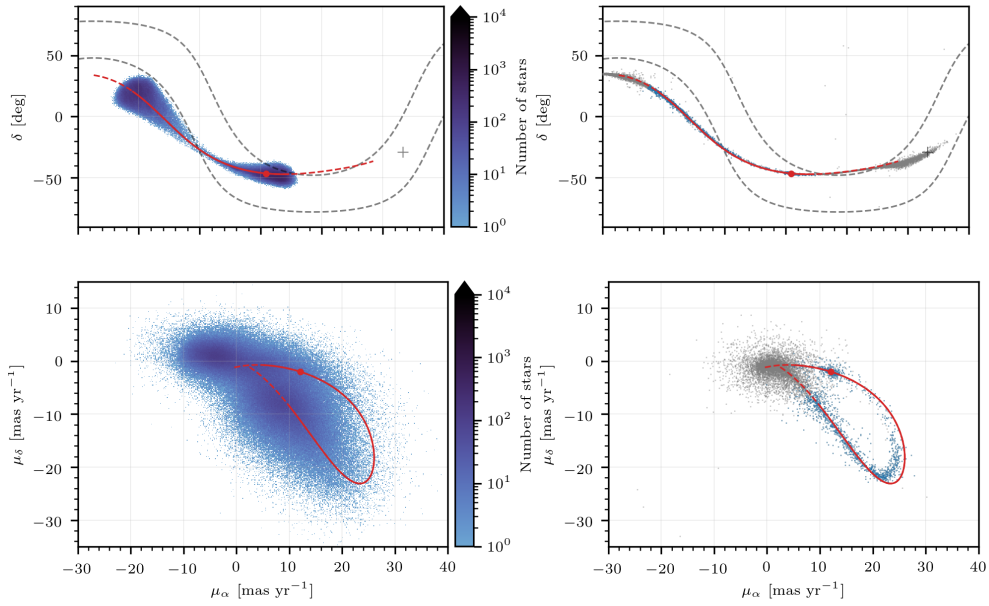
Figure 3.2: Computed orbit of NGC 3201, with its present position shown as the red dot, from −60 Myr to +10 Myr from the present (solid red line), and from −200 Myr to +200 Myr (dashed red line). The grey cross is the Galactic centre, and grey dashed lines mark Galactic latitude $b = \pm 15$ deg. *Left-hand panels:* Blue dots show coordinates and proper motions of stars in the GOG18 catalogue pre-selected for our search for stream candidates. *Right-hand panels:* Coordinates and proper motions of the simulated tidal stream stars are shown as blue dots if they are in our pre-selected sample, and as grey dots if they are not.

The cluster orbit is shown in equatorial coordinates in the top panels of Figure 3.2, from 200 Myr in the past to 200 Myr in the future, as the dashed red line, with the red dot indicating the present position. The orbital path from 60 Myr ago to 10 Myr in the future is highlighted as the red solid line. We shall see that this is the part of the tidal stream where stars are most easily identified from proper motions in the *Gaia* catalogue. The Galactic centre is indicated by the grey cross, and dashed grey lines show the Galactic latitude lines at $b \pm 15$ deg. We also plot the cluster orbit in proper motion space in the bottom panels of Figure 3.2. The interval that is highlighted as the solid line lies in a region of higher proper motion than the rest of the orbit, which helps us to reduce the density of foreground stars and facilitates the identification of stream candidates.

3.2.2   Tests with the simulated *Gaia* catalogue

We now use the stars in our model tidal stream to simulate how they would be observed with *Gaia*. While computing proper motions and parallaxes from the kinematics of each star in the tidal stream is trivial, the observational errors depend on the magnitude and colour of the stars, which we therefore need to simulate. We follow the same procedure as in Chapter 2: we first obtain the H-R diagram of NGC 3201 from the *Gaia* data itself, by selecting a total of 7064 stars that are within 0.14 deg of the globular cluster centre and pass additional conditions specified in Appendix B.1. This H-R diagram is shown in Figure 3.3, where the derived absolute magnitude without dust correction, M'_G, computed assuming a distance $r_h = 4.9$ kpc, is plotted against the observed colour index $(G_{\mathrm{BP}} - G_{\mathrm{RP}})'$, and the primes generally indicate that magnitudes are not corrected for dust extinction. We randomly assign to each escaped star an absolute magnitude and colour from this H-R diagram, and compute an apparent magnitude using its simulated distance. Dust obscuration and reddening is not taken into account here, this will be included only in the next section when selecting stream candidates from the real data.

We then generate measurement error covariance matrices for the phase-space coordinates of the simulated stream stars using the Python toolkit PY-GAIA[1], and following the same procedure as in Section 2.3.2. We assign these errors to each star, and also use them to alter the positions and velocities from the stream model by variations generated as Gaussian distributions following the same error covariance matrices. We plot as grey dots in the right-hand panels of Figure 3.2 the 8319 stars with G-band magnitude $G < 21$ that constitute our simulated catalogue of the stellar stream as seen by *Gaia*.

We next take a simulation of the entire *Gaia* catalogue, the 18th version of the Gaia Object Generator (GOG18; Luri et al., 2014b). This catalogue includes ~ 1.5 billion sources with G-band magnitude $G \lesssim 20$, so a pre-selection of a greatly reduced sample of tidal stream candidates is necessary before we can computationally implement a maximum-likelihood method to fit a tidal stream to the candidates. We apply various pre-selection cuts as described in 2.3.3: (1) $G < 21$, to reduce faint stars with large errors; (2) parallax $\pi > 1/0.3$

---

[1]https://pypi.org/project/PyGaia/
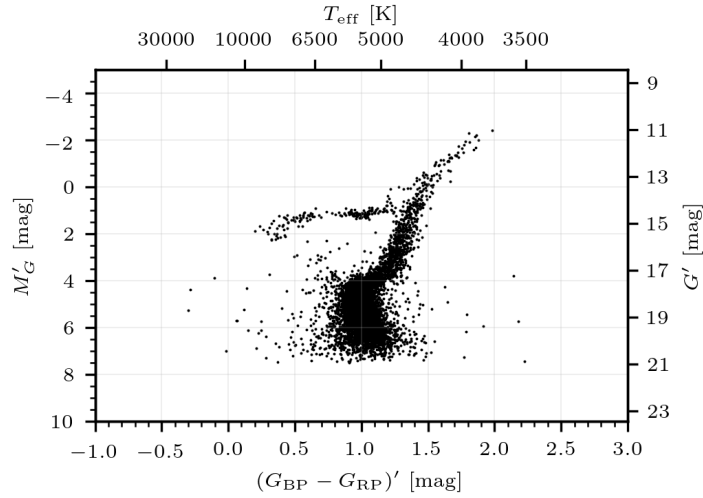
Figure 3.3: Absolute magnitude without dust extinction correction, M_G' versus observed $(G_{BP} - G_{RP})'$ colour index for 7064 stars within 0.14 deg of the centre of NGC 3201, selected with the conditions of the query given in Appendix B.1. The absolute magnitude is computed assuming a heliocentric distance $r_h = 4.9$ kpc.

mas, to eliminate foreground disc stars; a third cut in Chapter 2 that removed stars at low Galactic latitude is not applied here.

The fourth cut is the most important one, causing the greatest reduction in the number of star candidates. It is defined in Appendix A.3. Basically, we define a phase-space volume around the cluster orbit. By calculating the intersection of each star with this volume, we can choose stars close enough to the initial tidal stream model to be feasible stream stars in the final best-fitting model. We construct this volume by computing a bundle of orbits around the cluster orbit by variations of the current phase-space position of the cluster within observational errors, and variations of the Milky Way dark halo parameters. For the halo parameters, we randomly generate values following uniform distributions within the intervals: $\rho_{0dh} \sim (8 \pm 1) \times 10^6$ M$_\odot$ kpc^{-3}, $a_{1dh} \sim 20.2 \pm 4$ kpc, $a_{3dh} \sim 16.16 \pm 4$ kpc, and $\beta_{dh} \sim 3.1 \pm 0.2$. The selection threshold and the above distributions are defined such that the pre-selection criterion is broad enough to remove very few true stream stars. We require the pre-selected stars to be in the interval going from a time 60 Myr in the past to 10 Myr in the future (shown as solid red line in Figures 3.1 and 3.2) because the dense stellar foreground and large distance to the stream make it difficult to find stream stars outside this interval. Finally, the fifth cut removes stars within 1.5 deg of the cluster centre, to remove stars that may still be bound to the cluster and are not part of the tidal stream.

The GOG18 pre-selected stars after these cuts (a total of 486 664, as listed in Table 3.2) are plotted in the left-hand panels of Figure 3.2 as blue dots. The right-hand panels also shows as blue dots the 1609 stars in our simulated tidal stream that pass the same pre-selection cuts. Most of the other stars in our simulated stream are eliminated because they are far from our orbital

interval from -60 to $10\,\mathrm{Myr}$, where detecting the candidates is more difficult. We can see how within this interval, only a few simulated stream stars have not passed these cuts (grey dots) proving that our fourth cut does not bias the selection. The density of contaminating foreground stars is minimum in the range $\alpha \in [80\,\text{-}\,120]$ deg, corresponding to the section of the stream closest to the Sun where the proper motion is largest. Our pre-selection volume cuts out most of the leading arm, as well as the distant ends of the simulated stream. These cut out regions are far from the Sun, projected near the disc and with proper motions that have a high density of foreground stars. We will focus in the search for candidates in the portion of the tidal stream defined by our cuts in this chapter, although other stream stars are expected to be found over the more extended, complete simulated stream in future work.

3.3   Selection and detection of the NGC 3201 stream stars from GDR2

Our goal in this section is to obtain a best-fitting model of the stellar stream associated with NGC 3201 varying parameters of the Milky Way potential and the globular cluster kinematics, showing at the same time that the kinematic data of the GDR2 catalogue proves the existence of this stellar stream with a high degree of statistical confidence. A list of candidate stellar stream members that are also photometrically consistent with the NGC 3201 H-R diagram will be given. While each of these candidates has some probability of being a false member (a projected foreground or background star), our method relies on the statistical detection and maximizes the stream-likelihood function based on the number of candidates identified with a high membership probability.

3.3.1   Pre-selection of GDR2 stars

We first apply our pre-selection method to the GDR2 catalogue to reduce the number of stars used to fit the stellar stream to a computationally manageable level. This catalogue includes a total of ~ 1.7 billion sources with parallaxes, sky coordinates and proper motions, and ~ 7.2 million sources with radial velocities. The number of stars that pass each of our cuts defined in Section 3.2 is specified in Table 3.2, together with the same number for the simulated catalogue GOG18. The first two cuts (1 and 2) eliminate a small number of stars, and the main reduction is achieved in cut 4, leaving $492\,983$ for GOG18 and $250\,764$ for GDR2. The difference of a factor ~ 2 between the two catalogues in the pre-selected fraction is caused by imperfect modelling of the disc stellar population or inaccurate estimation of observational errors in GOG18. Observational errors are provided only for end-of-mission results in GOG18, while GDR2 is based on data collected during the first $2\,\mathrm{yr}$ of the *Gaia* mission, so we have corrected the GOG18 errors as in Section 2.3.1 but this correction may be inaccurate. Incompleteness of the GDR2 catalogue in areas with lower than average exposure or high stellar density and inaccurate modelling of dust extinction in GOG18 may be other reasons for the difference of the simulated and real catalogues. Cut 5 has again a relatively small impact and removes more stars in the vicinity of NGC 3201 in GDR2 than in GOG18 because the latter does not include globular clusters.

Table 3.2: Total number of stars in GOG18 and GDR2 and number that pass each cut. For cuts 6 and 7, the number of stars left is shown divided in six sky regions, where the tidal tail is seen under different foreground conditions, and a different value of the threshold χ_{sel} defined in Section 3.3.4 is used, specified in units of $\mathrm{yr}^3 \, \mathrm{deg}^{-2} \, \mathrm{pc}^{-1} \, \mathrm{mas}^{-3}$. Numbers in parentheses for GOG18 indicate the expected number of stars if GOG18 had the same number of pre-selected stars as GDR2 in each region. Note that cut 7 is not used to obtain the best-fitting tidal stream model, but only for the final selection of candidate stream members. The number of selected stars combining all six regions is shown at the bottom.

Pre-selection cut	GOG18	GDR2
All catalogue	1510 398 719	1692 919 135
(1) - (2)	1490 962 149	1313 216 777
(4)	492 983	250 764
(5)	486 664	218 065
Region (i) Disc foreground 1		
(6) $\chi_{\mathrm{sel}} = 4.9 \times 10^{-2}$	2 (1)	18
(7)	1 (0)	12
Region (ii) Disc foreground 2		
(6) $\chi_{\mathrm{sel}} = 7 \times 10^{-3}$	1 (0)	14
(7)	1 (0)	8
Region (iii) Stream		
(6) $\chi_{\mathrm{sel}} = 5 \times 10^{-3}$	10 (4)	55
(7)	8 (4)	51
Region (iv) Dust		
(6) $\chi_{\mathrm{sel}} = 5.38 \times 10^{-4}$	1 (0)	7
(7)	0 (0)	6
Region (v) Globular Cluster		
(6) $\chi_{\mathrm{sel}} = 2.9 \times 10^{-3}$	11 (5)	75
(7)	2 (1)	71
Region (vi) Disc foreground 3		
(6) $\chi_{\mathrm{sel}} = 6 \times 10^{-3}$	3 (1)	28
(7)	2 (1)	22
All regions combined		
(6)	28 (13)	197
(7)	14 (6)	170

Cuts 6 and 7 are applied only after the best fit to the stream has been computed, to obtain a list of the most likely candidate stream members. Cut 6 involves an accurate kinematic consistency with the best-fitting stream model, and cut 7 requires photometric compatibility with the progenitor cluster H-R diagram, and will be discussed in detail in Section 3.3.4.

The pre-selected stars, passing cuts 1 to 5, are shown in the top panel of Figure 3.4 as grey dots, in an equatorial coordinates sky map with the Galactic latitude $b = \pm 15$ deg shown as dashed lines, and the position of NGC 3201 shown as a blue dot. These pre-selected stars follow roughly the cluster orbit only because we have required this in cut 4 when selecting stars consistent with a bundle of orbits around that of NGC 3201, including uncertainties in the distance and kinematic measurements and in the Galactic potential model. However, the black dots in the top panel include the additional cut 7 (imposing a consistent color with the NGC 3201 H-R diagram at the distance of the stream model, see Section 3.3.4). The narrow band of these black dots seen in the range $70 \lesssim \alpha \lesssim 100$ degrees is already a visual evidence of the presence of the stream.

3.3.2   Best fit to tidal stream from GDR2 kinematic data

We now apply the method of maximum likelihood to compute the best-fitting parameters of the stream model, varying both orbital parameters of NGC 3201 with the prior of the distance, radial velocity and proper motion observational determinations, and parameters for the Galactic halo determining the gravitational potential. The method we use is fully described in Chapter 2 and is based on an approximate calculation of a likelihood function, computed from a stellar density of the tidal stream inferred from our stream simulation, and from a model distribution function of the foreground stars belonging to the general Milky Way stellar populations. As explained in Section 2.2.5, the simulation that is used to compute a model of the stream stellar distribution is performed by following the trajectory of stars that are initially in orbits with a significant escaping probability (obeying equation 2.21), derived from a tidal radius $r_t = R_c[M_{gc}/(3M_t)]^{1/3}$, where R_c is a characteristic orbital radius of the cluster, $M_t = 5.2 \times 10^{11} M_\odot$ is the total Galaxy mass, and M_{gc} is the globular cluster mass given in Table 3.1. The true tidal radius is somewhat smaller than r_t because only the Galaxy mass interior to R_c counts for generating the tidal stress on the cluster, but in practice we adjust R_c so that fewer than 30 per cent of the stars that escape are missed because of not including them in our fast simulations that follow only stars with a high escape probability. We have chosen on this basis $R_c = 15$ kpc for NGC 3201 in this chapter.

We do not apply this method using the entire *Gaia* stellar catalogue, which would be prohibitively expensive computationally, but we use only the pre-selected stars to compute our likelihood function. This essentially neglects the possibility that any stars outside our pre-selected sample might be stream members. The free parameters we use and their best-fitting results are listed in Table 3.3: the fraction of stars τ in the stellar stream, parameters of the halo density profile (ρ_{0dh}, a_{1dh}, a_{2dh}, and β_{dh}), and the heliocentric distance, radial velocity and proper motions of the globular cluster. Gaussian priors from the
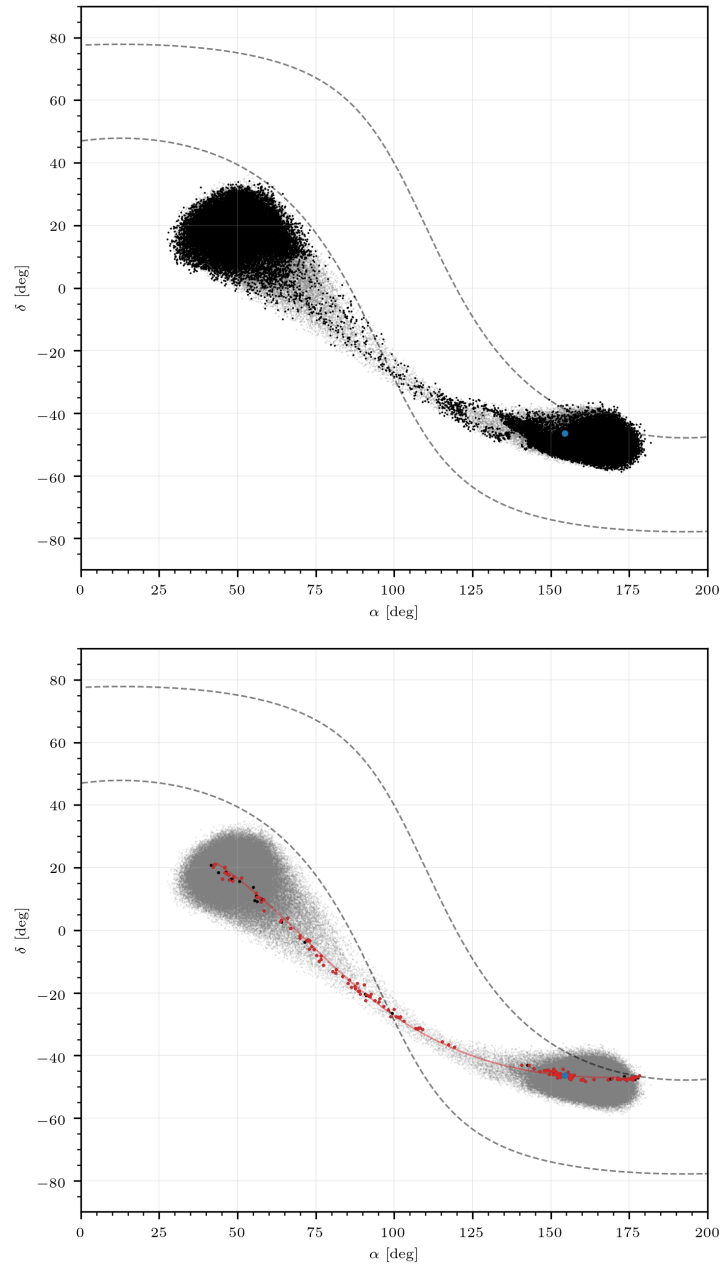
Figure 3.4: *Top*: Sky map in equatorial coordinates of the pre-selected stars from GDR2 passing cuts 1, 2, 4, 5 (grey dots), which are the stars that are judged to be roughly compatible with stream membership before the fit is done, and are used to obtain the final fit. Stars that are also compatible with the H-R diagram of NGC 3201 (passing cut 7) are highlighted in black. An elongated overdensity in the range $\alpha \sim [75\text{-}100]$ deg and an obscured region by dust in $\alpha \sim [120\text{-}145]$ deg can be seen, which is much sharper and clearer for stars passing cut 7, indicating the presence of the stream. The blue dot is the present cluster position, and the grey lines indicate Galactic latitude $b = \pm 15$ deg. *Bottom*: Final selection of GDR2 stars. The grey small dots are the same as in the top panel, black dots are stars compatible with the density model of the best-fitting stellar stream (stars passing cut 6 with our chosen values of χ_{sel} in different regions), and red dots are stars that are also compatible with the NGC 3201 H-R diagram (passing cut 7). The red line is the best-fitting orbit of NGC 3201 from -60 to $+10$ Myr from the present time.

Table 3.3: Best-fit parameters obtained for the NGC 3201 orbit and the Galactic dark halo, using the GDR2 pre-selected data.

Statistical parameters		
Λ		364.61
τ		$(2.74 \pm 0.35) \times 10^{-4}$
Q		17.95
Best-fitting kinematics of NGC 3201		
r_{h}	(kpc)	4.79 ± 0.05
v_r	(km s^{-1})	494.304 ± 0.14
μ_δ	(mas yr^{-1})	-1.9859 ± 0.0014
μ_α	(mas yr^{-1})	12.1048 ± 0.0022
Dark halo best-fitting parameters		
$\rho_{0\mathrm{dh}}$	(M$_\odot$ kpc^{-3})	$(6.87 \pm 0.09) \times 10^6$
$a_{1\mathrm{dh}}$	(kpc)	18.67 ± 0.27
$a_{3\mathrm{dh}}$	(kpc)	16.29 ± 0.25
β_{dh}	-	2.845 ± 0.035
q	-	0.87 ± 0.02
q_Φ	-	0.94 ± 0.01
c_{200}	-	9.14 ± 0.2
r_{200}	(kpc)	202.2 ± 5.2
M_{200}	(M$_\odot$)	$(9.71 \pm 0.75) \times 10^{11}$
Derived NGC 3201 orbital parameters		
r_{peri}	(kpc)	7.67 ± 0.03
r_{apo}	(kpc)	37.62 ± 1.41
L_z	(km s^{-1} kpc)	2728.8 ± 18.4

observational results listed in Table 3.1 are used for the cluster present phase-space coordinates, while the remaining parameters are given uniform priors wide enough to be unimportant for the results. Errors listed in Table 3.3 are from the diagonal elements of a full covariance matrix of all the free parameters, computed from the second derivatives of the posterior function. A few other derived parameters for the NGC 3201 orbit, and statistical measures defined in Chapter 2, are also included in Table 3.3.

Our results can be described according to the following three points:

1. A tidal stream of NGC 3201 is detected at a very high confidence level. This is inferred by maximizing the likelihood function, which essentially corresponds to maximizing the overlap of the stream phase-space distribution model with the stellar distribution in our pre-selected data. The value of $\tau \sim 3 \times 10^{-4}$ we find for our best fit, which is the fraction of stars

in our pre-selected sample that belong to the stream if the best-fitting model is correct, has a relatively error of only 12 per cent, so it is greater than zero with a very high statistical significance. Note that this number does not have a useful physical interpretation because it depends on our pre-selection method, and also on the complex details of the selection of the *Gaia* catalogue. In addition, the value of the statistic Λ indicates the confidence level at which the presence of the stream is detected, as explained in Section 2.2.1. When $\Lambda > 6.6$, the existence of the stream is confirmed at the 99 per cent confidence level compared to the null hypothesis that no stream is present. The large value of Λ implies a very high detection statistical significance.

2. The best-fitting orbit of NGC 3201 matching the detected stream is remarkably close to the orbit that is derived exclusively from the independent observational determinations of the cluster phase-space coordinates. The statistical parameter Q quantifies the deviation of the best-fitting present phase-space coordinates of NGC 3201 from the observational determinations in Table 3.1. Its expected value is the number of parameters of the globular cluster orbit that are fitted (in this case 4, as given in Table 3.3). The larger obtained value $Q \simeq 18$ is mostly due to the deviation of the best-fitting from the observed proper motion along right ascension, a 4.3σ deviation. We note that this deviation, while significant compared to the small statistical measurement errors of the GDR2 proper motion of the globular cluster, are actually less than 0.2 per cent of the proper motion. This small deviation may be caused by underestimates of errors provided by Gaia Collaboration et al. (2018c) for globular cluster proper motions, obtained by averaging measuremens of a large number of member stars. Both Vasiliev (2019b) and Baumgardt et al. (2019) provide bigger uncertainties compatible with our results.

3. In our Galactic potential model where only halo parameters are allowed to vary, our best-fit result for these parameters (listed in Table 3.3) has relatively small errors, and is close to our best-fitting M68 stream model from Chapter 2 (with values listed in Table 3.1). These small errors are of course the result of assuming a fixed model for the disc and bulge parameters. If these are allowed to vary, parameter degeneracies arise which are expected to increase the error in the halo parameters by a large factor. In addition, the computation of the uncertainties by the second derivative of the likelihood function underestimates the errors of the free parameters when the posterior function is not smooth over the entire range of possible parameter values. Mainly, this occurs for the halo parameters.

3.3.3   Visualization of stream including photometric selection

Apart from obtaining the best fit to the stream using the kinematic data and noting the large value of Λ in Table 3.3, there is an alternative way to test the reality of the stream: we can search for stars with photometry that is compatible

with the H-R diagram of NGC 3201, assuming that they are stream members and are at the distance predicted by the stream model. These stars should be distributed along a narrow region of phase-space corresponding to the stream when compared to the whole pre-selected sample.

We define a seventh cut (7) that selects stars consistent with the H-R diagram of the globular cluster NGC 3201, obtained directly from the GDR2 catalogue as described in Appendix B.1. The method is the same as that described in Section 2.3.5 and Appendix A.4, which basically defines a density model in the H-R diagram based on the cluster member stars, and then selects stream stars with a position in the H-R diagram above a threshold density (we use in this chapter a threshold $P_{\mathrm{CR}} \gtrsim 0.035$ mag^{-2}, as defined in equation A.15). An important difference from Chapter 2 is, however, introduced: we take into account dust extinction, which in this case is important because the cluster is located close to the Galactic plane in a region of moderately high extinction, and the stream is also affected by varying amounts of extinction over its long extent. The corrections applied to stars to both the magnitude and color for dust extinction and reddening are from Schlafly and Finkbeiner (2011), known as the SF dust extinction map model, and is described in detail in Appendix B.2. Note that this dust correction is obtained from the SF model assuming that all the dust is foreground to the stars, an assumption that is valid in most cases for stars with low *Gaia* parallax except when looking at very low Galactic latitude (in which case extinction is very high anyway).

Among all the pre-selected stars shown as grey dots in Figure 3.4, those that are in addition compatible with the NGC 3201 H-R diagram (cut 7) are shown as black dots of larger size in the top panel. The large blue dot is the present position of NGC 3201. An elongated overdensity which is narrower than the whole pre-selected sample is clear in the range $70 \lesssim \alpha \lesssim 100$ deg. We note that the region very close to the Galactic plane has very few stars that pass this cut 7. The reason is the very large extinction present in this region.

The stream and selected stars are better visualized by plotting these maps in rotated spherical coordinates, where the angle ϕ_1 varies along a major circle that approximately follows the stellar stream, and the angle ϕ_2 is a polar angle from the axis perpendicular to this major circle. The bottom panel of Figure 4 shows stars that pass not only cut 7, but also cut 6 which requires kinematic consistency with the best-fitting stream model (described in detail in the next subsection). This is replotted in the stream coordinates (ϕ_1, ϕ_2) in Figure 3.5 in the top panel. The bottom panel of Figure 3.5 adds the dust extinction map of the SF model (Schlafly and Finkbeiner, 2011). We can see that the region of the stream with an absence of stars compatible with all our cuts coincides with the region of highest dust extinction. The globular cluster NGC 3201 is seen at a moderately low, northern Galactic latitude, where dust extinction is close to 1 magnitude, and the trailing arm is the one that passes closest to the Solar System and is therefore most visible to us. This trailing arm crosses the Galactic disc and reappears on the southern Galactic hemisphere, where most of the stream candidates in the GDR2 catalogue can be identified.
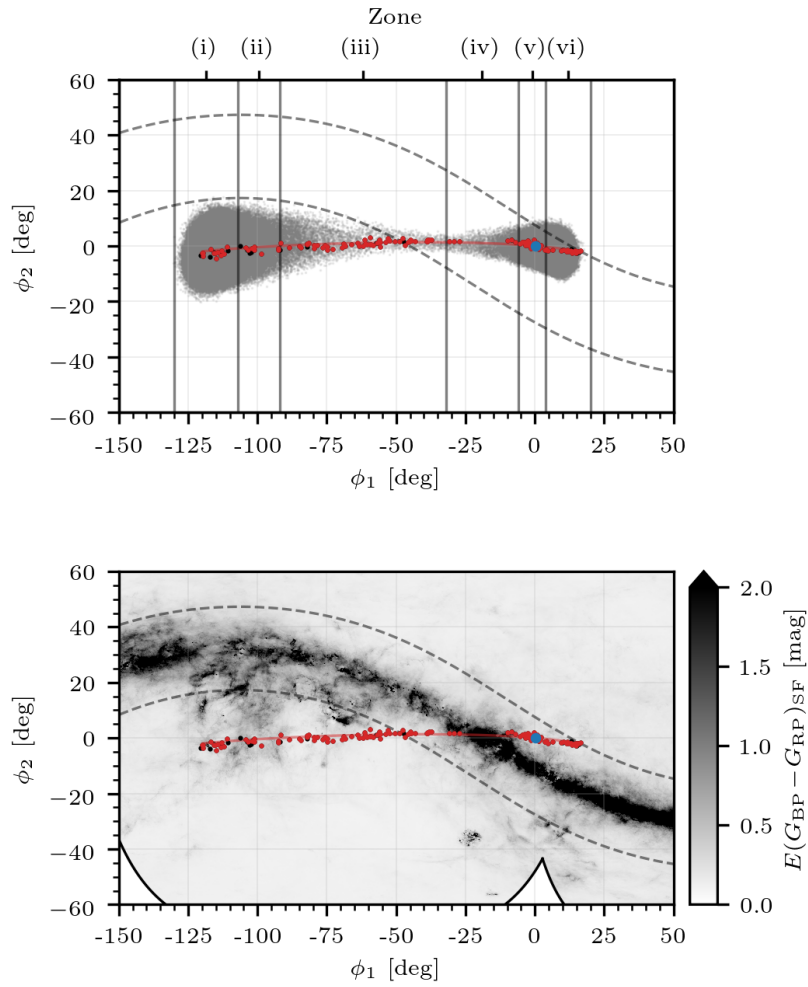
Figure 3.5: Same as bottom panel of Figure 3.4, expressed in a stream coordinate system with the ϕ_1 axis following the cluster orbit, as specified in Appendix D. *Top:* The solid vertical lines mark selection zone limits. *Bottom:* Colour excess of the $G_{\mathrm{BP}} - G_{\mathrm{RP}}$ colour index from the SF extinction map (Schlafly and Finkbeiner, 2011), a recalibrated version of the SFD extinction map (Schlegel et al., 1998). Only the best-fitting stream candidate member stars after cut (6) are shown here.

3.3.4   Final stream star selection including photometry

The final procedure in our study of the tidal stream is to select a list of stars that are most likely to be stream members, using both the stellar density of the stream model that gives the maximum likelihood, and the photometric condition of consistency with the cluster H-R diagram. First, cut 6 selects the stars with kinematic variables that are compatible with the best-fitting stream model, and then cut 7 restricts our final list to stars compatible with the H-R diagram.

The stream phase-space density model is constructed as in Chapter 2, similar to the way we evaluate the likelihood function, from the superposition of several Gaussian distributions along the stream. We compute the phase-space density at the phase-space position of each of the pre-selected stars for the best-fitting density model, convolving it with the observational errors of the phase-space coordinates, and we select stars with a value of this convolved phase-space density above a threshold χ_{sel}, which is expressed in units of $\mathrm{yr}^3\,\mathrm{deg}^{-2}\,\mathrm{pc}^{-1}\,\mathrm{mas}^{-3}$. The procedure is also done with the simulated stars in the GOG18 catalogue, and the threshold is chosen in each zone so that a small number of GOG18 stars are selected as stream members (this small number obviously represents our noise level of false candidates because there are no streams in the GOG18 simulation).

In practice, the stream we are analysing is very long and the different regions of the sky over which it is projected have very different levels of foreground contamination. To optimize our stream candidate list, we divide the sky into six different zones and use a different value of χ_{sel} in each one. We set the zone limits in the stream coordinate ϕ_1, defined to be the angle along a major circle that is approximately followed by the stream. The transformation from equatorial to these stream coordinates is given in Appendix B.4. The six regions, shown in the top panel of Figure 3.5, are defined as follows:

(i)   *Disc foreground 1*: $-130 \leqslant \phi_1 < -107$ (deg)

(ii)   *Disc foreground 2*: $-107 \leqslant \phi_1 < -92$ (deg)

(iii)   *Clean stream*: $-92 \leqslant \phi_1 < -32$ (deg)

(iv)   *High dust*: $-32 \leqslant \phi_1 < -6$ (deg)

(v)   *Globular cluster*: $-6 \leqslant \phi_1 < 4$ (deg)

(vi)   *Disc foreground 3*: $4 \leqslant \phi_1 \leqslant 20$ (deg)

We list in Table 3.2 the number of stars of the GOG18 and GDR2 catalogues that pass cuts 6 and 7, and the value of the selection threshold χ_{sel} we choose for each zone.

In zones (i), (ii), and (vi), the density of foreground stars is very high because the proper motions and parallaxes of most disc stars are small and cannot be distinguished from the stream stars. This makes our cuts less effective

at reducing the number of stars in our pre-selected sample. Taking these three zones together, we select 60 stars from GDR2 that pass cut 6, while only six are found by chance in GOG18 with the same values of $\chi_{\rm sel}$. This suggests most of the 60 stars found in this zone are real stream members, even before applying our cut 7. Actually, the number of six stars found in GOG18 in these three zones is an overestimate of the number of false candidates we should expect in GDR2, because the number of stars that are pre-selected in GOG18 is larger than in GDR2 (as seen in Table 3.2 in the total number of pre-selected stars after cut 5). A more reasonable estimate of the expected number of false candidates in GDR2 is obtained by correcting the number found in GOG18 according to the ratio of pre-selected stars after cut 5 in GOG18 and GDR2 in each of our six zones. This corrected estimate is written in parenthesis after the GOG18 number in each zone. For these three zones, the expected number of false candidates is reduced to 2 or 3. When applying in addition cut 7, the stream candidates are reduced to 42. In GOG18, the noise candidates are not reduced very much by cut 7 because most of the contaminating disc stars in these regions have colours that happen to be compatible with the NGC 3201 H-R diagram when the model stream distance is assumed.

Zone (iv) is highly obscured by dust (see Figure 3.5). Only seven stars are selected, of which six are compatible with the cluster H-R diagram. These stars are actually all located at the edges of zone (iv), where the dust extinction is not so high, and we therefore think they are most likely true stream members.

Zone (v) corresponds to the vicinity of NGC 3201. We select 75 stars, of which 71 are compatible with the cluster H-R diagram. In contrast, in GOG18 only 11 stars pass cut 6, of which only 2 pass cut 7, indicating that most of our final 71 stars from this zone are truely associated with the cluster. Our cut 5 removes stars only within an angle of 1.5 deg from the centre of NGC 3201, and there may still be some cluster member stars outside this angle that are bound to the cluster; in fact, the 71 stars in zone (v) we include in our final selection are rather concentrated towards the cluster. It is in general ambiguous to separate stars that are still bound from those that are already considered as stream members.

Finally, zone (iii) is the cleanest because it contains the part of the stream that is closest to us, located at ~ 3.2 kpc from the Sun, with proper motions that are larger than those of most foreground stars. Dust extinction is also relatively low. To analyze the selection in this particularly favourable zone more carefully, Figure 3.6 shows the number of selected stars, $N_{\rm sel}$, as a function of the selection threshold for this zone. The solid black line is the number of GDR2 stars selected for each threshold value, and the red one shows the number that are also compatible with the NGC 3201 H-R diagram. The two lines coincide up to $N_{\rm sel} \sim 100$, whereas at larger numbers (or lower $\chi_{\rm sel}$) we start having many stars passing cut 6 which do not pass cut 7. This implies that for $N_{\rm sel} \lesssim 100$, most selected stars should be true members. Dashed lines are the same for GOG18 stars. The shaded area below the dashed stars indicates the range by which the number of stars found in GOG18 drops because of the correction applied for the fact that GOG18 contains more stars than are detected in GDR2
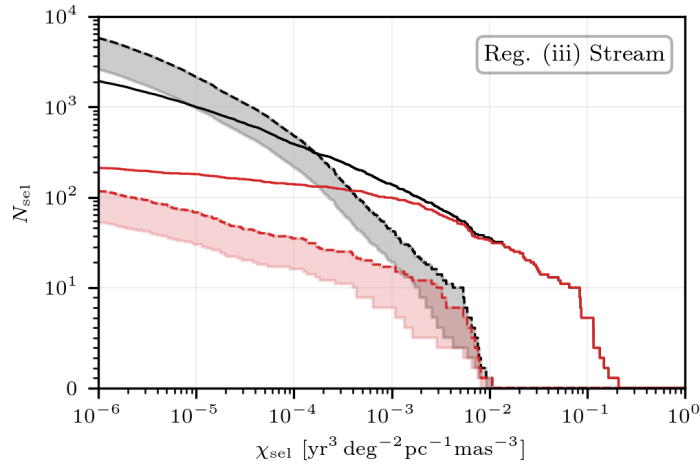
Figure 3.6: Number of selected stars N_{sel} in zone (iii) as a function of the selection threshold χ_{sel}. *Black solid line:* number of GDR2 stars compatible with the best-fitting stream model, passing cut 6. *Red solid line* number of stars also compatible with NGC 3201 H-R diagram (cut 7). *Dashed lines:* same quantities for GOG18 stars. Shaded areas mark the reduction due to correcting for the larger number of pre-selected stars in GOG18 than in GDR2.

in our pre-selected sample. As χ_{sel} is dropped, the number of selected stars in GOG18 rises to an increasing fraction of the ones found in GDR2. For our chosen value of χ_{sel} in zone (iii), we select 55 stars of which 51 also pass cut 7, expecting a number of wrongly selected stars of only ~ 4.

Our final selection over all regions contains 170 stars compatible with our best-fitting stream model and the cluster H-R diagram. Our GOG18 estimate of the foreground contamination predicts that the number of false members in this list is probably as low as ~ 6. These stars are plotted as red dots in the bottom panel of Figure 3.4 and in Figure 3.5, with black dots being for stars that pass only cut 6 but not cut 7. We also show the best-fitting orbit of NGC 3201 as a red solid line.

Figure 3.7 shows other variables for these same stars: parallax versus declination in the top panel, proper motions in the middle panel, and the H-R diagram in the bottom panel (with cluster members as small grey dots). Observational errors are indicated as thin black lines. The top panel shows that the parallax is not a very useful discriminant because the distance to the stream is too large for present *Gaia* uncertainties, but is nevertheless of some use and fits well the expected orbit. Proper motions are the most valuable information when detecting and modelling the stream. We note that, remarkably, using only the kinematic selection for stream members (up to cut 6, which are both the red and black dots), and inferring their absolute magnitude from the stream model distance and correcting for dust, we reproduce the H-R diagram of the cluster notably well.
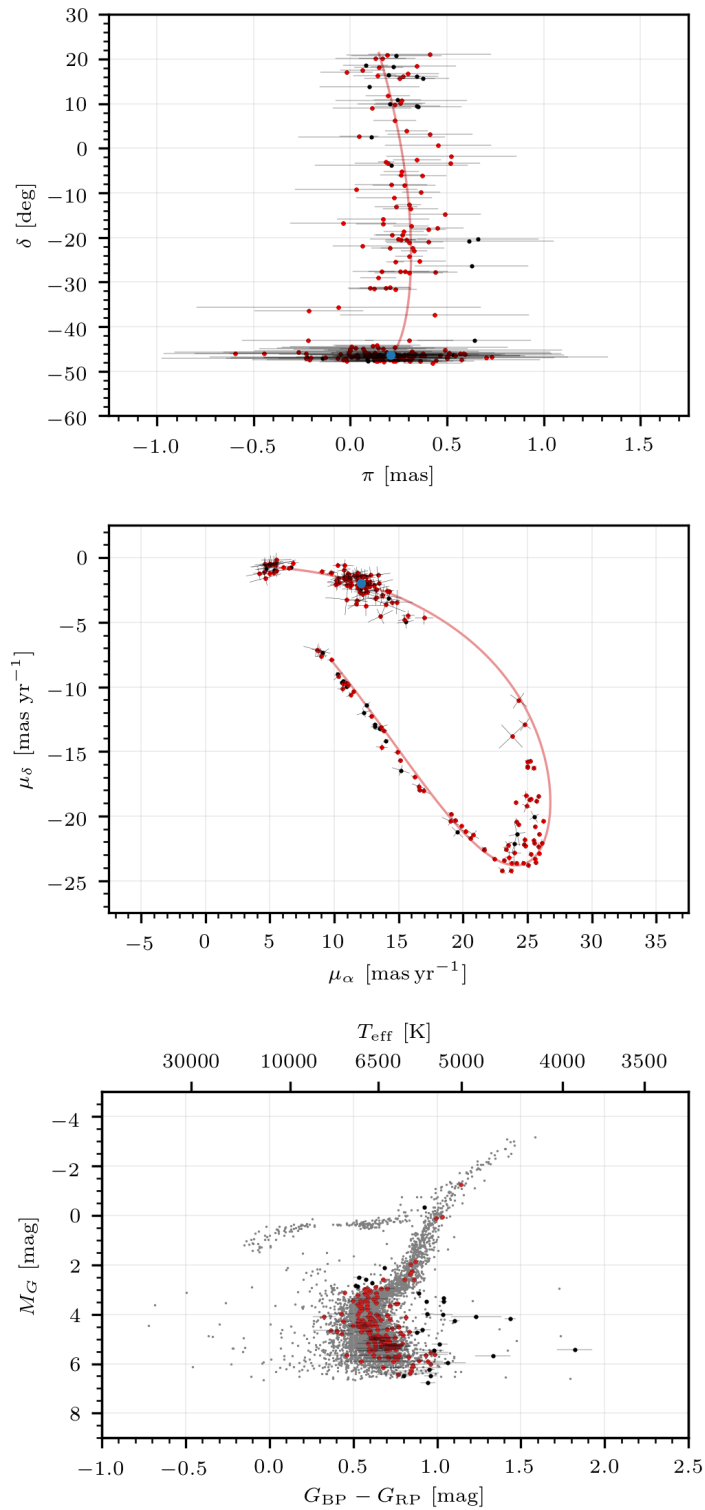
Figure 3.7: Parallax versus declination (top), proper motions (middle), and dust-corrected $G_{BP} - G_{RP}$ colour versus absolute G-band magnitude (bottom) for the 197 stars in our final selection after cut 6, with 170 of them passing also cut 7 shown in red, and the remaining 27 in black. Thin black lines are observational errors. Small grey dots in bottom panel are stars in NGC 3201.

The list of our final 170 stream member candidates is in Appendix B.3, with their measured coordinates, parallax and proper motion, colour index $G_{BP} - G_{RP}$, and G-band magnitude. Only one star has a *Gaia* radial velocity in GDR2 of 499.29 km s^{-1}, which we find to be in agreement with the orbital radial velocity prediction of 498.75 km s^{-1}. We have checked the RAVE DR5 (Kunder et al., 2017) and the LAMOST DR4 (Luo et al., 2015) catalogues, and have not found any matches to this list.

3.4 Conclusions

The method presented in Chapter 2 is applied to search for a tidal stream associated with the globular cluster NGC 3201. This method identifies the stellar stream by statistically detecting star overdensities in a sample of observational data with respect to a phase-space density model of the Milky Way. For the best-fitting location of the globular cluster and the parameters of the gravitational potential, we construct a density model of the stream and select the stars with the highest intersection. Finally, we present as a final selection the stars that are also compatible with the H-R diagram of the progenitor cluster.

We detect a total of 170 stars candidates along the leading and the trailing arm of the stellar stream, extending over ~140 deg on the sky, from 40 to 180 deg in the Southern Galactic hemisphere, following an orbit of $L_z = 2728.8 \pm 18.4$ km s^{-1} kpc. The clearest section of the stream spans from 70 to 105 deg, close to the Galactic disc, at about 3.2 kpc from the Sun. This section coincides with the known stellar stream Gjöll discovered by Ibata et al. (2019b) using the method Streamfinder (Malhan and Ibata, 2018; Malhan et al., 2018b), which spans from 70 to 90 deg in the Southern Galactic hemisphere, at 3.38 ± 0.1 kpc from the Sun, following an orbit of $L_z = 2721 \pm 159$ km s^{-1} kpc. This association based on *Gaia* phase-space, colours, and magnitudes together with the chemical tagging of stars in the stream to NGC 3201 (Hansen et al., 2020), proves that Gjöll is a section of the trailing tail of NGC 3201.

Our best-fitting parameters are consistent with the observations of NGC 3201 and provide a consistent model of the Milky Way. Even so, our computation underestimates the uncertainties of the halo parameters and cannot be considered representative of our current understanding of the density and potential of the Galaxy. In the following chapter, we will be using a combination of several streams to study the constraints that can be set on the Milky Way potential, especially the shape of the dark matter halo, by fitting models with sufficient parametric freedom on all the Galactic components to the observed data on all the stellar streams. Our success in detecting this stream opens the possibility to detect many more fainter stellar streams associated with globular clusters, as the Gaia data improve and the separation from foreground stars becomes more efficient.

CHAPTER 4

MEASUREMENT OF THE AXIS RATIO OF THE MILKY WAY DARK MATTER HALO

4.1 Introduction

The dark halo of the Milky Way is the least known component of our Galaxy. Determining its density profile and three-dimensional shape is an important astrophysical goal that can help us understand how galaxies form and evolve and constrain dark matter properties.

Simulations of the formation and evolution of galaxies have been one of the main tools to predict the shape of the dark halo of galaxies similar to the Milky Way. In general, simulations including dark matter only produce halos with triaxial shapes following the Navarro, Frenk & White (NFW Navarro et al., 1996) density profile. When baryons are included, interactions between baryons and dark matter in disk galaxies make halos rounder and approximately axisymmetric, with the minor axis perpendicular to the disc (see e.g. Bailin et al., 2005; DeBuhr et al., 2012; De Martino et al., 2020).

Testing these predictions from observations has proved difficult. Galaxy rotation curves provide ambiguous constraints on the shape of the dark halo because of the uncertainties in subtracting the baryonic component of stars and gas, and depend only on the potential in the disc plane. In the Milky Way, dynamical equilibrium methods of tracers like globular clusters or halo stars, as well as the orbits from stellar debris of the Sagittarius dwarf galaxy, have been applied to constrain the potential. The shape of the dark halo is still poorly constrained by these methods, and varying results of oblate, prolate, spherical, and triaxial configurations have been obtained depending on the method and the source of observational data (see e.g. Bland-Hawthorn and Gerhard, 2016b).

Here we use dynamically cold stellar streams in the Milky Way halo to study the shape of the Milky Way halo. These structures are formed when a progenitor satellite galaxy or globular cluster is perturbed by tidal shocks, generally when the progenitor approaches the centre of the galaxy or crosses the disc. The ensuing loss of stars from the bound system populates the leading and trailing tails of the stream. The tidally stripped stars approximately follow the orbit of the progenitor with a small variation of the orbital energy, with stars that gain energy moving to the trailing arm (a longer period orbit), and those that lose energy moving to the leading arm (a shorter period orbit). Models of the phase-space structure of stellar streams can help reconstruct the orbit of

the progenitor and use it to constrain the gravitational potential of the galaxy (see e.g. Varghese et al., 2011; Price-Whelan et al., 2014; Bonaca et al., 2014).

Several streams have been discovered in the inner region of the Milky Way (Grillmair and Carlin, 2016), and some of them have been used to constrain the potential of the Galaxy. For example, the GD-1 stellar stream, one of the most populated, has no known progenitor. This makes it difficult to model to constrain the Galactic potential. Another prominent stellar stream is the one generated by the Palomar 5 globular cluster, at ~ 16 kpc from the Galactic centre and far above the disk. This location is ideal to study the inner halo shape because the stream shape depends on the vertical acceleration, which is sensitive to the halo oblateness (see e.g. Pearson et al., 2015).

The publication of the second version of the *Gaia* star catalogue (GDR2), with more than 1 billion sources (Gaia Collaboration et al., 2016, 2018b), has improved the quality of the existing data of the Palomar 5 tidal stream, providing parallaxes and proper motions of many stars along the stream. Furthermore, this catalogue has made it possible to discover other stellar streams (see e.g. Ibata et al., 2018; Malhan et al., 2018a; Ibata et al., 2019b), some of them associated with globular clusters (Grillmair, 2019; Ibata et al., 2019a). Two of the main examples are the streams of M68 and NGC 3201 (Chapter 2 and 3). These streams are dynamically cold and relatively close to the Sun, greatly facilitating their study with the Gaia data. Each stellar stream provides independent constraints on the Milky Way mass distribution, helping resolve degeneracies that inevitably arise when modeling all the Milky Way components with many parameters.

In this chapter, we present a method to fit a model of the Milky Way halo using several stellar streams combined with other traditional observational constraints. We apply it to the three streams of NGC 3201, M68, and Palomar 5, leaving for future studies the use of many other streams that are being discovered and characterized. This combination of multiple observations is essential to help separate the contributions from the disk, bulge and halo, and reduce model degeneracies. In Section 4.2, we discuss our mass model of the Galaxy and the prior constraints on the free parameters from observational data. In Section 4.3, we present the kinematic constraints and a description of each stellar stream. In Section 4.4, the stream-fitting methodology is explained and the method is applied to the observational data. Results with each stream separately are presented in Section 4.5 and for all streams together in Section 4.6. In Section 4.7 we compare the halo axis ratio to previous estimates in the literature, and we present our conclusions in Section 4.8.

4.2 Mass model of the Milky Way

We model the mass distribution of the Milky Way as the sum of three components: disc, bulge and halo. We now describe the parameterized models used for each of them.

4.2.1 The disc density profile

The Milky Way stellar disc is modelled as the sum of two exponential profiles for the thin and thick disc. We do not separate the contribution of gas from

stars; the total gas mass is approximately $M_{\mathrm{gas}} \sim 10^{10}$ $M_\odot$, smaller than the stellar mass of $M_{\mathrm{d}} \sim 4 \times 10^{10}$ $M_\odot$ (e.g. Bland-Hawthorn and Gerhard, 2016b), and we neglect the different scale heights for the gas and stellar components. We note that the thin gas and young stars component may increase the strength of tidal shocks when crossing the disk and therefore the number and ejection velocities of stars that populate the tidal tails, so a more precise modeling of the vertical profile will be useful in future work.

In Galactocentric Cylindrical coordinates (R, φ, z), the mass density for each stellar component is

$$\rho_\gamma(R, z) = \frac{\Sigma_\gamma}{2z_\gamma} \exp\left(-\frac{R}{h_\gamma} - \frac{|z|}{z_\gamma}\right) \;, \tag{4.1}$$

where the subindex takes two values: $\gamma = \mathrm{n}$ denotes the thin disc, and $\gamma = \mathrm{k}$ the thick disc. The central mass surface density is Σ_γ, h_γ is the radial scale length, and z_γ the vertical scale height. The scale lengths and scale heights are constrained at the solar vicinity by star counts in optical and infrared bands to values $h_{\mathrm{n}} \sim 2.5$ kpc, $z_{\mathrm{n}} \sim 300$ pc for the thin disc, and $h_{\mathrm{k}} \sim 2$ kpc, $z_{\mathrm{k}} \sim 900$ pc for the chemically defined thick disc (e.g. Jurić et al., 2008; Bovy et al., 2015). The mass surface density ratio of the two components is also estimated in the solar vicinity (e.g. Jurić et al., 2008; Just and Jahreiß, 2010).

As a consistent methodology to fit our mass distribution model to various observations, we will let these model parameters vary in our maximum likelihood fits, constrained by Gaussian priors defined by various observational determinations with estimated errors. We choose the estimates for scale lengths and scale heights given in the review article of Bland-Hawthorn and Gerhard (2016b), and we list them in Table 4.1 with their errors that are assumed to be uncorrelated. The surface densities Σ_k and Σ_n are left free with a uniform positive prior. In practice, they will be constrained by observational conditions like the local ratio of the thin and thick disk surface densities,

$$f_\Sigma \equiv f_\rho \frac{z_{\mathrm{k}}}{z_{\mathrm{n}}} = 0.12 \pm 0.04 \;. \tag{4.2}$$

where $f_\rho \equiv \rho_{\mathrm{k}}(R_\odot, z_\odot)/\rho_{\mathrm{n}}(R_\odot, z_\odot)$ is the local density ratio, that we take from the same reference.

In general, Table 4.1 lists all our variable parameters, with indication of their priors, and Table 4.2 lists all our fixed parameters, for which we consider their errors to be of negligible impact for our modeling purpose.

4.2.2 The bulge density profile

We consider the Milky Way bulge and bar (see e.g. Portail et al., 2015; Wegg et al., 2015; Clarke et al., 2019) as a single component in this chapter. In our case, the streams we are studying do not penetrate to the innermost part of the Galaxy and their dynamics are therefore only weakly affected by the detailed mass distribution of this component. We assume for simplicity an axisymmetric bulge with a power-law density profile with core h_{b}, slope α_{b} and a Gaussian truncation at a scale length $a_{1\mathrm{b}}$,

$$\rho_{\mathrm{b}}(s) = \rho_0^{\mathrm{b}} \left(1 + \frac{s}{h_{\mathrm{b}}}\right)^{-\alpha_{\mathrm{b}}} \exp\left(-\frac{s^2}{a_{1\mathrm{b}}^2}\right) \;, \tag{4.3}$$

Table 4.1: Free parameters θ. The priors p_θ are assumed to be Gaussian distributions $\mu \pm \sigma$ with mean μ and standard deviation σ or uniform distributions when they are not specified.

Sun		**Gaussian Prior**	**Ref.**
$R_\odot$	(kpc)	8.178 ± 0.026	[1]
$U_\odot$	(km s^{-1})	11.1 ± 1.25	[2]
$V_\odot$	(km s^{-1})	12.24 ± 2.05	[2]
$W_\odot$	(km s^{-1})	7.25 ± 0.62	[2]
Disc			
$\Sigma_{\rm n}$	(M$_\odot$ kpc^{-2})		
$h_{\rm n}$	(kpc)	2.6 ± 0.5	[3]
$z_{\rm n}$	(kpc)	0.3 ± 0.05	[3]
$\Sigma_{\rm k}$	(M$_\odot$ kpc^{-2})		
$h_{\rm k}$	(kpc)	2.0 ± 0.2	[3]
$z_{\rm k}$	(kpc)	0.9 ± 0.18	[3]
Bulge			
$\rho_0^{\rm b}$	(M$_\odot$ kpc^{-3})		
Dark halo			
$\rho_0^{\rm dh}$	(M$_\odot$ kpc^{-3})		
α			
a_1	(kpc)		
β			
$q_\rho^{\rm dh}$			
NGC 3201			
$r_{\rm h}$	(kpc)	4.9 ± 0.11	[4]
v_r	(km s^{-1})	494.34 ± 0.14	[5]
μ_δ	(mas yr^{-1})	-1.991 ± 0.044	[6]
$\mu_{\alpha*}$	(mas yr^{-1})	8.324 ± 0.044	[6]
M68 (NGC 4590)			
$r_{\rm h}$	(kpc)	10.3 ± 0.52	[4]
v_r	(km s^{-1})	-92.99 ± 0.22	[5]
μ_δ	(mas yr^{-1})	1.762 ± 0.053	[6]
$\mu_{\alpha*}$	(mas yr^{-1})	-2.752 ± 0.054	[6]
Palomar 5			
$r_{\rm h}$	(kpc)	20.6 ± 0.2	[7]
v_r	(km s^{-1})	-58.6 ± 0.21	[5]
μ_δ	(mas yr^{-1})	-2.646 ± 0.064	[6]
$\mu_{\alpha*}$	(mas yr^{-1})	-2.736 ± 0.064	[6]

Note.
[1]: Gravity Collaboration et al. (2019)   [5]: Baumgardt et al. (2019)
[2]: Schönrich et al. (2010)   [6]: Vasiliev (2019b)
[3]: Bland-Hawthorn and Gerhard (2016b)   [7]: Price-Whelan et al. (2019)
[4]: Harris (1996, 2010)

which is constant over the ellipsoids of constant s,

$$s^2 \equiv R^2 + \frac{z^2}{q_\rho^2} \, , \tag{4.4}$$

with axis ratio $q_\rho = q_\rho^{\mathrm{b}}$. This model is an axisymmetric version of Bissantz and Gerhard (2002) introduced by McMillan (2011). We fix all the bulge parameters following McMillan (2017) to the values listed in Table 4.2, except for the density normalization parameter ρ_0^{b}, which we leave as a free parameter. We note that we have not imposed any central hole in the surface density model of the disk, so our model for the central bulge is a rough one because the resulting mass distribution includes the central part of our exponential disk. The scale density is proportional to the bulge mass M_{b}, which we constrain in the range following McMillan (2017):

$$M_{\mathrm{b}} = (8.9 \pm 0.89) \times 10^9 \ \mathrm{M}_\odot \, . \tag{4.5}$$

4.2.3 The dark matter density profile

Cosmological simulations suggest that the dark matter halo is well described by a NFW profile (Navarro et al., 1996). In our mass model, we choose a generalisation of this density profile based on an axisymmetric two power-law with scale density ρ_0^{dh}, inner slope α, outer slope β, and scale length a_1:

$$\rho_{\mathrm{dh}}(s) = \rho_0^{\mathrm{dh}} \left(\frac{s}{a_1} \right)^{-\alpha} \left(1 + \frac{s}{a_1} \right)^{\alpha - \beta} \, , \tag{4.6}$$

constant over ellipsoids of equation 4.4 with axis ratio $q_\rho = q_\rho^{\mathrm{dh}}$. When $q_\rho^{\mathrm{dh}} = 1$ the halo has spherical symmetry and s is equal to the Galactocentric Spherical radius r. This model is reduced to a NFW when $\alpha = 1$ and $\beta = 3$.

In our model, we keep α as a free parameter, and we do not assume any knowledge of its distribution by choosing a uniform prior in the range $\alpha \in [-3\text{-}3]$. This prior gives sufficient freedom to fit the observations without significantly restricting the posterior distribution. The scale length a_1 characterises the transition between the inner and the outer slope of the dark matter density profile. We take this scale length as a free parameter following a uniform prior in the range $[0\text{-}100]$ kpc. The outer slope β defines the shape of the dark matter halo for $R \gg a_1$. Observations of the Milky Way's circular velocity narrow its possible range of values. They exclude $\beta < 2$ to avoid raising rotational curves, as well as $\beta \gtrsim 6$ to avoid rotational curves decreasing too fast. We limit $\beta \in [0\text{-}6]$ using a uniform prior to avoid extreme values of the distribution for computational reasons (see Section 4.4). Even so, β is almost unconstrained within this range because our main constraints of the halo, the rotational curve (see Section 4.3.3) and the stellar streams (see Section 4.3.4), only introduce constraints for $R \lesssim a_1$. Assuming that β is strongly correlated with the mass of the halo, it can be constrained by measurements of the total mass of the Galaxy.

Table 4.2: Fixed properties of the Sun, bulge, and globular clusters.

Sun		Value	Ref.
$z_\odot$	(pc)	25	[1]
Bulge			
h_{b}	(pc)	75	[2]
$a_{1\mathrm{b}}$	(kpc)	2.1	[2]
q_ρ^{b}		0.5	[2]
α_{b}		1.8	[2]
NGC 3201			
M_{gc}	$(10^4\,\mathrm{M_\odot})$	6.47	[5]
a_{gc}	(pc)	4.9	[5]
δ	(deg)	-46.412	[4]
α	(deg)	154.403	[4]
M68 (NGC 4590)			
M_{gc}	$(10^4\,\mathrm{M_\odot})$	5.7	[3]
a_{gc}	(pc)	6.4	[3]
δ	(deg)	-26.744	[4]
α	(deg)	189.867	[4]
Palomar 5			
M_{gc}	$(10^3\,\mathrm{M_\odot})$	4.3	[5]
a_{gc}	(pc)	8.43	[5]
δ	(deg)	-0.112	[4]
α	(deg)	229.022	[4]

Note.
[1]: Jurić et al. (2008)
[2]: McMillan (2017)
[3]: Lane et al. (2010)
[4]: Harris (1996, 2010)
[5]: Sollima and Baumgardt (2017)

In the cosmological context, dark matter halos are characterized by the virial mass M_{vir}, defined as the mass inside a radius r_{vir} within which the mean density is Δ_{c} times larger than the critical density of the universe:

$$\rho_{\text{crit}} \equiv \frac{3H_0^2}{8\pi G} = 140 \text{ M}_\odot \text{ kpc}^{-3} \ , \tag{4.7}$$

where we use a Hubble constant $H_0 = 71$ km s^{-1} Mpc^{-1}. For $\Delta_{\text{c}} = 200$, we set the dark halo virial mass as $M_{200}^{\text{dh}} \equiv M_{\text{vir}}$, and r_{200} as the radius that solves the equation:

$$M_{200}^{\text{dh}} \equiv \frac{4\pi}{3} r_{200}^3 \Delta_{\text{c}} \rho_{\text{crit}} = 4\pi q_\rho^{\text{dh}} \int_0^{r_{200}} s^2 \rho_{\text{dh}}(s) \, \mathrm{d}s \ . \tag{4.8}$$

Several methods have been applied to infer the Milky Way mass using the properties of luminous populations, such as the Milky Way's satellites or the kinematics of various dynamical tracers of the Galactic halo (see Wang et al., 2020, for a review article). In general, these studies use observational data contained in the inner region of the Galaxy. In order to compute the virial mass, they require extrapolations to the virial radius which is about $r_{200} \sim 200$ kpc for the Milky Way. Instead, Callingham et al. (2019) use the phase-space distribution of the classical satellites of the Milky Way, which are spanned over a range of $r \sim [50\text{-}250]$ kpc from the Galactic centre, to estimate the total mass of the Galaxy:

$$M_{200}^{\text{MW}} \equiv M_{\text{bar}} + M_{200}^{\text{dh}} \ , \tag{4.9}$$

where M_{bar} is the total baryonic mass. Our model includes the mass of the bulge, thin, and thick disc, thus $M_{\text{bar}} = M_{\text{b}} + M_{\text{d}}^{\text{n}} + M_{\text{d}}^{\text{k}}$. We take as a constraint for the slope β the measurement of Callingham et al. (2019) of the mass within a radius of $r_{200} = 215.3 \pm 12.9$ kpc with symmetrized uncertainties:

$$M_{200}^{\text{MW}} = (1.17 \pm 0.21) \times 10^{12} \text{ M}_\odot \ . \tag{4.10}$$

By imposing that the density of the dark matter halo is constant over ellipsoids of equation 4.4, we have assumed an axisymmetric halo with axis of symmetry perpendicular to the disc. In principle, the Large Magellanic Cloud (LMC) should be the main cause of deviations from an overall axisymmetric Galactic potential (see e.g. Erkal et al., 2019; Gardner et al., 2020; Patel et al., 2020). We neglect the LMC despite its large mass of about $[1.4\text{-}25] \times 10^{10}$ M$_\odot$ because it is located far from our constraints, at ~ 50 kpc from the Sun. In our model, we assume that possible deviations from the axisymmetric configuration of the dark matter halo can be neglected because they should be smaller than the effects of the Milky Way's satellites that we are not taking into account.

The flattening of the Milky Way's halo has been investigated using different kind of methods. For example, constructing self-consistent models of the Galaxy assuming that the distribution of stars in the halo or the globular clusters are in equilibrium. Stellar streams has also been used for this purpose, specially the Sagittarius stream, GD-1, and Palomar 5. We provide a detailed compilation of all these measurements in Section 4.7.1. On the other hand, cosmological simulations statistically predict the shape of the dark halos of Milky

Way-like galaxies. In general, simulations that only use dark matter obtain prolate triaxial halos. The introduction of baryons and several feedback effects produce significant rounder halos. A detailed exposition of these results and a comparison with observational measurements is included in Section 4.7.2. Here, we take the axis ratio as a free parameter following a uniform prior large enough not to significantly restrict the posterior distribution in the range $q_\rho^{\mathrm{dh}} \in [0\text{-}6]$.

We also take the scale density ρ_0^{dh} as a free parameter because it cannot be directly constrained. We adopt a uniform prior in the range $\rho_0^{\mathrm{dh}} \in [0\text{-}1.5] \times 10^8$ $\mathrm{M}_\odot \, \mathrm{kpc}^{-3}$ to cut larger values for computational purposes (see Section 4.4). All the parameters of the halo are specified in Table 4.1.

4.3 Dynamical and kinematical constraints

In addition to the priors derived from observed star distributions and mass estimates introduced in Section 4.2, we include more detailed kinematical and dynamical constraints from observations in the solar neighbourhood and the local disc: the position and velocity of the Sun, the proper motion of Sgr A*, the vertical gravitational acceleration in the disc at the solar position, and the circular velocity curve of the Milky Way. These constraints, discussed in Subsections 4.3.1, 4.3.2 and 4.3.3, are important to reduce the multiple parameter degeneracies of our model potential. We also present in Section 4.3.4 the way we incorporate the additional independent constraints from the the observations of the stellar streams of NGC 3201, M68, and Palomar 5.

4.3.1 Position and velocity of the Sun

The position and velocity of the Sun are required to determine the relation between the Galactocentric and Heliocentric coordinate systems. The distance from the Sun to the Galactic centre is now measured to 0.3 per cent accuracy by comparing radial velocities and proper motions of stars orbiting the Galaxy central black hole Sgr A* (Gravity Collaboration et al., 2019), $R_\odot = 8.178 \pm 0.026$ kpc (including both statistical and systematic error). For the Sun vertical position, we adopt the central value of the estimate $z_\odot = 25 \pm 5$ pc from Jurić et al. (2008) (the measurement error is negligible for our purpose in this case).

For the Solar velocity with respect to the Local Standard of Rest, we use the value obtained from the stellar kinematics of the Solar neighbourhood by Schönrich et al. (2010),

$$v_\odot \equiv \begin{pmatrix} U_\odot \\ V_\odot \\ W_\odot \end{pmatrix} = \begin{pmatrix} 11.1 \pm 1.25 \\ 12.24 \pm 2.05 \\ 7.25 \pm 0.62 \end{pmatrix} \ \mathrm{km \, s}^{-1} \ , \tag{4.11}$$

where U points to the Galactic centre, V is positive along the direction of the Sun's rotation (clockwise when viewed from the North Galactic Pole), and W is positive towards the North Galactic Pole. We take $R_\odot$ and $v_\odot$ as free parameters of our model with Gaussian priors given by these observational errors, with values listed in Table 4.1, to properly take into account the implied uncertainties.

The gradient of the total gravitational potential at the solar position determines the circular velocity of the Local Standard of Rest (LSR), Θ_0. The total

tangential velocity of the Sun is constrained by the observed proper motion of the Sgr A* source, the nuclear black hole of the Milky Way, measured by Reid and Brunthaler (2004). The component along Galactic longitude of this proper motion, μ_l, is:

$$\mu_l \equiv -\frac{\Theta_0 + V_\odot}{R_\odot} = -6.379 \pm 0.026 \text{ mas yr}^{-1} \ . \tag{4.12}$$

We use this proper motion and error as one of the observations to constrain our model, assuming the black hole is located at the Galactic center and static. This could be redefined as a new prior and included in Table 4.1 after an adequate transformation of our parameter variables, but including it as an observation or prior to compute our likelihood function is conventional and does not affect our results. The component along Galactic latitude measured in Reid and Brunthaler (2004) is consistent with the vertical component of the solar motion $W_\odot$, and the measurement of $R_\odot$, but with a larger error, so we neglect it in our analysis.

4.3.2 Vertical gravitational acceleration

The vertical gravitational acceleration K_z near the disk is used to constrain the disk surface density, and several studies have obtained values $K_z \sim 2 \, (\text{km/s})^2$ pc^{-1} at $z \sim 1$ kpc (e.g. Kuijken and Gilmore, 1991; Holmberg and Flynn, 2004; Zhang et al., 2013; Bienaymé et al., 2014). Bovy and Rix (2013) were able to obtain measurements at several radial distances along the Galactic plane. We do not include these observations because they were obtained assuming a spherical dark matter halo, and this might introduce an unwanted bias in our model fit. We use only the measurement by Holmberg and Flynn (2004) at $z = 1.1$ kpc in the solar neighborhood:

$$\begin{aligned} |K_{z=1.1}| &= 2 \pm 0.16 \text{ km}^2 \, \text{pc}^{-1} \, \text{s}^{-2} \\ &= 2\pi G \, (74 \pm 6) \text{ M}_\odot \, \text{pc}^{-2} \ . \end{aligned} \tag{4.13}$$

4.3.3 The Milky Way's circular velocity curve

The Milky Way rotation curve for $R < R_\odot$ has been measured using the tangent-point method (see e.g. Luna et al., 2006; McClure-Griffiths and Dickey, 2007, 2016), and for $R > R_\odot$ using velocities and distances of various tracers (e.g. Kafle et al., 2012; López-Corredoira, 2014; Huang et al., 2016). These measurements have recently been improved by Eilers et al. (2019) with a large sample of red giant stars with 6-dimensional phase-space coordinates obtained by combining spectral data from APOGEE with photometric information from WISE, 2MASS, and *Gaia*. They determine the circular velocity from 5 to 25 kpc with an accuracy characterised by a standard error $\lesssim 3$ km s^{-1} and a systematic uncertainty at the ~ 2-5 per cent level of the measurement. Their modeling is compatible with ours to avoid any systematic bias (they assume an axisymmetric potential and approximately the same values of $R_\odot$ and Θ_0 that we use).

We constrain our model using the 38 measurements of the rotation curve of Eilers et al. (2019) at different radii, V_c^i, where $i = 1, \dots, 38$. We assume the

measurements follow a Gaussian distribution, with a dispersion equal to the symmetrized statistical errors given in Eilers et al. (2019). We add a constant systematic error of 3 per cent, a good approximation in the range $R \sim [5\text{-}15]$ kpc. The rotation curve with our assumed errors is shown in Section 4.5.3.

4.3.4   Stellar Streams

Several tidal streams have been discovered in the Milky Way (see e.g. Grillmair and Carlin, 2016; Shipp et al., 2018; Malhan et al., 2018a; Ibata et al., 2019b), and each may afford us interesting constraints on the Galactic potential. In this work, we will use only three of them, the streams of the globular clusters Palomar 5 (Odenkirchen et al., 2001), M68 (Chapter 2), and NGC 3201 (Chapter 3). These streams are chosen because it has been possible to discover a particularly large number of member stars in the *Gaia* catalogue, with good proper motion data. In the case of Palomar 5, there are also several radial velocities that add useful information. In the previous chapters, we showed how reliable stream members can be identified in the *Gaia* catalogue and used to obtain a model of the streams for M68 and NGC3201. In the latter case, we substantially extended the known length of the stream and demonstrated the importance of correcting for dust absorption to check for consistency of the photometry with the globular cluster H-R diagram. Here we will also use a list of highly likely members of the Palomar 5 stream obtained from the *Gaia* catalogue. These combined 3 streams will then be used to fit a best model for the Galactic potential, together with all other constraints discussed above.

Future work should use most of the large number of streams that are being discovered (see e.g. Belokurov et al., 2006a; Grillmair and Johnson, 2006; Grillmair, 2019). The most massive streams in the Milky Way are associated with the Large Magellanic Cloud and the Sagittarius dwarf galaxy, which have been used to study the potential of the Galaxy by numerous authors (see Section 4.2.3). Even though, streams that are thinner and dynamically cold are easier to model to constrain the potential because the stream itself is already a good approximation to a Galactic orbit, and self-gravity and hydrodynamic effects on gas clouds that result in star formation complicate the picture in the massive streams. Some of the thin streams, such as GD-1 and Orphan streams, do not have an identified progenitor and are believed to be the remnants of totally destroyed globular clusters. The lack of a progenitor makes these streams more difficult to model but they can also be useful as the data improve. When a progenitor is known with a measured distance and kinematics, the known progenitor orbit eliminates degeneracies to create a phase-space model of the stream. Most globular clusters should have associated stellar streams, so many more will be discovered in the future which should be added to improve the analysis and modelling we do in this chapter.

NGC 3201 stellar stream

The stellar stream of NGC 3201 was initially discovered by Ibata et al. (2019b) and was named Gjöll, without identifying it with its progenitor NGC 3201. The identified stream was actually a section of the trailing arm, moving behind the cluster. The extent of the stream was revealed to be much larger, and was

identified with the tidal stream of the globular cluster NGC 3201 in Chapter 3. Part of the stream is not easily observable because it is projected behind the Galactic disc, strongly obscured by dust and with a high density of foreground stars. This makes the selection of member stars difficult, mostly in the leading arm and near the globular cluster.

We select a subset of 54 *Gaia* stars that were found to be highly likely stream members in the study of Chapter 3. We limit the selection to the region where the stream is more clearly seen. This section is limited by the right ascension $65 < \alpha < 130$ deg, and excludes the areas deeply obscured by dust and with the highest foreground contamination. It also excludes the stars located in the outermost part of the cluster to avoid possible biases in the orbit determination. Figure 4.1 shows the parallax π, declination δ, right ascension α, and proper motion components μ_δ and $\mu_{\alpha*} \equiv \mu_\alpha \cos(\delta)$ of the stream stars. The small dots are represent these 54 stars, and the large dot is the globular cluster NGC 3201. The black dashed lines in the $\alpha - \delta$ diagram indicate the region within 15 degrees of the Galactic plane, and the colored curve is the best-fitting orbit of the globular cluster, showing an integration time of 60 Myr backward (dashed line) and forward (solid line) in time. The stream spans about 60 degrees on the southern Galactic hemisphere and is located close to the Galactic disc, and comes to a closest distance of 3 to 4 kpc from the present position of the Sun. The stream stars that are passing close to us have relatively large proper motions of ~ 20 mas yr^{-1}, which facilitate their identification and makes them useful for kinematic studies using Gaia proper motions. Note that the parallaxes are too small to provide much information, and the useful kinematic information of the streams are the Gaia proper motions.

The kinematics of NGC 3201 are specified in Table 4.1 and Table 4.2. We use the coordinates of Harris (1996, 2010), with negligible errors, and the heliocentric distance r_h from the same catalogue assuming a 2.3 per cent uncertainty. The radial velocity v_r is from Baumgardt et al. (2019), who compile several measurements. We use proper motions from Vasiliev (2019b), based on GDR2 data. We take these properties as free parameters and take the quoted errors from the observations, listed in Table 4.1, as a prior assuming they are Gaussian.

We use the mean values of the phase-space coordinates of the cluster and a fiducial Galactic potential to simulate this stream (see Section 4.4). We assume that the mass and size of the cluster are fixed throughout the orbit. These properties are listed in Table 4.2. In Figure 4.2 we plot in Galactocentric Cartesian coordinates the simulated stars stripped from the cluster during the last 1.5 Gyr, and we highlight in blue the simulated stars that approximately fit with our selection of *Gaia* stars. We also indicate the position of NGC 3201 with a big blue dot. We see that the observed portion of the stream is located approximately at [10 - 13] kpc from the Galactic centre and very close to the Galactic disc, in the range [−3 - 0] kpc.

M68 stellar stream

The stellar stream associated with the globular cluster M68 (NGC 4590) is a long and thin structure that spans about 190 deg over the north Galactic
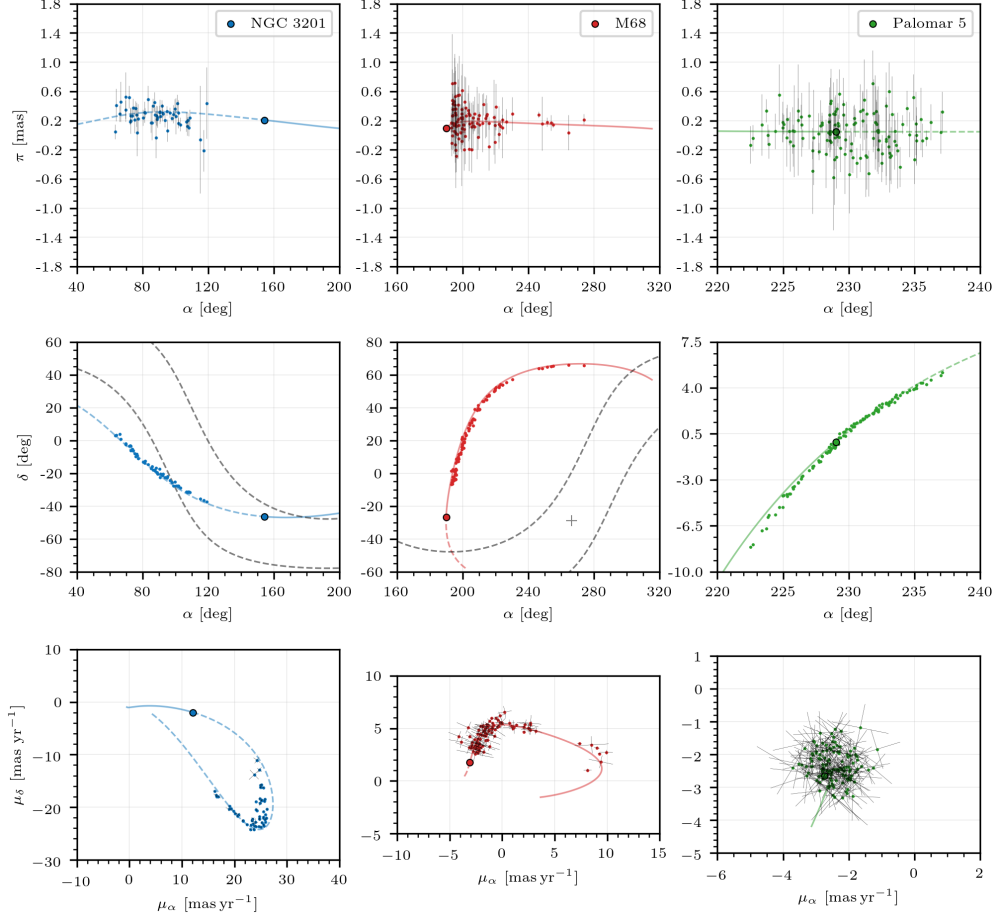
Figure 4.1: Phase-space position of stream stars from the GDR2 catalogue (points with error bars) for globular clusters NGC 3201 (blue), M68 (red), and Palomar 5 (green). Big dots show the current phase-space position of clusters and lines show their orbits forwards (solid) and backwards (dashed) during 60 Myr computed using the best-fitting orbit parameters listed in Table C.1. *Middle panels:* The grey dashed lines mark the Milky Way disc limits at $b = \pm 15$ deg and the grey cross the Galactic centre.
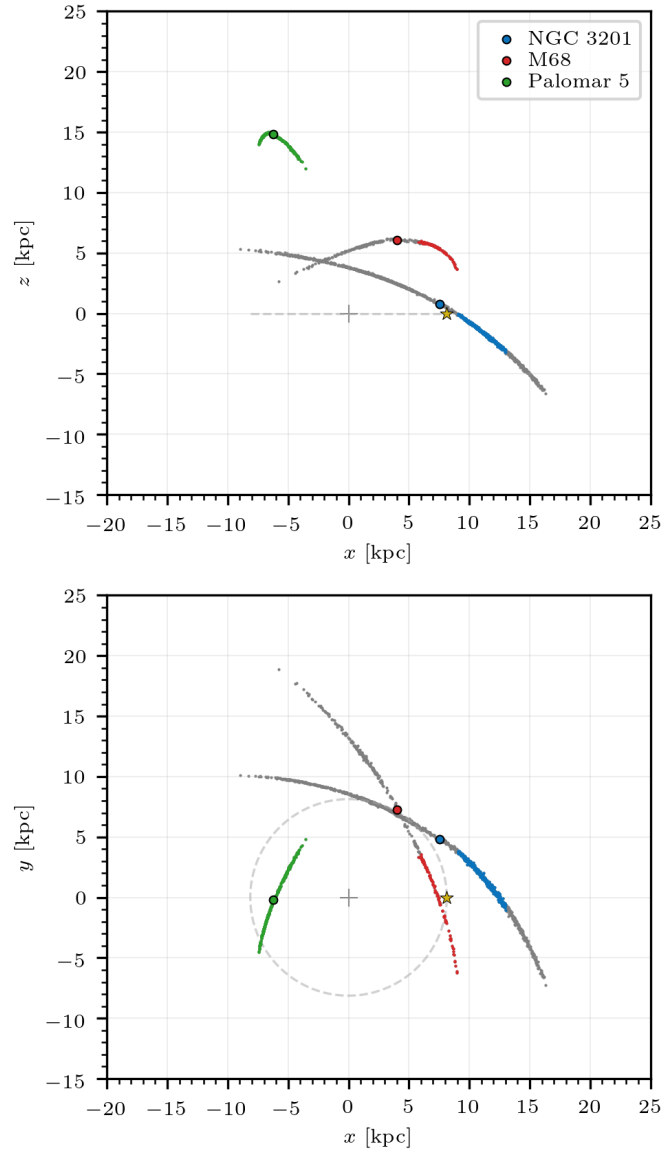
Figure 4.2: Simulated stream stars in Galactocentric coordinates, taking the stars stripped from the globular cluster during the last 1.5 Gyr for NGC 3201, and M68 and 4 Gyr for Palomar 5. The big dots show the current position of the globular clusters NGC 3201 (blue), M68 (red), and Palomar 5 (green). The coloured stars display approximately the section of the stream that fits with our *Gaia* selection plotted in Figure 4.1. The yellow star marks the Sun's position and the grey dashed line shows its orbit assuming a circular motion. The grey cross marks the Galactic centre.

hemisphere. This stream appears in Ibata et al. (2019b) named as Fjörm without being associated with M68. We use a 98-star subset of the stream candidates selected in Chapter 2, corresponding to the stars with $\delta > -8$ deg. With this cut, we exclude stars located close to the Galactic disc, where the correct determination of stream members is uncertain due to the high level of foreground contamination. This selection includes stars along almost the entire leading arm of the stream which appears projected onto the halo. We plot the stars in red in Figure 4.1. Most of them are located very close to the Sun at ~ 5.5 kpc and they have proper motions approximately in the range [5 - 10] $\mathrm{mas\,yr^{-1}}$ which make them easily identifiable with respect to the foreground. On the other hand, the section closer to the globular cluster and all the trailing arm are completely obscured by foreground stars, most of them belonging to the disc. For M68, we also take its sky coordinates as fixed parameters and the remaining phase-space coordinates as free parameters, assuming a 5 per cent of uncertainty for the heliocentric distance. We list their values in Table 4.2 and in Table 4.1 respectively. In Figure 4.2 we observe that the stream is located at about [9 - 12] kpc from the Galactic centre and about [4 - 6] kpc from the Galactic disc.

Palomar 5 stellar stream

The Palomar 5 tidal tails were discovered by Odenkirchen et al. (2001) by noticing an excess of stars around the globular cluster using photometric data provided by Sloan Digital Sky Survey. Further work improved the definition of the tidal tails and extended its length up to 23 deg in the sky (e.g. Carlberg et al., 2012). Its full phase-space distribution has been described by the identification of individual stars in the tidal stream (e.g. Kuzma et al., 2015; Ibata et al., 2016, 2017), and improved using the GDR2 catalogue (Starkman et al., 2020; Price-Whelan et al., 2019).

In this chapter, we use our selection of stars made following the method described in Chapter 2. The Palomar 5 stream appears as an overdensity that is statistically identified when compared to a phase-space model of the Milky Way. The stars that most likely belong to the stream are selected by choosing those with the largest intersection with a best-fitting phase-space density model of the stream. Our final selection only includes the stars that are colour and magnitude compatible with the H-R diagram of the progenitor cluster. We show in green the 126 selected stars in Figure 4.1. We list the phase-space coordinates, colours and magnitudes and explain the details of the selection procedure in Appendix C.5. None of the selected stars has radial velocity in the *Gaia* catalogue, but 15 of them match with stars with radial velocity measured by Ibata et al. (2017). We take their measurements, list them in Appendix C.5, and display the radial velocity in function of right ascension in Figure 4.3.

The Palomar 5 tidal stream is projected onto the halo just over the Galactic centre. Our selection covers about 16 deg in the sky, almost the entire stream. We observe a well-defined structure, with two long and thin arms connected to the globular cluster. Recent observations using grz photometry from DECaLS (Bonaca et al., 2020b), which include stars up to 24 mag, show a low surface-
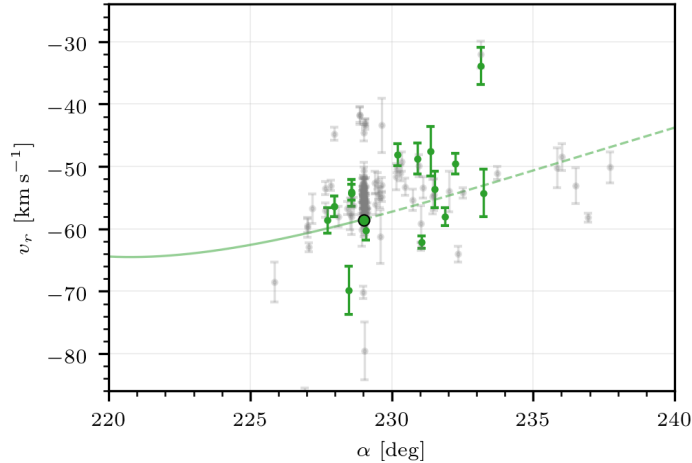
Figure 4.3: Right ascension and radial velocity of the stream stars of Palomar 5 from Ibata et al. (2017) (grey) with error bars. The green points mark the 15 stars that match with our *Gaia* selection. The big dot shows the current position of the cluster and the lines show its orbit forwards (solid) and backwards (dashed) during 60 Myr computed using the best-fitting values of the free parameters.

brightness extension of ~ 10 deg on the trailing arm. Our selection does not include this extension, as the *Gaia* G-band magnitude limitation of $G < 21$ mag makes it difficult to identify stars in the trailing arm faint extension. In the proper motion space, we observe a bunch of stars. We do not observe the elongated shape of the stream because the dispersion of proper motions of the stellar stream is much smaller than the *Gaia* errors for sources located at about 20 kpc from the Sun.

For the phase-space coordinates of Palomar 5, we take the values from the same references as in the previous cases (see Table 4.1 and 4.2), except for the heliocentric distance r_{h} taken from Price-Whelan et al. (2019). In general, the measurements of r_{h} approximately range in [20 - 23] kpc, here we use 20.6 ± 0.2 kpc. The simulation of the stream (green dots in Figure 4.2) shows that the stream is located at about [13 - 17] kpc from the Galactic centre and about [12 - 15] kpc from the Galactic disc.

4.4 Statistical methodology

Given a set of free parameters θ and a set of observational measurements d, the probability density function of each parameter $p(\theta|d)$ can be determined by the Baye's Theorem:

$$p(\theta|d) = \frac{\mathcal{L}(d|\theta)\, p(\theta)}{p(d)} \ , \tag{4.14}$$

where $\mathcal{L}(d|\theta)$ is the likelihood function, $p(\theta)$ is the product of the prior distribution of each parameter, and $p(d)$ is a normalisation constant. In our model, we use 4 parameters that characterise the position of the Sun, 12 for the potential of the Milky Way, and 4 for the phase-space position of each globular cluster. The free parameters, including their prior distribution functions, are described

in Section 4.2 and listed in Table 4.1.

The likelihood function is the product of the likelihoods associated with each constraint. For each observation defined in Section 4.2, 4.3.1, 4.3.2, and 4.3.3:

$$d_{\rm c}^i \equiv \left\{ f_\Sigma, M_{\rm b}, M_{200}^{\textsc{mw}}, \mu_{\rm SgrA^*}, |K_{z=1.1}|, V_{\rm c}^1, \ldots, V_{\rm c}^{38} \right\} , \qquad (4.15)$$

where $i = 1, \ldots, 43$, we use as a likelihood a Gaussian distribution $G(d_{\rm c}^i \,|\, \mu_i, \sigma_i^2)$ where μ_i is the mean value of the i measurement and σ_i its standard deviation. For the observed streams, the data comes in form of a list of stars selected from the *Gaia* catalogue. For all of them, we have measurements of all phase-space coordinates, including the correlation matrix of the uncertainties, except for the radial velocity, which is only available for some stars belonging to Palomar 5 stellar stream. We define the likelihood as the intersection of the observed mean position of the star convolved with its uncertainties and a phase-space probability density model of the stellar stream (see Section 4.4.1). We include a detailed definition of the likelihood function in Appendix C.1.

To explore the parameter space we use a Metropolis-Hastings algorithm which is a Markov Chain Monte Carlo method for obtaining random samples following a probability density function. This algorithm depends on an initial value for the free parameters and an arbitrary Gaussian distribution that defines the size of the steps of the random walk. To figure out the best-fitting values of the parameters, we compute a relative maximum of the probability density function around an initial guess using a Nelder-Mead Simplex algorithm. In Section 4.5 we give the probability distribution of the parameters and our best-fitting model.

4.4.1 Phase-space model of the stellar stream

The phase-space probability density model of the stellar stream is constructed from simulated particles escaped from the globular cluster due to the tidal forces of the Milky Way. It depends on the potential of the Galaxy, the characteristics of the globular cluster, and its phase-space coordinates at the present time. Several methods have been developed to quickly simulate stellar streams. For example, the streak-line or particle-spray method avoids calculating the orbit of non-escaping stars and the small time steps required within the cluster by releasing particles from the Lagrange points (see e.g. Küpper et al., 2012). Alternatively, some methods rely on the simple structure of the stream in action-angle coordinates to create prescriptions for its phase-space structure (see e.g. Bovy, 2014; Fardal et al., 2015). None of these methods is fast enough to compute a random sample large enough to adequately describe the posterior function defined in equation 4.14 in a reasonable time with our computational resources.

For this reason, we do not simulate a stellar stream for each evaluation of the likelihood function. We simulate as accurately as possible each stream once and assume that the position of the stream with respect to the orbit of the progenitor, as well as its velocity dispersion do not change for small variations of the potential of the Galaxy. The numerical simulation is carried out using the method described in Chapter 2. This method allows us to obtain an

approximation of the phase-space structure of the stream without the intrinsic complications of an N-Body simulation. We summarize the procedure we apply here with these steps:

1. We compute 10 Gyr backwards in time the orbit of the globular cluster from the present mean position and velocity in a fiducial potential of the Galaxy defined in Chapter 2.

2. We assume the globular cluster is initially in dynamical equilibrium and we spread out stars around it using the self-consistent phase-space distribution derived from a density model. Here, we adopt a Plummer sphere, which is function of a core radius a_{gc}, and the total mass of the cluster M_{gc}. We list these properties for each globular cluster in Table 4.2.

3. We assume that the stars behave as test particles, and we compute their orbits forwards in time until the present day. We take into account the potential of the Galaxy and a moving potential of the cluster with its mass fixed.

4. In order to match the size and the length of the observed stream, we select the stars that have escaped during the last 1.5 Gyr for NGC 3201, and M68 and 4 Gyr for Palomar 5.

Given the simulation, we select a section of the cluster orbit corresponding to the movement during 60 Myr for NGC 3201, and M68 and 40 Myr for Palomar 5 backwards and forwards with respect to their current location. We assign to each star the Frenet-Serret trihedron corresponding to point in the orbit section closest to the star, determined with a Euclidean distance. We store the position and velocity of the star with respect to the reference frame defined by the trihedron, and assume that this relative phase-space location is independent for small variations of the orbit of the cluster. We also store the relative position of the trihedron along the orbit section. For each evaluation of the likelihood function, we compute a new section of the orbit using the given values of the parameters. We compute the Frenet-Serret trihedrons corresponding to the new orbit at the same relative positions along the orbit section that we have previously stored. Finally, we locate each stream star at the relative phase-space location that we have previously stored and assumed to be independent of the orbit, with respect to the reference frame defined by the new trihedrons. We give the precise mathematical description of this procedure in Appendix C.2.

Once the stars are placed, we compute their coordinates in the Heliocentric spherical reference frame where we have the observational data ($\pi, \delta, \alpha, v_r, \mu_\delta, \mu_\alpha$). The phase-space probability density model is constructed in these coordinates using a Kernel Density Estimation method, with a Gaussian distribution as a kernel. We locate the mean of the kernel distributions in the current position of the simulated stream stars, and we compute their covariance matrix from the distribution of the neighbouring stars. We describe this method in detail in Appendix C.1.

4.5 Results for each stream

The stellar streams generated by NGC 3201 and M68 are located at about the same distance from the Galactic centre. They cover approximately a range from $r \sim 6$ to 13 kpc, but their distance from the disc is significantly different. The stream of NGC 3201 is almost on the disc, and the stream of M68 is about 5 kpc above it. On the other hand, the Palomar 5 stream is a little further away, at about 16 kpc from the centre and about 14 kpc from the disc. This implies that each stream covers different regions of the Galactic halo, and each one can be used to study the dark matter density distribution and the overall potential of the Galaxy at different locations. For this reason, we provide three different mass models obtained by fitting the streams individually. We also provide an additional model that includes all three streams together.

In Appendix C.3, we provide a table of the median and the 1σ levels of the free parameters of our model. We also include several derived properties of the model and the value of the constraints listed in equation 4.15 except for the circular velocity, which is described in Section 4.5.3. In addition, for each model, we provide the value of the parameters and the derived properties for the best-fitting configuration.

4.5.1 Stellar mass model, Sun properties, and globular clusters position and velocity

We plot the marginalised probability density distributions of the free parameters associated with the Sun and the stellar disc in Figure 4.4. These distributions have been drawn from a random sample estimated by a Kernel Density Estimation with Gaussian distribution as a kernel and the best-fitting scale parameter. Each colour shows the result obtained using as a constraint the stellar stream of NGC 3201 (blue), M68 (red), Palomar 5 (green), and all the streams together (purple). We also include the Gaussian priors as a dashed black lines. We show the same in Figure 4.5 but for some constraints and computed properties of the model.

We see how the three streams do not require significant deviations from the prior distributions of the Sun's position and velocity, being all the estimates at less than 1.2σ from the adopted priors. The main discrepancy between the streams occurs for the $U_\odot$ component of the velocity. NGC3021 and M68 present deviations from the prior of -0.9σ and -0.8σ respectively, and Palomar 5 a deviation of 0.8σ. The discrepancy of 0.9σ in the transverse velocity of Sgr A* in the case of M68, and 1.5σ in the case of Palomar 5, do not result in a significant difference in the transverse speed of the Sun, being $\Theta_0 + V_\odot \simeq 246$ km s^{-1} for all the streams. The velocity of the LSR is also compatible in all three models being $\Theta_0 \simeq 231$ km s^{-1}. This results are consistent with $\Theta_0 + V_\odot = 247 \pm 4$ km s^{-1} and $\Theta_0 = 236 \pm 7$ km s^{-1} measured by Reid et al. (2019) for a $R_\odot = 8.15 \pm 0.15$ kpc using parallaxes and proper motions of molecular masers associated with young high-mass stars. They are also compatible with $\Theta_0 + V_\odot = 246.9 \pm 1.6$ km s^{-1} and $\Theta_0 = 233.6 \pm 2.8$ km s^{-1} from Mróz et al. (2019) for a $R_\odot = 8.122 \pm 0.031$ kpc, obtained using measurements of the proper motion and radial velocities from *Gaia* for classical Cepheids.
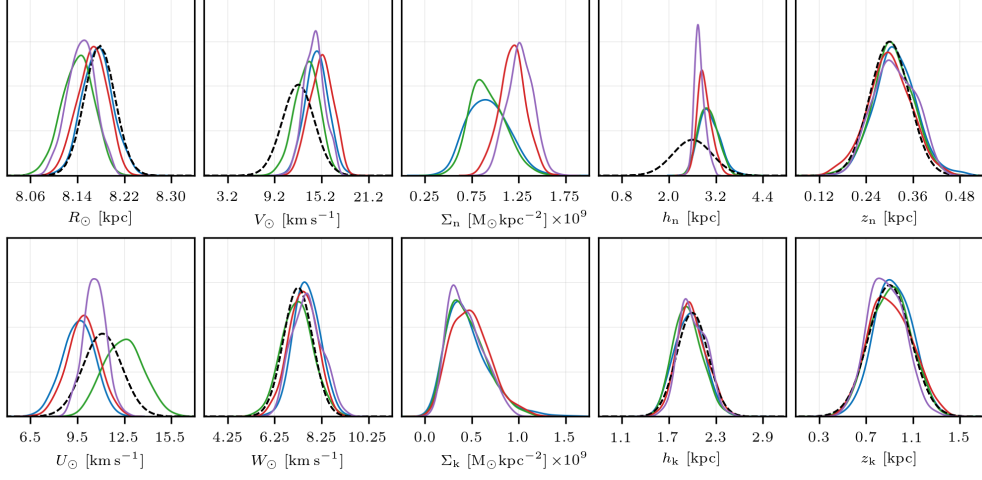
Figure 4.4: Marginalised probability density function of the parameters describing the Sun's position $R_\odot$, and velocity $(U_\odot, V_\odot, W_\odot)$ and the thin and thick disc mass surface density Σ, radial scale length h, and vertical scale height z. They are obtained using as a constraint the streams associated with the globular clusters NGC 3201 (blue), M68 (red), Palomar 5 (green), and all the streams together (purple). We include the distribution of the Gaussian priors listed in Table 4.1 as black dashed lines.
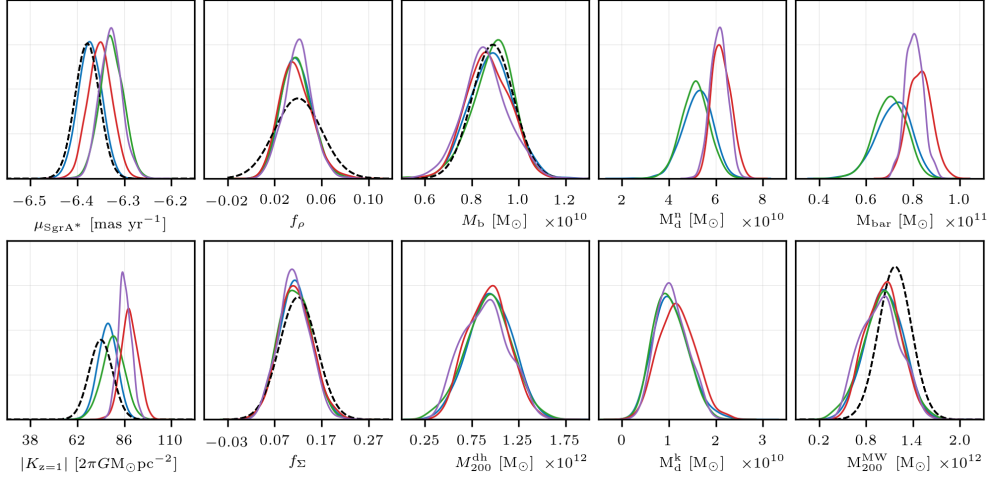
Figure 4.5: Same as Figure 4.4, but for constraints and computed properties of the model. We show the proper motion of Sgr A* $\mu_{\mathrm{SgrA}*}$, the vertical force at Sun's position $|K_{z=1.1}|$, the local disc density ratio f_ρ and surface ratio f_Σ, the mass of the bulge M_{b}, thin disc $M_{\mathrm{d}}^{\mathrm{n}}$, thick disc $M_{\mathrm{d}}^{\mathrm{k}}$, dark halo M_{200}^{dh} and the baryonic components M_{bar}, and total mass of the Galaxy M_{200}^{MW}.

All the streams require the same distribution of mass for the thick disc, but there is a discrepancy in the model of the thin disc. The stream of M68 needs about 20 per cent more mass than the other streams. In all cases, the required scale lengths and scale heights are the same for all models, and they follow almost exactly their Gaussian priors. The only exception is h_n that follows a distribution narrower than its prior. Therefore, the discrepancy is entirely explained by the difference in the mass surface density Σ_n. We are not constraining this parameter using direct observations, we assume that it follows a uniform prior, but we constrain it by the local surface density ratio (eq. 4.2). None of the models require a significant deviation from the observations. This implies that the ratio between the density of the thick disc and the thin disc at Solar position is well described by all models.

Considering that we get the same mass for the bulge in the all three cases, the discrepancy in the total baryonic mass is a consequence of the difference in the thin disc model. For NGC 3201 and Palomar 5, we get a total baryonic mass of $M_{\text{bar}} = (7.22 \pm 0.7) \times 10^{10}$ and $(7.04 \pm 0.66) \times 10^{10}$ $M_\odot$ respectively. These values are compatible with $(6.43 \pm 0.63) \times 10^{10}$ $M_\odot$ from McMillan (2011), $(5.6 \pm 1.6) \times 10^{10}$ $M_\odot$ from Piffl et al. (2014), and $(7.25^{+0.39}_{-0.68}) \times 10^{10}$ $M_\odot$ from Cautun et al. (2020), but they are not compatible with the required mass by M68 of $(8.3 \pm 0.49) \times 10^{10}$ $M_\odot$. The mass excess in the disc for M68 implies a bigger vertical force $|K_{z=1.1}|$ with a tension of 2σ with respect to the assumed prior (eq. 4.13). This large discrepancy may be caused by a poor modelling of the disc at the Solar neighbourhood as we have neglected the gas and dust components. On the other hand, the value of $|K_{z=1.1}|$ that we are taking as a constraint is calculated using a different model of the Galactic disc and different values for the position and velocity of the Sun, so it can be systematically biased. This discrepancy does not appear in the total mass of the Milky Way since it is dominated by the dark halo, we obtain $M_{200}^{\text{MW}} \simeq 1.03 \times 10^{12}$ $M_\odot$ at 0.4σ from the prior (eq. 4.10) for all the streams.

There are also no significant discrepancies in the phase-space location of NGC 3201 or M68. In the case of Palomar 5, we get a discrepancy of 2.4σ for the heliocentric radius, and 1.5σ and 3.1σ for the proper motions. There are several measurements of the heliocentric radius ranging from 20 to 23 kpc. Our prior has a mean value close to the lower limit and uncertainty much smaller than this range. Despite this, the most likely explanation for this discrepancy, along with the discrepancies in the estimates of the proper motions, is that the computed phase-space location of the cluster is fitting the mean position of the overall stream and not the position of the cluster. As we can see in the right-hand upper and right-hand lower panels of Figure 4.1, the errors of the measurements are much larger than the real dispersion of the stream.

4.5.2 Dark matter halo

We plot the posterior distributions of the parameters that characterise the dark matter halo density in Figure 4.6. We include the distributions marginalised over two parameters (contour panels) and one parameter (function panels) for all models. For NGC 3201 and Palomar 5 we get a scale length $a_1 \simeq 12^{+18}_{-6}$ kpc which implies that the inner slope α describes the distribution of dark

matter of the inner region of the Galaxy, corresponding to approximately half the disc length. For both streams, we get $\alpha \simeq 0.7 \pm 0.5$. The mean value is smaller than the slope of a NFW obtained from dark matter-only simulations ($\alpha = 1$), but the uncertainty does not allow us to distinguish between a cuspy or a cored configurations. In the case of M68, we get a bigger scale length of $a_1 = 18.63^{+10.08}_{-5.41}$ and a inner slope $\alpha = -0.23 \pm 0.39$. A configuration with $\alpha < 0$ implies a hole in the distribution of dark matter with radius $R_{\text{hole}} = -a_1\alpha/\beta$. This configuration is not dynamically consistent with the cosmological models of formation and evolution of galaxies. Despite this, we get a small hole of $R_{\text{hole}} = 1.72 \pm 1.1$ kpc, which is smaller than the scale length of the bulge. For $r \gtrsim 5$ kpc, where we have all dynamical constraints, the distribution of dark matter decreases monotonically as the radius increases. This is compatible with the over-estimate of the mass of the thin disc required by M68. As we put more mass in form of an exponential disc, we need less dark matter to explain the discrepancy between the predicted gravitational field and the observed field. The upper limit of the estimate of α for M68 is bigger than zero, which implies that this stream is compatible with a cored dark matter halo. One possible explanation for this result is that the observed section of the stream associated with M68, which is located at about 5 kpc from the disc plane, requires a flattened potential that cannot be reproduced by a halo consistently with the other constraints, but can be well described by a more massive disc.

The outer slope β is almost unconstrained by the stellar streams and the rotational curve of the Milky Way. For all models, this parameter is correlated with the total mass M_{200}^{MW} and a_1 with a Pearson correlation coefficient with absolute value always bigger than 0.53 and 0.61 respectively. Thus, and taking into account that we don't get a significant deviation for M_{200}^{MW}, it implies that β is adjusted to fit with the constraint imposed to the total mass (eq. 4.10). The three distributions of β are asymmetric, with an elongated tail towards values of $\beta > 3$. These tails are cut off by the upper limits of the priors, so the upper uncertainties could be underestimated. The three models are in good agreement with a value of $\beta \sim 3.3 \pm 1$, and they are at 0.3σ, 1.3σ, and -0.2σ from $\beta = 3$ for NGC 3201, M68, and Palomar 5 respectively.

The distribution of the scale density ρ_0^{dh} is almost the same for all the models. They peak about $[0.7\text{-}4] \times 10^7$ M$_\odot$ kpc^{-3} and have a long tail extended up to the limit imposed by the prior. This parameter is correlated with a_1 and α with a Pearson correlation coefficient with an absolute value bigger than 0.54 for all cases. The dark matter density at Solar position $\rho_{\text{dh}}(R_\odot)$ is often estimated in the range $[0.3\text{-}0.8]$ GeV cm^{-3} (see e.g. de Salas, 2020). Our estimates are systematically smaller, of about $[0.17\text{-}0.31]$ GeV cm^{-3}. This property is strongly correlated with the flattening parameter q_ρ^{dh} (see Section 4.5.2). We get a correlation of -0.76 for NGC 3201, -0.84 for M68, and -0.58 Palomar 5. Thus, the prolate halos obtained for NGC 3201 and M68 favour small densities of $\rho_{\text{dh}}(R_\odot) \sim 0.2$ GeV cm^{-3}, and the spherical halo obtained by Palomar 5 implies a larger values of $\rho_{\text{dh}}(R_\odot) \sim 0.28$ GeV cm^{-3}. In general, spherical halos are assumed in the literature, which may explain the systematic deviation towards smaller values in our results.
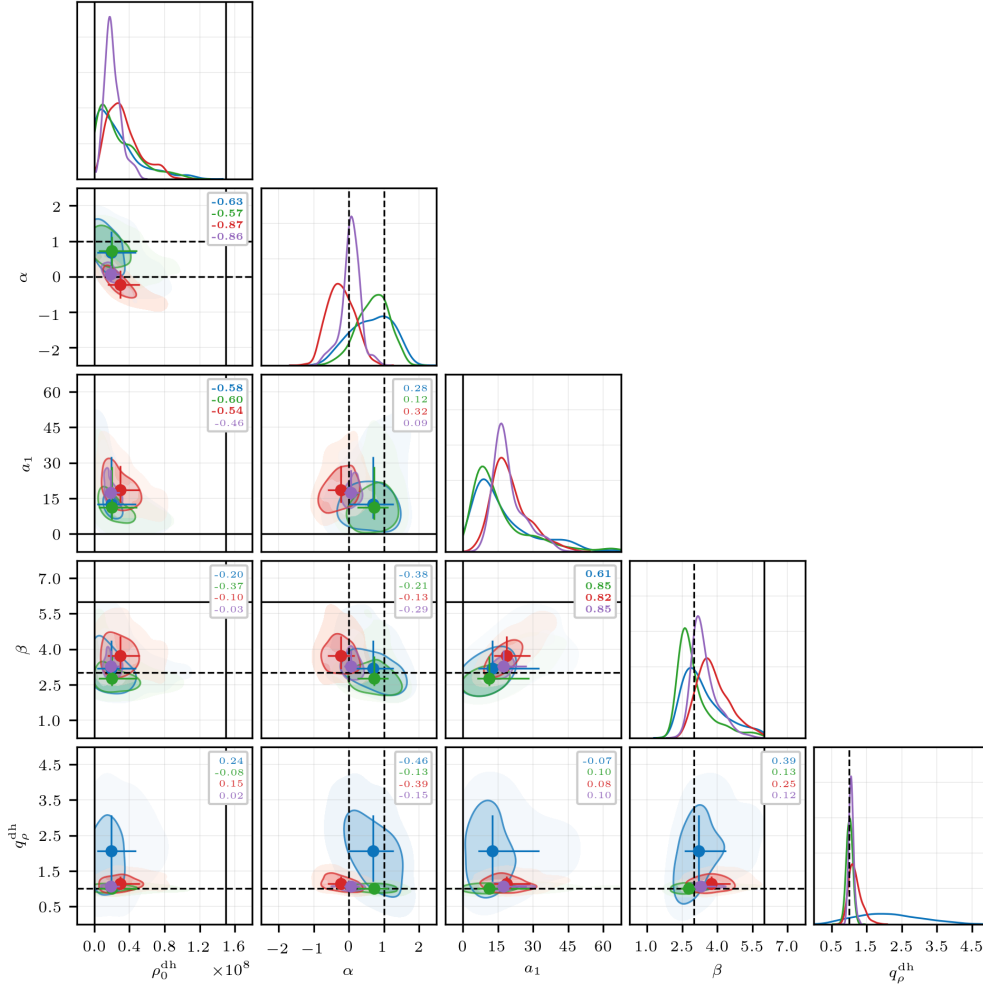
Figure 4.6: Halo parameters corner plot. Each panel shows the posterior probability density function marginalised over two parameters (contours) and one parameter (functions) for the results obtained with the streams generated by NGC 3201 (blue), M68 (red), Palomar 5 (green), and all the streams together (purple). The bright shade displays the area that encloses the 1σ level of the distributions and the faint area the 2σ level. The contour of the 1σ area is highlighted with a solid line. The dots mark the median of the distribution and the bounded coloured lines the 1σ levels marginalised over each parameter. The solid black lines mark the limits of the uniform priors when they are within the limits of the displayed space. The dashed lines mark the slopes of the NFW halo ($\alpha = 1$, $\beta = 3$), the flat inner slope ($\alpha = 0$), and the spherical configuration ($q_\rho^{\mathrm{dh}} = 1$). The legend of each panel shows the Pearson correlation coefficient.
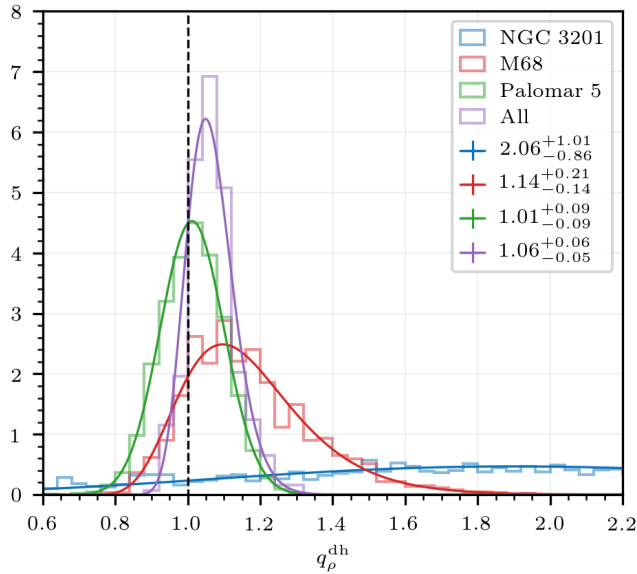
Figure 4.7: Histogram of a random sample following the marginalised posterior probability density function of the flattening parameter q_ρ^{dh}. The distributions are computed using as constraints the streams associated with NGC 3201 (blue), M68 (red), Palomar 5 (green), and all the streams together (purple). In the legend, we include the median and the 1σ levels of the random sample. The solid lines show the best-fitting log-Normal distributions (see Appendix C.4), and the dashed vertical line marks the spherical configuration.

We get a halo concentration c_{200} of $13.48^{+4.82}_{-3.06}$ for NGC 3201, 8.24 ± 0.58 for M68, and $10.43^{+2.95}_{-1.92}$ for Palomar 5. Cautun et al. (2020) obtained $c_{200} = 12^{+2.6}_{-2.4}$ assuming a spherical NFW density profile for the dark halo, and a lower value of $8.2^{+1.7}_{-1.5}$ calculated by including the effects of halo contraction produced by the interactions between baryons and dark matter. Comparing to the latter result, our estimates of M68 and Palomar 5 are compatible with this work, and NGC 3201 has a discrepancy of 1.5σ. In addition, our results for NGC 3201 and Palomar 5 are consistent with $c_{200} = 10.9^{+2.6}_{-2.0}$ from Callingham et al. (2019), computed using a NFW profile, and M68 is almost consistent at -1.3σ. This ensures the self-consistency of the model since we are using the total mass estimate of Callingham et al. (2019) as a constraint.

Halo axis ratio or flattening parameter

We display in Figure 4.7 the histogram of the marginalised probability density function of the halo axis ratio or flattening parameter q_ρ^{dh}. We show the median and the 1σ levels in the legend and we include the best-fitting log-Normal distributions for each case. We show the best-fitting parameters and additional properties of the distributions in Appendix C.4.

We find that the stream generated by NGC 3201 barely constraints this parameter, giving $q_\rho^{\mathrm{dh}} = 2.06 \pm 0.93$. This distribution is somewhat asymmetric, whit a bias towards larger values with respect to the pick. This broad distri-
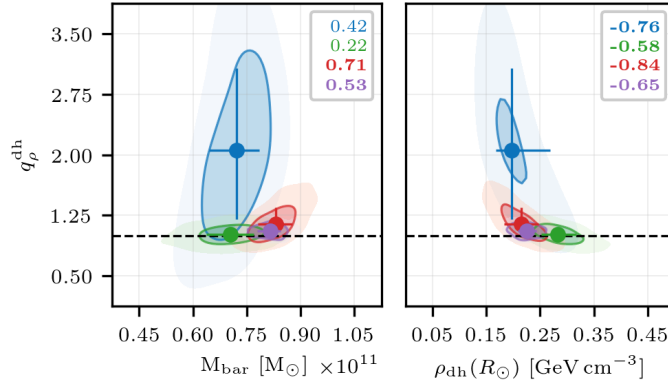
Figure 4.8: Same as Figure 4.6. It is only shown the posterior probability density function marginalised over the flattening parameter q_ρ^{dh}, the total baryonic mass M_{bar} (left-hand panel), and the density of dark matter at the position of the Sun $\rho_{\mathrm{dh}}(R_\odot)$ (right-hand panel).

bution may be a consequence of the fact that the stream is short, located near the pericenter, and with an equatorial projection that makes its phase-space distribution in these coordinates insensitive to the variation of the potential of the Galaxy. Although it is located close to the disc, the halo flattening parameter shows no correlation with M_{bar}. It only correlates with the total amount of dark matter in the inner region of the Galaxy, which is proportional to $\rho_{\mathrm{dh}}(R_\odot)$, with a correlation coefficient of -0.76. We include the posterior probability density function marginalised over q_ρ^{dh}, M_{bar}, and $\rho_{\mathrm{dh}}(R_\odot)$ in Figure 4.8.

For Palomar 5, we get a symmetric distribution with median and deviation of 1.01 ± 0.09. This stellar stream is compatible with a spherical halo ($q_\rho^{\mathrm{dh}} = 1$). The flattening parameter is not correlated with the distribution of baryonic mass because the globular cluster and its stream are located far from the disc. It only has a small correlation of -0.58 with $\rho_{\mathrm{dh}}(R_\odot)$, and the heliocentric radius of the cluster with a correlation of -0.58. For M68, we obtain $q_\rho^{\mathrm{dh}} = 1.14^{+0.21}_{-0.14}$. This result is in good agreement with Palomar 5, although the streams are located at different distances with respect to the Galactic centre and the plane of the disc. This stream is compatible with the spherical configuration but it has a median bigger than one and a tail elongated towards larger values, thus favouring prolate configurations. For M68, the flattening parameter is correlated with the total baryonic mass M_{bar} with a coefficient of 0.71. The dominant component is the thin disc with a correlation of 0.55 with h_{n} and 0.5 with the $M_{\mathrm{d}}^{\mathrm{n}}$. It is explained because the stellar stream is located close to the disc, at 5 kpc from the disc plane. The tidal stream of M68 tends to over-estimate the total mass of the thin disc in comparison with other studies (see Section 4.5.1), this may explain the preference for prolate configurations.

4.5.3   Circular velocity curve

We plot the circular velocity curve of the Milky Way in the top panel of Figure 4.9. The solid lines correspond to the median of the total circular velocity and the dashed lines the circular velocity explained by the baryonic mass. The black

dots with error bars are the data taken from Eilers et al. (2019) with errors computed as described in Section 4.3.3. In the bottom panel, we show the residuals between the models and the observed data. There are no significant differences between the rotational curves described by all the models, and all the curves are consistent with the observations with a high degree of accuracy. In the range $R \sim [5\text{-}20]$ kpc, all the computed values have deviations with an absolute value $\lesssim 1.1\sigma$. Eilers et al. (2019) do not provide any measurement for $R > 25$ kpc, to verify the models for larger radius, we include in the plot as brown dots with error bars the rotational curve measured by Huang et al. (2016) using a sample of halo K giant stars (HKG in the reference). The measurements extend from ~ 16 to 100 kpc and have a typical uncertainty of ~ 20 km s^{-1}. This rotational curve presents discrepancies with our models and with the measurements of Eilers et al. (2019) in the range $R \sim [15\text{-}25]$ kpc. For $R \gtrsim 40$ up to 100 kpc, the observed rotational curve decreases steadily from $V_c \sim 200$ to 150 km s^{-1} and agrees with our models with discrepancies with absolute values in the range $[0.04\text{-}1.08]\,\sigma$.

4.6 Results for all streams together

When we include all three streams together, we constrain the halo over a larger area. It extends about $[9\text{-}17]$ kpc from the Galactic centre and about $[-3\text{-}15]$ kpc from the plane of the disc. The stream of M68 determines the total baryonic mass because it is the only one that imposes constraints on the disc. It requires a larger mass for the thin disc than the other streams (see Section 4.5.1). Thus, we obtain $M_d^n = (6.07 \pm 0.39) \times 10^{10}$ and $M_{bar} = (8.01 \pm 0.38) \times 10^{10}$ M$_\odot$, similar results to those obtained using only the stream of M68. Similarly, we obtain an overestimated vertical gravitational acceleration at the position of the Sun, about 1.8σ from the observation (eq. 4.13). This model does not require a significant deviation from the measurements of Sun's position and velocity. The only characteristic with a significant discrepancy is the transverse velocity of Sgr A*, at -1.8σ from the observation (eq. 4.12), similar to Palomar 5. In this case, we obtain a velocity of the LSR of $\Theta_0 = 230.67 \pm 1.55$ km s^{-1} and a transverse velocity of the Sun $\Theta_0 + V_\odot = 244.38 \pm 0.91$ km s^{-1}. These results are consistent with previous measurements (see Section 4.5.1).

All the streams together favour a cored dark halo, with an inner slope $\alpha = 0.06 \pm 0.22$, a result in the intersection of our previous estimates. This parameter is correlated with the scale density, obtaining $\rho_0^{dh} = 1.84^{+1.05}_{-0.62} \times 10^7$ M$_\odot$ kpc^{-3}, a value also at the intersection of our previous estimates. The scale length is close to the stream of M68, we obtain $a_1 = 17.36^{+9.77}_{-2.74}$. This parameter is strongly correlated with the outer slope $\beta = 3.29^{+0.66}_{-0.28}$. As a consequence of the fact that NGC 3201 does not constrain the flattening parameter, the value obtained for all the streams together is approximately the intersection between M68 and Palomar 5. We find $q_\rho^{dh} = 1.06 \pm 0.06$, following an nearly symmetric distribution as shown as a purple line in Figure 4.7. Therefore, these streams prefer a moderately prolate halo but compatible with a spherical shape. The flattening parameter has a small positive correlation with M_{bar}, implying that the larger baryonic mass imposed by the stream of M68 biases the distribution of q_ρ^{dh} towards prolate configurations. It is also correlated with $\rho_{dh}(R_\odot)$ as it is
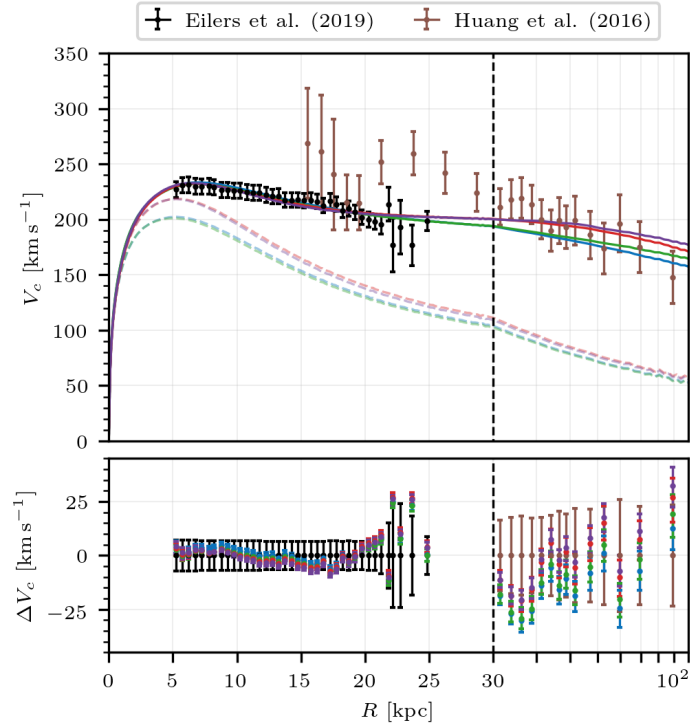
Figure 4.9: Circular velocity curve of the Milky Way. *Top panel:* The solid lines mark the median of the rotational curve of the models obtained with the streams of NGC 3201 (blue), M68 (red), Palomar 5 (green), and all the streams together (purple). The dashed lines mark the contribution of the baryonic components. The black dots with error bars are the rotational curve observed by Eilers et al. (2019) with errors computed as described in Section 4.3.3, and the brown dots with error bars are the observations of Huang et al. (2016) for the HKG sample. The dashed vertical black line marks the change in the horizontal scale from linear to logarithmic. *Bottom panel:* Residuals between the models and the observational data. The error bars mark the limits that enclose the 1σ levels of the distribution of V_c for each radius.

shown in Figure 4.8.

The circular velocity curve of this model is consistent with the measurements, with discrepancies with absolute value in the range $[0.08\text{-}1.2]\,\sigma$ for $R \sim [5\text{-}20]$ kpc as shown in the bottom panel of Figure 4.9. The rotational curve is very close to that required by the stream of M68, with slightly larger values for $R > 40$ kpc. This is because the mass of the dark halo is larger for this model $M_{200}^{\mathrm{dh}} = (1.08 \pm 0.22) \times 10^{12}$ M$_\odot$, with approximately 14 per cent more mass than the previous models.

4.7 Comparison to previous studies of the dark halo

Several studies have described the shape of the Milky Way's dark matter halo using parametric models for the density profile constrained by observational data. In addition, the properties of the Galactic halo have also been statistically inferred from cosmological simulations of Milky Way-like galaxies in which baryonic effects on the dark matter distribution have been taken into account. In this section, we review these studies focusing on the halo axis ratio and compare them with our results.

4.7.1 Studies based on observational constraints

Studies based on analytical models, in general, assume that the dark matter halo is axisymmetric and the axis of symmetry is perpendicular to the disc. Most studies adopt a NFW density profile for the halo or a generalised version where the slopes are free (gNFW). Otherwise, the total Galactic potential is assumed to follow a logarithmic profile. Here we exclude studies that use a symmetry axis not perpendicular to the disc. We summarise the obtained results in Figure 4.10 and 4.11. We show the values of the dark halo axis ratio as stated in the source, using different colours for the density q_ρ^{dh} (red) and potential q_Φ^{dh} (black). When a stellar stream is the main source of observational data, estimates are assumed to be given at the position of the progenitor cluster and about 14 kpc for the case of GD-1. We also include a dashed vertical line marking the spherical configuration. We indicate the parametric model of the density or the potential in the vertical axis under each reference.

In Figure 4.10, we show how early studies do not provide a consistent picture. Some studies using Sagittarius stellar stream obtained triaxial shapes (Law et al., 2009; Law and Majewski, 2010; Deg and Widrow, 2013), but these configurations have been criticised for their instability and their incompatibility with other constraints from Palomar 5 or Sagittarius's tidal debris (see e.g. Ibata et al., 2013; Debattista et al., 2013; Belokurov et al., 2014; Pearson et al., 2015). We do not include these results in this figure. We only show results from the studies that assumed axisymmetry: Johnston et al. (2005) and Fellhauer et al. (2006) obtained an oblate halo close to the sphere and Helmi (2004) a prolate halo. Likewise, assuming that the distribution of halo stars is in equilibrium, Loebman et al. (2012, 2014) obtained that the dark matter halo is oblate and Bowden et al. (2016) prolate.

On the other hand, recent studies offer a more consistent picture preferring spherical-prolate configurations. For example, Fardal et al. (2019) using the Sagittarius stream mapped with RR Lyrae from Pan-STARRS1 obtained a
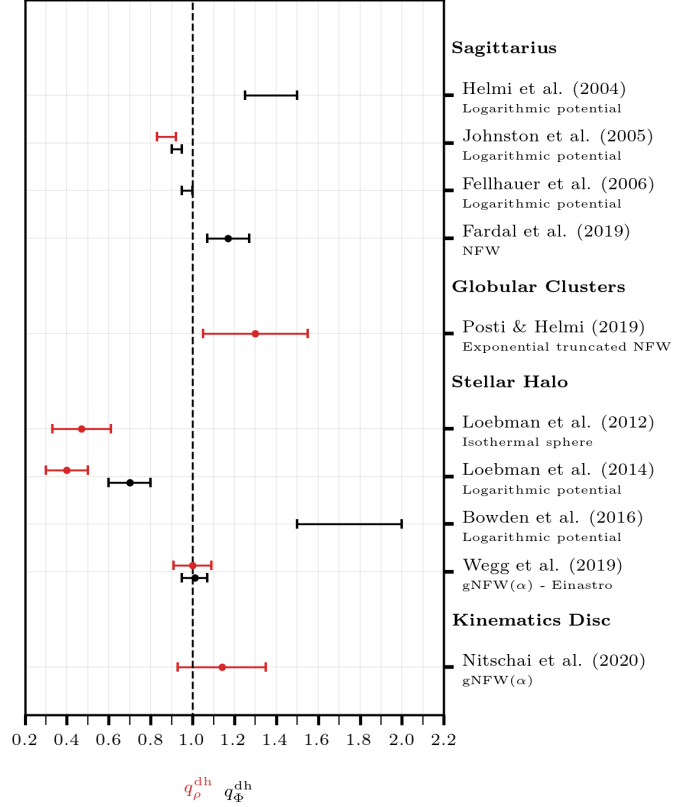
Figure 4.10: Comparison of our estimated axis ratio for the dark matter halo density q_ρ^{dh} (red) and dark matter halo potential q_Φ^{dh} (black) to previous estimates. The results are grouped according to the main source of observational data. We include under the reference the assumed axisymmetric density profile or potential model. For a gNFW, we indicate the adopted free slopes in parentheses. The dots show the mean or the median value (as stated in the source), and the bars the 1σ deviations. The dot is not included when the result is provided with an interval. When stellar streams are used, the value of the axis ratios are evaluated at the position of the clusters, and about a Galactocentric radius of $r \sim 14$ kpc for GD-1. The vertical dashed line marks the spherical configuration.
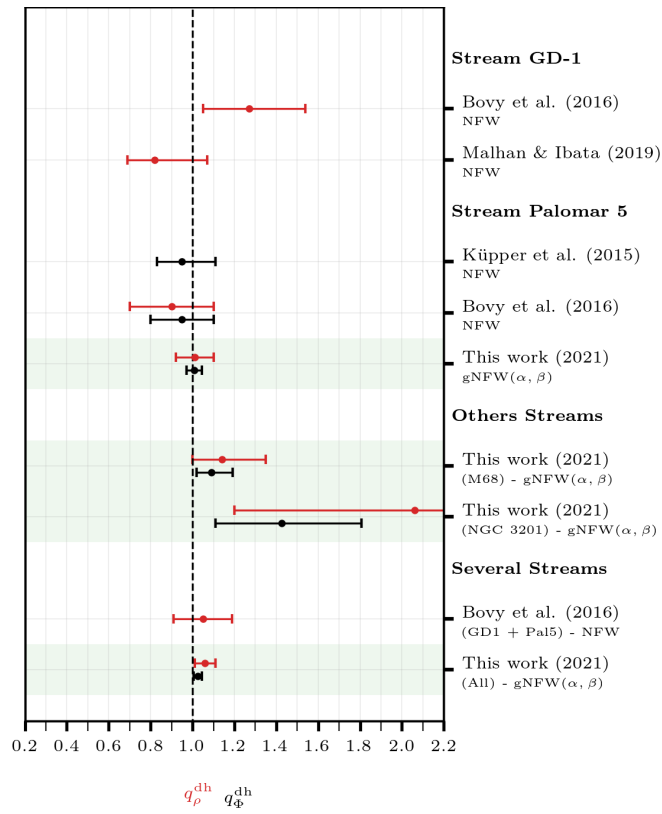
Figure 4.11: Same as Figure 4.10. The green shaded regions highlight our estimates.

prolate halo potential with $q_\Phi^{\mathrm{dh}} = 1.17 \pm 0.1$. This result is close to Wegg et al. (2019) who, using a distribution of RR Lyrae from the halo in the range $r \sim 2$ to 20 kpc, conclude that the halo is spherical with $q_\rho^{\mathrm{dh}} = 1 \pm 0.09$. In this case, they use different models for the halo, obtaining almost the same result for a gNFW and a Einastro profile.

Similarly, Posti and Helmi (2019) using the distribution of globular clusters conclude that the halo is prolate with $q_\rho^{\mathrm{dh}} = 1.3 \pm 0.25$. This study uses the AGAMA package (Vasiliev, 2019a) to compute the distribution function of the globular clusters in an angle-action framework. This software applies only to oblate axisymmetric potentials. For this reason, this estimate cannot be completely reliable. Hattori et al. (2020) use a similar method based on orbital actions computed with AGAMA but restricting to oblate halo models. They use a sample of halo stars and obtain 99 per cent of the posterior distribution of the axis ratio at $q_\rho^{\mathrm{dh}} > 0.963$, which strongly disfavours a flattened halo. Moreover, the same authors (Hattori and Valluri, 2020) conclude that the halo flattening distribution peaks at $q_\rho^{\mathrm{dh}} \simeq 1.5$ using a hypervelocity star and assuming that it was ejected from the Galactic centre. These results agree with Nitschai et al. (2020) that use kinematic data of the disc at $R \sim [4\text{-}12]$ kpc and $z \sim \pm 2$, finding a prolate halo compatible with the spherical shape of $q_\rho^{\mathrm{dh}} = 1.14 \pm 0.21$.

In general, studies using stellar streams are more consistent with each other. We plot their results in Figure 4.11 along with our estimates highlighted with a green shade. We exclude from this figure the first studies using GD-1 stellar stream (Koposov et al., 2010; Bowden et al., 2015) because they did not constrain the dark matter halo directly but the overall potential of the Galaxy. These studies assume a single logarithmic component and obtain a slightly oblate potential at the location of the stream, which is about 14 kpc from the Galactic centre and about 5 kpc from the disc. We include in Figure 4.11 the study of Bovy et al. (2016) using GD-1 which concludes that the halo is prolate with $q_\rho^{\mathrm{dh}} \simeq 1.27 \pm 0.27$. Using the same stream, Malhan and Ibata (2019) obtain a oblate halo of $q_\rho^{\mathrm{dh}} = 0.82^{+0.25}_{-0.13}$. The latter study uses better constraints, as it uses more stars and their phase-space coordinates are taken from GDR2 catalogue. Although there is a small tension between the two previous estimates of 1.22σ, both results are compatible with the spherical shape.

We can compare the results obtained with the GD-1 stellar stream with our estimates from the observed section of the M68 stellar stream because they are at a similar distance from the Galactic disc. However, we note that M68 stellar stream is about 5 kpc closer to the Galactic centre than GD-1. Our estimate favours a prolate configuration but is compatible with a spherical shape. This result is in better agreement with Bovy et al. (2016) at 0.38σ than with Malhan and Ibata (2019) at 1.12σ. On the other hand, the stream of NGC 3201 is located at about the same radius as GD-1 but closer to the disc. This stream barely constrains the axis ratio, but still favours prolate configurations compatible with M68 and Bovy et al. (2016).

Studies using Palomar 5 stellar stream

Küpper et al. (2015) carried out a study using data including sky coordinates and line-of-sight velocities along the stellar stream of Palomar 5. They model

the Milky Way using a Miyamoto-Nagai potential for the disc and a NFW density profile for the dark halo. They adopt wide uniform prior distributions for the position and velocity of the globular cluster that includes our prior assumptions. They produce density maps of the stellar stream by the streak-line method based on releasing particles from the Lagrange points of the cluster, and compare them with the observations using the Bayesian framework developed by Bonaca et al. (2014). They found $q_\Phi^{\mathrm{dh}} = 0.95^{+0.16}_{-0.12}$. Similarly, Bovy et al. (2016) use similar data and almost the same model of the Galaxy than Küpper et al. (2015). The main difference is that Bovy et al. (2016) use a different stream-fitting methodology based on action-angle modelling introduced by Bovy (2014). In this case, the position and velocity of the cluster is also compatible with our priors, except the proper motions with about a 2σ discrepancy since they use pre-*Gaia* measurements. They obtain a oblate halo but compatible with the spherical shape of $q_\rho^{\mathrm{dh}} = 0.9 \pm 0.2$. When Bovy et al. (2016) combines GD-1 with Palomar 5 stellar stream, they obtain a spherical shape with $q_\Phi^{\mathrm{dh}} = 1.05 \pm 0.14$, indicating that Palomar 5 is a stronger constraint.

These estimates have larger uncertainties than ours, even though our halo model has more free parameters. The most likely explanation is that we have a larger sample of stars with five phase-space parameters measured by GDR2 and 15 stars with radial velocity. We conclude that our measurements are fully consistent with these studies, and all of them favour a halo close to the spherical configuration.

4.7.2   Studies based on cosmological simulations

In general, cosmological simulations that only include dark matter predict triaxial halos. These halos become more rounded due to the effect of the growth of baryonic structures at their centers. When the structure is a disc, the halo becomes axisymmetric, and the axis of symmetry of the halo and the disc align at angles approximately in the range 0 ± 20 deg (Bailin et al., 2005; Shao et al., 2016; Prada et al., 2019). We note that discs may be aligned with nearby galaxies (Tenneti et al., 2016) and the halos may have twists due to the decoupling of their inner parts from the outer ones (see e.g. DeBuhr et al., 2012). Consequently, to compare the simulations with our estimates, we assume that the halos have an axis of symmetry closely aligned with the disc, and compare the axis ratio along this axis with the parameter q_ρ^{dh}.

In Figure 4.12 we plot our estimates of q_ρ^{dh} in function of the normalised Galactocentric radius. We plot in orange and yellow the results from simulated galaxies that resemble the Milky Way (Bryan et al., 2013; Velliscig et al., 2015; Tomassetti et al., 2016; Butsky et al., 2016). In general, they preset discs at redshift $z = 0$ and a total mass of about 10^{12} M$_\odot$. When the source indicates that they are studying Milky Way-like galaxies, we plot the results in black (Dai et al., 2018; Chua et al., 2019; Prada et al., 2019). All simulations predict oblate dark halos. Taking only the estimates in the range $r \approx [5 \text{-} 20]$ kpc, where we have all our constraints, the simulations predict $q_\rho^{\mathrm{dh}} \sim 0.74 \pm 0.15$. These results are not compatible with our estimates. The closest case is Chua et al. (2019) which gets $q_\rho^{\mathrm{dh}} = 0.79 \pm 0.15$ at $0.15\,r_{200}$ when the dark halo is assumed to be aligned with the disc axis. This measurement disagrees with our Palomar
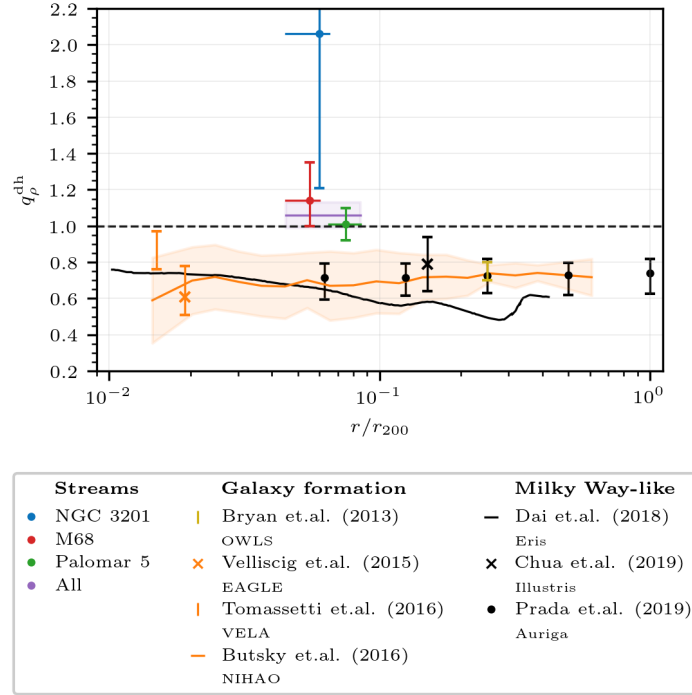
Figure 4.12: Comparison of our estimates of q_ρ^{dh} to simulations of formation and evolution of galaxies. Solid lines and markers indicate mean values and shaded regions and error bars 1σ levels. When the marker is a vertical line, it indicates that the estimate is shown as an interval. For the galaxy formation simulations, we take the galaxies of about $\sim 10^{12}$ $M_\odot$ at redshift $z = 0$ (orange and yellow). When the sources state that the galaxies resemble the Milky Way, we group them as Milky Way-like simulations (black). We include under the reference the name of the simulation. In general, the galaxies have $r_{200} \sim [200\text{-}240]$ kpc. For the stream of NGC 3201 (blue), M68 (red), and Palomar 5 (green) we indicate the mean location of the stream with a dot and the range that covers the stream and the globular cluster with a horizontal bar. For all the streams together (purple), we mark all the range covered by the globular clusters and their streams. The dashed horizontal line marks the spherical shape.

5 estimate at 1.3σ.

4.8   Conclusions

Four different mass models of the Milky Way have been presented presented. Each of them is obtained by fitting the stellar stream generated by NGC 3201, M68, and Palomar 5 separately, and all the above streams together. We assume an axisymmetric mass model of the Milky Way composed of a bulge and two exponential discs. We include a dark matter halo that follows a two power-law density profile function of five free parameters. These models are also constrained by star counts, observations of the Sun's position and velocity, the vertical gravitational force at the position of the Sun, the circular velocity curve from 5 to 25 kpc from the Galactic centre, and the total mass of the Galaxy.

The constraints using NGC 3201 and Palomar 5 result in two similar density models that fit well to all imposed dynamical and kinematical constraints.

These streams require a similar dark halo with inner slope $\alpha = 0.68 \pm 0.64$ for NGC 3201 and $\alpha = 0.73 \pm 0.45$ for Palomar 5. The main difference between the two models is the halo flattening. NGC 3201 does not strongly constrain this parameter, giving $q_\rho^{\mathrm{dh}} = 2.06 \pm 0.93$. This is because we only observe a short section of the stream, insensitive to variations in the dark halo model due to its projection in equatorial coordinates. By contrast, Palomar 5 strongly constrains this parameter giving $q_\rho^{\mathrm{dh}} = 1.01 \pm 0.09$, fully compatible with a spherical halo.

The stream of M68 requires more baryonic mass in form of a more massive thin disc than the other streams. This is also in tension with previous estimates of the total baryonic mass of the Galaxy. As a consequence, this model does not fit well the vertical gravitational acceleration at the position of the Sun. Because of the massive thin disc, this model requires less dark matter in the inner region of the Milky Way. It prefers a halo with a hole in the centre of the Galaxy with $\alpha = -0.23 \pm 0.39$. An additional consequence is that this stream favours prolate halos compatible with a spherical shape with $q_\rho^{\mathrm{dh}} = 1.14_{-0.14}^{+0.21}$. This correlation between the halo flattening and the total baryonic mass can be explained because we only observe a section of this stream located near the disc, about 5 kpc from the Galactic plane and between 5 and 10 kpc from the Galactic centre. At this location, the influence of the disc is significant. Thus, to properly constrain the halo flattening for this case, we need to include more observational constraints (e.g. kinematical data of the stars of the disc) and improve the density model of the disc (e.g., by including gas and dust components). The flattening parameter is not correlated with any other halo parameter. The same applies to all models. This is because the flattening determines the deviation from the radial direction of the gravitational acceleration, and the remaining ones, determine its magnitude and radial variation.

For all three models, we get a halo scale length of about $a_1 \sim 15_{-8}^{+14}$ kpc. This parameter determines the transition between the inner and the outer slope of the halo density profile. As a consequence of the fact that all our observational constraints are in the range $r \sim [5\text{-}25]$ kpc, the outer slope of the dark matter density is only constrained by the total mass of the Galaxy. This propertie of the model has been imposed from observations of the Milky Way satellites. Since the outer slope is function of the total mass, and the range it describes is determined by the scale length, these two parameters are strongly correlated in all our models. Furthermore, the scale density is also correlated with the scale length and the inner slope. These degeneracies imply that the density profile can be simplified by assuming a different model with fewer free parameters.

When we include all the streams in the fit, we obtain better constraints. The resulting model requires a total baryonic mass closer to that required by M68 as it is the only stream that imposes constraints on the mass of the disc. For the inner slope of the dark matter density, we find $\alpha = 0.06 \pm 0.22$, approximately the intersection between the above models. For the halo flattening, we get the intersection of M68 and Palomar 5 $q_\rho^{\mathrm{dh}} = 1.06 \pm 0.06$ because NGC 3201 does not significantly constraint this parameter. We find a outer slope of $\beta = 3.29_{-0.28}^{+0.66}$, which is determined by the scale length $a_1 = 17.36_{-2.74}^{+9.77}$ kpc, and

a total mass of the Galaxy of $M_{200}^{\mathrm{dh}} = (1.18 \pm 0.23) \times 10^{12}$ M$_\odot$, in agreement with the imposed constraint. Thus, all the streams together favour a prolate dark halo but compatible with a spherical shape with a more massive thin disc compared with other studies.

To improve the density model of the Milky Way, especially the description of the dark halo, it is possible to include more stellar streams in the fit. The most suitable cases are the streams generated by the globular clusters NGC 5466 and M5. These streams have similar characteristics and locations to those already used in this study. Thus, they can be useful to add more constraints to the inner region of the Galaxy. To improve the accuracy of the model, it may be necessary to include the effects of the LMC and other satellite galaxies since the phase-space density models of the streams used in the fit could be significantly perturbed by their influence.

Our estimates of the dark halo flattening agree remarkably well with previous studies using different observational data and different fitting methodology. In general, most of the recent studies obtain spherical-prolate halos. This is in tension with cosmological simulations that systematically predict oblate halos, with no studies describing spherical-prolate halos for a Milky Way-like galaxies. This discrepancy invites us to study in detail the initial conditions, evolution, and stability of the dark matter particles leading to the halo flattening predicted by the simulations. It also opens the possibility to improve our models by relaxing some basic assumptions such as halo axisymmetry, alignment with the disc, rotation, or use more complicated models with a variable axis ratio along the Galactocentric radius.

Chapter 5

Concluding remarks and future work

5.1 Concluding remarks

In this thesis, we have presented a new method to search for new tidal streams generated by globular clusters in the *Gaia* catalogue. It is based on the maximum likelihood technique to distinguish stream stars from the foreground field stars. This statistical method uses a numerically computed phase-space density model of the stellar stream. It is constructed assuming that each star is a test particle, and their orbits are calculated in a potential of the Milky Way plus a potential of the progenitor orbiting around the Galaxy. This model depends on the parameters that characterise the potential of the dark halo and the initial conditions of the motion of the cluster. Assuming that the stellar stream is an over-density of stars with respect to the foreground, the algorithm changes the values of the free parameters looking for the configuration that maximises the fit between the phase-space model of the stream and the stellar over-density. This configuration is used to compute the probability that a star belongs to the stream, in terms of its phase-space coordinates convolved with its observational errors. This probability is compared with the probability that a star belongs to the Milky Way, computed from a realistic phase-space model of the Galaxy. This comparison is the basis of a statistical test that establishes whether the stellar stream exists or not. If it gives a positive result, we construct a realistic model of the stellar stream and use it to choose the stars with the highest intersection with the model. Finally, we select only those that are compatible with colours and magnitudes with the progenitor.

The validity of this method is tested by detecting a simulation of the stellar stream generated by the globular cluster M68. We chose this cluster because its heliocentric distance and proper motions have been measured with high accuracy, and its predicted orbit brings a section of its expected stream close to us, about 5 kpc from the Sun. Moreover, its long radial period (~ 400 Myr) ensures that the tidal stream has not been strongly broadened and dispersed by phase mixing. The simulation of the stellar stream generated by M68 includes the magnitude extinction and the observational uncertainties expected in the second year of the *Gaia* mission. The simulated stars are accurately recovered from a sample where the foreground stars are taken from the 18th version of the *Gaia* Object Generator (Luri et al., 2014a), a simulated *Gaia* catalogue based on Besançon Galaxy Model (Robin et al., 2003).

Applying the statistical method to the GDR2 catalogue, we detected a clear tidal stream generated by M68. A section of this stream matches one previously discovered by Ibata et al. (2019b), who named it Fjörm and provided 148 probable members. They found the stream in a blind search using the Streamfinder method (Malhan and Ibata, 2018) and did not associate the stream with its progenitor. Instead, we have identified this stream by specifically searching for one associated with M68 and generated by tidal shocking of the globular cluster. The section we see most clearly belongs to the leading arm and stretches over the entire North Galactic hemisphere. Most of the stars in this section are located very close to the Sun, at ∼ 5.5 kpc, and have proper motions approximately in the range [5 - 10] mas yr^{-1}. These characteristics make them easily identifiable with respect to the halo stars, the main contribution to the foreground in this region. On the other hand, the section closest to the globular cluster and the entire trailing arm are completely obscured by foreground stars, most of them belonging to the disc. We find 151 stars compatible with the best-fitting model of the stellar stream of which 115 are colour-magnitude compatible with the progenitor cluster. We expect about 4 foreground stars to be erroneously selected as members of the stream from the estimates made with the simulations.

We have also applied the statistical method to the globular cluster NGC 3201 and detected a long tidal stream formed by stars compatible with being tidally stripped from the cluster. It extends over ~140 deg on the sky, from 40 to 180 deg in the Southern Galactic hemisphere. The leading arm, the section closest to the globular cluster, and a portion of the trailing arm are strongly obscured by foreground disc stars. In addition, the sections of the stream closest to the plane of the disc are obscured by dust. Even so, we clearly observe a section of the trailing arm, close to the Galactic disc, spanning from 70 to 105 deg. This section is located at about [3 - 4] kpc from the Sun and the stars have large proper motions of ∼ 20 mas yr^{-1} due to the effect of apparent acceleration when approaching the Sun. These characteristics facilitate the identification of stream stars with respect to the foreground disc stars. This section fits the stream Gjöll previously catalogued by Ibata et al. (2019b), who provided 57 star candidates with no association with any cluster. We identify 197 stars using only their *Gaia* kinematic data along a much longer section of the stream including the trailing and the leading arm. Once the colours and magnitudes of the stars are corrected for dust absorption and reddening, most of these stars are consistent with being members of NGC 3201. We finally select 170 stars with a high probability of being members of the stream, expecting about 4 per cent to be foreground random objects. Of these stars, 77 are located in the trailing arm, 71 near the cluster and 22 in the leading arm.

We applied the same procedure described above to select star candidates to the already known stellar stream of Palomar 5. We clearly detected both arms extended across 18 deg in the sky. We selected 126 stars dynamically compatible with the stream and compatible with the H-R diagram of the progenitor. These stars are found in the most populated sections of the stream, which are closest to the cluster. These sections are more easily observable than

the fainter extensions of the trailing arm because the *Gaia* catalogue is limited to 21 mag. Using data from DECam Legacy Survey (Dey et al., 2019) which includes stars with magnitudes up to 24 mag, Bonaca et al. (2020b) observed an extension of about 10 deg of the trailing arm that is not included in our selection. We complemented our data with radial velocities for 15 stars from Ibata et al. (2017).

The streams of NGC 3201, M68, and Palomar 5 are narrow and dynamically cold, they are located about 10 kpc from the Galactic centre and between 4 and 15 kpc from the disc. These characteristics allow us to use these streams to constrain the shape of the dark halo of the Milky Way within 20 kpc from the Galactic centre. In our study of the dark halo, we assume an axisymmetric mass model of the Galaxy. It is constructed from the sum of two exponential profiles for the thin and thick disc, a flattened bulge, and a two power-law density profile for the dark matter halo. We compute the best-fitting values of the parameters that characterise the model using a Bayesian statistical method that, in addition to the constraints from our three tidal streams, includes constraints on the mass distribution, the circular velocity curve of the Galaxy, and several kinematic and dynamical properties of the Galaxy in the vicinity of the Sun. We focused our analysis on the shape of the dark matter halo out of the plane of the disc. In particular, we study the halo density axis ratio or halo flattening parameter q_ρ^{dh}.

We present four different mass models of the Milky Way. The first three are computed with each stream separately, and the last one includes all the streams together. The streams generated by NGC 3201 and Palomar 5 require a similar mass model that fits well all the imposed constraints. The main difference between them is the distribution of the halo flattening. This parameter is not strongly constrained by the stream of NGC 3201 because we only observe a short section of the stream. This section is insensitive to variations in the dark halo mass model due to its projection in equatorial coordinates. Still, NGC 3201 favours prolate halos with $q_\rho^{\mathrm{dh}} = 2.06 \pm 0.93$. By contrast, Palomar 5 constrains this parameter with uncertainties of 10 per cent, requiring a prolate or oblate halo of $q_\rho^{\mathrm{dh}} = 1.01 \pm 0.09$ consistent with spherical shape. These two streams prefer halos with an inner density slope of $\alpha = 0.68 \pm 0.64$ and 0.73 ± 0.45 respectively. The stream generated by M68 introduces constraints on the total baryonic mass because it is located close to the disc, about 5 kpc from the disc plane. It requires a more massive thin disc than the previous streams, which is also in tension with other estimates of the baryonic mass (see e.g. McMillan, 2011, 2017). As a consequence, this model does not fit well the observed vertical gravitational acceleration at the position of the Sun. In addition, it needs less dark matter in the inner region of the Galaxy, requiring halos with an inner slope $\alpha = -0,23 \pm 0.39$. An additional consequence is that this stream favours moderately prolate halos with $q_\rho^{\mathrm{dh}} = 1.14_{-0.14}^{+0.21}$.

For all models, the streams impose a scale length of $a_1 \sim 15_{-8}^{+14}$ kpc. This parameter determines the transition between the inner and the outer slope of the density profile of the dark halo. Consequently, the outer slope β is almost not constrained by the streams. It is also not constrained by the rotational curve

of the Milky Way since it extends from 5 to 25 kpc from the Galactic centre. The outer slope is constrained by assuming that the distribution of positions and velocities of the classical satellites of the Milky Way is in equilibrium. We include this constraint indirectly by imposing the virial mass of the Galaxy from Callingham et al. (2019). Since the outer slope is determined by the total mass, and the range it describes is determined by the scale length, a_1 and β are strongly correlated in all our models. Furthermore, the scale density ρ_0^{dh} is also correlated with a_1 and α. These degeneracies imply that the density profile can be simplified by assuming a different model with fewer free parameters. The flattening parameter is not correlated with any other halo parameter for any model. This is because q_ρ^{dh} determines the deviation from the radial direction of the gravitational acceleration. The magnitude, and its radial variation, are determined by the other parameters.

The constraints on the Milky Way mass model improve when we include all the streams in the fit. In general, this model fits the observational data that we use as constraints. We find that it requires a total baryonic mass close to that required by M68 since it is the only stream that constrains the mass of the disc. All the streams together favour a dark halo with inner slope $\alpha = 0.06 \pm 0.22$, which is approximately the intersection between the above models. The halo flattening is approximately the intersection of M68 and Palomar 5 $q_\rho^{\mathrm{dh}} = 1.06 \pm 0.06$ since NGC 3201 does not constrain this parameter as much. We find an outer slope $\beta = 3.29_{-0.28}^{+0.66}$, correlated with the scale length $a_1 = 17.36_{-2.74}^{+9.77}$ kpc, and a total mass of the Galaxy of $M_{200}^{\mathrm{MW}} = (1.18 \pm 0.23) \times 10^{12}$ M$_\odot$ similarly to the previous models. Thus, all the streams together favour a prolate dark halo but compatible with a spherical shape.

These results are compatible with previous studies using stellar streams. For example, Fardal et al. (2019) obtained $q_\rho^{\mathrm{dh}} = 1.17 \pm 0.1$ using the stellar stream of Sagittarius, and Bovy et al. (2016) and Malhan and Ibata (2019) find $q_\rho^{\mathrm{dh}} = 1.27_{-0.27}^{+0.22}$ and $q_\rho^{\mathrm{dh}} = 0.82_{-0.25}^{+0.13}$ using the GD-1 stream. Our estimate of the halo flattening from Palomar 5 is also compatible with Bovy et al. (2016) which finds $q_\rho^{\mathrm{dh}} = 0.9 \pm 0.2$. In addition, recent studies using globular clusters (Posti and Helmi, 2019) and halo stars (Wegg et al., 2019) assuming they are in equilibrium, and using kinematics of the disc (Nitschai et al., 2020), obtained similar results of $q_\rho^{\mathrm{dh}} = 1.3 \pm 0.25$, $q_\rho^{\mathrm{dh}} = 1 \pm 0.09$, $q_\rho^{\mathrm{dh}} = 1.14 \pm 0.21$ respectively. In conclusion, studies based on observational constraints tend to prefer spherical-prolate halos.

This is in tension with cosmological simulations in which baryonic processes have been included. For example, Prada et al. (2019) studied a set of 30 Milky Way-like galaxies at redshift $z = 0$ from Auriga simulations. They find a strong influence of baryons on the distribution of dark matter, making the halos axisymmetric and flattened, with symmetry axis perpendicular to the disc. They obtain $q_\rho^{\mathrm{dh}} \simeq 0.7 \pm 0.1$ consistently from a galactocentric radius in the range $r \in [1/16 \text{-} 1] \, r_{200}$. Chua et al. (2019) obtained the most recent estimate of the mean flattening based on several thousand Milky Way-like galaxies from the Ilustris simulation. The find $q_\rho^{\mathrm{dh}} = 0.79 \pm 0.15$ at $0.15 \, r_{200}$. In general, simulations of Milky Way-like galaxies predict oblate halos with $q_\rho^{\mathrm{dh}} \sim [0.6 \text{-} 0.8]$

for radii in the range $r \in [0.05\text{-}1]\, r_{200}$. In general, similar results are obtained from cosmological simulations for different stellar systems, not only for galaxies resembling the Milky Way (see e.g. Bryan et al., 2013; Velliscig et al., 2015; Tomassetti et al., 2016; Butsky et al., 2016).

5.2   Future work

These results open the way for the following research:

(1) The statistical method can be applied to other globular clusters to discover new stellar streams. The recently published *Gaia* Early Data Release 3 (EDR3) (Gaia Collaboration et al., 2020) offers an opportunity to observe even fainter structures which cannot be seen with previous versions of the catalogue. Some of the best candidates for discovering new streams are the globular clusters NGC 5272, NGC 5024, NGC 5139, and NGC 5824 (Bonaca et al., 2020a).

(2) Stellar streams can be used to study the formation, evolution, and current characteristics of the Milky Way and its globular clusters. For example, accurate measurements of proper motions and radial velocities should allow us to trace the stellar stream orbits back in time and infer the time when the stars were ejected from the cluster. In this way, we can derive the mass loss that occurred at different positions of the cluster along its orbit, to see how it is increased during Galactic disc crossings. With this information, for example, we can determine whether dark matter surrounds globular clusters, and constrain its amount and distribution.

(3) There are other known stellar streams associated with globular clusters than can be used to introduce new constraints to the Galactic dark halo within a radius of 30 kpc from the Galactic centre. The most suitable streams are the generated by NGC 5466, M5 (NGC 5904), and Palomar 13 (Shipp et al., 2020).

(4) These streams can be used to study the influence of the LMC on the inner regions of the Milky Way. We can determine whether it affects the estimates of the total amount of dark matter and its shape, as well as the total mass of the Galaxy.

(5) The tension between the spherical-prolate halos obtained with observations and the oblate halos predicted by simulations invites to focus the study on the initial conditions, evolution, and interaction between dark matter particles and baryonic matter that lead to the predicted halo flattening in simulations. Furthermore, we can study whether this discrepancy is caused by an oversimplified model that assumes, for example, axisymmetry and neglects internal rotation of the halo.

Bibliography

Anguiano B., De Silva G. M., Freeman K., et al. Identification of Globular Cluster Stars in RAVE data II: Extended tidal debris around NGC 3201. MNRAS, 457(2):2078–2085, Apr 2016. doi: 10.1093/mnras/stw083.

Arcadi G., Dutra M., Ghosh P., et al. The waning of the WIMP? A review of models, searches, and constraints. *European Physical Journal C*, 78(3):203, March 2018. doi: 10.1140/epjc/s10052-018-5662-y.

Bailin J., Kawata D., Gibson B. K., et al. Internal Alignment of the Halos of Disk Galaxies in Cosmological Hydrodynamic Simulations. ApJL, 627(1): L17–L20, July 2005. doi: 10.1086/432157.

Banik N., Bovy J., Bertone G., et al. Evidence of a population of dark subhaloes from Gaia and Pan-STARRS observations of the GD-1 stream. MNRAS, 502 (2):2364–2380, April 2021. doi: 10.1093/mnras/stab210.

Baumgardt H., Hilker M., Sollima A., and Bellini A. Mean proper motions, space orbits, and velocity dispersion profiles of Galactic globular clusters derived from Gaia DR2 data. MNRAS, 482(4):5138–5155, Feb 2019. doi: 10.1093/mnras/sty2997.

Belokurov V., Evans N. W., Irwin M. J., et al. The Discovery of Tidal Tails around the Globular Cluster NGC 5466. ApJL, 637(1):L29–L32, Jan 2006a. doi: 10.1086/500362.

Belokurov V., Zucker D. B., Evans N. W., et al. The Field of Streams: Sagittarius and Its Siblings. ApJL, 642(2):L137–L140, May 2006b. doi: 10.1086/504797.

Belokurov V., Koposov S. E., Evans N. W., et al. Precession of the Sagittarius stream. MNRAS, 437(1):116–131, Jan 2014. doi: 10.1093/mnras/stt1862.

Bianchini P., Ibata R., and Famaey B. Exploring the Outskirts of Globular Clusters: The Peculiar Kinematics of NGC 3201. ApJL, 887(1):L12, Dec 2019. doi: 10.3847/2041-8213/ab58d1.

Bienaymé O., Famaey B., Siebert A., et al. Weighing the local dark matter with RAVE red clump stars. A&A, 571:A92, Nov 2014. doi: 10.1051/0004-6361/201424478.

Binney J. and Tremaine S. *Galactic dynamics*. Princeton series in Astrophysics, 1987.

Bissantz N. and Gerhard O. Spiral arms, bar shape and bulge microlensing in the Milky Way. MNRAS, 330(3):591–608, Mar 2002. doi: 10.1046/j. 1365-8711.2002.05116.x.

Bland-Hawthorn J. and Gerhard O. The Galaxy in Context: Structural, Kinematic, and Integrated Properties. ARA&A, 54:529–596, September 2016a. doi: 10.1146/annurev-astro-081915-023441.

Bland-Hawthorn J. and Gerhard O. The Galaxy in Context: Structural, Kinematic, and Integrated Properties. ARA&A, 54:529–596, Sep 2016b. doi: 10.1146/annurev-astro-081915-023441.

Blumenthal G. R., Faber S. M., Primack J. R., and Rees M. J. Formation of galaxies and large-scale structure with cold dark matter. Nature, 311: 517–525, October 1984. doi: 10.1038/311517a0.

Bonaca A., Geha M., Küpper A. H. W., et al. Milky Way Mass and Potential Recovery Using Tidal Streams in a Realistic Halo. APJ, 795(1):94, November 2014. doi: 10.1088/0004-637X/795/1/94.

Bonaca A., Hogg D. W., Price-Whelan A. M., and Conroy C. The Spur and the Gap in GD-1: Dynamical Evidence for a Dark Substructure in the Milky Way Halo. APJ, 880(1):38, July 2019. doi: 10.3847/1538-4357/ab2873.

Bonaca A., Naidu R. P., Conroy C., et al. Orbital Clustering Identifies the Origins of Galactic Stellar Streams. *arXiv e-prints*, art. arXiv:2012.09171, December 2020a.

Bonaca A., Pearson S., Price-Whelan A. M., et al. Variations in the Width, Density, and Direction of the Palomar 5 Tidal Tails. APJ, 889(1):70, January 2020b. doi: 10.3847/1538-4357/ab5afe.

Bovy J. Dynamical Modeling of Tidal Streams. APJ, 795:95, November 2014. doi: 10.1088/0004-637X/795/1/95.

Bovy J. and Rix H.-W. A Direct Dynamical Measurement of the Milky Way's Disk Surface Density Profile, Disk Scale Length, and Dark Matter Profile at 4 kpc ¡~R ¡~9 kpc. APJ, 779(2):115, December 2013. doi: 10.1088/0004-637X/ 779/2/115.

Bovy J., Bird J. C., García Pérez A. E., et al. The Power Spectrum of the Milky Way: Velocity Fluctuations in the Galactic Disk. APJ, 800(2):83, Feb 2015. doi: 10.1088/0004-637X/800/2/83.

Bovy J., Bahmanyar A., Fritz T. K., and Kallivayalil N. The Shape of the Inner Milky Way Halo from Observations of the Pal 5 and GD–1 Stellar Streams. APJ, 833(1):31, Dec 2016. doi: 10.3847/1538-4357/833/1/31.

Bowden A., Belokurov V., and Evans N. W. Dipping our toes in the water: first models of GD-1 as a stream. MNRAS, 449:1391–1400, May 2015. doi: 10.1093/mnras/stv285.

Bowden A., Evans N. W., and Williams A. A. Is the dark halo of the Milky Way prolate? MNRAS, 460(1):329–337, Jul 2016. doi: 10.1093/mnras/stw994.

Brown A. G. A., Velázquez H. M., and Aguilar L. A. Detection of satellite remnants in the Galactic Halo with Gaia- I. The effect of the Galactic background, observational errors and sampling. MNRAS, 359:1287–1305, June 2005. doi: 10.1111/j.1365-2966.2005.09013.x.

Bryan S. E., Kay S. T., Duffy A. R., et al. The impact of baryons on the spins and shapes of dark matter haloes. MNRAS, 429(4):3316–3329, March 2013. doi: 10.1093/mnras/sts587.

Bullock J. S., Kolatt T. S., Sigad Y., et al. Profiles of dark haloes: evolution, scatter and environment. MNRAS, 321(3):559–575, March 2001. doi: 10. 1046/j.1365-8711.2001.04068.x.

Buote D. A., Jeltema T. E., Canizares C. R., and Garmire G. P. Chandra Evidence of a Flattened, Triaxial Dark Matter Halo in the Elliptical Galaxy NGC 720. APJ, 577(1):183–196, September 2002. doi: 10.1086/342158.

Butsky I., Macciò A. V., Dutton A. A., et al. NIHAO project II: halo shape, phase-space density and velocity distribution of dark matter in galaxy formation simulations. MNRAS, 462(1):663–680, October 2016. doi: 10.1093/mnras/stw1688.

Callingham T. M., Cautun M., Deason A. J., et al. The mass of the Milky Way from satellite dynamics. MNRAS, 484(4):5453–5467, April 2019. doi: 10.1093/mnras/stz365.

Capitanio L., Lallement R., Vergely J. L., et al. Three-dimensional mapping of the local interstellar medium with composite data. A&A, 606:A65, October 2017. doi: 10.1051/0004-6361/201730831.

Carballo-Bello J. A., Martínez-Delgado D., Navarrete C., et al. Tails and streams around the Galactic globular clusters NGC 1851, NGC 1904, NGC 2298 and NGC 2808. MNRAS, 474(1):683–695, Feb 2018. doi: 10.1093/ mnras/stx2767.

Carlberg R. G. Star Stream Folding by Dark Galactic Subhalos. ApJL, 705: L223–L226, November 2009. doi: 10.1088/0004-637X/705/2/L223.

Carlberg R. G., Grillmair C. J., and Hetherington N. The Pal 5 Star Stream Gaps. APJ, 760(1):75, Nov 2012. doi: 10.1088/0004-637X/760/1/75.

Carrasco J. M., Jordi C., and Masana E. Stellar astrophysical parameters combining JPLUS and {Gaia} surveys. In *Highlights on Spanish Astrophysics X*, pages 548–553, Mar 2019.

Casella G. and Berger R. *Statistical Inference.* Duxbury advanced series in statistics and decision sciences. Thomson Learning, 2002. ISBN 9780534243128.

Cautun M., Benítez-Llambay A., Deason A. J., et al. The milky way total mass profile as inferred from Gaia DR2. MNRAS, 494(3):4291–4313, May 2020. doi: 10.1093/mnras/staa1017.

Chen C. W. and Chen W. P. Morphological Distortion of Galactic Globular Clusters. APJ, 721(2):1790–1819, Oct 2010. doi: 10.1088/0004-637X/721/2/1790.

Chua K. T. E., Pillepich A., Vogelsberger M., and Hernquist L. Shape of dark matter haloes in the Illustris simulation: effects of baryons. MNRAS, 484 (1):476–493, Mar 2019. doi: 10.1093/mnras/sty3531.

Clarke J. P., Wegg C., Gerhard O., et al. The Milky Way bar/bulge in proper motions: a 3D view from VIRAC and Gaia. MNRAS, 489(3):3519–3538, Nov 2019. doi: 10.1093/mnras/stz2382.

Conn A., Scheinberg K., and Vicente L. *Introduction to Derivative-free Optimization*. SIAM, 2009. ISBN 9780898718768.

Dai B., Robertson B. E., and Madau P. Around the Way: Testing ΛCDM with Milky Way Stellar Stream Constraints. APJ, 858(2):73, May 2018. doi: 10.3847/1538-4357/aabb06.

de Blok W. J. G. The Core-Cusp Problem. *Advances in Astronomy*, 2010: 789293, Jan 2010. doi: 10.1155/2010/789293.

De Martino I., Broadhurst T., Henry Tye S. H., et al. Dynamical evidence of a dark solitonic core of $10^9 M_\odot$ in the milky way. *Physics of the Dark Universe*, 28:100503, May 2020. doi: 10.1016/j.dark.2020.100503.

de Salas P. F. Dark matter local density determination based on recent observations. In *Journal of Physics Conference Series*, volume 1468 of *Journal of Physics Conference Series*, page 012020, February 2020. doi: 10.1088/1742-6596/1468/1/012020.

Debattista V. P., Roškar R., Valluri M., et al. What's up in the Milky Way? The orientation of the disc relative to the triaxial halo. MNRAS, 434(4): 2971–2981, Oct 2013. doi: 10.1093/mnras/stt1217.

DeBuhr J., Ma C.-P., and White S. D. M. Stellar discs in Aquarius dark matter haloes. MNRAS, 426(2):983–999, October 2012. doi: 10.1111/j.1365-2966. 2012.21910.x.

Deg N. and Widrow L. The Sagittarius stream and halo triaxiality. MNRAS, 428(1):912–922, Jan 2013. doi: 10.1093/mnras/sts089.

Dey A., Schlegel D. J., Lang D., et al. Overview of the DESI Legacy Imaging Surveys. AJ, 157(5):168, May 2019. doi: 10.3847/1538-3881/ab089d.

Eilers A.-C., Hogg D. W., Rix H.-W., and Ness M. K. The Circular Velocity Curve of the Milky Way from 5 to 25 kpc. APJ, 871(1):120, Jan 2019. doi: 10.3847/1538-4357/aaf648.

Eilers A.-C., Hogg D. W., Rix H.-W., et al. The Strength of the Dynamical Spiral Perturbation in the Galactic Disk. APJ, 900(2):186, September 2020. doi: 10.3847/1538-4357/abac0b.

Erkal D., Belokurov V., Laporte C. F. P., et al. The total mass of the Large Magellanic Cloud from its perturbation on the Orphan stream. MNRAS, 487 (2):2685–2700, Aug 2019. doi: 10.1093/mnras/stz1371.

Famaey B. and McGaugh S. S. Modified Newtonian Dynamics (MOND): Observational Phenomenology and Relativistic Extensions. *Living Reviews in Relativity*, 15(1):10, September 2012. doi: 10.12942/lrr-2012-10.

Fardal M. A., Huang S., and Weinberg M. D. Generation of mock tidal streams. MNRAS, 452:301–319, September 2015. doi: 10.1093/mnras/stv1198.

Fardal M. A., van der Marel R. P., Law D. R., et al. Connecting the Milky Way potential profile to the orbital time-scales and spatial structure of the Sagittarius Stream. MNRAS, 483(4):4724–4741, March 2019. doi: 10.1093/ mnras/sty3428.

Fellhauer M., Belokurov V., Evans N. W., et al. The Origin of the Bifurcation in the Sagittarius Stream. APJ, 651(1):167–173, Nov 2006. doi: 10.1086/ 507128.

Feng J. L. Dark Matter Candidates from Particle Physics and Methods of Detection. ARA&A, 48:495–545, September 2010. doi: 10.1146/ annurev-astro-082708-101659.

Gaia Collaboration . The Gaia mission. A&A, 595:A1, November 2016. doi: 10.1051/0004-6361/201629272.

Gaia Collaboration , Prusti T., de Bruijne J. H. J., et al. The Gaia mission. A&A, 595:A1, November 2016. doi: 10.1051/0004-6361/201629272.

Gaia Collaboration , Brown A. G. A., Vallenari A., et al. Gaia Data Release 2. Summary of the contents and survey properties. A&A, 616:A1, Aug 2018a. doi: 10.1051/0004-6361/201833051.

Gaia Collaboration , Brown A. G. A., Vallenari A., et al. Gaia Data Release 2. Summary of the contents and survey properties. A&A, 616:A1, August 2018b. doi: 10.1051/0004-6361/201833051.

Gaia Collaboration , Helmi A., van Leeuwen F., et al. Gaia Data Release 2. Kinematics of globular clusters and dwarf galaxies around the Milky Way. A&A, 616:A12, Aug 2018c. doi: 10.1051/0004-6361/201832698.

Gaia Collaboration , Brown A. G. A., Vallenari A., et al. Gaia Early Data Release 3: Summary of the contents and survey properties. *arXiv e-prints*, art. arXiv:2012.01533, December 2020.

Gardner S., Hinkel A., and Yanny B. Applying Noether's Theorem to Matter in the Milky Way: Evidence for External Perturbations and Non-steady-state Effects from Gaia Data Release 2. APJ, 890(2):110, February 2020. doi: 10.3847/1538-4357/ab66c8.

Gibbons S. L. J., Belokurov V., and Evans N. W. 'Skinny Milky Way please', says Sagittarius. MNRAS, 445:3788–3802, December 2014. doi: 10.1093/mnras/stu1986.

Gravity Collaboration , Abuter R., Amorim A., et al. A geometric distance measurement to the Galactic center black hole with 0.3% uncertainty. A&A, 625:L10, May 2019. doi: 10.1051/0004-6361/201935656.

Grillmair C. J. Detection of a 60°-long Dwarf Galaxy Debris Stream. ApJL, 645(1):L37–L40, July 2006. doi: 10.1086/505863.

Grillmair C. J. and Dionatos O. Detection of a 63° Cold Stellar Stream in the Sloan Digital Sky Survey. ApJL, 643(1):L17–L20, May 2006. doi: 10.1086/505111.

Grillmair C. J. and Johnson R. The Detection of a 45° Tidal Stream Associated with the Globular Cluster NGC 5466. ApJL, 639(1):L17–L20, Mar 2006. doi: 10.1086/501439.

Grillmair C. J. Detection of a 50° long Trailing Tidal Tail for the Globular Cluster M5. APJ, 884(2):174, Oct 2019. doi: 10.3847/1538-4357/ab441d.

Grillmair C. J. and Carlin J. L. Stellar Streams and Clouds in the Galactic Halo. In Newberg H. J. and Carlin J. L., editors, *Tidal Streams in the Local Group and Beyond*, volume 420 of *Astrophysics and Space Science Library*, page 87, Jan 2016. doi: 10.1007/978-3-319-19336-6_4.

Hansen T. T., Riley A. H., Strigari L. E., et al. A Chemo-dynamical Link between the Gjöll Stream and NGC 3201. APJ, 901(1):23, September 2020. doi: 10.3847/1538-4357/ababa5.

Harris W. E. A Catalog of Parameters for Globular Clusters in the Milky Way. AJ, 112:1487, October 1996. doi: 10.1086/118116.

Harris W. E. A New Catalog of Globular Clusters in the Milky Way. *arXiv e-prints*, art. arXiv:1012.3224, Dec 2010.

Hattori K. and Valluri M. The shape of the dark matter halo revealed from a hypervelocity star. In Valluri M. and Sellwood J. A., editors, *Galactic Dynamics in the Era of Large Surveys*, volume 353, pages 96–100, January 2020. doi: 10.1017/S1743921319008718.

Hattori K., Valluri M., and Vasiliev E. Action-based distribution function modelling for constraining the shape of the Galactic dark matter halo. *arXiv e-prints*, art. arXiv:2012.03908, December 2020.

Helmi A. Velocity Trends in the Debris of Sagittarius and the Shape of the Dark Matter Halo of Our Galaxy. ApJL, 610(2):L97–L100, Aug 2004. doi: 10.1086/423340.

Holmberg J. and Flynn C. The local surface density of disc matter mapped by Hipparcos. MNRAS, 352(2):440–446, Aug 2004. doi: 10.1111/j.1365-2966. 2004.07931.x.

Huang Y., Liu X. W., Yuan H. B., et al. The Milky Way's rotation curve out to 100 kpc and its constraint on the Galactic mass distribution. MNRAS, 463(3):2623–2639, Dec 2016. doi: 10.1093/mnras/stw2096.

Ibata R., Lewis G. F., Martin N. F., et al. Does the Sagittarius Stream Constrain the Milky Way Halo to be Triaxial? ApJL, 765(1):L15, Mar 2013. doi: 10.1088/2041-8205/765/1/L15.

Ibata R. A., Malhan K., Martin N. F., and Starkenburg E. Phlegethon, a Nearby 75°-long Retrograde Stellar Stream. APJ, 865:85, October 2018. doi: 10.3847/1538-4357/aadba3.

Ibata R., Thomas G., Famaey B., et al. Detection of Strong Epicyclic Density Spikes in the GD-1 Stellar Stream: An Absence of Evidence for the Influence of Dark Matter Subhalos? APJ, 891(2):161, March 2020. doi: 10.3847/ 1538-4357/ab7303.

Ibata R. A., Lewis G. F., and Martin N. F. Feeling the Pull: a Study of Natural Galactic Accelerometers. I. Photometry of the Delicate Stellar Stream of the Palomar 5 Globular Cluster. APJ, 819(1):1, Mar 2016. doi: 10.3847/ 0004-637X/819/1/1.

Ibata R. A., Lewis G. F., Thomas G., et al. Feeling the Pull: A Study of Natural Galactic Accelerometers. II. Kinematics and Mass of the Delicate Stellar Stream of the Palomar 5 Globular Cluster. APJ, 842(2):120, June 2017. doi: 10.3847/1538-4357/aa7514.

Ibata R. A., Bellazzini M., Malhan K., et al. Identification of the long stellar stream of the prototypical massive globular cluster ω Centauri. Nature Astronomy, 3:667–672, Apr 2019a. doi: 10.1038/s41550-019-0751-x.

Ibata R. A., Malhan K., and Martin N. F. The Streams of the Gaping Abyss: A Population of Entangled Stellar Streams Surrounding the Inner Galaxy. APJ, 872(2):152, Feb 2019b. doi: 10.3847/1538-4357/ab0080.

Johnston K. V., Law D. R., and Majewski S. R. A Two Micron All Sky Survey View of the Sagittarius Dwarf Galaxy. III. Constraints on the Flattening of the Galactic Halo. APJ, 619(2):800–806, Feb 2005. doi: 10.1086/426777.

Jordi C., Gebran M., Carrasco J. M., et al. Gaia broad band photometry. A&A, 523:A48, November 2010a. doi: 10.1051/0004-6361/201015441.

Jordi C., Gebran M., Carrasco J. M., et al. Gaia broad band photometry. A&A, 523:A48, Nov 2010b. doi: 10.1051/0004-6361/201015441.

Jurić M., Ivezić Ž., Brooks A., et al. The Milky Way Tomography with SDSS. I. Stellar Number Density Distribution. APJ, 673(2):864–914, Feb 2008. doi: 10.1086/523619.

Just A. and Jahreiß H. Towards a fully consistent Milky Way disc model - I. The local model based on kinematic and photometric data. MNRAS, 402(1): 461–478, Feb 2010. doi: 10.1111/j.1365-2966.2009.15893.x.

Kafle P. R., Sharma S., Lewis G. F., and Bland -Hawthorn J. Kinematics of the Stellar Halo and the Mass Distribution of the Milky Way Using Blue Horizontal Branch Stars. APJ, 761(2):98, Dec 2012. doi: 10.1088/0004-637X/ 761/2/98.

Koposov S. E., Rix H.-W., and Hogg D. W. Constraining the Milky Way Potential with a Six-Dimensional Phase-Space Map of the GD-1 Stellar Stream. APJ, 712:260–273, March 2010. doi: 10.1088/0004-637X/712/1/260.

Kot D., Kissinger G., Schubert M., and Sattler A. Current stage of the investigation of the composition of oxygen precipitates in czochralski silicon wafers. ECS Journal of Solid State Science and Technology, 6:N17–N24, 01 2017. doi: 10.1149/2.0081704jss.

Kuijken K. and Gilmore G. The Galactic Disk Surface Mass Density and the Galactic Force K Z at Z = 1.1 Kiloparsecs. ApJL, 367:L9, Jan 1991. doi: 10.1086/185920.

Kunder A., Bono G., Piffl T., et al. Spectroscopic signatures of extratidal stars around the globular clusters NGC 6656 (M 22), NGC 3201, and NGC 1851 from RAVE. A&A, 572:A30, Dec 2014. doi: 10.1051/0004-6361/201424113.

Kunder A., Kordopatis G., Steinmetz M., et al. The Radial Velocity Experiment (RAVE): Fifth Data Release. AJ, 153:75, February 2017. doi: 10.3847/ 1538-3881/153/2/75.

Kundu R., Minniti D., and Singh H. P. Search for extra-tidal RR Lyrae stars in Milky Way globular clusters from Gaia DR2. MNRAS, 483(2):1737–1743, Feb 2019. doi: 10.1093/mnras/sty3239.

Küpper A. H. W., Balbinot E., Bonaca A., et al. Globular Cluster Streams as Galactic High-Precision Scales-the Poster Child Palomar 5. APJ, 803:80, April 2015. doi: 10.1088/0004-637X/803/2/80.

Küpper A. H. W., MacLeod A., and Heggie D. C. On the structure of tidal tails. MNRAS, 387(3):1248–1252, July 2008. doi: 10.1111/j.1365-2966.2008. 13323.x.

Küpper A. H. W., Kroupa P., Baumgardt H., and Heggie D. C. Tidal tails of star clusters. MNRAS, 401(1):105–120, January 2010. doi: 10.1111/j. 1365-2966.2009.15690.x.

Küpper A. H. W., Lane R. R., and Heggie D. C. More on the structure of tidal tails. MNRAS, 420(3):2700–2714, March 2012. doi: 10.1111/j.1365-2966. 2011.20242.x.

Kuzma P. B., Da Costa G. S., Keller S. C., and Maunder E. Palomar 5 and its tidal tails: a search for new members in the tidal stream. MNRAS, 446(4): 3297–3309, Feb 2015. doi: 10.1093/mnras/stu2343.

Lallement R., Capitanio L., Ruiz-Dern L., et al. Three-dimensional maps of interstellar dust in the Local Arm: using Gaia, 2MASS, and APOGEE-DR14. A&A, 616:A132, September 2018. doi: 10.1051/0004-6361/201832832.

Lane R. R., Küpper A. H. W., and Heggie D. C. The tidal tails of 47 Tucanae. MNRAS, 423:2845–2853, July 2012. doi: 10.1111/j.1365-2966.2012.21093.x.

Lane R. R., Kiss L. L., Lewis G. F., et al. Halo globular clusters observed with AAOmega: dark matter content, metallicity and tidal heating. MNRAS, 406 (4):2732–2742, Aug 2010. doi: 10.1111/j.1365-2966.2010.16874.x.

Law D. R. and Majewski S. R. The Sagittarius Dwarf Galaxy: A Model for Evolution in a Triaxial Milky Way Halo. APJ, 714(1):229–254, May 2010. doi: 10.1088/0004-637X/714/1/229.

Law D. R., Majewski S. R., and Johnston K. V. Evidence for a Triaxial Milky Way Dark Matter Halo from the Sagittarius Stellar Tidal Stream. ApJL, 703 (1):L67–L71, Sep 2009. doi: 10.1088/0004-637X/703/1/L67.

Lelli F., McGaugh S. S., and Schombert J. M. SPARC: Mass Models for 175 Disk Galaxies with Spitzer Photometry and Accurate Rotation Curves. AJ, 152(6):157, December 2016. doi: 10.3847/0004-6256/152/6/157.

Li P., Lelli F., McGaugh S., and Schombert J. A Comprehensive Catalog of Dark Matter Halo Models for SPARC Galaxies. ApJS, 247(1):31, March 2020. doi: 10.3847/1538-4365/ab700e.

Loebman S. R., Ivezić Ž., Quinn T. R., et al. Constraints on the Shape of the Milky Way Dark Matter Halo from Jeans Equations Applied to Sloan Digital Sky Survey Data. ApJL, 758(1):L23, Oct 2012. doi: 10.1088/2041-8205/758/ 1/L23.

Loebman S. R., Ivezić Ž., Quinn T. R., et al. The Milky Way Tomography with Sloan Digital Sky Survey. V. Mapping the Dark Matter Halo. APJ, 794 (2):151, Oct 2014. doi: 10.1088/0004-637X/794/2/151.

López-Corredoira M. Milky Way rotation curve from proper motions of red clump giants. A&A, 563:A128, Mar 2014. doi: 10.1051/0004-6361/ 201423505.

Luna A., Bronfman L., Carrasco L., and May J. Molecular Gas, Kinematics, and OB Star Formation in the Spiral Arms of the Southern Milky Way. APJ, 641(2):938–948, Apr 2006. doi: 10.1086/500163.

Luo A. L., Zhao Y.-H., Zhao G., et al. The first data release (DR1) of the LAMOST regular survey. *Research in Astronomy and Astrophysics*, 15(8): 1095, Aug 2015. doi: 10.1088/1674-4527/15/8/002.

Luri X., Palmer M., Arenou F., et al. Overview and stellar statistics of the expected Gaia Catalogue using the Gaia Object Generator. A&A, 566:A119, June 2014a. doi: 10.1051/0004-6361/201423636.

Luri X., Palmer M., Arenou F., et al. Overview and stellar statistics of the expected Gaia Catalogue using the Gaia Object Generator. A&A, 566:A119, June 2014b. doi: 10.1051/0004-6361/201423636.

Malhan K. and Ibata R. A. STREAMFINDER - I. A new algorithm for detecting stellar streams. MNRAS, 477:4063–4076, July 2018. doi: 10.1093/mnras/sty912.

Malhan K., Ibata R. A., and Martin N. F. Ghostly tributaries to the Milky Way: charting the halo's stellar streams with the Gaia DR2 catalogue. MNRAS, 481:3442–3455, December 2018a. doi: 10.1093/mnras/sty2474.

Malhan K. and Ibata R. A. Constraining the Milky Way halo potential with the GD-1 stellar stream. MNRAS, 486(3):2995–3005, Jul 2019. doi: 10.1093/mnras/stz1035.

Malhan K., Ibata R. A., Goldman B., et al. STREAMFINDER II: A possible fanning structure parallel to the GD-1 stream in Pan-STARRS1. MNRAS, 478(3):3862–3870, Aug 2018b. doi: 10.1093/mnras/sty1338.

Mateu C., Cooper A. P., Font A. S., et al. Predictions for the detection of tidal streams with Gaia using great-circle methods. MNRAS, 469:721–743, July 2017. doi: 10.1093/mnras/stx872.

Mateu C., Read J. I., and Kawata D. Fourteen candidate RR Lyrae star streams in the inner Galaxy. MNRAS, 474(3):4112–4129, March 2018. doi: 10.1093/mnras/stx2937.

McClure-Griffiths N. M. and Dickey J. M. Milky Way Kinematics. I. Measurements at the Subcentral Point of the Fourth Quadrant. APJ, 671(1):427–438, Dec 2007. doi: 10.1086/522297.

McClure-Griffiths N. M. and Dickey J. M. Milky Way Kinematics. II. A Uniform Inner Galaxy H I Terminal Velocity Curve. APJ, 831(2):124, Nov 2016. doi: 10.3847/0004-637X/831/2/124.

McConnachie A. W. The Observed Properties of Dwarf Galaxies in and around the Local Group. AJ, 144(1):4, July 2012. doi: 10.1088/0004-6256/144/1/4.

McMillan P. J. Mass models of the Milky Way. MNRAS, 414(3):2446–2457, Jul 2011. doi: 10.1111/j.1365-2966.2011.18564.x.

McMillan P. J. The mass distribution and gravitational potential of the Milky Way. MNRAS, 465(1):76–94, February 2017. doi: 10.1093/mnras/stw2759.

Moore B., Quinn T., Governato F., et al. Cold collapse and the core catastrophe. MNRAS, 310(4):1147–1152, Dec 1999. doi: 10.1046/j.1365-8711.1999.03039.x.

Mróz P., Udalski A., Skowron D. M., et al. Rotation Curve of the Milky Way from Classical Cepheids. ApJL, 870(1):L10, Jan 2019. doi: 10.3847/2041-8213/aaf73f.

Mukhanov V. *Physical Foundations of Cosmology*. Cambridge University Press, 2005. doi: 10.2277/0521563984.

Myeong G. C., Jerjen H., Mackey D., and Da Costa G. S. Tidal Tails around the Outer Halo Globular Clusters Eridanus and Palomar 15. ApJL, 840(2): L25, May 2017. doi: 10.3847/2041-8213/aa6fb4.

Navarro J. F., Frenk C. S., and White S. D. M. The Structure of Cold Dark Matter Halos. APJ, 462:563, May 1996. doi: 10.1086/177173.

Nitschai M. S., Cappellari M., and Neumayer N. First Gaia dynamical model of the Milky Way disc with six phase space coordinates: a test for galaxy dynamics. MNRAS, 494(4):6001–6011, April 2020. doi: 10.1093/mnras/staa1128.

Odenkirchen M., Grebel E. K., Rockosi C. M., et al. Detection of Massive Tidal Tails around the Globular Cluster Palomar 5 with Sloan Digital Sky Survey Commissioning Data. ApJL, 548(2):L165–L169, Feb 2001. doi: 10.1086/319095.

Patel E., Kallivayalil N., Garavito-Camargo N., et al. The Orbital Histories of Magellanic Satellites Using Gaia DR2 Proper Motions. APJ, 893(2):121, April 2020. doi: 10.3847/1538-4357/ab7b75.

Pearson S., Küpper A. H. W., Johnston K. V., and Price-Whelan A. M. Tidal Stream Morphology as an Indicator of Dark Matter Halo Geometry: The Case of Palomar 5. APJ, 799(1):28, January 2015. doi: 10.1088/0004-637X/799/1/28.

Piatti A. E. and Carballo-Bello J. A. The tidal tails of Milky Way globular clusters. A&A, 637:L2, May 2020. doi: 10.1051/0004-6361/202037994.

Piffl T., Binney J., McMillan P. J., et al. Constraining the Galaxy's dark halo with RAVE stars. MNRAS, 445(3):3133–3151, Dec 2014. doi: 10.1093/mnras/stu1948.

Portail M., Wegg C., Gerhard O., and Martinez-Valpuesta I. Made-to-measure models of the Galactic box/peanut bulge: stellar and total mass in the bulge region. MNRAS, 448(1):713–731, Mar 2015. doi: 10.1093/mnras/stv058.

Posti L. and Helmi A. Mass and shape of the Milky Way's dark matter halo with globular clusters from Gaia and Hubble. A&A, 621:A56, Jan 2019. doi: 10.1051/0004-6361/201833355.

Prada J., Forero-Romero J. E., Grand R. J. J., et al. Dark matter halo shapes in the Auriga simulations. MNRAS, 490(4):4877–4888, Dec 2019. doi: 10.1093/mnras/stz2873.

Price-Whelan A. M. and Bonaca A. Off the Beaten Path: Gaia Reveals GD-1 Stars outside of the Main Stream. ApJL, 863(2):L20, August 2018. doi: 10.3847/2041-8213/aad7b5.

Price-Whelan A. M., Hogg D. W., Johnston K. V., and Hendel D. Inferring the Gravitational Potential of the Milky Way with a Few Precisely Measured Stars. APJ, 794(1):4, October 2014. doi: 10.1088/0004-637X/794/1/4.

Price-Whelan A. M., Mateu C., Iorio G., et al. Kinematics of the Palomar 5 Stellar Stream from RR Lyrae Stars. AJ, 158(6):223, Dec 2019. doi: 10.3847/1538-3881/ab4cef.

Rees M. *New Perspectives in Astrophysical Cosmology*. Cambridge University Press, 2000.

Reid M. J. and Brunthaler A. The Proper Motion of Sagittarius A*. II. The Mass of Sagittarius A*. APJ, 616(2):872–884, Dec 2004. doi: 10.1086/424960.

Reid M. J., Menten K. M., Brunthaler A., et al. Trigonometric Parallaxes of High-mass Star-forming Regions: Our View of the Milky Way. APJ, 885(2): 131, Nov 2019. doi: 10.3847/1538-4357/ab4a11.

Renaud F., Gieles M., and Boily C. M. Evolution of star clusters in arbitrary tidal fields. MNRAS, 418:759–769, December 2011. doi: 10.1111/j.1365-2966.2011.19531.x.

Robin A. C., Reylé C., Derrière S., and Picaud S. A synthetic view on structure and evolution of the Milky Way. A&A, 409:523–540, October 2003. doi: 10.1051/0004-6361:20031117.

Robin A. C., Luri X., Reylé C., et al. Gaia Universe model snapshot. A statistical analysis of the expected contents of the Gaia catalogue. A&A, 543: A100, July 2012. doi: 10.1051/0004-6361/201118646.

Robin A. C., Reylé C., Fliri J., et al. Constraining the thick disc formation scenario of the Milky Way. A&A, 569:A13, September 2014. doi: 10.1051/0004-6361/201423415.

Rubin V. C., Ford J., W. K., and Thonnard N. Extended rotation curves of high-luminosity spiral galaxies. IV. Systematic dynamical properties, Sa - Sc. ApJL, 225:L107–L111, November 1978. doi: 10.1086/182804.

Sanderson R. E., Helmi A., and Hogg D. W. Action-space Clustering of Tidal Streams to Infer the Galactic Potential. APJ, 801:98, March 2015. doi: 10.1088/0004-637X/801/2/98.

Schlafly E. F. and Finkbeiner D. P. Measuring Reddening with Sloan Digital Sky Survey Stellar Spectra and Recalibrating SFD. APJ, 737(2):103, Aug 2011. doi: 10.1088/0004-637X/737/2/103.

Schlegel D. J., Finkbeiner D. P., and Davis M. Maps of Dust Infrared Emission for Use in Estimation of Reddening and Cosmic Microwave Background Radiation Foregrounds. APJ, 500(2):525–553, Jun 1998. doi: 10.1086/305772.

Schönrich R., Binney J., and Dehnen W. Local kinematics and the local standard of rest. MNRAS, 403(4):1829–1833, Apr 2010. doi: 10.1111/j.1365-2966.2010.16253.x.

Shao S., Cautun M., Frenk C. S., et al. Alignments between galaxies, satellite systems and haloes. MNRAS, 460(4):3772–3783, August 2016. doi: 10.1093/mnras/stw1247.

Shipp N., Drlica-Wagner A., Balbinot E., et al. Stellar Streams Discovered in the Dark Energy Survey. APJ, 862(2):114, August 2018. doi: 10.3847/1538-4357/aacdab.

Shipp N., Price-Whelan A. M., Tavangar K., et al. Discovery of Extended Tidal Tails around the Globular Cluster Palomar 13. AJ, 160(5):244, November 2020. doi: 10.3847/1538-3881/abbd3a.

Sollima A. and Baumgardt H. The global mass functions of 35 Galactic globular clusters: I. Observational data and correlations with cluster parameters. MNRAS, 471(3):3668–3679, Nov 2017. doi: 10.1093/mnras/stx1856.

Springel V., Wang J., Vogelsberger M., et al. The Aquarius Project: the subhaloes of galactic haloes. MNRAS, 391(4):1685–1711, December 2008. doi: 10.1111/j.1365-2966.2008.14066.x.

Springel V., White S. D. M., Jenkins A., et al. Simulations of the formation, evolution and clustering of galaxies and quasars. Nature, 435(7042):629–636, June 2005. doi: 10.1038/nature03597.

Springel V., Frenk C. S., and White S. D. M. The large-scale structure of the Universe. Nature, 440(7088):1137–1144, April 2006. doi: 10.1038/nature04805.

Starkman N., Bovy J., and Webb J. J. An extended Pal 5 stream in Gaia DR2. MNRAS, 493(4):4978–4986, April 2020. doi: 10.1093/mnras/staa534.

Tenneti A., Mandelbaum R., and Di Matteo T. Intrinsic alignments of disc and elliptical galaxies in the MassiveBlack-II and Illustris simulations. MNRAS, 462(3):2668–2680, November 2016. doi: 10.1093/mnras/stw1823.

Tomassetti M., Dekel A., Mandelker N., et al. Evolution of galaxy shapes from prolate to oblate through compaction events. MNRAS, 458(4):4477–4497, June 2016. doi: 10.1093/mnras/stw606.

Umetsu K. Cluster-galaxy weak lensing. AApR, 28(1):7, December 2020. doi: 10.1007/s00159-020-00129-w.

van den Bergh S. *The Galaxies of the Local Group*. Cambridge Astrophysics, 2000.

Varghese A., Ibata R., and Lewis G. F. Stellar streams as probes of dark halo mass and morphology: a Bayesian reconstruction. MNRAS, 417(1):198–215, October 2011. doi: 10.1111/j.1365-2966.2011.19097.x.

Vasiliev E. AGAMA: action-based galaxy modelling architecture. MNRAS, 482(2):1525–1544, January 2019a. doi: 10.1093/mnras/sty2672.

Vasiliev E. Proper motions and dynamics of the Milky Way globular cluster system from Gaia DR2. MNRAS, 484(2):2832–2850, Apr 2019b. doi: 10.1093/mnras/stz171.

Velliscig M., Cacciato M., Schaye J., et al. The alignment and shape of dark matter, stellar, and hot gas distributions in the EAGLE and cosmo-OWLS simulations. MNRAS, 453(1):721–738, October 2015. doi: 10.1093/mnras/stv1690.

Wang W., Han J., Cautun M., et al. The mass of our Milky Way. *Science China Physics, Mechanics, and Astronomy*, 63(10):109801, May 2020. doi: 10.1007/s11433-019-1541-6.

Webb J. J. and Bovy J. Searching for the GD-1 stream progenitor in Gaia DR2 with direct N-body simulations. MNRAS, 485(4):5929–5938, June 2019. doi: 10.1093/mnras/stz867.

Wegg C., Gerhard O., and Portail M. The structure of the Milky Way's bar outside the bulge. MNRAS, 450(4):4050–4069, Jul 2015. doi: 10.1093/mnras/stv745.

Wegg C., Gerhard O., and Bieth M. The gravitational force field of the Galaxy measured from the kinematics of RR Lyrae in Gaia. MNRAS, 485(3):3296–3316, May 2019. doi: 10.1093/mnras/stz572.

Zhang L., Rix H.-W., van de Ven G., et al. The Gravitational Potential near the Sun from SEGUE K-dwarf Kinematics. APJ, 772(2):108, Aug 2013. doi: 10.1088/0004-637X/772/2/108.

Zwicky F. On the Masses of Nebulae and of Clusters of Nebulae. APJ, 86:217, October 1937. doi: 10.1086/143864.

Appendix A

Chapter 2

A.1   Coordinate transformations

The phase-space coordinates of the stars are transformed to the Galactocentric Coordinate System using the solar position and velocity from Bland-Hawthorn and Gerhard (2016a). The position of the Sun, $x^i_\odot$, in the Galactocentric Coordinate System and Cartesian coordinates (x, y, z), is

$$x^i_\odot = \begin{pmatrix} 8.2 \pm 0.1 \\ 0 \\ 0.025 \pm 0.005 \end{pmatrix} \quad \text{(kpc)} . \tag{A.1}$$

The velocity of the Sun, with the components with respect to the LSR U, pointing to the Galactic Centre, V, positive along the direction of the Sun's rotation, and W, positive towards the North Galactic Pole, are:

$$v_\odot \equiv \begin{pmatrix} v_U \\ v_V \\ v_W \end{pmatrix} = \begin{pmatrix} 14 \\ 12.24 \\ 7.25 \end{pmatrix} \quad (\text{km s}^{-1}) . \tag{A.2}$$

The rotational velocity of the LSR along v is assumed to be

$$v_{\text{LSR}} = 238 \pm 15 \quad (\text{km s}^{-1}) . \tag{A.3}$$

A.2   Colour-Magnitude diagram of M68

We reproduce here the ADQL query we have used to obtain the GDR2 photometry in G, G_{BP}, and G_{RP} passbands in a circle centred on M68, giving 2929 stars:

```
1  SELECT bp_rp, phot_g_mean_mag, phot_bp_mean_flux,
       phot_bp_mean_flux_error, phot_rp_mean_flux,
       phot_rp_mean_flux_error, phot_g_mean_flux,
       phot_g_mean_flux_error
2  FROM gdr2.gaia_source
3  WHERE 1 = CONTAINS( POINT('ICRS', ra, dec), CIRCLE('ICRS'
       , 189.8651, -26.7454, 0.1) )
4  AND parallax <= 10.0
5  AND SQRT((pmra+2.78)*(pmra+2.78) + (pmdec-1.81)*(pmdec
       -1.81)) <= 1.78
6  AND bp_rp <= 2.0;
```

Host server: https://gaia.aip.de/
Description of the `gaia_source` table:
https://gea.esac.esa.int/archive/documentation/GDR2/Gaia_archive/
chap_datamodel/sec_dm_main_tables/ssec_dm_gaia_source.html

A.3   The Pre-selection

A.3.1   General method

Given a tidal stream progenitor, a set of M orbits with phase-space components $\eta_m^\mu(t)$ (where $m = 1, \ldots, M$) are computed over a time interval $-l < t < l$, from the present phase-space coordinates $\eta_m^\mu(0)$ and different values of the potential free parameters $\theta_{\phi m}$, following the distributions:

$$\eta_m^\mu(0) \sim G\big(\bar{\eta}^\mu, \varepsilon_\mu^2\big) \; , \tag{A.4}$$

$$\theta_{\phi m} \sim U\big(\bar{\theta}_\phi - \varepsilon_\phi, \bar{\theta}_\phi + \varepsilon_\phi\big) \; , \tag{A.5}$$

where G is a Gaussian distribution and $U(b, c)$ is a uniform distribution over $b < x < c$.

The bundle of M orbits defines a phase-space region with a probability density V of finding stars belonging to any orbit in the bundle. We smooth the distribution of the simulated orbits describing it as the sum of $N - 1$ Gaussian distributions, obtained from N points along each orbit uniformly distributed in time, labelled by the index $n = 0, \ldots, N$ with time intervals $\Delta t \equiv 2l/N$, and defining

$$\eta_{mn}^\mu \equiv \eta_m^\mu(-l + n\Delta t) \; . \tag{A.6}$$

The means and covariance matrices of the Gaussian distributions are computed as:

$$\bar{\eta}_n^\mu = \frac{1}{M} \sum_{m=1}^{M} \eta_{mn}^\mu \qquad\qquad 0 < n < N \; ; \tag{A.7}$$

$$\Xi_n^{\mu\nu} = \frac{1}{3M} \sum_{i=n-1}^{n+1} \sum_{m=1}^{M} (\eta_{mi}^\mu - \bar{\eta}_n^\mu)(\eta_{mi}^\nu - \bar{\eta}_n^\nu) \qquad 0 < n < N \; . \tag{A.8}$$

The distribution is given by

$$V(w^\mu) \equiv \frac{1}{N-1} \sum_{n=1}^{N-1} G\big(w^\mu - \bar{\eta}_n^\mu | \Xi_n^{\mu\nu}\big) \; . \tag{A.9}$$

The intersection of a star with observed phase-space coordinates w_o^μ and errors $\sigma^{\mu\nu}$ with the region V is now expressed as the convolution of the two Gaussian distributions,

$$P_{\mathrm{REG}} = \frac{1}{N-1} \sum_{n=1}^{N-1} G\big(w_o^\mu - \bar{\eta}_n^\mu | \sigma^{\mu\nu} + \Xi_n^{\mu\nu}\big) \; . \tag{A.10}$$

Table A.1: Pre-selection parameters used to compute the bundle of orbits for M68.

	π (mas)	δ (deg)	α (deg)	v_r (km s^{-1})	μ_δ (mas yr^{-1})	μ_α (mas yr^{-1})
$\bar{\eta}^\mu$	0.0971	-26.75	189.87	-94.7	1.7916	-3.0951
ε_μ	0.0023	2.5	2.5	0.2	0.0039	0.0056

	$\rho_{0\mathrm{dh}}$ (M$_\odot$ kpc^{-3})	$a_{1\mathrm{dh}}$ (kpc)	$a_{3\mathrm{dh}}$ (kpc)	β_{dh}
$\bar{\theta}_\phi$	8×10^6	20.2	16.16	3.1
ε_ϕ	1×10^6	4	4	0.2

Table A.2: Coordinates of the globular clusters that lie in the pre-selection region and radius of the angular circle.

Globular Cluster		δ (deg)	α (deg)	ξ (deg)
	NGC5466	28.5331	211.3614	0.08
M3	NGC5272	28.3760	205.5486	0.2
M53	NGC5024	18.1661	198.2262	0.2
	NGC5053	17.7008	199.1124	0.2
M68	NGC4590	-26.7454	189.8651	0.3

Note. Ref.: Gaia Collaboration et al. (2018c)

A.3.2   Pre-selection for M68

For the case of M68, the region V has been described with $N = 101$ Gaussian distributions computed using a bundle of $M = 100$ orbits of length $l = 50$ Myr. The parameters used to compute the bundle of orbits are listed in Table A.1. Stars obeying $P_{\mathrm{REG}} \geqslant 1.4893\times10^{-4}$ yr^3 deg^{-2} pc^{-1} mas^{-3} have been chosen for our pre-selection.

Table A.2 lists the globular clusters that lie inside the pre-selection region and the angular radius ξ of the circle within which stars are removed.

A.4   Colour-Magnitude Selection

A.4.1   Method

A colour-magnitude index of the progenitor cluster is first constructed from a sample of N_e stars with observed G_{BP}–G_{RP} colour index and a G-band absolute magnitude M'_G. Defining a position of the i star as $x_i^\mu \equiv (G_{\mathrm{BP}}-G_{\mathrm{RP}}, M'_G)$, the density is modelled using a Kernel Density Estimator with a Gaussian kernel,

and with covariance matrices

$$\Xi_i^{\mu\nu} \equiv \left(\sum_{j=1}^{N_e} c_{ij} \right)^{-1} \sum_{j=1}^{N_e} c_{ij} \left(x_j^\mu - x_i^\mu \right) \left(x_j^\nu - x_i^\nu \right) . \qquad (A.11)$$

Weights are defined using the constant $d_0 = 0.07$ mag,

$$c_{ij} \equiv \left(d_0 + d_{ij} \right)^5 , \qquad d_{ij}^2 \equiv \sum_{l=1}^{2} (x_j^l - x_i^l)^2 . \qquad (A.12)$$

Given the integrated G mean flux f_G, its observational error ε_{f_G} and assuming a symmetric error distribution and neglecting the uncertainty of the zero-point magnitude in the Vega scale, the error of the associated G-band magnitude is

$$\varepsilon_G = \frac{2.5}{\ln(10)} \frac{\varepsilon_{f_G}}{f_G} . \qquad (A.13)$$

The deviation of the colour index is computed as of equation (A.13) for both magnitudes and subtracting their errors

$$\varepsilon_{BP-RP} = \sqrt{\varepsilon_{BP}^2 - \varepsilon_{RP}^2} . \qquad (A.14)$$

In the case of GOG18, it is necessary to correct the discrepancy between the simulation and GDR2 catalogue. Defining the scale factor $\lambda_\mu \equiv (2, 1.6)$, the scaled errors are $\lambda_\mu \varepsilon_\mu$.

A star in magnitude-space is represented by a Gaussian distribution with mean observed position x_o^μ convolved with uncorrelated uncertainties, its co-variance matrix is

$$\sigma^{\mu\nu} \equiv \begin{cases} \varepsilon_\mu^2 & \mu = \nu \\ 0 & \mu \neq \nu \end{cases} .$$

Neglecting dust extinction, the intersection between a star and the density model is given by the convolution

$$P_{\text{CR}} = \frac{1}{N_e} \sum_{i=1}^{N_e} G\left(x_o^\mu - x_i^\mu | \sigma^{\mu\nu} + \Xi_i^{\mu\nu} \right) . \qquad (A.15)$$

A.4.2   Colour-Magnitude selection for M68

For M68, we use a sample of $N_e = 2929$ stars to construct the density model, using the selection described in Appendix A.2. Stars with $P_{\text{CR}} \geqslant 0.08$ mag^{-2} have been selected.

A.5   Selected Stars

The selected stars from GDR2 catalogue are listed in Table A.3.

Table A.3: Selected stars from GDR2 catalogue. They are compatible with a phase-space density model of the tidal stream of M68 and with its H-R diagram. GDR2 does not provide radial velocity for any of these stars.

N	source_id	π (mas)	δ (deg)	α (deg)	μ_δ (mas yr^{-1})	$\mu_{\alpha*}$ (mas yr^{-1})	$G_{BP}-G_{RP}$ (mag)	G (mag)	χ_{sel} (yr^3 deg^{-2} pc^{-1} mas^{-3})
1	3496364826490984832	0.0666	−26.9401	189.5268	1.7746	−2.7097	1.1689	14.0009	7.9446E+02
2	3496397262084464128	0.2211	−26.6147	190.1435	1.7706	−2.7786	0.9929	16.4954	3.8387E+01
3	6133483847268997632	0.1142	−44.0194	190.4956	1.0431	−2.0908	0.8980	17.6564	2.2383E+00
4	3496359908751562496	−0.1533	−27.0259	189.6791	1.5048	−2.5199	0.7139	18.5297	1.8531E+00
5	6129336321904932224	0.0825	−45.8545	191.0678	1.1946	−2.3981	0.9346	18.3756	1.6943E+00
6	3496403270742208768	−0.0047	−26.5809	190.1661	1.5555	−2.4028	0.6775	18.9026	1.6537E+00
7	3496413819180463616	0.2016	−26.8035	189.4730	1.3666	−2.5346	0.7607	18.3398	1.6298E+00
8	6128205985298801408	0.1692	−47.5466	191.4542	1.0899	−2.1682	0.9766	17.2226	1.5785E+00
9	6153341199065073536	0.1632	−38.9526	189.3009	1.4558	−2.7846	0.9022	16.9682	1.4216E+00
10	3496363825761763840	0.2272	−26.9772	189.5723	1.7695	−2.7182	0.6242	19.4263	9.9037E−01
11	3496426983257641216	0.2179	−26.5627	189.5454	1.6971	−2.5965	1.0683	15.4868	9.6922E−01
12	3496351250097506816	0.3829	−27.0117	190.0502	1.6874	−2.8738	0.9253	17.7917	9.5428E−01
13	3496465702385628928	−0.0691	−26.3824	189.6310	1.5405	−2.5617	0.9822	17.0284	9.2144E−01
14	3496383857489983232	0.4248	−26.6971	190.2375	1.6487	−2.7174	0.6725	18.9987	8.5381E−01
15	3496417912286695936	0.2415	−26.7512	189.3964	1.2602	−2.3346	0.9350	17.7570	7.2085E−01
16	3496385266239278976	−0.2349	−26.6352	190.1922	1.5076	−2.2656	0.6959	19.0733	6.7434E−01
17	3692120708467214208	0.0521	+2.0591	194.8744	3.2952	−2.4461	0.8598	16.7081	5.9697E−01
18	3496354101955858432	−0.0606	−26.9265	190.1141	0.9713	−2.3555	0.6465	18.9647	5.5831E−01
19	1606236095606481280	0.1245	+54.2566	223.1041	5.1230	1.2085	0.5928	17.4589	2.5816E−01
20	1458389959637031296	0.1198	+33.0455	206.2680	5.4940	−0.7652	0.5769	17.4817	1.9672E−01
21	3677284104720388224	−0.0056	−6.5245	193.5543	2.6362	−2.3346	0.6176	17.7979	1.5302E−01
22	3730942295084892928	−0.0484	+8.7147	197.5589	3.9250	−2.5897	0.6311	18.0954	1.2550E−01
23	1455844345403174016	0.2761	+29.3251	204.2349	5.3560	−1.2723	0.6308	18.3614	1.1934E−01
24	3691856546503440128	0.1471	+1.7067	195.5511	3.4746	−2.1421	0.6608	18.8550	1.1440E−01
25	3675964587688060416	0.1004	−6.6935	192.9816	2.7575	−2.4202	0.6885	18.3793	1.1291E−01
26	1456842495802767744	0.1670	+32.3278	205.7151	5.3068	−0.7095	0.5872	17.3960	1.0621E−01
27	3678259474613592960	0.3630	−4.1679	195.2089	3.1499	−2.9547	0.8179	17.1344	1.0476E−01
28	3729366935440429952	0.2786	+6.2290	195.7788	3.5696	−2.4608	0.6158	17.9548	1.0185E−01
29	3678958794072858112	0.4306	−4.2433	193.8940	3.0850	−2.5129	0.6187	17.7100	9.4803E−02
30	3938507382917888512	0.2424	+17.7672	199.7684	4.2657	−1.4890	0.6077	17.5658	7.7959E−02
31	3730306639925232384	0.1831	+7.2101	196.3747	3.9700	−2.0812	0.6286	18.4781	7.5430E−02
32	3736013929907004928	0.1335	+11.2735	197.5279	4.4459	−2.2741	0.6227	18.8557	6.9948E−02
33	1504696231140527232	0.4210	+43.8973	212.8308	5.5413	−0.1608	0.6686	18.3991	6.9580E−02
34	3686001101624868352	0.1303	−1.1354	195.9989	3.2547	−2.3681	0.6370	17.5221	6.0207E−02
35	1605773136787896320	0.0124	+52.9402	221.9906	5.0068	1.4966	0.6926	18.9247	4.8143E−02
36	3731064894927486976	0.1237	+8.6340	196.1463	4.2136	−3.0731	0.5780	18.0480	4.5961E−02
37	1455852248142764288	0.1545	+29.4651	204.2691	5.1368	−0.8114	0.6936	18.4129	4.5207E−02
38	3677590211334628992	−0.1124	−5.6794	193.4493	2.8830	−2.1745	0.6168	18.0113	4.4703E−02
39	3677713562794613504	0.4733	−5.2572	193.5804	2.8342	−2.1752	0.7574	19.3068	4.3766E−02
40	1600425932567734784	0.1829	+55.3254	226.6320	4.7296	1.8281	0.7136	18.7518	4.2661E−02
41	1603928701735870336	0.1355	+50.4873	219.6809	4.9731	0.6445	0.6951	18.5037	4.2338E−02
42	3736784721917729152	0.2377	+12.7628	198.6407	3.8432	−1.5178	0.6232	18.2278	4.0618E−02
43	3939089398230332928	0.0781	+19.1721	200.8586	4.4500	−1.3995	0.6745	18.6470	4.0158E−02
44	1634945752956687104	0.1780	+64.8292	251.4316	3.1381	3.8373	0.8572	16.9145	3.8506E−02
45	1505103084803276160	0.2284	+44.9951	213.9660	5.4822	0.4941	0.7598	19.2384	3.5483E−02
46	3736463664522214656	0.0303	+11.7794	198.7358	4.2984	−1.6778	0.6700	18.6768	3.4229E−02
47	1506844779940816384	0.2853	+46.7914	214.8890	5.2314	0.5913	0.6458	18.2705	3.4038E−02
48	3729915076346434304	0.4170	+7.1123	197.1414	3.5768	−2.1621	0.7025	18.5110	3.3254E−02
49	3678969243729036032	0.2682	−4.1958	193.5954	3.3351	−2.5662	0.9471	16.8203	3.2393E−02
50	3690547165593837312	0.1666	+1.4787	193.0467	3.3546	−2.8934	0.6077	17.5944	3.1051E−02
51	1496589879802806528	0.1163	+39.0498	207.1911	5.9647	−0.7894	0.6743	16.7684	3.0905E−02
52	1496266863902585728	0.2228	+39.5427	209.3919	5.2231	−0.2448	0.5933	18.2511	2.9648E−02
53	1496030911283208576	0.1392	+39.1041	210.2471	5.4324	−0.0120	0.6456	18.4847	2.8611E−02
54	1498889611451314816	−0.0300	+41.4624	209.2182	5.9579	−0.4318	0.6810	18.5142	2.7590E−02
55	1604273437287099776	−0.0990	+51.4980	219.8012	5.3673	1.3525	0.8035	19.4194	2.7511E−02
56	3678292459962501376	0.3620	−3.8740	195.7269	3.2026	−2.6585	0.8230	17.6250	2.6342E−02
57	3685425060611225472	0.4647	−2.5588	194.5278	3.5328	−2.2110	0.6830	19.2702	2.6098E−02

Table A.3: - *continued.*

N	source_id	π (mas)	δ (deg)	α (deg)	μ_δ (mas yr^{-1})	$\mu_{\alpha*}$ (mas yr^{-1})	$G_{BP}-G_{RP}$ (mag)	G (mag)	χ_{sel} (yr^3 deg^{-2} pc^{-1} mas^{-3})
58	3731172780210011264	0.0096	+8.9611	196.7009	3.6435	−2.8289	0.6399	19.2347	2.5511E−02
59	3678889254257425664	0.1613	−4.5256	194.3135	3.6767	−2.3650	0.6577	18.3852	2.4068E−02
60	1605598138344043904	0.1489	+52.1831	221.9488	4.8273	1.6527	0.8305	19.4252	2.3852E−02
61	3690382170130121984	0.1339	+1.3929	194.3795	3.2183	−2.9074	0.6628	19.0984	2.2914E−02
62	1456411624683879296	0.1173	+30.7712	205.5668	4.9705	−0.8631	0.6354	18.8292	2.2258E−02
63	1442304443823114752	0.4577	+21.0880	201.0665	5.2465	−1.7063	0.7897	19.1160	2.1508E−02
64	3744325138301094784	0.1423	+15.3030	200.4737	4.3564	−1.8696	0.8476	19.0354	2.0853E−02
65	3688452737676950400	0.3545	−2.2653	194.0000	3.0246	−2.2345	0.7619	16.7977	2.0055E−02
66	1603533873982622592	0.2436	+49.9313	219.0180	5.1240	0.7174	0.8574	19.8819	1.9860E−02
67	3702709520838936064	0.2749	+2.3905	194.0326	3.2250	−2.2645	0.5742	18.0258	1.9167E−02
68	3940514399659927296	0.0898	+20.9339	199.6473	4.4686	−1.9810	0.6312	18.0733	1.9045E−02
69	1606249122242914688	0.2103	+53.9305	224.3375	4.6520	1.2271	0.6511	17.3305	1.6830E−02
70	1629009390895385728	0.2782	+63.7497	246.4188	3.5416	3.2517	0.7459	16.6089	1.5032E−02
71	1448109899577010688	0.2991	+25.9842	203.5458	5.1577	−1.6772	0.8423	19.6347	1.4980E−02
72	3690318879491794816	0.7154	+1.0770	194.9856	3.2560	−1.1810	0.6733	19.3076	1.4842E−02
73	3692071982062671872	0.0273	+2.6639	195.8328	3.9871	−2.3096	0.6086	19.0058	1.4675E−02
74	1504902668745341568	0.2623	+44.7623	214.4142	6.1911	−0.1412	0.7564	19.2867	1.4605E−02
75	3691940624783331968	−0.2046	+1.9962	195.6238	3.6968	−3.8815	0.7665	19.9206	1.4019E−02
76	1606240768531075840	0.0999	+53.7979	224.1231	5.4837	1.5892	0.7981	19.9199	1.3801E−02
77	1635385046508786432	0.1401	+65.3460	254.9531	2.5866	3.8704	0.8620	15.9535	1.3366E−02
78	3744739963422459648	0.2229	+16.8007	199.5876	4.9930	−1.5486	0.8518	19.3988	1.3101E−02
79	3939039542249768704	−0.2004	+18.7968	200.7388	5.1992	−1.9285	0.7052	18.9435	1.2349E−02
80	1602451748381843840	0.2900	+57.0243	230.1132	5.3363	1.4649	0.6810	18.9183	1.2198E−02
81	1454872239685951232	0.2356	+28.8703	206.4059	5.3194	−1.1628	0.6408	18.4768	1.1805E−02
82	3688651916785064320	0.4148	−1.1125	195.0655	3.1597	−3.1376	0.8037	19.7906	1.1723E−02
83	1448864714313741184	0.3428	+27.5361	203.2331	4.9445	−0.8370	0.6315	18.3315	1.1234E−02
84	2257502327664371328	0.2131	+65.4879	273.9369	1.0117	3.3762	0.8663	17.0513	1.1005E−02
85	1495975420305337728	0.2719	+38.5514	209.8212	5.6724	−0.9194	0.8382	19.4064	1.0926E−02
86	1506911987588666112	0.1596	+47.0514	215.9830	5.3300	0.9153	0.5956	17.4090	1.0210E−02
87	1446439500896662016	−0.0118	+24.5145	201.5676	4.7772	−1.6017	0.9760	19.6123	1.0080E−02
88	3677279569234130048	0.7083	−6.6177	193.6215	2.5629	−2.5554	0.8683	20.1710	1.0038E−02
89	1443176738796291584	0.2635	+23.2662	201.9803	4.6112	−0.9136	0.6071	17.8110	9.9017E−03
90	3689436968086686592	0.5275	+0.1543	195.5130	2.7430	−1.7675	0.6331	19.3850	9.8457E−03
91	3743823932797933312	−0.0844	+14.5741	199.2608	3.9796	−2.2242	0.8309	20.0393	9.6899E−03
92	1458262618153176192	0.2948	+32.7413	207.3543	5.1408	−0.3751	0.7559	18.9859	9.6086E−03
93	3940420357056044288	0.3519	+20.8439	199.4598	4.7599	−1.6054	0.6726	18.3198	8.9874E−03
94	1507371072349542144	−0.1597	+47.8610	215.9188	5.5026	−0.0514	0.8711	19.4371	8.8737E−03
95	3938479650312918656	0.6125	+17.5560	199.5950	4.4924	−1.4851	0.8348	19.5584	8.2065E−03
96	1456251169001507584	0.2697	+30.5236	204.2348	4.8161	−1.0784	0.6146	18.0593	7.8983E−03
97	3938871179532201728	0.1450	+18.9098	200.2058	4.2659	−0.6811	0.5948	18.5974	7.8864E−03
98	3689019428546525440	0.3076	−0.9438	195.4987	3.3426	−1.8699	0.6213	19.6326	7.8563E−03
99	1633029475988441856	0.0342	+65.8413	264.5104	1.8194	3.8462	0.8345	19.1037	7.6960E−03
100	1635011792373656448	0.1679	+65.1211	253.8823	2.7241	4.1788	0.5981	17.8074	7.5587E−03
101	3744580156279785600	0.2913	+16.0645	199.2184	3.8843	−1.3277	0.7673	20.0798	7.4507E−03
102	3691972098303496192	−0.2897	+1.9209	196.0260	3.1704	−2.0277	0.5907	18.0558	7.3961E−03
103	3730783072057224064	0.5447	+8.0236	196.8188	4.2337	−4.0880	0.6855	19.5750	6.9686E−03
104	1443127570010678400	0.3753	+22.8453	201.7464	4.9070	−0.6215	0.8291	19.4308	6.9297E−03
105	3732743570009103488	0.2201	+9.7921	197.2683	4.6305	−1.6454	0.7821	19.9412	6.7403E−03
106	3736593170672106496	0.5514	+11.7588	197.8533	5.0609	−3.1560	0.9104	19.8379	6.5168E−03
107	1458436890741975936	0.1259	+33.0617	206.2575	5.7670	−0.3490	0.8147	19.4588	6.4103E−03
108	3685090289385421440	−0.1285	−3.3308	195.3744	2.8122	−2.7455	0.6930	18.3146	6.3728E−03
109	1456784049887562496	−0.1976	+31.6569	205.4463	4.7322	−1.0968	0.8699	19.5363	6.2448E−03
110	1505368857379439232	0.1609	+43.9625	212.0110	6.5511	0.1754	0.9058	19.8964	6.1957E−03
111	1496065515539578112	0.1647	+38.4511	208.6889	5.5450	−0.0661	0.8831	19.9410	6.1851E−03
112	1448703983748127104	−0.1921	+27.2718	204.0384	5.1016	−1.2913	0.7961	19.1699	6.0476E−03
113	3943652440204771328	0.0945	+21.9936	199.5465	4.8426	−2.0650	0.6397	18.4953	5.8078E−03
114	1628882805322936192	0.1545	+63.7692	248.5402	3.4299	3.7673	0.6974	19.6397	5.7581E−03
115	1605837320778662528	0.3849	+52.3964	220.2742	4.9615	1.5494	0.8261	19.6347	5.6522E−03

Appendix B

Chapter 3

B.1 Colour-Magnitude diagram of NGC 3201 from GDR2

We reproduce here the ADQL query we have used to obtain the photometry of all GDR2 stars in the G, G_{BP}, and G_{RP} passbands in a circle of radius 0.14 deg centred on NGC 3201, which yields 7064 stars:

```
1  SELECT bp_rp, phot_g_mean_mag, phot_bp_mean_flux,
       phot_bp_mean_flux_error, phot_rp_mean_flux,
       phot_rp_mean_flux_error, phot_g_mean_flux,
       phot_g_mean_flux_error
2  FROM gdr2.gaia_source
3  WHERE 1 = CONTAINS( POINT('ICRS', ra, dec), CIRCLE('ICRS'
       , 154.3987, -46.4125, 0.14) )
4  AND parallax BETWEEN -1.6 AND 1.4
5  AND SQRT((pmra-8.3344)*(pmra-8.3344) + (pmdec+1.9895)*(
       pmdec+1.9895)) <= 0.7
6  AND bp_rp IS NOT NULL;
```

Host server: https://gaia.aip.de/
Description of the gaia_source table:
https://gea.esac.esa.int/archive/documentation/GDR2/Gaia_archive/
chap_datamodel/sec_dm_main_tables/ssec_dm_gaia_source.html

B.2 Dust extinction correction

To select stars that are consistent with the H-R diagram of NGC 3201, the $G_{\mathrm{BP}}-G_{\mathrm{RP}}$ colour index and the G-band magnitude observed by *Gaia* need to be corrected for the effects of dust extinction, both for the cluster stars and the candidate stream stars. In general, for any observed colour index M', the corrected colour index M is computed by subtracting the colour excess E_M,

$$M = M' - E_M \; . \tag{B.1}$$

We use the colour excess $E_{B\text{-}V}$ for B-V colour predicted by the Galactic dust model of Schlafly and Finkbeiner (2011), known as the SF model. This is the same as the colour excess model of B-V from Schlegel et al. (1998) reduced by a factor 0.86. The B-V colour of stars can be related to the *Gaia* colour $G_{\mathrm{BP}}-G_{\mathrm{RP}}$, for most common stellar metallicities and gravities, using the approximate expression of Jordi et al. (2010b), from their Table 3:

$$G_{\mathrm{BP}}-G_{\mathrm{RP}} = 0.0981 + 1.429\,(B\text{-}V) - 0.0269\,(B\text{-}V)^2 + 0.0061\,(B\text{-}V)^3 \; . \tag{B.2}$$

We also follow the approximation of Jordi et al. (2010b) that the dust extinction colour excess runs nearly parallel to this colour-colour relation. Neglecting the small coefficients of the second- and third-order terms in B-V, we can use the simple approximation

$$E_{G_{\mathrm{BP}}-G_{\mathrm{RP}}} = 1.429\, E_{B\text{-}V} \; . \tag{B.3}$$

The extinction correction in the G-band magnitude A_{G} can be approximately expressed in terms of the colour excess $G_{\mathrm{BP}} - G_{\mathrm{RP}}$. We use the expression calibrated at a typical dust extinction $A_{\lambda=550\,\mathrm{nm}} = 1$ mag, given in table 13 of Jordi et al. (2010b):

$$A_{\mathrm{G}} = 1.98 E(G_{\mathrm{BP}} - G_{\mathrm{RP}}) \; . \tag{B.4}$$

B.3 Final Candidate Stream Member Stars

The selected stars from GDR2 catalogue after all our cuts from 1 to 7 are applied, which are our final list of best candidate stream members, are listed in Table B.1. Only one star in this list, star number 144, has a radial velocity:

N	source_id	v_r	ϵ_{v_r}
		(km s^{-1})	(km s^{-1})
144	5365576065920333440	499.29	1.29

B.4 Definition of stream coordinates

We have defined stream spherical coordinates on the sky by defining the angle ϕ_1 along a major circle that approximately contains the stream, and ϕ_2 to be the polar angle from the axis perpendicular to this major circle. An approximate adjustment to these coordinates by eye has resulted in the following coordinate transformation matrix from the usual equatorial coordinates (α, δ):

$$\begin{pmatrix} \cos(\phi_2)\cos(\phi_1) \\ \cos(\phi_2)\sin(\phi_2) \\ \sin(\phi_2) \end{pmatrix} = M \times \begin{pmatrix} \cos(\delta)\cos(\alpha) \\ \cos(\delta)\sin(\alpha) \\ \sin(\delta) \end{pmatrix} \; , \tag{B.5}$$

where the transformation matrix is:

$$M = \begin{pmatrix} -0.6209 & 0.2992 & -0.7245 \\ -0.4004 & -0.9157 & -0.0350 \\ -0.6739 & 0.2684 & 0.6883 \end{pmatrix} \; . \tag{B.6}$$

Table B.1: List of candidate stream member stars from the GDR2 catalogue, having passed all our 7 cuts. They are compatible with the best-fitting phase-space density model of the tidal stream of NGC 3201 and its H-R diagram from GDR2 after dust extinction correction.

N	source_id	π (mas)	δ (deg)	α (deg)	μ_δ (mas yr^{-1})	$\mu_{\alpha*}$ (mas yr^{-1})	$G_{\rm BP}-G_{\rm RP}$ (mag)	G (mag)	$\chi_{\rm sel}$ (yr^3 deg^{-2} pc^{-1} mas^{-3})
1	85111820717084288	0.1651	+20.1781	42.2098	−7.9041	9.1652	0.8645	17.6426	8.1257E−02
2	85463664437883264	0.4112	+21.1340	42.5690	−7.1268	8.0718	1.1816	18.7109	5.3786E−02
3	85259674966320512	0.1913	+20.9929	42.8676	−7.1869	8.2032	1.2189	18.1123	2.9994E−01
4	34258896831609984	0.1405	+16.3693	45.1634	−9.6897	10.4887	0.9566	17.5377	5.3842E−02
5	35721109857582464	0.3439	+18.4065	45.9215	−9.1765	9.7779	1.0528	18.0348	6.4986E−02
6	60185926474933632	0.1295	+20.1024	46.0006	−7.6207	8.4273	0.8544	18.1997	5.3196E−02
7	34901557082616576	0.1467	+18.1273	46.4329	−9.8855	10.5074	0.7827	17.6309	6.2463E−02
8	58640189220402432	0.0641	+17.6070	47.2249	−9.7492	10.2046	0.8839	17.2243	2.0020E−01
9	31456447850977536	0.2736	+16.1339	47.4120	−9.7023	10.2854	1.1301	16.8443	2.1423E−01
10	31185242140302080	0.2541	+15.7169	48.4324	−10.1471	10.2482	0.9355	18.2953	8.7513E−02
11	55510772969455232	−0.0189	+17.0169	48.7138	−10.3461	10.9882	1.1011	16.5356	7.4714E−02
12	54919579310541568	0.2956	+16.7824	51.1901	−10.6029	10.7765	0.8089	17.7362	6.3037E−02
13	37334471374125696	0.1933	+11.8852	55.9878	−12.2495	12.5768	1.3554	17.3445	4.3200E−02
14	36354359837010816	0.2640	+10.6748	56.0746	−13.0978	13.3644	0.9893	18.5810	2.0527E−02
15	3302763471907603840	0.2579	+10.0905	57.2163	−15.0372	14.6607	0.9197	17.4677	2.7800E−02
16	3302347405538192768	0.1123	+9.0186	57.5283	−14.6794	13.5157	0.9866	18.1334	7.7986E−03
17	3302517627978790784	0.2305	+9.7887	58.3446	−13.4025	13.6600	0.8746	17.0933	1.1627E−02
18	3273949498390088448	0.2311	+6.2544	58.3769	−15.6878	15.0130	0.9952	17.1423	7.7895E−03
19	3259376124600082688	0.0439	+2.7632	63.5494	−18.0006	16.5966	1.0363	16.9342	1.0527E−02
20	3283413643508855168	0.4116	+3.2175	63.9090	−17.6916	16.5187	0.8983	18.2204	4.3555E−02
21	3283707732806011776	0.2904	+3.8795	66.0409	−16.9729	16.1823	1.0192	16.8527	7.6543E−03
22	3278904202725707776	0.4538	+0.6731	66.8839	−18.0428	16.9354	0.8860	18.3811	2.6335E−02
23	3205031181848570240	0.3451	−2.6066	69.8346	−19.8285	19.0347	0.6952	17.5299	6.7108E−03
24	3229172192289896576	0.5220	−1.8187	69.8390	−20.3993	19.0081	0.9991	19.1580	6.6485E−03
25	3225714404316322048	0.5186	−3.3168	72.0153	−20.3162	19.3406	0.9340	17.5908	1.3595E−02
26	3225088713480594304	0.1847	−3.0706	72.5461	−20.7489	19.8459	0.9562	15.6898	1.7710E−02
27	3188312385993123968	0.2624	−6.0464	72.9310	−23.3288	22.2830	0.7262	17.4658	7.0712E−03
28	3225017378367519232	0.1945	−3.3841	72.9781	−21.1877	20.1364	0.7722	18.1341	2.3440E−02
29	3212479479773005696	0.2639	−5.2492	73.6805	−22.6205	21.5271	0.6668	17.0226	2.9807E−02
30	3187421678493781888	0.3710	−6.0663	74.5026	−21.6876	20.4548	0.7595	17.7014	1.1591E−01
31	3183889733612983296	0.2107	−8.0801	75.1650	−24.2181	22.8004	0.9031	18.1802	5.9379E−03
32	3182335646943552000	0.3665	−9.8777	75.9863	−23.4187	22.8338	0.8467	17.0998	1.0542E−02
33	3183733710337675136	0.2786	−8.2173	76.5810	−22.5581	21.3874	0.8088	18.0632	6.5451E−02
34	3182771152330545152	0.0302	−9.2063	76.6356	−21.4523	20.5276	1.1081	18.9625	6.5732E−03
35	2989805452906457216	0.2265	−11.1401	77.4576	−24.2242	23.2763	0.9121	18.4459	5.6177E−03
36	2985707611726244480	0.2369	−13.1102	80.3573	−23.6520	23.4954	0.7765	17.4529	6.0301E−03
37	2985448500643184896	0.3116	−13.5979	81.3864	−22.5934	22.6676	0.8775	17.9810	1.6029E−02
38	2985851682109593728	0.3032	−12.5971	81.5529	−23.6375	23.2202	0.8874	16.3023	3.2902E−02
39	2984359674895283072	0.4909	−14.7883	83.5002	−22.2270	22.7071	0.8658	18.4725	6.4990E−03
40	2971024729152562176	0.1691	−16.9745	85.2735	−23.8125	23.9815	0.8599	17.9274	6.5887E−03
41	2971248857726512128	0.1681	−15.7976	85.7306	−23.1975	22.6792	1.0410	18.7166	9.8945E−03
42	2967677373378985472	0.4029	−18.1238	86.3326	−23.3190	24.2962	0.7562	17.2588	2.2519E−02
43	2967743511577557120	0.4519	−17.9255	87.4169	−22.9684	24.0202	0.8708	17.7389	3.1562E−02
44	2967375007681446784	0.2755	−18.6319	87.6077	−23.5623	24.2818	0.7710	17.5950	3.9916E−02
45	2991860440139396608	−0.0381	−16.8690	88.2245	−22.8467	22.9447	0.9589	18.7355	6.0765E−03
46	2966606032438342144	0.2674	−19.4013	88.5997	−22.2754	23.4095	0.8417	18.0282	1.4813E−01
47	2966413828356833152	0.2144	−19.5051	88.8025	−22.2084	23.3199	0.7694	17.3525	2.0891E−01
48	2918181822364292736	0.2471	−20.3285	89.1767	−22.3439	24.2402	0.8385	18.1034	1.6488E−02
49	2990877854701797888	0.3134	−17.4093	90.4209	−23.6439	23.5650	0.9256	17.1479	1.0600E−02
50	2916935594654099712	0.3217	−22.3985	90.8435	−22.0852	24.1436	0.7733	17.7879	5.6818E−03
51	2917978004694480128	0.2612	−20.5596	90.9743	−22.0869	23.9064	0.7235	17.1207	8.3623E−02
52	2941157702670871680	0.4038	−20.9649	91.8675	−21.8820	23.8108	0.7327	16.6851	5.0665E−02
53	2941141931553193856	0.3032	−21.1686	92.2365	−21.8213	23.1047	0.8605	17.9485	1.6438E−01
54	2941295279065097472	0.2902	−20.4353	92.5552	−22.8800	24.2738	0.6464	16.0479	2.0424E−02
55	2937577417936027008	0.2063	−22.4331	93.8184	−20.6428	22.4657	0.7654	17.5514	1.1616E−01
56	2936748248729371008	0.3291	−22.9566	95.0570	−21.4088	23.8275	0.7250	16.8219	2.2029E−02
57	2937679290262547584	0.0609	−21.8367	95.3396	−20.4362	22.4033	0.9023	18.3712	8.8452E−03
58	2924361047651213184	0.3045	−24.2864	96.6325	−20.8322	23.3102	0.6946	17.0423	1.1522E−01
59	2923332351444848896	0.2326	−25.4506	98.1197	−18.9226	21.7545	0.8182	16.1500	5.3253E−02
60	2919762198531603456	0.2841	−27.6668	98.8488	−18.8438	22.7615	0.9272	18.1750	5.9658E−03
61	2923457523971828480	0.3593	−25.2914	99.9176	−20.4000	23.7148	0.8881	18.0914	1.4250E−02
62	2919619949213987200	0.2580	−27.6074	100.5084	−19.2244	22.0807	0.9075	18.6624	2.2055E−02
63	2918864520305483264	0.4388	−27.7485	101.3058	−18.7304	22.2778	0.9241	18.1616	1.3436E−01

Table B.1: - *continued.*

N	source_id	π (mas)	δ (deg)	α (deg)	μ_δ (mas yr^{-1})	$\mu_{\alpha*}$ (mas yr^{-1})	$G_{BP}-G_{RP}$ (mag)	G (mag)	χ_{sel} (yr^3 deg^{-2} pc^{-1} mas^{-3})
64	2918802226100396032	0.3037	−27.9478	101.8551	−18.4146	21.9682	1.1722	18.6582	8.6932E−02
65	2919192204830525312	0.1634	−27.5619	102.0146	−18.6500	22.3833	0.7739	16.7921	8.5157E−02
66	5608974194743618304	0.1431	−29.0134	103.0615	−18.4799	22.6030	0.9807	17.2841	6.2600E−03
67	5604401257167040896	0.1817	−31.3957	106.9045	−16.2835	21.7660	0.9967	18.2635	5.6973E−03
68	5604387551929978624	0.1216	−31.4825	107.4312	−15.7999	21.3128	0.8960	17.8501	2.8356E−02
69	5604416031855199360	0.2044	−31.2087	107.7262	−16.2320	21.3956	1.0559	17.4261	3.0635E−02
70	5605860210317910656	0.1027	−31.2627	108.2240	−16.1830	21.3612	0.8866	18.1165	5.1754E−03
71	5605025887150553344	0.2347	−31.7202	109.0093	−15.7407	21.4371	0.8631	17.5631	1.4133E−02
72	5587654118824699136	−0.0611	−35.6350	115.3624	−13.8094	19.3400	1.7499	20.5729	1.1787E−03
73	5587324089239122688	−0.2146	−36.4645	117.2742	−12.9198	19.9370	1.5662	19.2243	9.6739E−04
74	5539044602383550720	0.4356	−37.2963	119.2984	−11.0610	19.3346	2.4144	19.6161	5.4508E−04
75	5424452710261263872	−0.2191	−43.1483	140.7367	−4.6507	12.3840	1.6736	19.5148	1.1320E−03
76	5424980029168882560	0.3051	−43.1169	142.9833	−4.7781	11.2861	1.6641	19.0377	6.2820E−03
77	5412717553938252544	0.1385	−44.1282	144.6515	−4.4577	11.2894	1.1298	18.8000	1.2108E−02
78	5412394400600530432	−0.0005	−45.1641	146.4960	−3.4355	10.2152	1.0007	19.0347	6.6114E−03
79	5411987340783459840	0.0278	−44.7558	147.9285	−4.5372	9.6447	1.2994	19.8551	3.5455E−03
80	5412063585038036096	0.1458	−44.7961	148.5284	−2.7358	8.7963	1.0250	19.5906	4.3700E−03
81	5411902609663942272	0.2299	−44.7107	149.0004	−3.4370	10.5574	1.4347	20.2248	4.8709E−03
82	5408678635415016576	0.2071	−46.0086	149.5061	−2.6238	9.9105	0.9979	17.5241	1.2022E−01
83	5411828465645835648	0.1680	−44.9974	149.6303	−2.9013	9.7088	1.0017	19.0311	1.5012E−01
84	5414808107804098432	0.4901	−45.2014	150.4793	−3.6007	9.8601	1.1010	20.3807	6.1875E−03
85	5408722242225130880	−0.4469	−46.0245	150.6442	−3.1488	9.1825	1.1029	19.4458	2.9276E−03
86	5414950318459476864	0.0050	−44.4130	150.9149	−3.2737	8.4006	1.0093	19.3326	4.7786E−03
87	5414797898662111744	0.0673	−44.8816	151.1779	−3.7119	8.8205	1.1339	20.1646	5.2609E−03
88	5414539822663808768	0.3201	−45.6822	151.4893	−2.5543	9.8544	0.9911	18.8864	3.3081E−02
89	5414564183718662016	0.3195	−45.5630	151.5356	−2.8157	8.5250	1.0473	19.2840	4.9625E−02
90	5414524021482764672	0.5664	−46.0519	151.5567	−2.8607	9.5367	1.0047	20.1461	9.0886E−03
91	5414568478687775616	0.0000	−45.4720	151.7814	−1.9550	9.4562	1.0643	19.8742	1.9126E−02
92	5414568203809849600	0.0741	−45.4956	151.8199	−2.5132	9.2889	0.9280	18.2477	2.2365E−01
93	5414470175475053440	0.0939	−46.0117	152.0382	−2.0447	8.5806	0.9803	18.2909	1.5857E−01
94	5407680210138297472	0.3190	−47.0962	152.1243	−2.1293	8.9009	1.0210	19.3478	6.8538E−03
95	5414514808777843968	0.1885	−45.7093	152.1831	−3.2370	7.6466	1.1894	20.4158	3.7572E−03
96	5414489799181004160	0.5853	−46.0332	152.2404	−2.4198	9.1888	1.0093	19.8201	2.8798E−02
97	5413703854532103040	0.5427	−46.4378	152.2645	−1.4183	8.4917	1.2109	19.5160	1.0050E−02
98	5413703403553024896	0.4628	−46.5002	152.2753	−1.3476	8.8112	1.1792	19.9166	8.7105E−03
99	5414501064881763584	0.5115	−45.8547	152.2918	−2.1137	9.1032	0.9609	18.9478	7.2786E−02
100	5413735804786642688	0.5939	−46.2623	152.4463	−1.7846	8.6619	1.1320	18.7962	1.1387E−02
101	5413736771158381056	0.3367	−46.1567	152.4470	−2.6524	8.7161	1.0038	19.3687	5.5646E−02
102	5413707531024130304	0.1513	−46.4227	152.4619	−2.1157	8.7608	1.4619	14.2777	1.2925E−01
103	5413686464201633024	0.3246	−46.6598	152.4782	−1.3244	9.1873	1.0932	19.8740	8.2365E−03
104	5413731922137962496	0.0330	−46.3127	152.6005	−1.4314	8.4122	1.0919	19.1534	1.7983E−02
105	5413746769842342912	−0.2302	−45.9664	152.6060	−1.4081	8.1404	0.9907	19.7287	3.9730E−03
106	5413694268165352704	0.1283	−46.5443	152.6153	−1.9544	8.7215	1.2519	16.1443	1.2764E+00
107	5413734224240710272	−0.0087	−46.1877	152.6410	−2.3915	8.6046	1.0492	18.7688	1.4529E−01
108	5413742268720312192	0.1306	−46.0010	152.6414	−2.2343	8.8286	1.2550	15.9851	1.8786E+00
109	5413721824672679552	0.2962	−46.2819	152.6430	−2.0587	8.7421	1.0147	18.2996	5.4112E−01
110	5413744364664262144	0.0805	−45.9321	152.6470	−3.1119	9.2018	0.9047	18.5161	9.4405E−03
111	5413743295212382208	0.3754	−45.9628	152.7251	−2.6614	8.3346	1.0136	18.5626	4.1028E−02
112	5413837204676171136	0.1280	−45.9449	152.7622	−2.3460	8.2183	1.0011	17.5443	1.7796E−02
113	5413720622081853824	0.2782	−46.3067	152.7667	−1.9144	8.6098	0.9940	17.6895	3.9211E−01
114	5413742951614948096	−0.5966	−46.0033	152.7743	−1.8458	8.8833	1.0139	19.5849	3.3428E−03
115	5413827996266328064	−0.0091	−45.8243	152.9341	−2.2238	8.5120	0.9132	17.3248	6.2819E−02
116	5413634654017870336	0.2101	−46.9412	152.9942	−2.0045	8.5502	1.2115	16.4645	1.9360E−01
117	5413835894705134208	−0.2688	−45.7065	153.0241	−1.8431	8.3532	0.9813	20.1126	5.5075E−03
118	5414389537468984064	0.1168	−44.3112	153.8987	−3.5476	8.3693	1.0589	18.4613	3.8191E−03
119	5414057892972812160	−0.0016	−45.2555	155.4083	−2.1204	7.7283	0.8449	17.6746	4.6860E−03
120	5365783216481459840	0.1342	−46.8392	155.8449	−1.4280	8.0469	1.1206	19.4101	1.7484E−02
121	5365391073082942336	0.2777	−47.3759	155.8568	−1.4592	8.4773	0.8594	17.7940	1.0584E−02
122	5365780398982621696	0.2621	−46.9529	155.8643	−1.3769	7.8673	1.0697	19.2203	2.2998E−02
123	5365399383845390976	−0.0230	−47.2051	155.9170	−1.2253	7.5164	0.9504	18.4153	1.0633E−02
124	5365789504313726080	0.0047	−46.7820	155.9225	−1.7586	6.9475	1.0258	19.1421	3.0141E−03
125	5365876365730787328	0.3279	−46.2400	155.9265	−2.0997	8.1445	0.9316	18.5095	5.3858E−02
126	5365792016874464640	0.0931	−46.6439	155.9438	−1.7115	8.1138	0.9518	17.1936	1.0490E−01

Table B.1: - *continued.*

N	source_id	π (mas)	δ (deg)	α (deg)	μ_δ (mas yr^{-1})	$\mu_{\alpha*}$ (mas yr^{-1})	$G_{BP}-G_{RP}$ (mag)	G (mag)	χ_{sel} (yr^3 deg^{-2} pc^{-1} mas^{-3})
127	5365873445153019008	0.0975	−46.2453	155.9449	−1.3040	7.6397	1.3341	19.7425	5.1718E−03
128	5365865959033473152	0.2407	−46.3788	156.0361	−2.1501	8.4814	0.9965	19.1296	9.3859E−03
129	5365785965260649216	0.1707	−46.7892	156.0661	−1.4949	7.4019	0.9192	18.7294	1.9158E−02
130	5365819019327251840	0.5079	−46.3904	156.0674	−1.4804	7.4436	1.0385	19.3859	5.7243E−03
131	5365784178553932544	−0.1314	−46.9102	156.0887	−1.6961	7.5548	1.1499	19.4999	7.6562E−03
132	5365817163903821184	0.0751	−46.5291	156.1047	−1.6714	8.3504	0.9041	18.6001	1.5036E−02
133	5365825414540727296	0.1149	−46.3280	156.1078	−2.0940	7.8422	1.1164	19.7862	9.0039E−03
134	5365827476119277184	−0.0518	−46.2354	156.2146	−1.9832	7.0940	1.0906	19.5436	3.1556E−03
135	5365810261890643840	0.2137	−46.7570	156.2188	−2.0729	6.9264	0.7268	18.8097	2.9639E−03
136	5365921445707194624	0.2320	−46.1857	156.2351	−1.5871	7.4213	1.0728	19.0933	1.1313E−02
137	5365193706449182592	0.3000	−47.4672	156.2907	−1.2538	7.5130	0.8539	18.2828	2.5675E−02
138	5365768338714318080	0.7031	−47.0099	156.3480	−1.1768	8.0557	1.1333	19.4720	3.4492E−03
139	5365819775241396224	0.0269	−46.4617	156.3699	−2.0587	8.1793	0.9681	18.6001	1.4942E−02
140	5365190682792082048	0.1500	−47.5861	156.3725	−1.4167	8.1328	0.8341	18.3808	2.2653E−02
141	5365809437262578176	0.2534	−46.4901	156.4128	−1.7321	7.5130	1.0855	19.4212	8.7985E−03
142	5365578294999961344	0.4987	−47.1869	156.4923	−1.9379	7.6787	0.8898	18.8358	5.5409E−03
143	5365579016555060096	0.2704	−47.1131	156.5143	−1.9269	7.0518	1.0797	19.3789	4.2389E−03
144	5365576065920333440	0.1539	−47.1961	156.6824	−1.6095	7.6348	1.5148	12.9366	1.0524E+01
145	5365898355962610688	0.3840	−46.5396	156.7343	−1.5688	7.0853	0.9684	18.9476	5.4961E−03
146	5365601629562571008	0.2543	−47.0240	156.8280	−0.9371	7.3243	1.1609	18.9579	5.2161E−03
147	5365736178000020864	0.3027	−46.1942	157.4884	−2.2346	7.7748	0.9663	17.0385	2.0367E−02
148	5364616737729276928	0.3602	−47.7895	159.6636	−0.6013	7.2650	1.0342	19.2178	4.9192E−03
149	5366070189016080384	0.4429	−47.5857	160.3078	−1.1778	6.6145	1.1561	18.3634	7.2854E−03
150	5366058407925709568	−0.0212	−47.7929	160.3254	−1.1813	6.5427	0.9288	17.8935	7.3902E−03
151	5363031246257881984	0.4249	−48.2777	161.0511	−0.5582	6.8420	0.9608	18.1045	9.4285E−03
152	5363251045501068160	0.3074	−47.6732	163.6266	−1.0451	6.0923	0.9211	17.9304	2.4429E−02
153	5374364767295481856	0.1341	−47.8018	168.1795	−0.4224	4.5801	0.7357	18.7395	1.1996E−02
154	5374570105393379072	0.1369	−47.2856	169.4423	−0.8148	4.3892	1.2607	14.4835	1.2424E−01
155	5373850234514547712	0.2316	−47.6973	171.1533	−0.3389	3.6895	1.0015	19.0083	1.0363E−02
156	5373847481435744512	0.1238	−47.1102	171.3746	−1.1421	3.6006	1.0540	18.0519	9.0333E−03
157	5373628957800529280	0.1411	−47.6738	172.1138	−0.7113	4.0836	0.8235	18.1147	2.4378E−02
158	5375101959778889216	−0.2126	−47.3622	173.2150	−0.5569	3.3159	0.8618	19.1182	9.8719E−03
159	5375091376982888192	0.2061	−47.4674	173.5502	−0.5459	3.5834	0.8895	18.6912	4.3155E−02
160	5372062218149409536	0.1720	−47.9061	174.1886	−0.4939	3.0765	1.0942	19.4563	7.8447E−03
161	5372147915636764544	0.5759	−47.4353	174.6326	−0.5447	3.6150	0.7032	19.3034	9.9653E−03
162	5371948693572713856	−0.0380	−47.4375	175.3823	−1.2254	2.8094	0.9519	19.9073	7.7881E−03
163	5372345617270244480	0.0380	−46.9986	175.7310	−1.5697	3.1700	1.2063	20.0780	8.1299E−03
164	5372254082932197248	0.2239	−47.7630	176.1961	−0.4725	3.3897	1.0882	19.2860	2.2251E−02
165	5372296551563595520	−0.2300	−47.1799	176.3097	−0.4701	3.3724	0.9962	19.5314	2.4790E−02
166	5372386608438137600	−0.2060	−46.9739	176.5707	−1.1318	3.1125	1.0581	19.7879	4.4448E−02
167	5372378877496792064	−0.0659	−47.1248	176.6575	−1.2263	3.3820	0.7079	19.4287	1.3672E−02
168	5371655196988321152	0.7329	−46.8830	177.0731	−0.5633	3.7295	0.7188	20.2820	1.4290E−02
169	5377605302940159232	0.5001	−46.8489	177.7541	−0.1653	3.7658	0.9804	20.0362	1.3828E−02
170	5377724707328398592	0.3648	−46.4346	178.2477	−1.0006	3.7925	0.8342	20.0085	8.0794E−03

Appendix C

Chapter 4

C.1 Definition of the likelihood function

The likelihood function is composed of the product of the likelihoods corresponding to the constraints d_c, enumerated in equation 4.15 plus the stellar steams:

$$\mathcal{L}(d|\theta) \equiv \mathcal{L}_{d_\mathrm{c}}(d|\theta)\, \mathcal{L}_{\mathrm{str}}(d|\theta) \; . \tag{C.1}$$

We assume that the model of the constraints d_c is a Dirac's delta distribution and each observational measurement a Gaussian distribution with mean μ and standard deviation σ. For the constraint i we have:

$$\int_{-\infty}^{\infty} \delta\big(x - d_\mathrm{c}^i(\theta)\big)\, G\big(x|\mu_i, \sigma_i^2\big)\, \mathrm{d}x = G\big(d_\mathrm{c}^i(\theta)|\mu_i, \sigma_i^2\big) \; , \tag{C.2}$$

from which we get the likelihood function:

$$\mathcal{L}_{d_\mathrm{c}}(d|\theta) = \prod_{i=1}^{44} G\big(d_\mathrm{c}^i(\theta)|\mu_i, \sigma_i^2\big) \; . \tag{C.3}$$

The likelihood function of a stellar streams is defined from a phase-space probability density model of the stream. The model is defined in Heliocentric spherical coordinates because we have the observed stars in this same coordinate system. It is constructed using a Kernel Density Estimation method with a Gaussian distribution as a kernel. Given a simulation of the stellar stream made of N stars, we locate the mean of a Gaussian distribution at the phase-space position η_n^ν of each n star, and we compute its covariance matrix $\Xi_n^{\nu\epsilon}$ from the position of the neighbouring stars:

$$\Xi_n^{\nu\epsilon} = \left(\sum_{m=1}^{N} c_{nm} \right)^{-1} \sum_{m=1}^{N} c_{nm} (\eta_m^\nu - \eta_n^\nu)(\eta_m^\epsilon - \eta_n^\epsilon) \; , \tag{C.4}$$

where the indices $\nu, \epsilon \equiv (\pi, \delta, \alpha, v_r, \mu_\delta, \mu_\alpha)$. The weighting factors determine the kernel size, and are defined as:

$$c_{nm} = (d_0 + d_{nm})^{-9/2} \; , \qquad d_{nm}^2 = \sum_{l=1}^{3} (x_m^l - x_n^l)^2 \; , \tag{C.5}$$

where x^l are the Galactocentric Cartesian coordinates of each star at present time, and $d_0 = 250$ pc. This constant and the slope $9/2$ have been optimised to reproduce properly the distribution of the escaped stars. For NGC 3201, M68, and Palomar 5, we use 240, 300, and 170 simulated stars respectively. We find that these numbers are sufficient to build a smooth density model and evaluate the likelihood function with minimal computational time.

We assume that the observed stars follow a Gaussian distribution centred at the mean phase-space position of the star w^ν, where the covariance matrix $\Sigma^{\nu\epsilon}$ is the value of the observational errors and their correlations. If the stars do not have radial velocity we take $v_r = 0 \pm 10^3$ km s^{-1}. This is a value with an uncertainty much bigger than the expected distribution of radial velocities of the stellar stream. It is almost equivalent to use a uniform distribution for the missing radial velocity, but simplifies the definition of the likelihood function. For the j observed star we have:

$$\sum_{n=1}^{N} \int_{-\infty}^{\infty} G(w^\nu | \eta_n^\nu, \Xi_n^{\nu\epsilon}) \, G(w^\nu | \nu_j^\nu, \Sigma_j^{\nu\epsilon}) \, \mathrm{d}^6 w =$$
$$= \sum_{n=1}^{N} G(\eta_n^\nu | \nu_j^\nu, \Xi_n^{\nu\epsilon} + \Sigma_j^{\nu\epsilon}) \; . \tag{C.6}$$

If J is the total number of observed stars in the stream, we get the following likelihood function:

$$\mathcal{L}_{\mathrm{str}}(d|\theta) = \prod_{j=1}^{J} \sum_{n=1}^{N} G(\eta_n^\nu | \nu_j^\nu, \Xi_n^{\nu\epsilon} + \Sigma_j^{\nu\epsilon}) \; . \tag{C.7}$$

C.2   Stream coordinates

To minimise the time required to evaluate the likelihood function, we apply a method to obtain an approximate distribution of stream stars from a pre-calculated simulation.

To carry out this simulation, we choose the mean position of the globular cluster and a fiducial potential of the Galaxy. We take the orbit of a globular cluster in Galactocentric Cartesian coordinates x_{o}^i, where $i = (x, y, z)$, during T Myr backwards and forwards from the present position of the cluster, and the current position of a simulated stream stars x_e^i. For each star e, we compute the closest point of the orbit to the star using an Euclidean distance. This point is expressed in function of the parameter t:

$$\hat{t}_e \equiv \underset{t \in [-T,T]}{\operatorname{argmin}}(d_e(t)) \; , \qquad d_e^2(t) = \sum_{i=1}^{3} (x_{\mathrm{o}}^i(t) - x_e^i)^2 \; . \tag{C.8}$$

Defining $v \equiv v_{\mathrm{o}}^i(\hat{t}_e)$ as the velocity of the cluster and $a \equiv \mathrm{d}v/\mathrm{d}t \, (\hat{t}_e)$ its acceleration, assuming $v > 0$ and $a > 0$ for any t, we compute the corresponding Frenet-Serret trihedron at the point $x_{\mathrm{o}}^i(\hat{t}_e)$:

$$e_1 = \frac{v}{|v|} \; , \qquad e_2 = \frac{a}{|a|} \; , \qquad e_3 = \frac{e_1 \times e_2}{|e_1 \times e_2|} \; . \tag{C.9}$$

We store the parameter $\hat{t}_e$ and the position and velocity of the stream star expressed in the coordinate system defined by the vector basis (e_1, e_2, e_3).

When we evaluate the likelihood function for different values of the free parameters, we compute a new orbit of the cluster $\bar{x}_o^i$. We assume that the stored values are independent of the orbit for small variations with respect to x_o^i. Then, for each star e, we compute the Frenet-Serret trihedron corresponding to the position $\bar{x}_o^i(\hat{t}_e)$, and we locate the star at the stored values in the reference frame defined by the new trihedron $(\bar{e}_1, \bar{e}_2, \bar{e}_3)$. Finally, we put back the stars on the Galactocentric Cartesian coordinate system to get an approximation of the stellar stream for the new values of the free parameters.

C.3   Numerical results

In Table C.1 we provide the median and the 1σ levels of the free parameters and derived properties of our model computed for each stream separately and for all streams together. We give a symmetric uncertainty when the difference between the upper and the lower uncertainty is inferior to 20 per cent, and we give the mean of both uncertainties. We also indicate the value of the parameters for the best-fitting configuration.

Table C.1: Median and 1σ levels of the free parameters and derived properties of our model. The values have been computed using each stream separately and all streams together. The values without uncertainties correspond to the best-fitting configuration.

Parameter		NGC 3201		M68		Palomar 5		All	
$R_\odot$	(kpc)	8.17 ± 0.02	8.17	8.17 ± 0.03	8.16	8.14 ± 0.03	8.14	$8.15^{+0.02}_{-0.03}$	8.16
$U_\odot$	(km s^{-1})	9.61 ± 1.01	9.11	9.89 ± 0.97	9.98	12.47 ± 1.27	12.64	$10.58^{+0.89}_{-0.42}$	10.55
$V_\odot$	(km s^{-1})	14.58 ± 1.43	14.96	15.24 ± 1.56	15.19	13.39 ± 1.57	13.40	$13.64^{+1.84}_{-1.2}$	15.22
$W_\odot$	(km s^{-1})	7.61 ± 0.56	8.00	7.45 ± 0.59	7.33	7.22 ± 0.64	7.24	7.33 ± 0.51	7.59
ρ_0^{b}	($10^{10}\,\mathrm{M_\odot\,kpc^{-3}}$)	9.80 ± 1.02	10.14	9.62 ± 1.03	9.86	$9.97^{+0.78}_{-1.08}$	9.84	$9.84^{+0.69}_{-0.95}$	9.43
Σ_{n}	($10^{9}\,\mathrm{M_\odot\,kpc^{-2}}$)	0.92 ± 0.22	0.97	1.19 ± 0.13	1.29	$0.9^{+0.21}_{-0.15}$	1.00	$1.25^{+0.14}_{-0.2}$	1.28
h_{n}	(kpc)	$3.01^{+0.29}_{-0.23}$	2.70	$2.88^{+0.21}_{-0.14}$	2.75	2.99 ± 0.25	2.81	$2.78^{+0.18}_{-0.1}$	2.72
z_{n}	(kpc)	0.31 ± 0.05	0.32	0.30 ± 0.05	0.31	0.31 ± 0.05	0.31	$0.31^{+0.04}_{-0.03}$	0.33
Σ_{k}	($10^{8}\,\mathrm{M_\odot\,kpc^{-2}}$)	$4.17^{+2.66}_{-1.66}$	4.18	4.75 ± 2.06	4.32	$4.25^{+2.39}_{-1.7}$	3.62	$3.77^{+2.44}_{-1.37}$	2.52
h_{k}	(kpc)	1.97 ± 0.19	1.91	1.98 ± 0.18	2.03	1.93 ± 0.18	2.01	$2.06^{+0.14}_{-0.21}$	2.19
z_{k}	(kpc)	0.93 ± 0.16	0.94	0.90 ± 0.18	0.91	0.91 ± 0.17	0.92	$0.79^{+0.25}_{-0.12}$	0.86
ρ_0^{dh}	($10^{7}\,\mathrm{M_\odot\,kpc^{-3}}$)	$1.92^{+2.85}_{-1.6}$	3.17	$2.94^{+2.22}_{-1.44}$	3.81	$2.0^{+2.88}_{-1.5}$	1.95	$1.84^{+1.05}_{-0.62}$	1.71
α		0.68 ± 0.64	0.46	-0.23 ± 0.39	-0.41	0.73 ± 0.45	0.73	0.06 ± 0.22	0.28
a_1	(kpc)	$12.58^{+20.06}_{-6.13}$	9.98	$18.63^{+10.08}_{-5.41}$	17.38	$11.22^{+17.14}_{-5.1}$	10.49	$17.36^{+9.77}_{-2.74}$	16.33
β		$3.19^{+1.19}_{-0.61}$	3.31	$3.73^{+0.83}_{-0.56}$	3.64	$2.77^{+0.93}_{-0.33}$	2.71	$3.29^{+0.66}_{-0.28}$	3.10
q_ρ^{dh}		2.06 ± 0.93	1.96	$1.14^{+0.21}_{-0.14}$	1.08	1.01 ± 0.09	1.06	1.06 ± 0.06	1.01
$r_{\mathrm{h}}^{\mathrm{NGC3201}}$	(kpc)	4.82 ± 0.02	4.83					4.83 ± 0.02	4.82
v_r^{NGC3201}	(km s^{-1})	494.32 ± 0.14	494.34					494.31 ± 0.13	494.33
$\mu_\delta^{\mathrm{NGC3201}}$	(mas yr^{-1})	-1.962 ± 0.023	-1.946					$-1.931^{+0.03}_{-0.019}$	-1.929
$\mu_{\alpha*}^{\mathrm{NGC3201}}$	(mas yr^{-1})	8.309 ± 0.042	8.316					8.293 ± 0.056	8.297
$r_{\mathrm{h}}^{\mathrm{M68}}$	(kpc)			$10.01^{+0.08}_{-0.11}$	10.00			10.03 ± 0.06	10.04
v_r^{M68}	(km s^{-1})			-92.95 ± 0.22	-92.94			$-92.9^{+0.2}_{-0.29}$	-92.92
$\mu_\delta^{\mathrm{M68}}$	(mas yr^{-1})			1.766 ± 0.027	1.763			1.782 ± 0.027	1.779
$\mu_{\alpha*}^{\mathrm{M68}}$	(mas yr^{-1})			-2.750 ± 0.028	-2.752			$-2.744^{+0.02}_{-0.026}$	-2.750
$r_{\mathrm{h}}^{\mathrm{Palomar5}}$	(kpc)					21.19 ± 0.15	21.16	21.20 ± 0.15	21.19
v_r^{Palomar5}	(km s^{-1})					-58.44 ± 0.20	-58.45	$-58.5^{+0.17}_{-0.12}$	-58.41
$\mu_\delta^{\mathrm{Palomar5}}$	(mas yr^{-1})					-2.546 ± 0.016	-2.539	$-2.544^{+0.013}_{-0.018}$	-2.559
$\mu_{\alpha*}^{\mathrm{Palomar5}}$	(mas yr^{-1})					-2.533 ± 0.017	-2.525	$-2.513^{+0.015}_{-0.02}$	-2.522

Table C.1: - *continued*

Parameter		NGC 3201		M68		Palomar 5		All	
μ_{SgrA^*}	(mas yr^{-1})	-6.37 ± 0.02	-6.37	-6.35 ± 0.02	-6.35	-6.33 ± 0.02	-6.33	-6.32 ± 0.02	-6.34
Θ_0	(km s^{-1})	232.39 ± 1.38	231.96	230.70 ± 1.44	230.50	230.79 ± 1.48	230.88	230.67 ± 1.55	229.74
$\Theta_0 + V_\odot$	(km s^{-1})	246.95 ± 1.14	246.93	245.92 ± 1.14	245.69	244.15 ± 1.12	244.28	244.38 ± 0.91	244.96
f_ρ		0.04 ± 0.01	0.04	0.04 ± 0.01	0.04	0.04 ± 0.01	0.04	0.04 ± 0.01	0.04
f_Σ		0.11 ± 0.03	0.13	0.11 ± 0.04	0.12	0.11 ± 0.03	0.12	0.11 ± 0.03	0.10
$\left\|K_{z=1}\right\|$	($2\pi G\,\mathrm{M}_\odot\,\mathrm{pc}^{-2}$)	77.58 ± 4.73	63.63	88.49 ± 4.31	83.63	80.37 ± 5.47	74.31	$86.81^{+2.93}_{-3.84}$	83.00
	($10^1\,\mathrm{km}^2\,\mathrm{pc}^{-1}\,\mathrm{s}^{-2}$)	7.76 ± 0.47	6.36	8.85 ± 0.43	8.36	8.04 ± 0.55	7.43	$8.68^{+0.29}_{-0.38}$	8.30
$\rho_{\mathrm{dh}}(R_\odot)$	($10^6\,\mathrm{M}_\odot\,\mathrm{kpc}^{-3}$)	$5.2^{+1.87}_{-0.77}$	6.31	5.66 ± 0.84	5.89	7.43 ± 0.86	7.57	5.95 ± 0.60	6.62
	(GeV cm^{-3})	$0.2^{+0.07}_{-0.03}$	0.24	0.21 ± 0.03	0.22	0.28 ± 0.03	0.29	0.23 ± 0.02	0.25
r_{200}	(kpc)	200.56 ± 16.38	188.47	$199.89^{+13.52}_{-19.16}$	206.70	199.85 ± 17.33	206.24	$209.6^{+12.79}_{-16.71}$	210.86
c_{200}		$13.48^{+4.82}_{-3.06}$	15.98	8.24 ± 0.58	8.07	$10.43^{+2.95}_{-1.92}$	10.97	$7.86^{+0.57}_{-0.44}$	8.24
M_{b}	($10^9\,\mathrm{M}_\odot$)	8.84 ± 0.92	9.15	8.68 ± 0.93	8.89	$9.0^{+0.71}_{-0.97}$	8.87	$8.87^{+0.62}_{-0.86}$	8.51
$M_{\mathrm{d}}^{\mathrm{n}}$	($10^{10}\,\mathrm{M}_\odot$)	5.26 ± 0.60	4.46	6.22 ± 0.40	6.14	5.13 ± 0.56	4.94	6.07 ± 0.39	5.96
$M_{\mathrm{d}}^{\mathrm{k}}$	($10^{10}\,\mathrm{M}_\odot$)	1.02 ± 0.36	0.96	1.16 ± 0.39	1.12	1.00 ± 0.36	0.92	$1.01^{+0.4}_{-0.29}$	0.76
M_{bar}	($10^{10}\,\mathrm{M}_\odot$)	7.22 ± 0.70	6.34	8.30 ± 0.49	8.15	7.04 ± 0.66	6.75	8.01 ± 0.38	7.57
M_{200}^{dh}	($10^{12}\,\mathrm{M}_\odot$)	0.95 ± 0.23	0.78	0.94 ± 0.22	1.04	0.94 ± 0.24	1.03	1.08 ± 0.22	1.10
M_{200}^{MW}	($10^{12}\,\mathrm{M}_\odot$)	1.03 ± 0.23	0.86	1.03 ± 0.23	1.13	1.02 ± 0.25	1.11	1.18 ± 0.23	1.19

Table C.2: Median with 1σ levels, mean and stardard deviation, and best-fitting parameters of a log-Normal distribution of the marginalised posterior probability density function of the flattening parameter $q_\rho^{\rm dh}$.

	Median$^{+\sigma}_{-\sigma}$	Mean	s	μ	τ	ϵ
NGC 3201	$2.06^{+1.01}_{-0.86}$	2.13	0.88	-2.79	0.18	4.84
M68	$1.14^{+0.21}_{-0.14}$	1.17	0.18	0.60	0.31	0.54
Palomar 5	$1.01^{+0.09}_{-0.09}$	1.01	0.09	-8.18	0.01	9.19
All	$1.06^{+0.06}_{-0.05}$	1.07	0.07	0.66	0.16	0.40

C.4 Halo flattening

In Table C.2, we show the median with the 1σ levels and the mean with the standard deviation of the marginalised posterior probability density function of the flattening parameter $q_\rho^{\rm dh}$. We also include the best-fitting parameters of a log-Normal probability density function defined as:

$$\log{\rm N}(x|\mu,\tau,\epsilon) \equiv \frac{1}{\sqrt{2\pi}(x-\mu)\tau} \exp\left[\frac{-\log\left(\frac{x-\mu}{\epsilon}\right)^2}{2\tau^2}\right] \qquad (C.10)$$

C.5 Final selection of Palomar 5 tidal stream members

To select the stars most likely to belong to the Palomar 5 stellar stream, we use the method described in Chapter 2. First, we apply the pre-selection cuts defined in 2.3.3 to reduce the number of foreground stars surrounding the stream. These cuts basically select stars near the orbit of the cluster, in a ± 20 Myr section of the orbit from the cluster centre. They also remove the stars belonging to the globular cluster Palomar 5 and M5 (NGC 5904) to avoid detecting overdensities that do not correspond to streams. After the pre-selection, we obtain 320 302 GDR2 sources. We apply the same pre-selection to a simulation of the GDR2 catalogue, the 18th version of the Gaia Object Generator (GOG18, Luri et al., 2014b) obtaining 450 622 sources. This 30 per cent difference can be explained by imperfect modeling of the stellar halo in GOG18, by inaccuracies in the simulation of GDR2 uncertainties, or because GDR2 does not include all sources with G-band magnitude $G < 21$ mag in low exposure areas.

We apply the maximum likelihood method explained in Section 2.2 to compute the best-fitting parameters of the stream model, as well as the statistic Λ indicating the confidence level with which the stream is detected. When $\Lambda > 6.6$, the existence of the stream is confirmed at the 99 per cent confidence level, as opposed to the null hypothesis that no stream is present in the preselection. We detect the stellar stream with $\Lambda = 14.44$, which implies a high statistical significance of the detection. We compute an accurate phase-space density model of the stream using the best-fitting configuration of the free parameters. We select the stars with the largest intersection with this model.

Table C.3: Stars from Table C.4 with radial velocity measured by Ibata et al. (2017).

N	source_id	v_r (km s^{-1})	ϵ_{v_r} (km s^{-1})
28	4418156892309715456	-58.64	2.00
32	4418265022406118784	-56.36	1.64
35	4418305219004364416	-69.85	3.90
38	4418688536245813888	-54.24	2.19
41	4418306490314700288	-54.12	1.30
54	4418724923208864128	-60.28	1.54
68	4420607768151633408	-48.15	1.75
74	4420717139494655360	-48.75	2.50
76	4420553479766045824	-62.16	0.98
80	4421128077670137472	-47.55	3.94
82	4420942432004721408	-53.68	2.91
84	4420970057233967360	-58.02	1.46
92	4421075644710040960	-49.59	1.65
105	4427116091010101888	-33.85	2.97
106	4427119350890013312	-54.28	3.80

We define a threshold for the value of the intersection χ_{sel}, and choose stars with $\chi_{\text{sel}} > 4.6$ yr^3 deg^{-2} pc^{-1} mas^{-3}. We obtain 229 stars from the GRD2 catalogue compatible with the phase-space density model of the stream. For the chosen threshold, we select no stars from the GOG18 catalogue. This minimizes the number of expected foreground stars erroneously selected as Palomar 5 stream members.

Finally, we only select stars that are compatible in colour and magnitude with the H-R diagram of Palomar 5. We follow the procedure described in Appendix A.4 and include the correction for dust extinction described in Appendix B.2. In Table C.4, we list the 126 star candidates belonging to the Palomar 5 tidal stream selected from the GDR2 catalogue. None of these stars have radial velocity measured by *Gaia*, but 15 of them match stars with radial velocity measured by Ibata et al. (2017). We list their values in Table C.3.

Table C.4: Stars compatible with the best-fitting phase-space density model of the tidal stream of Palomar 5 and its H-R diagram from GDR2 after dust extinction correction.

N	source_id	π (mas)	δ (deg)	α (deg)	μ_δ (mas yr^{-1})	$\mu_{\alpha*}$ (mas yr^{-1})	$G_{\mathrm{BP}}-G_{\mathrm{RP}}$ (mag)	G (mag)	χ_{sel} (yr^3 deg^{-2} pc^{-1} mas^{-3})
1	6327240546525053824	−0.1349	−8.1333	222.5158	−2.4483	−2.4054	1.0417	17.5562	5.9454E+00
2	6327454916932476800	−0.0426	−7.9192	222.6962	−2.4659	−2.3107	1.0067	17.8507	8.2674E+00
3	6333632175119962368	0.1395	−6.8635	223.3798	−2.4777	−2.6496	0.9335	19.4622	5.6500E+00
4	6333638840909351808	0.3333	−6.7025	223.7207	−2.6044	−2.5148	1.0312	17.8252	1.3563E+01
5	6334133694157081856	0.0026	−5.8463	223.8334	−2.3926	−2.7662	1.1181	17.5348	1.2756E+01
6	6337139376694381440	−0.1242	−5.6805	223.9155	−2.4263	−2.7577	0.9366	17.4458	4.8662E+00
7	6334151110248964224	0.0510	−5.6672	224.4260	−3.1251	−2.0798	1.0594	18.7005	1.4053E+01
8	6334300162794237184	0.5529	−5.0987	224.7233	−2.7727	−1.9366	1.0851	19.0335	6.7220E+00
9	6338851453738047488	0.1009	−4.2145	224.9720	−2.6403	−2.1383	1.0813	18.4176	9.9368E+00
10	6334298169929419392	0.1771	−5.0869	224.9823	−2.4609	−2.7599	1.0623	18.1751	6.6524E+00
11	6338874990158885376	0.1463	−4.1744	225.0625	−2.7762	−2.3852	1.0872	17.7758	3.4422E+01
12	6338879564298848640	−0.0324	−4.0963	225.3011	−2.4097	−1.2524	1.1311	18.9155	4.8295E+00
13	6338859562636251904	0.2195	−4.2534	225.3258	−2.5176	−1.7848	1.1024	18.0456	3.3353E+01
14	6338880487717174528	0.0521	−4.0583	225.4573	−2.3537	−3.1365	1.1220	17.6939	1.0366E+01
15	6338869149003524224	−0.0925	−4.0479	225.5377	−3.0576	−2.0272	1.0265	19.2443	2.1193E+01
16	6339016002525065472	0.0639	−3.5563	225.7535	−2.3171	−3.4270	1.1729	19.0526	5.8216E+00
17	6338987758819995776	−0.1428	−3.6964	225.7778	−2.4940	−2.3050	1.1700	18.7510	8.4701E+01
18	6339017823591238400	0.0527	−3.5147	225.8524	−2.6521	−3.2807	1.3766	20.0483	7.4983E+00
19	6339403580374320896	0.2071	−3.2162	226.1388	−2.8443	−2.8832	1.1255	19.7879	5.9449E+00
20	6339405195282047232	0.3347	−3.1899	226.1702	−1.9488	−2.9943	1.1956	17.8007	7.7164E+00
21	6339486112465206528	0.2516	−2.9349	226.3743	−2.9628	−2.5859	1.1431	18.1520	2.8470E+01
22	6339492091059869696	0.1419	−2.7626	226.4066	−1.7571	−2.2625	1.0337	19.6753	5.6089E+00
23	6339498589346000768	−0.0427	−2.7155	226.4922	−2.9333	−2.4861	0.5547	17.4368	8.3411E+00
24	6339607745939180928	0.2627	−2.2781	226.9747	−1.9119	−2.3462	0.9989	19.5513	1.8167E+01
25	6339642724153085056	−0.4911	−1.9832	227.2439	−2.5559	−3.2388	0.7922	19.9143	5.0767E+00
26	6339639666136263040	−0.2089	−2.0898	227.2613	−2.4832	−2.1312	0.8322	17.1603	1.3918E+02
27	4418107238191732352	−0.0317	−1.9491	227.3442	−3.2361	−2.4779	0.7086	20.1749	5.3026E+00
28	4418156892309715456	0.0184	−1.5275	227.7144	−2.7810	−2.9716	0.9151	18.6426	1.2555E+01
29	4418142117622280192	−0.2247	−1.6319	227.7547	−2.2909	−2.6730	0.5875	17.3171	8.1503E+00
30	4418143968756451968	0.1305	−1.5872	227.8667	−2.7425	−2.7935	0.9761	19.4101	5.1128E+00
31	4418261930029664256	0.1726	−1.2314	227.9615	−2.4465	−2.4811	0.8722	17.4131	3.7794E+02
32	4418265022406118784	0.1443	−1.2007	227.9690	−2.5811	−2.7873	1.1245	17.1479	1.0070E+01
33	4418300339922183040	−0.2577	−0.9056	228.2730	−1.2246	−2.4189	1.1503	19.2080	5.7784E+00
34	4418296800869119488	−0.0699	−0.9458	228.3485	−2.5452	−2.5164	1.0382	18.2234	9.5543E+01
35	4418305219004364416	0.0308	−0.8191	228.4767	−2.3525	−3.1096	1.0936	18.2519	2.0354E+01
36	4418876999410407808	0.1810	−0.5154	228.4965	−2.6434	−2.8694	1.0682	18.4087	5.3204E+00
37	4418292299742718336	0.2783	−0.8791	228.5547	−3.1739	−2.0598	1.2035	18.9636	4.8350E+00
38	4418688536245813888	0.0397	−0.5523	228.5716	−2.8887	−2.5161	1.0884	17.9491	8.2213E+00
39	4418306490314700416	−0.0735	−0.7719	228.5788	−2.9618	−2.6038	1.0582	18.5771	1.1654E+01
40	4418306387235478784	0.0103	−0.7888	228.5841	−2.9801	−2.6432	1.1172	18.7119	1.0503E+01
41	4418306490314700288	0.0571	−0.7728	228.5863	−2.6047	−2.1894	1.1371	17.5508	1.8540E+02
42	4418307899063987584	0.4335	−0.7168	228.6229	−1.9881	−2.0470	0.9793	19.0673	1.4992E+01
43	4418687161856244096	−0.0988	−0.6207	228.6410	−2.4472	−2.8298	0.7099	17.1817	4.8383E+00
44	4418889815592901248	0.0445	−0.2970	228.6474	−2.2003	−2.2111	1.0924	17.7308	1.2297E+02
45	4418683485364220160	0.4711	−0.6612	228.6626	−2.3617	−3.3018	1.0654	19.4714	5.8224E+00
46	4418696404625960448	−0.5780	−0.4148	228.8240	−2.7140	−1.9526	0.7559	19.6628	6.0292E+00
47	4418692040939128832	0.2891	−0.5483	228.8315	−2.1215	−3.1551	1.1364	19.1036	8.0271E+00
48	4418698397490799232	−0.3326	−0.3732	228.9090	−2.4365	−1.7305	0.6510	20.0514	6.3760E+00
49	4418679396555391616	0.2885	−0.5816	228.9582	−2.5619	−2.6261	1.1009	18.5081	5.8196E+00
50	4418723583179057024	0.1416	−0.2626	228.9601	−2.5273	−2.7952	1.1119	17.4493	1.2010E+01
51	4418723583179058944	−0.0373	−0.2577	228.9661	−2.1354	−2.8744	1.0769	19.5808	9.7810E+00
52	4418693724566344192	0.3241	−0.4672	229.0063	−2.7870	−2.5274	1.1007	18.3871	4.6609E+00
53	4418926855391616000	−0.3033	+0.0552	229.0700	−2.0931	−2.7288	1.0322	19.2253	5.8788E+00
54	4418724923208864128	0.3599	−0.2139	229.0981	−3.3158	−2.1848	0.9962	19.1438	5.1160E+00
55	4418734165978521728	−0.0129	−0.0736	229.1446	−2.4978	−2.5807	0.4412	17.4019	5.0599E+01
56	4418727225312005504	0.1660	−0.2543	229.1711	−2.4135	−2.2349	1.0770	18.4655	2.0530E+01
57	4418726404973230080	0.1299	−0.2695	229.2028	−2.3950	−2.1456	0.8950	17.5034	7.0368E+01
58	4419023234457620352	−0.0293	+0.2043	229.2407	−2.4698	−2.3608	1.0275	17.9991	1.4207E+02
59	4419073575769649664	0.5628	+0.5239	229.3062	−1.9015	−2.2912	1.0387	18.1476	7.4501E+00
60	4419026842229420800	−0.1750	+0.2297	229.3883	−2.7700	−2.0247	1.1586	18.8187	1.6267E+01
61	4419052405874782592	0.2759	+0.3638	229.5968	−1.8983	−2.9869	1.1136	18.5392	4.7960E+00
62	4419078145614843776	0.4212	+0.6351	229.6086	−2.3773	−2.0128	1.1781	19.0422	1.5265E+01
63	4419068108275272448	−0.2572	+0.6591	229.7104	−1.4688	−2.4685	0.9486	19.7550	6.3516E+00

Table C.4: - *continued.*

N	source_id	π (mas)	δ (deg)	α (deg)	μ_δ (mas yr^{-1})	$\mu_{\alpha*}$ (mas yr^{-1})	$G_{\mathrm{BP}}-G_{\mathrm{RP}}$ (mag)	G (mag)	χ_{sel} (yr^3 deg^{-2} pc^{-1} mas^{-3})
64	4418864767344458112	−0.0649	+0.3228	229.7453	−2.1466	−2.5965	1.1113	17.9590	7.6772E+00
65	4420584403529433728	0.1415	+0.8509	229.8402	−2.4470	−1.9695	1.0419	18.6502	2.9890E+01
66	4420577943898627968	−0.5387	+0.8701	230.0352	−2.1109	−2.9124	0.9411	19.3734	5.3310E+00
67	4420385323205469568	−0.2093	+0.7329	230.1499	−2.6252	−2.1064	0.9883	18.7577	5.4691E+00
68	4420607768151633408	−0.1165	+1.1328	230.2065	−2.3018	−2.7923	1.0686	17.8563	2.3135E+01
69	4420603301385612928	−0.3072	+1.0489	230.3098	−2.7339	−2.0564	1.0515	18.1806	2.5285E+01
70	4420616289367861760	0.1482	+1.2596	230.4004	−2.1897	−2.6394	1.1677	18.6286	5.1850E+01
71	4420608562721387776	0.2343	+1.0585	230.4380	−2.4493	−2.2273	1.0231	18.2679	5.9114E+01
72	4420616048849698304	0.1699	+1.2814	230.4905	−2.0212	−1.9596	1.0675	18.3503	1.0720E+02
73	4420708888861661440	−0.3825	+1.3479	230.6310	−1.9221	−2.4611	0.9986	18.0155	2.2752E+01
74	4420717139494655360	−0.3145	+1.4909	230.9006	−2.8521	−2.1866	1.0547	17.9769	8.1542E+00
75	4420528568955338112	0.3247	+1.4158	230.9018	−1.9665	−3.1172	0.9347	18.5703	1.3916E+01
76	4420553479766045824	0.1958	+1.5626	231.0663	−1.8110	−3.3450	0.9903	19.1601	1.2707E+01
77	4420744283688076672	0.3469	+1.6499	231.0725	−2.8218	−1.8201	1.0634	18.6081	1.0371E+01
78	4420749364634207104	0.4852	+1.6694	231.1743	−2.4018	−3.7009	1.2444	19.8641	5.1075E+00
79	4421127944526566272	−0.2777	+1.8523	231.3147	−3.3017	−2.4256	0.8227	19.4204	5.1616E+00
80	4421128077670137472	−0.3001	+1.8510	231.3650	−2.1888	−3.1238	1.0839	19.0124	6.0021E+00
81	4420939958103532416	0.2914	+1.8132	231.3706	−2.4673	−1.3992	1.0720	18.7013	4.9887E+00
82	4420942432004721408	−0.5258	+1.9198	231.5243	−1.6142	−2.4104	0.9329	18.6265	2.0817E+01
83	4420974111684168320	0.7073	+2.0716	231.8210	−2.9927	−2.4544	1.0667	19.6251	5.2512E+00
84	4420970057233967360	−0.0405	+2.0212	231.8757	−2.6548	−2.9159	1.0609	18.2706	5.5142E+00
85	4420973256984758912	0.3024	+2.1114	231.9175	−3.2737	−1.8754	1.1691	19.7097	5.4066E+00
86	4420985003720258688	0.1753	+2.2946	232.0258	−1.5876	−3.0622	0.8244	20.1691	5.0991E+00
87	4420985553476080768	0.1695	+2.3329	232.0740	−2.3067	−2.7102	0.6363	19.7382	1.4372E+01
88	4421270739303308032	0.3234	+2.4940	232.0890	−1.7718	−2.4556	0.7487	17.3115	1.8315E+01
89	4421075889522936832	0.1513	+2.3026	232.1542	−1.2829	−2.2284	1.1461	18.8079	2.1412E+01
90	4420980914911383552	0.0622	+2.2497	232.1790	−1.1811	−1.6482	0.9222	19.7160	5.5746E+00
91	4421074820076313088	0.0669	+2.2627	232.2309	−2.7257	−2.5686	1.1896	19.8201	6.3718E+00
92	4421075644710040960	−0.1957	+2.3202	232.2445	−2.4874	−2.1497	1.0964	17.9998	8.3941E+01
93	4420967892569667200	0.0372	+2.1748	232.2447	−1.9914	−1.7972	1.0749	18.4407	2.0904E+01
94	4421063034685042048	0.0499	+2.2580	232.2667	−1.7235	−2.9694	1.1849	18.4620	1.1119E+01
95	4421279741554833664	−0.0775	+2.6654	232.3405	−2.6957	−1.9749	0.8748	19.0484	6.0000E+00
96	4421086261868313216	−0.3842	+2.5208	232.5209	−2.4458	−2.3528	1.0164	18.5634	1.0815E+01
97	4421118388224664448	−0.2525	+2.7875	232.5409	−1.8784	−2.6760	1.0045	18.8868	8.5105E+00
98	4421120896484661504	−0.0837	+2.7778	232.8360	−2.2849	−3.5261	1.2619	19.8009	4.7386E+00
99	4421122648831334784	0.3999	+2.8572	232.8419	−1.3443	−2.8624	1.1055	19.5430	7.7608E+00
100	4421121102643098880	−0.0570	+2.8128	232.8420	−3.1021	−2.8906	1.0554	19.5488	5.8235E+00
101	4427109146047429120	−0.0208	+2.7260	233.0561	−2.4877	−2.6084	1.0095	18.4947	2.9412E+01
102	4421056922947507584	−0.1575	+2.6563	233.0629	−1.7088	−2.6912	0.9611	17.5178	7.0492E+00
103	4427115605678338048	0.5960	+2.8795	233.0941	−1.9663	−2.2967	1.0083	19.2071	1.3374E+01
104	4427116365888010496	−0.2454	+2.9255	233.1339	−1.8015	−1.8290	0.8261	19.4928	1.3035E+01
105	4427116091010101888	−0.3001	+2.9078	233.1520	−1.6010	−2.4964	1.0085	18.9371	2.0755E+01
106	4427119350890013312	−0.2800	+2.9388	233.2521	−2.0540	−1.7483	1.0091	18.9006	9.9676E+00
107	4427149587458915328	0.2883	+3.1325	233.3049	−1.9897	−2.8823	0.9629	19.6203	6.1447E+00
108	4427072385423018112	−0.0852	+2.9171	233.4837	−1.3629	−2.5185	0.8760	19.2556	4.8170E+00
109	4427159070746889088	0.0524	+3.3349	233.5535	−2.0658	−2.0261	1.0945	18.0417	1.4151E+02
110	4427267342578834816	−0.1346	+3.4730	233.6187	−2.3678	−2.0626	1.1503	17.8807	1.5292E+01
111	4427108080895293440	−0.2145	+3.2197	233.7217	−2.6400	−1.9216	0.8551	19.9234	7.9206E+00
112	4427252391796247936	−0.4364	+3.4275	233.9223	−2.3541	−1.6143	1.0031	18.5629	8.8254E+00
113	4427286068636375552	0.1463	+3.6697	234.1154	−1.8386	−2.5410	0.8207	17.4965	4.3439E+01
114	4427242118235062400	0.3643	+3.6487	234.4303	−1.8013	−2.5729	1.2051	18.6923	3.2961E+01
115	4427620281515156608	0.0090	+3.8090	234.6403	−1.8909	−2.7907	1.0151	18.9503	2.9022E+01
116	4427616364504699264	0.5170	+3.9037	234.9541	−2.2568	−1.8675	1.1695	18.9193	7.3622E+00
117	4427617051699467264	−0.3315	+3.9052	234.9959	−1.6459	−2.7952	0.9918	19.0932	8.2553E+00
118	4427641206595577728	0.1592	+4.0049	235.1233	−3.0101	−2.6033	0.9046	19.6347	4.7413E+00
119	4427638079859372288	−0.0039	+3.9687	235.1463	−1.8371	−1.1354	0.9195	19.4172	4.6017E+00
120	4427657149514263680	−0.0730	+4.1916	235.1697	−2.0171	−3.0982	1.1434	19.2056	6.1437E+00
121	4427749061814709504	0.2200	+4.3595	235.5140	−1.6084	−3.0522	0.9691	19.2026	4.7347E+00
122	4427746076813323520	−0.0727	+4.3656	235.6363	−2.5033	−1.9675	1.1675	18.5294	1.7471E+01
123	4424743718578674688	−0.0442	+4.2818	235.9371	−2.4113	−2.2675	1.0670	17.3253	1.0274E+01
124	4424779727584949120	0.1786	+4.6100	236.2725	−1.7183	−2.3518	1.0645	18.5830	2.3745E+01
125	4426303478901609344	0.0403	+4.9487	237.0251	−2.1590	−1.7255	1.1713	18.9585	6.5246E+00
126	4426315848407518336	0.3195	+5.1591	237.1373	−1.8922	−1.9475	1.0778	18.8793	5.0225E+00

LIST OF FIGURES

LIST OF TABLES

List of Acronyms

APOGEE	Apache Point Observatory Galactic Evolution Experiment
BP	Blue Passband
EGDR3	Early *Gaia* Data Release 3
GDR2	*Gaia* Data Release 2
GOG18	*Gaia* Object Generator 18th
GUMS	*Gaia* Universe Model Snapshot
H-R	Hertzsprung–Russell
LAMOST	Large Sky Area Multi-Object Fiber Spectroscopic Telescope
LMC	Large Magellanic Cloud
LSR	Local Standard of Rest
NFW	Navarro, Frenk, and White
NGC	New General Catalogue
Pan-STARRS	Panoramic Survey Telescope and Rapid Response System
RAVE	Radial Velocity Experiment
RP	Red Passband
SDSS	Sloan Digital Sky Survey
SF	Schlafly and Finkbeiner
Sgr	Sagittarius
STILISM	Structuring by Inversion the Local Interstellar Medium
WISE	Wide-field Infrared Survey Explorer
2MASS	Two Micron All-Sky Survey